Wake dynamics of flow past a curved circular cross-section body under cross-flow vibration

Adelaide de Vecchi

Department of Aeronautics
Imperial College London
Prince Consort Road
London SW7 2BY

A thesis submitted for the degree of Doctor of Philosophy of the University of London

2009

Declaration

I declare that all the work that is contained within this thesis has been undertaken by the author and carried out at Imperial College London.

Adelaide de Vecchi

Abstract

The principal objective of this thesis was to investigate the fundamental mechanism of vortex shedding past curved oscillating bluff bodies of circular cross-section exposed to an external uniform flow.

Two different geometrical configurations have been studied: in both cases the main component of the body is a circular cylinder, whose centreline axis is prescribed by a quarter ring and the plane of curvature is aligned to the free-stream direction. According to whether the inflow is directed towards the outside or the inside of the quarter ring, two different configurations are identified, named respectively "convex" and "concave". Fully three dimensional and a sectional two-dimensional simulations were performed to assess the validity of strip theory for complex non-straight bodies. Each geometry was tested in forced and free cross-flow vibration and the outcome of these simulations was compared to the fixed body case. Forced vibration simulations rely on the assumptions of sinusoidal motion, rigid body and locked-in wake dynamics and represent a simplified approach to the study of Vortex-Induced Vibration: imposing a cross-flow displacement to the body can provide valuable information on the forces on the structure if frequencies and amplitude are set to match those of free vibrations. In the convex configuration, the forced translation generated in-phase shedding with vortices bent according to the body curvature. The sectional simulations could approximate the force distribution, but failed to capture correctly the wake topology, especially when vortex dislocations appeared in the near-wake. The lower part of the body, nearly aligned to the inflow direction, gave rise to a strong hydrodynamic damping: free vibration simulations achieved a maximum amplitude one order of magnitude smaller than the values found for a straight cylinder under the same conditions. For this reason, an oscillatory roll motion about the horizontal

extension axis was imposed as an alternative: the damping effect in the lower part of the body was inhibited and the resulting energy transfer was positive, making this type of motion a good basis for free vibration simulations.

In the absence of motion the concave geometry was found to suppress vortex shedding; the controlled oscillation disrupted the stabilising mechanism triggered by curvature and gave rise to two different vortex topologies, a wide and a narrow wake. None of these features could be reproduced with two-dimensional simulations, demonstrating the intrinsic limitation of the two-dimensional approach for curved geometries.

The present work highlights suggests that a redefinition of the lock-in boundaries for non-straight geometries should be undertaken to understand the combined influence of motion and curvature on the vortex shedding.

Acknowledgements

First and foremost I would like to thank my supervisors Prof. Mike Graham and Prof. Spencer Sherwin for their constant guidance and support over the past three years: as a result of their excellent supervision my studies at Imperial College were enjoyable and intellectually stimulating, allowing me to improve both personally and academically. I am also grateful to Dr. Richard Willden for his advice on structural dynamics and numerical issues. I would like to express my gratitude to the Engineering and Physical Sciences Research Council (EPSRC), who funded this work. The computing resources supplied by the Imperial College High Performance Computing Service are also gratefully acknowledged.

On a personal basis, I would like to thank my family and friends for their invaluable encouragement. Their enthusiasm and support have made these years some of the most enjoyable of my life and I would like to express my best wishes to them for their future. A special thank you goes to all my colleagues at Imperial College, especially to Bruno and Henrik, who helped me in the difficult moments with their experience and insight.

This thesis is dedicated to my parents, who have always encouraged and assisted me in everything I have done, helping me to maintain my motivation. I am most grateful to them for their endless support and understanding.

Contents

Abstract 1

Acknowledgements 2

Table of Contents 2

List of Figures 6

List of Tables 16

Notation 17

1 Introduction 23

1.1 Marine riser pipes overview 23

1.2 Motivation and aims 24

1.3 Synopsis 26

2 Literature review 27

2.1 Bluff body flows 27

2.2 Flow regimes for a straight cylinder in a uniform flow 30

2.2.1 Periodic laminar regime 31

2.2.1.1 Oblique and parallel shedding 33

2.2.2 Wake transition regime 35

2.2.2.1 Three-dimensional wake instabilities: Mode A and Mode B 36

2.2.2.2 Vortex dislocations in the near wake 40

2.2.3 Shear layer and boundary layer transition regimes 43
2.3 Flow past oscillating cylinders 43
2.3.1 Vortex-Induced Vibrations for flexibly mounted rigid cylinders 45
2.3.2 Force decomposition 47
2.3.3 Response branches 48
2.3.4 The concept of added mass 52
2.3.5 Modes of shedding 54
2.3.5.1 Fundamental modes: 2S, 2P, P+S 54
2.3.5.2 Other types of shedding modes: XY-motion and pivoted cylinders 56
2.3.6 Forced and free oscillations 59
2.3.7 Phase and timing of vortex shedding 63
2.4 Yawed cylinders and the Independence Principle 67
2.5 Uniform bluff bodies under shear flow 68
2.6 Bluff bodies with spanwise geometric variations 71
2.6.1 Tapered cylinders 71
2.6.2 Wavy cylinders 73

3 Problem definition **78**
3.1 Computational domain and geometrical models 79
3.1.1 Mesh generation 80
3.1.2 Boundary conditions 82
3.2 Data analysis and post-processing tools 84
3.2.1 The λ_2 criterion 84
3.2.2 Filtering the λ_2 isosurfaces 85
3.2.3 Lift force decomposition and phase angle 87

4 Computational framework **92**
4.1 Spectral/*hp* element methods 93
4.1.1 Galerkin weighted residual method 93
4.1.1.1 Solution of the one-dimensional Poisson equation . . 94
4.1.2 Expansion basis and global assembly 96

4.1.3 High-order expansion basis in the $p-$type extension 99
4.1.3.1 One-dimensional expansion basis 100
4.1.3.2 Multi-dimensional expansion basis 101
4.1.4 Error convergence 104
4.2 The Nektar code 105
4.2.1 The time-stepping scheme 105
4.2.2 Application of the $N\epsilon\kappa\tau\alpha r$ code to VIV problems 107
4.2.2.1 Coordinate transformation 108
4.2.2.2 Mathematical model for the flow and structure equations in three dimensions 108
4.2.3 Transformation of boundary conditions 110
4.2.4 Structural equation 111
4.3 Strip Theory model 112
4.3.1 The strip theory and its application to three-dimensional problems 113
4.4 The VIVIC code 113
4.4.1 Mathematical formulation 114
4.4.2 Streamfunction-velocity-vorticity method 115

5 Convex configuration **117**
5.1 Background studies: fixed cylinder in uniform flow 117
5.1.1 Effect of curvature: a three-dimensional problem 117
5.1.2 Two-dimensional simulations of the fixed cylinder case 120
5.2 Forced cross-flow vibration 122
5.2.1 Lock-in boundaries and flow regimes 124
5.2.1.1 Type A 125
5.2.1.2 Type B 132
5.2.2 Vortex shedding outside the two-dimensional lock-in region . . 134
5.2.3 Vortex dislocations at low frequencies and amplitudes 138
5.2.4 Vortex shedding phase and energy transfer 145
5.2.4.1 Effect of the frequency's variation 145

5.2.4.2 Effect of the amplitude's variation 149
5.2.5 Modified convex configurations 151
5.2.5.1 Effect of the horizontal extension 151
5.2.5.2 Effect of the radius of curvature 153
5.3 Forced cross-flow rotation 157
5.3.1 Wake topology at $f_o = 0.9f_s$ 158
5.3.2 Phase angle variation and energy transfer 160
5.4 Vortex-Induced Vibration 163
5.4.1 Free vibration simulations 164
5.4.1.1 Free translation in the cross-flow direction 164
5.4.1.2 Free rotation in the cross-flow direction 166

6 Concave configuration **170**
6.1 Background studies: fixed cylinder in uniform flow 170
6.1.1 Vortex shedding suppression 170
6.1.2 Vortex shedding resumption and weak form of shedding 172
6.2 A note on the two dimensional sectional approach 173
6.3 Forced cross-flow vibration 174
6.3.1 Lock-in boundaries and flow regimes 175
6.3.1.1 2S shedding with wide wake 176
6.3.1.2 2S shedding with narrow wake 180
6.3.1.3 Forced vibration outside the lock-in region 183
6.3.2 Effect of frequency's variation on the vortex shedding mode . 185
6.3.2.1 The onset of the wide wake mode from the steady shear layers 188
6.3.2.2 Effect of the symmetry boundary condition on the vortex shedding mode 193
6.3.3 Effect of amplitude and frequency variation on the shedding phase and energy transfer 194
6.3.4 Effect of the radius of curvature on the vortex shedding mode 198
6.4 Free vibration simulations 202

6.4.1 Results with zero structural damping 203
6.4.2 Effect of the structural damping on the vortex shedding 205

7 Conclusions **209**

References **217**

List of Figures

2.1 Filament-line sketch of the vortex formation region (Gerrard (1966)). 28

2.2 Strouhal-Reynolds number curve in the Reynolds number range $0 < Re < 10^7$ (Zdravkovich (1997). 31

2.3 Base suction coefficient variation with Reynolds number in the range $0 < Re < 10^7$ (Roshko (1993)). 32

2.4 Strouhal-Reynolds number relationship in the laminar and wake transition regime. 33

2.5 Vorticity isosurfaces for the two wake modes A and B. 37

2.6 Vorticity isosurfaces for the two quasi-periodic modes with standing waves and travelling waves. 38

2.7 Sketches of the two types of symmetry in Mode A and Mode B (Williamson (1996a)). 40

2.8 One-sided and two-sided dislocations. 41

2.9 Formation of vortex dislocations visualised through isosurfaces of spanwise and streamwise vorticity (Braza *et al.* (2001)). 42

2.10 Wake characteristic of an elastically mounted cylinder freely vibrating in air (Feng (1968)). 49

2.11 Comparison between the amplitude of response of a circular cylinder undergoing VIV in air and water. 51

2.12 Non-dimensional average peak response amplitude from DNS and experiments. 52

2.13 Map of vortex patterns for a circular cylinder forced to oscillate sinusoidally in the range $300 < Re < 1000$ (Williamson & Roshko (1988)). 55

2.14 2T shedding mode for XY motion (Jauvtis & Williamson (2004b)). . 56

2.15 Three-dimensional map of shedding modes for a pivoted cylinder in $XY-$motion (Flemming & Williamson (2005)). 57
2.16 Pivoted cylinder in $XY-$motion (Flemming & Williamson (2005)). . 58
2.17 Vorticity field for a tethered cylinder at the top of the oscillation cycle at $Re = 200$. 59
2.18 Time averaged value of the standing wave response energy versus the spanwise coordinate (Newman & Karniadakis (1997)). 63
2.19 Instantaneous streamlines and vorticity contours for $A/D = 0.4$, $Re = 1000$ and various frequencies of excitation (Lu & Dalton (1996)). . . . 64
2.20 Freely oscillating yawed cylinder at lock-in (Lucor & Karniadakis (2003)). 69
2.21 2S-2P hybrid mode of shedding past a tapered cylinder in streamwise motion (Techet *et al.* (1998)). 72
2.22 Relation between the streamwise vorticity and the wake width variation along the span (Darekar & Sherwin (2001b)). 76

3.1 Convex and concave configurations. 79
3.2 Surface triangulation and detail of the three-dimensional grid. 81
3.3 Two-dimensional mesh used in the VIVIC computations. 82
3.4 Filtering algorithm applied to isosurfaces at constant λ_2. 86
3.5 Spanwise variation of the integrated sectional lift coefficient against non-dimensional time. Convex body at $f_o = 1.1 f_s$ and $A/D = 0.5$. . . 89

4.1 Local and global expansion basis on a three-element domain Ω (Karniadakis & Sherwin (2005)). 98
4.2 Global assembly procedure to obtain the mass matrix (Karniadakis & Sherwin (2005)). 99
4.3 Shape function of the modal expansion of order $P = 5$ (Karniadakis & Sherwin (2005)). 101
4.4 Construction of a two-dimensional quadrilateral expansion of order $P = 4$ (Karniadakis & Sherwin (2005)). 102

4.5 Coordinate transformation to form an expansion basis on a triangular region (Karniadakis & Sherwin (2005)). 103
4.6 Coordinate transformation from the absolute to moving frame of reference in the case of rotation about the x axis. 109

5.1 Fixed convex body at $Re = 100$: isosurfaces at $\lambda_2 = -0.1$ and sectional lift coefficient distribution in time along the span. 118
5.2 Fixed convex body at $Re = 500$: isosurfaces at $\lambda_2 = -0.8$ and sectional lift coefficient distribution in time along the span. 119
5.3 Two-dimensional simulations for the steady convex configuration at $Re = 100$. 121
5.4 Effect of phase model on the spanwise variation of sectional lift coefficient against non-dimensional time in two-dimensional simulations. . 122
5.5 Flow states simulated for the convex body in forced vibration at $Re = 100$. 123
5.6 Wake topology for the flow past the convex body at $f_o = 1.1f_s$, $A/D = 0.5$ and time evolution of the sectional lift coefficient. 126
5.7 Shedding mechanism at $\frac{tU_\infty}{D} = 524.5$ for the case at $f_o = 1.1f_s$, $A/D = 0.5$. Isosurfaces at $\lambda_2 = -0.1$. 126
5.8 Isocontours of the v velocity component in the $y-$direction for the fixed and oscillating body. 127
5.9 Convex body at $A/D = 0.5$ and $f_o/f_s = 1.1$: lift signal at $s/D = 26.6$ and force signal given by the Morison's equation. 127
5.10 Convex body at $f_o = 1.1f_s$ and $A/d = 0.5$: spanwise variation of sectional lift coefficient against non-dimensional time (2D). 129
5.11 Convex body at $f_o = 1.1f_s$, $A/D = 0.5$: spanwise vorticity component at four different sections (3D). 130
5.12 Convex body at $f_o = 1.1f_s$, $A/D = 0.5$: spanwise vorticity component at four different sections (2D). 130

5.13 Spanwise vorticity in a section perpendicular to the inflow direction, corresponding to the bottom end of the quarter ring in the convex body. 131
5.14 Wake topology for the flow past the convex body at $f_o = 0.7f_s$, $A/D = 0.25$ and time evolution of the sectional lift coefficient. 132
5.15 Convex body at $f_o = 0.7f_s$, $A/D = 0.25$: dominant frequencies in the lift coefficient at three different spanwise locations. 133
5.16 Time evolution of the integrated lift coefficient in the case of the convex body at $f_o = 0.7f_s$, $A/D = 0.25$. 134
5.17 Time evolution of the sectional lift coefficient along the convex body's span at $f_e = 0.6f_s$ and $A/D = 0.5$. 135
5.18 Wake topology for the flow past the convex body at $f_o = 0.6f_s$, $A/D = 0.5$ and time evolution of the sectional lift coefficient. 136
5.19 Convex body at $f_o/f_s = 0.6, A/D = 0.5$: spanwise vorticity at t_1 and t_2. 137
5.20 Spanwise lift correlation coefficient in type A, B and outside the two-dimensional lock-in region. 138
5.21 Spanwise distribution of the total lift coefficient for the convex body at $A/D = 0.1$ and $f_o/f_s = 0.9$, $f_o/f_s = 0.8$ and $f_o/f_s = 0.7$ and dominant frequencies. 139
5.22 Spanwise distribution of the vortex shedding frequency for the convex body at $f_o/f_s = 0.9$, $f_o/f_s = 0.8$ and $f_o/f_s = 0.7$ and constant oscillation amplitude $A/D = 0.1$. 141
5.23 Detail of the lift coefficient distribution in time along the span of the curved part only for the convex body at $f_o/f_s = 0.7$ and $A/D = 0.1$. . 143
5.24 Convex body at $f_o/f_s = 1.1$, $A/D = 0.1$: detail of the lift coefficient distribution in time along the span of the quarter ring. 144
5.25 Wake topology for the flow past the convex body at $f_o = 0.9f_s$, $A/D = 0.1$ and time evolution of the sectional lift coefficient. 144
5.26 Convex body at $f_o = 0.9f_s$, $A/D = 0.1$: base pressure coefficient at three time instants. 145

5.27 Convex body at $A/D = 0.5$ and $A/D = 0.25$: spanwise variation of the time-averaged phase angle ϕ with the imposed frequency. 146
5.28 Convex body at $A/D = 0.5$: phase angle of total, pressure and viscous lift. 146
5.29 Convex body at $A/D = 0.5$: spanwise variation of the time-averaged lift coefficient in phase with the cylinder's velocity, CL_v, and of the total time-averaged lift coefficient, CL. 148
5.30 Convex body at $f_o = 0.7f_s$: effect of amplitude variation on the spanwise distribution of CL_v and CL. 150
5.31 Convex body at $f_o = 0.9f_s$: effect of amplitude variation on the spanwise distribution of CL_v and CL. 150
5.32 Convex body at $f_o = 1.1f_s$: effect of amplitude variation on the spanwise distribution of CL_v and CL. 150
5.33 Modified convex geometry at $f_o = 0.9f_s$ and $A/D = 0.1$: spanwise variation of sectional lift coefficient and comparison of CL_v distribution. 152
5.34 Modified convex geometry at $f_o = 1.1f_s$ and $A/D = 0.25D$ and $A/D = 0.5D$: comparison of CL_v distribution with a 10– and a 5–diameter long horizontal extension. 152
5.35 Convex body with double radius of curvature at $f_o = 1.1f_s$ and $A/D = 0.5$: wake topology. 154
5.36 Convex body with double radius of curvature at $f_o = 1.1f_s$ and $A/D = 0.5$: comparison of lift coefficient distribution. 154
5.37 Convex body with double radius of curvature at $f_o = 1.1f_s$ and $A/D = 0.5$: spanwise distribution of CL_v and CL. 155
5.38 Convex body with double radius of curvature at $f_o = 1.1f_s$ and $A/D = 0.5$: two-dimensional simulations of lift coefficient distribution. 155
5.39 Convex body at $f_o = 1.1f_s$ and $A/D = 0.5$: spanwise distribution of the time-averaged values of the vertical, normal and axial velocity component extracted $0.3D$ upstream in the radial direction. 156
5.40 Flow states simulated for the convex body in the case of forced rotation about the horizontal extension axis. 157

5.41 Forced rotation of the convex body at $f_o = 0.9f_s$: wake topology and time evolution of the integrated sectional lift coefficient. 158
5.42 Forced rotation of the convex body at $f_o = 0.9f_s$: vortex detachment dynamic. 159
5.43 Forced rotation of the convex body at two different imposed frequencies: sectional lift coefficient isocontours. 160
5.44 Effect of the oscillation frequency variation on the phase angle between lift force and displacement in forced rotation. 161
5.45 Effect of the oscillation frequency variation on the maximum lift coefficient in forced rotation. 162
5.46 Forced rotation of the convex body: moment of the lift coefficient in phase with the velocity and excitation regions. 162
5.47 Maximum amplitude of the cross-flow vibration of the convex body with $V_r = 6.77$, $m^* = 3$ and $\zeta = 0.012$. 165
5.48 Free vibration of the convex body at $V_r = 6.77$, $m^* = 3$ and $\zeta = 0.012$: wake topology and time evolution of the integrated sectional lift coefficient. 165
5.49 Maximum amplitude of the cross-flow vibration with $V_r = 6.77$, $m^* = 3$ and $\zeta = 0.0$. 166
5.50 Free rotation of the convex body at $V_r = 6.77$, $m^* = 3$ and $\zeta = 0.012$ and forced rotation at $f_o = 1.1f_s$ and $A/D = 0.5$: wake topology and time evolution of the integrated sectional lift coefficient. 167
5.51 Maximum amplitude of the transverse rotation of the convex body at $s/D = 0$ and corresponding angle of rotation. 168
5.52 Spanwise variation of phase angle ϕ and total lift coefficient CL in forced rotation with ($f_o = 1.1f_s$; $A/D = 0.5$) and in free rotation with $\zeta_T = 0.1$ and $\zeta_T = 0$ (both at $V_r = 5.5$). 169

6.1 *Left*: concave configuration at $Re = 100$, $\lambda_2 = -0.01$. *Right*: streamwise velocity in the wake and pressure distribution along the span. . . 171

6.2 Concave configuration with a 6−diameter vertical extension at $Re = 100$, $\lambda_2 = -0.01$ (left); time distribution of the integrated force coefficients at $P = 6$ (right). 173
6.3 Flow states for the concave configuration in forced cross-flow vibration, overlaid on the Willden *et al.* (2008) map obtained with two-dimensional simulations at the same Reynolds number ($Re = 100$). . 175
6.4 *Left*: wake topology past the concave configuration at $f_o = 1.1f_s$, $A/D = 0.5$ (wide wake 2S regime); isosurfaces at $\lambda_2 = -0.1$. *Right*: Time evolution of the sectional lift coefficient along the spanwise direction. 177
6.5 Forced translation of the concave body at $f_o = 1.1f_s$, $A/D = 0.5$: $\lambda_2 = -0.1$ isosurfaces overlaid on spanwise vorticity isocontours; the secondary core is visible between the two shear layers. 177
6.6 *Left*: wake topology past the concave configuration at $f_o = 1.1f_s$, $A/D = 0.1$ (wide wake 2S regime); isosurfaces at $\lambda_2 = -0.07$. *Right*: Time evolution of the sectional lift coefficient along the spanwise direction. 178
6.7 Spanwise vorticity distribution at the top of the concave body at $f_o = 1.1f_s$, $A/D = 0.1$. 179
6.8 *Left*: wake topology past the concave configuration at $f_o = 0.9f_s$, $A/D = 0.5$ (narrow wake 2S regime); isosurfaces at $\lambda_2 = -0.1$. *Right*: Time evolution of the sectional lift coefficient along the spanwise direction. 180
6.9 Forced translation of the concave body at $f_o = 0.9f_s$, $A/D = 0.5$: vorticity isocontours at $s/D = 0$ (*left*) and at $s/D = 7$ (*right*). 181
6.10 *Left*: wake topology past the concave configuration at $f_o = 0.8f_s$, $A/D = 0.5$; isosurfaces at $\lambda_2 = -0.1$. *Right*: Time evolution of the sectional lift coefficient along the spanwise direction. 181
6.11 Power spectra density of the integrated lift force coefficient for the flow past the concave body at $f_o = 0.8f_s$ and $A/D = 0.5$. 182

6.12 Power spectra density of the integrated lift force coefficient for the flow past the concave body at $f_o = 0.8f_s$ and $A/D = 0.5$. 183
6.13 *Left*: wake topology past the concave configuration at $f_o = 0.6f_s$, $A/D = 0.5$; isosurfaces at $\lambda_2 = -0.06$. *Right*: Time evolution of the sectional lift coefficient along the spanwise direction. 184
6.14 Spanwise vorticity component at $s/D = 0$ for the concave configuration with $A/D = 0.5$ and varying input frequency. 186
6.15 Spanwise vorticity component at $s/D = 7$ for the concave configuration with $A/D = 0.5$ and varying input frequency. 187
6.16 Time-averaged values of axial velocity (U_A/U_∞) and vertical velocity (w/U_∞) extracted along a line $0.3D$ downstream of the body in the radial direction. Fixed body case and forced vibration at $A/D = 0.5$ and varying oscillation frequencies. 190
6.17 Isocontours of the streamwise vorticity component ω_x extracted at $0.6D$ downstream of the body, at a time instant corresponding to the position $y = 0$. Narrow wake state at $f_o = 0.9f_s$ and $A/D = 0.5$ (*left*) and wide wake state at $f_o = 1.2f_s$ and $A/D = 0.5$ (*right*). 191
6.18 Time-averaged cross-flow velocity (v/U_∞) extracted along a line $0.3D$ downstream of the body in the radial direction. Narrow wake state at $f_o = 0.9f_s$ and $A/D = 0.5$ (*left*) and wide wake state at $f_o = 1.2f_s$ and $A/D = 0.5$ (*right*). 192
6.19 Time-averaged normal velocity (U_N/U_∞) extracted along a line $0.3D$ downstream of the body in the radial direction. Narrow wake state at $f_o = 0.9f_s$ and $A/D = 0.5$ (*left*) and wide wake state at $f_o = 1.2f_s$ and $A/D = 0.5$ (*right*). 192
6.20 Vertical velocity w isocontours. Forced translation at $A/D = 0.5$: $f_o = 0.9f_s$ (*left*) and at $f_o = 1.2f_s$ (*right*). 193

6.21 *Left*: Spanwise variation of the lift coefficient at three different imposed frequencies and $A/D = 0.5$, corresponding to the narrow wake state ($f_o = 0.8f_s$), the transitional state ($f_o = f_s$) and the wide wake state ($f_o = 1.2f_s$). *Right*: phase angle variation along the span for different input frequencies and $A/D = 0.5$. 195
6.22 Phase angle variation for $A/D = 0.1$ (*left*) and $A/D = 0.25$ (*right*). . 195
6.23 Spanwise lift correlation coefficient in the wide wake mode ($f_o = 1.2f_s$ and $A/D = 0.5$), narrow wake mode ($f_o = 0.9f_s$ and $A/D = 0.5$) and outside the two-dimensional lock-in region ($f_o = 0.6f_s$ and $A/D = 0.5$).197
6.24 Concave body with $R = 25D$ in forced vibration at $f_o = 1.1f_s$ and $A/D = 0.5$. Time evolution of the sectional lift distribution along the span (*left*) and spanwise vorticity distribution in a slice located at $s/D = 0$ (*right*). 199
6.25 Time-averaged values of axial velocity (U_A/U_∞) and vertical velocity (w/U_∞) extracted along a line $0.3D$ downstream of the body in the radial direction. Concave body with $R = 25D$ in forced vibration at $f_o = 1.1f_s$ and $A/D = 0.5$, compared to the wide and narrow wake states observed for $R = 12.5D$. 199
6.26 Time-averaged cross-flow velocity (v/U_∞) extracted along a line $0.3D$ downstream of the body in the radial direction. Concave body with $R = 25D$ in forced vibration at $f_o = 1.1f_s$ and $A/D = 0.5$. 200
6.27 Time-averaged cross-flow velocity (v/U_∞) extracted along a line $0.3D$ downstream of the body in the radial direction. Concave body with $R = 25D$ in forced vibration at $f_o = 1.1f_s$ and $A/D = 0.5$. 201
6.28 Concave body in free vibration, Case 1 with $\zeta = 0.0$. *Left*: oscillation amplitude A/D against non-dimensional time. *Right*: lift force F_y against non-dimensional time. 203
6.29 Concave body in free vibration, Case 2 with $\zeta = 0.0$. *Left*: oscillation amplitude A/D against non-dimensional time. *Right*: lift force F_y against non-dimensional time. 203

6.30 Concave body in free vibration, Case 2 with $\zeta = 0.0$. *Left*: Spanwise vorticity ω_z isocontours. *Right*: Time evolution of the sectional lift coefficient along the spanwise direction. 204
6.31 Oscillation amplitude A/D against non-dimensional time with and without structural damping ζ. *Left*: Case 1. *Right*: Case 2. 205
6.32 Wake topology isosurfaces at $\lambda_2 = -0.1$ and sectional lift coefficient distribution. *Left*: free uniform translation for Case 2 with $\zeta = 0.012$. *Right*: forced uniform translation at $f_o = 0.8f_s$ and $A/D = 0.35$. . . . 206
6.33 Comparison of the phase angle in free vibration Case 2 with $\zeta = 0.012$ and forced vibration at $f_o = 0.8f_s$ and $A/D = 0.35$. 207
6.34 Concave body in free vibration, Case 3 with $\zeta = 0.012$: oscillation amplitude A/D against non-dimensional time. 208
6.35 Concave body in free vibration, Case 3 and Case 2 with $\zeta = 0.012$. *Left*: drag force F_x against non-dimensional time. *Right*: isosurfaces for Case 3 at $\lambda_2 = -0.05$. 208

List of Tables

3.1 Overview of the different boundary condition imposed in the simulations. 83

Notation

Symbol	Definition
Roman	
A_{ij}	coordinate transformation matrix in the $ij-$plane
A/D	amplitude of oscillation
$\mathbf{a}$	acceleration vector
a_i, b_i	Fourier coefficients
c	viscous damping coefficient
c_0	critical viscous damping coefficient
C	damping matrix
C_θ	torsional damping matrix
C_a	added mass coefficient
C_D	drag coefficient
C_i	force coefficient in the $i-$direction
C_L	lift coefficient
CL_v	lift coefficient in phase with the body's velocity
CL_a	lift coefficient in phase with the body's acceleration
C_M	inertia coefficient
C_{pb}	base pressure coefficient
D	cross-sectional diameter
d'	wake width
$\mathbf{d}$	translation vector
E	mechanical energy

F_x	drag force ($x-$direction)
F_y	lift force ($y-$direction)
F_z	vertical force ($z-$direction)
f_{com}	natural frequency of the fluid/structural systems
f_n	cylinder's natural frequency (in vacuo)
f_o	oscillation frequency
f_s	Strouhal frequency
f_v	vortex shedding frequency
g_D	Dirichlet boundary condition
g_N	Neumann boundary condition
I_θ	mass moments of inertia matrix
J	Jacobian
J_e	order of the explicit time-integration scheme
J_i	order of the implicit time-integration scheme
K	stiffness matrix
K_θ	torsional stiffness matrix
KC	Keulegan-Carpenter number
k	spring stiffness coefficient
$\mathbf{L}$	linear diffusion operator
$\mathbb{L}$	linear partial differential equation
L/D	aspect ratio
M	mass matrix
M_θ	moment of the hydrodynamic forces
m	mass per unit span
m^*	mass ratio
$\mathbf{N}$	non-linear advection operator
N_{dof}	number of global degrees of freedom
N_{el}	number of elements
$\mathbf{n}$	unit outward normal
P	polynomial order
$P_p^{\alpha,\beta}$	Jacobi polynomial of order p

p_b	base pressure
p_∞	free-stream pressure
R_{ff}	correlation coefficient of the lift force
R/D	non-dimensional radius of curvature
Re	Reynolds number
Re_l	local Reynolds number
Re_N	normal Reynolds number
Q	number of quadrature points
St	Strouhal number
St_o	Strouhal number for parallel shedding
St_θ	Strouhal number for oblique shedding
St^*	universal Strouhal number (Roshko (1955))
S_{ij}	symmetric part of tensor $\nabla \mathbf{u}$
s/D	non-dimensional arc-length
$\mathbf{u}$	velocity vector
V_r	reduced velocity
v	test functions
w_i	quadrature weights
$\mathbf{x}$	spatial coordinates in the moving frame of reference
$\mathbf{x}'$	spatial coordinates in the absolute frame of reference
x, $\dot{x}$, $\ddot{x}$	in-line displacement, velocity, acceleration
y, $\dot{y}$, $\ddot{y}$	cross-flow displacement, velocity, acceleration
U_∞	free-stream velocity
U_A	axial velocity
U_N	normal component of the free-stream velocity
U_s	velocity at separation
T	period of oscillation
t^*	non-dimensional time unit

Greek

β	Stokes parameter

$\overline{\beta}$	shear parameter
Γ	circulation
Δt	time step
$\delta\Omega$	boundary of Ω
ϵ	solution error
ζ	structural damping
ζ_T	torsional structural damping
θ_i	angle of rotation about the $i-$axis
λ/D	vortex shedding wavelength
λ_1, λ_2, λ_3	eigenvalues of $\nabla\mathbf{u}$
μ	dynamic viscosity
ν	kinematic viscosity
$\boldsymbol{\xi}$, $\boldsymbol{\eta}$	general coordinates
ξ_i	quadrature points (eq. (4.23))
ρ	fluid density
$\boldsymbol{\Phi}$	global expansion mode
ϕ_o	phase angle between oscillating lift and y (also ϕ)
ϕ_s	phase angle between Strouhal lift component and y
ϕ_{press}	phase angle between pressure lift component and y
ϕ_{visc}	phase angle between viscous lift component and y
ϕ	local expansion mode
χ	parametric mapping
ψ	streamfunction (eq. (4.68)-(4.70))
ψ_o	phase angle between oscillating drag and x
ψ_s	phase angle between Strouhal drag component and x
Ω	solution domain
Ω_{st}	standard element domain
Ω_{ij}	anti-symmetric part of tensor $\nabla\mathbf{u}$
ω_x	streamwise vorticity ($x-$direction)
ω_y	vertical vorticity ($y-$direction)
ω_z	spanwise vorticity ($z-$direction)

Abbreviations

CFD	Computational Fluid Dynamics
CFL	Courant-Friedrichs-Lewy
DNS	Direct Numerical Simulation
FFT	Fast Fourier Transform
LES	Large Eddy Simulation
LHS	Left-Hand Side
RHS	Right-Hand Side
rms	root-mean square
SCR	Steel Catenary Riser
VIV	Vortex-Induced Vibration

Chapter 1

Introduction

1.1 Marine riser pipes overview

Fluid-structure interactions are important in many engineering applications. The wind can generate large and potentially dangerous forces on civil constructions, like chimneys or bridge decks, and the sea currents can similarly induce large amplitude vibrations in offshore structures, such as platforms and underwater pipelines. The understanding of the wake dynamics and force distribution on marine riser pipes is of fundamental importance for the offshore industry. The field of marine technology is an important application area for the fluid/structure interactions research: in recent years, there has been an extensive amount of studies, both experimental and numerical, aiming to provide greater insight into Vortex-Induced Vibrations (VIV) related problems, which affect flexible riser pipes. These structures are required to operate in depths up to 2000m and have a diameter up to 0.5m: due to this large aspect ratio, they are particularly sensitive to the fluid dynamic loading caused by waves and ocean currents, which induce large fluctuating forces and subsequent vibrations eventually leading to fatigue damage.

1.2 Motivation and aims

The aim of the present study is to investigate the intricate dynamics of vortex shedding past curved riser pipes of circular cross-section with the free-stream direction aligned with the plane of curvature. This problem can be classified under the vast category of bluff body flows, which have been broadly studied since the first observation of the vortex street in the wake of a cylinder made by von Kármán in 1912. The increasing need to exploit deep-water reservoirs has highlighted the lack of a complete insight into the Vortex-Induced Vibrations (VIV) dynamics on long structures such as the marine riser pipes used to convey fluids from the seabed to the sea surface. Steel catenary riser pipes and flexible pipes are being increasingly used offshore; in proximity of the touch-down point, where the pipe lies nearly parallel to the seabed, the radius of curvature can reach a limit value in the range of $12 - 13D$. In this study the radius of curvature had been set equal to $12.5D$ to simulate the riser's behaviour in such extreme condition. For deep-water reservoirs, curved pipes are generally preferred to vertical top tensioned risers, as they can accommodate larger motions of the vessels, but in spite of their practical importance, curved configurations have received much less attention in the past than straight cylinders.

A useful approach to understanding and eventually predicting a complex problem like Vortex-Induced Vibration is represented by forced vibrations simulations, in which the amplitude and the frequency of motion can be varied independently. Most of the numerical simulations presented in this work are focused on imposed cross-flow oscillations: this type of motion is in fact the most commonly induced in vortex shedding phenomena and accounts for larger amplitudes compared to in-line vibrations. Imposing a cross-flow displacement to the body can provide valuable information on the lift and drag forces on the structure if frequencies and amplitude are set to match those of free vibrations. To demonstrate this, a model for the prediction of free vibration has also been developed and the results are found to compare favourably to the forced vibration simulations. At low Reynolds numbers the wake of a cylinder is nominally two-dimensional. Nevertheless the curvature of the geome-

tries considered can introduce significant three-dimensional effects: for this reason, all the numerical simulations have been performed using a fully three-dimensional approach. However, solving the three-dimensional Navier-Stokes equations on such complex meshes at a realistic Reynolds number involves a high computational cost that can be only partially compensated by running the code in parallel. Even in this case, however, the computational requirements pose severe restriction on the feasibility of a complete parametric study of these geometries. For these reasons, a sectional approach has also been undertaken: the sectional method can provide a correct flow approximation in the case of vertical riser pipes, but its fundamental assumptions that the axial flow convection does not affect the force distribution on the body and the flow can be considered locally two-dimensional limit considerably its applicability to curved pipes, where the velocity in the spanwise direction is considerable. Two-dimensional simulations using a strip-theory based code have been performed to investigate the applicability of such approximation to the curved configurations. This is particularly relevant for industrial applications, as the computational cost involved in the two-dimensional analysis is orders of magnitude lower than the one of fully three-dimensional simulations.

The restriction dictated by the computational cost of the three-dimensional simulations strongly conditions the choice of the Reynolds number, which is set equal to 100 in all the simulations presented in this study. This is far from any realistic offshore condition, where the marine currents can reach $2m/s$ at $Re \approx 10^4 - 10^5$. However, this investigation does not represent an effort to model the fluid dynamic loading on real riser pipes, since the extremely high aspect ratio and Reynolds number of practical risers is not reproducible computationally. This study aims at understanding the basic mechanisms that govern the vortex shedding past curved bodies: the fundamental flow physics in these conditions has been investigated in forced and free vibration to understand the complex relationship between the motion of the body and the fluid dynamic loading: only once a complete picture of the problem is obtained at this low Reynolds number, the future research would be able to consider real industrial applications. However, for the reasons illustrated in the above paragraphs, the fully three-dimensional DNS is unable to provide a time

efficient approach to this problem at the current stage.

1.3 Synopsis

The motivations of the present study have been outlined, providing some important guidelines for the direction of research. The remainder of this thesis is organised as follows:

- Chapter 2 provides an overview of the past literature on bluff body flows; besides the fundamental studies on straight cylinders, research on wavy, tapered and yawed cylinders in free and forced vibration is also presented, since these geometrical variations will provide a good basis for understanding the flow physics in the case of curved bodies.

- Chapters 3 and 4 define the geometrical problem and the numerical framework. The mesh generation process is briefly described in chapter 3, together with the data analysis tools and some post-processing issues. Chapter 4 presents the numerical methods used by the three-dimensional code and by the strip theory code.

- Chapters 5 and 6 present and discuss the results of forced and free vibration simulations: the first geometrical configuration, named convex body, is analysed in chapter 5, whereas chapter 6 examines the flow dynamics in the concave concave configuration. A brief overview of the results previously obtained with stationary curved cylinders in the two configurations is also given at the beginning of each chapter.

- Finally, conclusions on the work presented are drawn in chapter 7.

Chapter 2

Literature review

2.1 Bluff body flows

The complexity of bluff body wakes and their direct engineering significance have lead to a remarkable surge of research since the first observations of this phenomenon at the beginning of the past century. In 1912, von Kármán (1912) analysed the stability of an infinite vortex street, consisting of two arrays of oppositely signed vortices in the absence of a body. He observed that the stability of this vortex street was intrinsically related to its configuration: only one specific antisymmetric geometry exhibited neutral stability when the ratio between the inter-vortices distance in one row to the distance between the rows attained a value of 0.28056. This first analysis triggered a considerable number of later investigations on stability of vortex arrays; however, the mechanism that leads to the vortex formation could only be studied considering the presence of a bluff body in the flow.

When such a body is exposed to a fluid stream, an extensive region of separated flow is generated over a large part of its surface; the extent of this disturbed flow region is strongly dependent on geometric factors, such as the shape and orientation of the body, and flow characteristics. However, the basic mechanism of vortex shedding past all bluff bodies has some common features, despite differences in shape and size: the boundary layers are subjected to a favourable pressure gradient, followed by a region of adverse pressure that causes separation when the local velocity

is greater than the free-stream one (Bearman (1998)). In the particular case of a cylinder with circular cross-section, the separation points are not fixed due to the lack of sharp edges and can move in response to the flow characteristics.

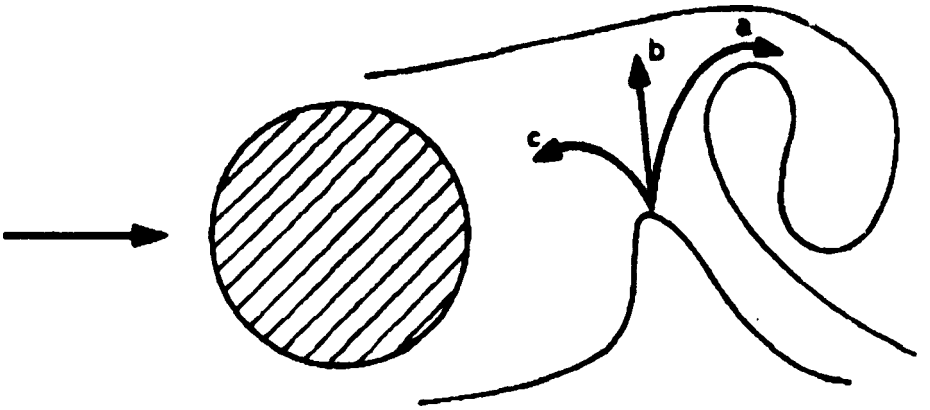


Figure 2.1: Filament-line sketch of the vortex formation region (Gerrard (1966)).

When the Reynolds number, $Re = \frac{U_\infty D}{\nu}$, reaches a critical value, instabilities start to develop in the wake and vortex shedding is initiated, with regions of vorticity shed from alternating sides of the body in a periodic fashion. The mechanics of this phenomenon have been described by Gerrard (1966) in terms of "variations of entrainment of vorticity-bearing fluid" in the shear layers. The growing vortex is fed by circulation from the shear layer, until it becomes strong enough to draw the opposite shear layer across the wake: this instant is schematically represented in figure 2.1. Part of the fluid is then directed to the interior of the formation region (labelled 'c' in figure 2.1), while the remaining is entrained by the growing vortex ('a') and by the shear layer that feeds it ('b'). When the percentage of this displaced, oppositely signed, vorticity is large enough to cut the supply of circulation, the vortex detaches from the corresponding shear layer and a similar process starts on the other side of the body. This fundamental mechanism is present in different types of flow, "irrespective of whether the separating boundary layers are laminar or turbulent" (Bearman (1984)), as it is an intrinsic characteristic of bluff bodies wakes.

The fundamental frequency, f_s, arises principally from the wake instability and is a key parameter in the study of vortex-induced vibrations problems. This is defined

as the frequency of a complete cycle of shedding for a non-vibrating body and can be expressed more conveniently in a non-dimensional way, the Strouhal number St:

$$St = \frac{f_s D}{U_\infty} \tag{2.1}$$

where D is the characteristic length of the bluff body and U_∞ the free-stream velocity. Roshko (1955) defined a universal Strouhal number based on the wake parameters instead of the bluff body characteristic length:

$$St^* = \frac{f_s d'}{U_s} \tag{2.2}$$

where d' is the wake width and U_s is the velocity at separation. Similarly Bearman (1967b) defined a Strouhal number based on the lateral displacement between the vortex rows as characteristic length. The relationship between Re and St is quite complex and depends on many factors, including the type of shedding and the end conditions of the cylinder; this will be further discussed in the next section, where the effect of increasing the Reynolds number and the corresponding flow regimes are presented.

As previously mentioned, the vortex shedding induces fluctuating forces on the body and, if it is non-rigid, causes it to oscillate in the transverse and in-line direction. In the following chapters, the fluid dynamic forces in the x and y direction, F_x and F_y, are reduced to the dimensionless coefficients, C_L and C_D for lift and drag, respectively:

$$C_L = \frac{F_y}{\frac{1}{2}\rho U_\infty^2 D} \qquad C_D = \frac{F_x}{\frac{1}{2}\rho U_\infty^2 D} \tag{2.3}$$

where ρ is the fluid density, U_∞ the free-stream velocity and D the cylinder diameter. Similarly, the base pressure coefficient is defined as:

$$C_{pb} = \frac{p_b - p_\infty}{\frac{1}{2}\rho U_\infty^2} \tag{2.4}$$

where p_b is the base pressure measured at 180° from the stagnation point and p_∞ the free-stream pressure. This parameter dominates the pressure drag generated by

the pressure drop at the rear of the bluff body during the process of vortex shedding and it is therefore very sensitive to changes in the vortex dynamics.

2.2 Flow regimes for a straight cylinder in a uniform flow

The transition to turbulence occurs in different stages and areas of the disturbed flow region: as the Reynolds number is increased, the instabilities first develop in the far wake, then move upstream in the shear layers, until they propagate into the boundary layer. At this stage, the flow is fully three-dimensional and turbulent. During this process, several regimes based on Re can be identified, resulting in different flow structures.

An initial categorisation of the flow regimes for a stationary circular cylinder was given by Roshko (1954). He identified a stable laminar regime in the range $40 < Re < 150$, characterised by periodic vortex shedding, followed by a transition regime for $150 < Re < 300$ and by an 'irregular' regime for $300 < Re < 10^4+$. The Strouhal number was found to increase monotonically in the laminar regime, whereas it remained approximately constant throughout the transition regime; finally, in the 'irregular' regime it exhibited an erratic behaviour. Figure 2.2 shows the Strouhal-Reynolds number curve over all the flow regimes, while the base suction coefficient variation with the Reynolds number is presented in figure 2.3. However, it should be noted that the Reynolds number can be considered a governing parameter only for disturbance-free flows, as disturbances can trigger transitions and generate many kind of irregular flow patterns that cannot be classified into distinct regimes.

Two key concepts are also relevant to the discussion of vortex shedding regimes: the vortex formation length and the mean recirculation region. One may define a vortex formation length as the point in the wake of the body where the velocity fluctuation level has attained a maximum and thereafter decays downstream (see Bearman (1965) and also the definition given by Bloor (1964)). Consistent with findings in experiments on cylinders fitted with splitter plates (Roshko (1955) and

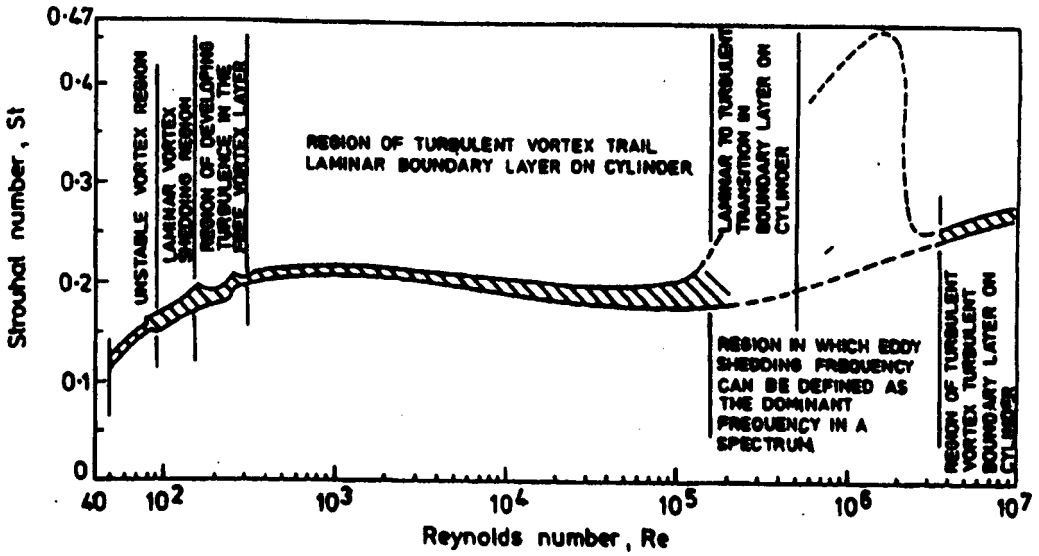


Figure 2.2: Strouhal-Reynolds number curve in the Reynolds number range $0 < Re < 10^7$ (Zdravkovich (1997)).

Bearman (1965)), the length of this region is found to scale inversely with this maximum and with the base suction, as well as with the shedding frequency. The mean recirculation region can be defined as the surface where the forces from shear stresses and pressure are in equilibrium in the mean: the resulting bubble is symmetric and closed. This balance plays a crucial role in the wake transition regime: section 2.2.2 will provide more insight on this point.

Accurate descriptions of the flow regimes for a disturbance-free flow past a straight cylinder can be found in Zdravkovich (1997) and Williamson (1996b). This section will provide an overview of these regimes, with special focus on the low Reynolds number states that are pertinent to the present investigation.

2.2.1 Periodic laminar regime

Henderson (1995) performed numerical simulations to identify the critical Reynolds number that demarcates the onset of vortex shedding. A Hopf bifurcation was found to occur at $Re = 45-50$, after which no steady state solution could be achieved: this change was marked by a sharp transition in the drag and base pressure coefficient curve.

For Reynolds numbers above the critical value, the instability in the near wake

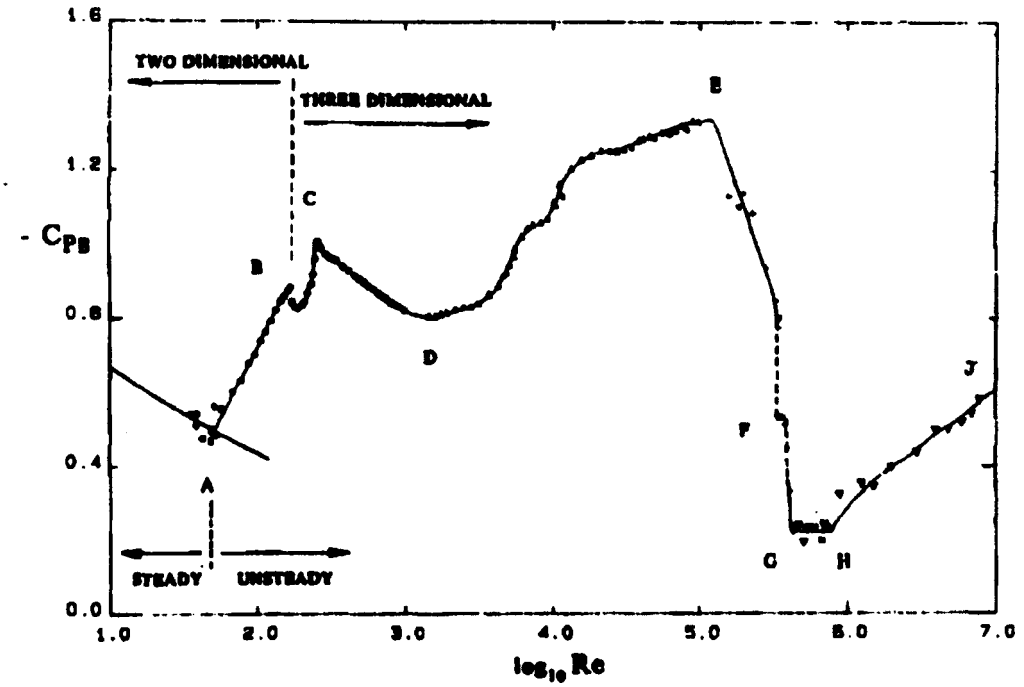


Figure 2.3: Base suction coefficient variation with Reynolds number in the range $0 < Re < 10^7$ (Roshko (1993)). The symbols refer to experimental and numerical data, while the solid line for $Re < 49$ comes from the numerical simulations performed by Henderson (1995) (laminar steady regime).

grows and a sinusoidal oscillation starts to develop, leading to a mutual interaction of the shear layers. The range $47 \leq Re \leq 180 - 200$ is characterised by a laminar and periodic vortex shedding. This process is initiated at the downstream end of the recirculation region, where a monotonic increase in the amplitude of maximum wake velocity fluctuation is observed with increasing Re, together with a gradual contraction of the formation length. The inception of the wake instability is associated with sinuous waves travelling downstream on the sides of the recirculation region, as pointed out by Gerrard (1978). As the laminar instability grows the Reynolds stresses in the near wake region increase and the recirculation cells shorten; a further increase in the Reynolds number causes the oscillating recirculation cells to detach from the rear of the cylinder, forming a staggered array of laminar vortices. This process is accompanied by a consistent increase in the base suction and in the unsteady forces, such as base drag and lift. At this stage, the flow is two-dimensional only if all eddy filaments are parallel to the cylinder's axis: this is referred to as

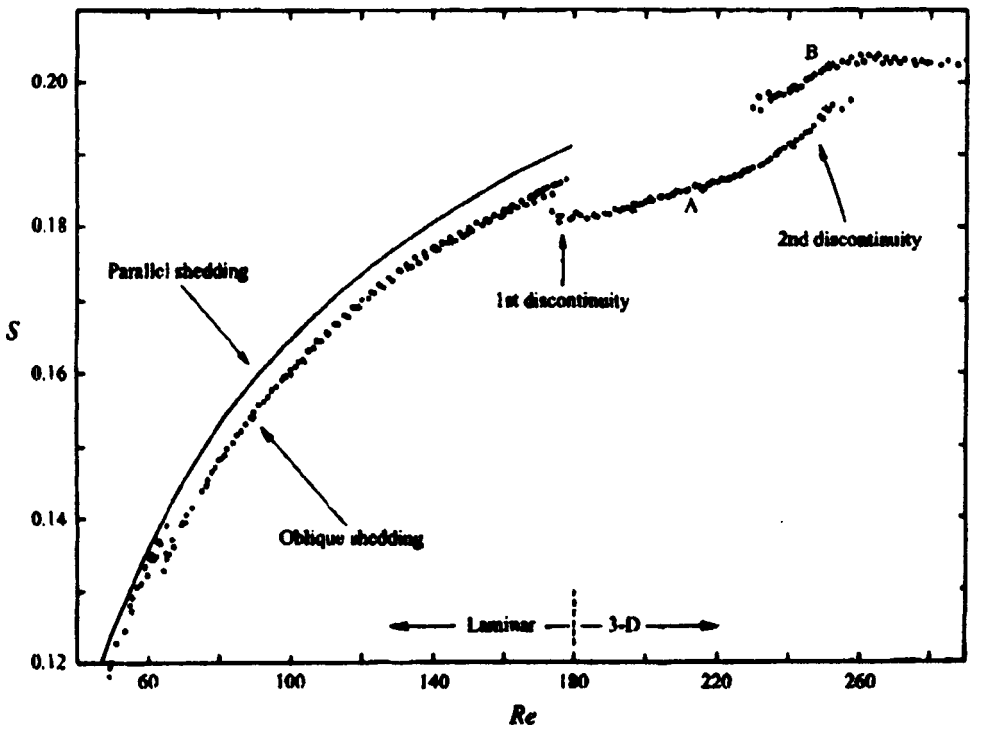


Figure 2.4: Strouhal-Reynolds number relationship in the laminar and wake transition regime (Williamson (1989)).

parallel shedding and corresponds to the continuous line in figure 2.4. When this condition is not fulfilled, the vortices are shed in an oblique way, corresponding to the dotted line in the same plot: however, in both cases the Strouhal number is found to increase monotonically with the Reynolds number (see figures 2.3 and 2.4).

2.2.1.1 Oblique and parallel shedding

One of the first observations of a discontinuity in the $St - Re$ curve was documented by Tritton (1959), who postulated the existence of two distinct modes of shedding, corresponding to two different Strouhal curves: he suggested that the discontinuity was caused by a transition from a near wake instability to an instability originating in the immediate vicinity of the cylinder, as the Reynolds number was increased above 100. Similarly, Berger & Wille (1972) related the discontinuity to the existence of two intrinsic modes of shedding and suggested that the level of turbulence in the free-stream determined the jump at a given Reynolds number.

Later investigations carried out by Gaster (1971) related the discontinuity in

the $St - Re$ curve to non-uniformities in the free-stream flow. In his experiment, spanwise cells of different frequency were found to occur by forcing the flow to be non-uniform along the span of the cylinder: variations of flow speed resulted in spanwise translation of the frequency cells and a Strouhal discontinuity was observed under these conditions. This discontinuity disappeared when the cylinder was fitted with small end-plates that limited the spanwise movement of the frequency cells.

On a different note, Van Atta & Gharib (1987) suggested that the presence of some Strouhal discontinuities was directly related to the cylinder's vibrations: by damping the cylinder's supports, they were able to suppress some Strouhal discontinuities and these findings lent credence to the existence of a continuous $St - Re$ plot if the cylinder was kept absolutely fixed. Two-dimensional numerical simulations performed by Karniadakis & Triantafillou (1989) confirmed the existence of a continuous $St - Re$ curve over the range $40 < Re < 250$, when the flow is two-dimensional.

A considerable number of investigations tried to shed light on whether the Strouhal discontinuity in the laminar shedding regime should be considered as an intrinsic phenomenon or be associated with the upstream flow conditions. Finally, Williamson (1989) demonstrated that the Strouhal discontinuity exists and is not due to any of the previously proposed mechanisms: instead, it is caused by a transition from one oblique shedding mode to another oblique mode. This transition was found to be related to the end boundary conditions and occurred at a Reynolds number of approximately 64. Above this value, an oblique shedding mode, labelled 'chevron pattern', appeared in the wake with slantwise vortices shed at one dominant frequency across the whole span. For Reynolds number below the discontinuity, a central cell with a frequency corresponding to the Strouhal value in the upper curve appeared between two cells of lower frequency (lower Strouhal curve): this mode of shedding is therefore associated with the presence of vortex dislocations, which are periodically formed when cells of different frequency move out of phase with each other. The phenomenon of oblique shedding was found to be entirely dependent on the end effects: in the initial phase of the experiment, the vortex shedding appeared parallel to the cylinder's axis and only at a later stage, when the influence

of the end effects became more significant, an oblique front propagated along the span from each end, eventually resulting in the chevron pattern. This suggested that the parallel mode is the most unstable one. According to the experimental findings of Hammache & Gharib (1991), the oblique shedding is the outcome of a pressure gradient at the rear of the cylinder caused by the pressure difference between the cylinder's ends; subsequently, the oblique shedding mode is characterised by the spanwise velocity component induced by this pressure difference. By placing control cylinders upstream of the test cylinder, a uniform pressure distribution was obtained across the span and consequently parallel shedding was achieved: this supported the conclusion that the parallel shedding mode can be considered as a truly two-dimensional type of vortex shedding, in absence of axial flow in the cores. It has been proved that the relationship between St and Re in the laminar periodic regime is highly dependent on the shedding angle and that this parameter can be controlled by manipulating the end conditions, i.e. by adding angled end plates at both extremities of the body to induce parallel shedding (Williamson (1989)). Similar results have been obtained by Eisenlohr & Ecklemann (1989) using two short cylinders of different diameter and by Williamson (1992) through the application of suction at both ends. Williamson (1989) also proved that the experimental curves associated with different shedding angles θ can be collapsed onto the parallel curve using the relationship:

$$St_o = St_\theta / \cos\theta \tag{2.5}$$

In a similar way, Hammache & Gharib (1989) showed that a continuous $St - Re$ curve could be attained once parallel shedding was induced.

2.2.2 Wake transition regime

For Reynolds numbers between $180 - 200$ and $350 - 400$ the vortices are still shed in a laminar and regular fashion: however, they become irregular and transitional further downstream and the two-dimensional state can no longer be preserved in the wake, even with careful control of the spanwise end conditions. This change

from laminar to three-dimensional shedding is hysteretic and is associated with a sudden fall in the Strouhal number and in the base suction coefficient, as highlighted by point B in figure 2.3. The lower transitional regime involves two successive stages in the vortex formation process: first, three-dimensional structures appear in the wake in the form of vortex loops at $Re \approx 180$, then the scale of these three-dimensionalities changes and smaller streamwise vortices are generated from the original loops. These two modes of instability have been labelled Mode A and Mode B by Williamson (see Williamson (1989, 1996b,a)) and are associated with discontinuities in the $St - Re$ curve illustrated in figure 2.4. Although both modes involve the formation of streamwise vortex pairs (that are then subject to stretching in the streamwise direction) their dynamics is significantly different.

2.2.2.1 Three-dimensional wake instabilities: Mode A and Mode B

Mode A is visualised through vorticity isosurfaces in figure 2.5 *left*. It exhibits a spanwise wavelength of the order of $3 - 4$ diameters and thus scales on the primary Kármán vortex: it appears to be the result of an elliptical instability of the near wake primary cores, which deform in a wavy fashion along their length, giving rise to vortex loops and streamwise vortex pairs (described as "fingers of dye" by Gerrard). The formation mechanism is self-sustaining and has been discussed in detail by Mittal & Balachandar (1995), who also proposed an "auto-generation" process for the streamwise vortices. Mode A also exhibits an out-of-phase symmetry of the streamwise vortex array, depicted in figure 2.7. This is a direct consequence of the physical mechanism where segments of the primary vortex are pulled back upstream of the shed core as this travels downstream and cause a delay in some spanwise portions of the newly formed vortex, by Biot-Savart induction (Williamson (1996a)). As shown in figure 2.4, the first discontinuity associated with Mode A involves a drop in the shedding frequency at $Re \approx 180$: however, due to the hysteretic nature of the transition, this critical value depends on whether the free-stream velocity is increased or decreased. As Re is further increased, the system response follows the curve A. This new lower pattern represents a combination of the small-scale instabilities typical of Mode A and vortex dislocations, which are triggered at some

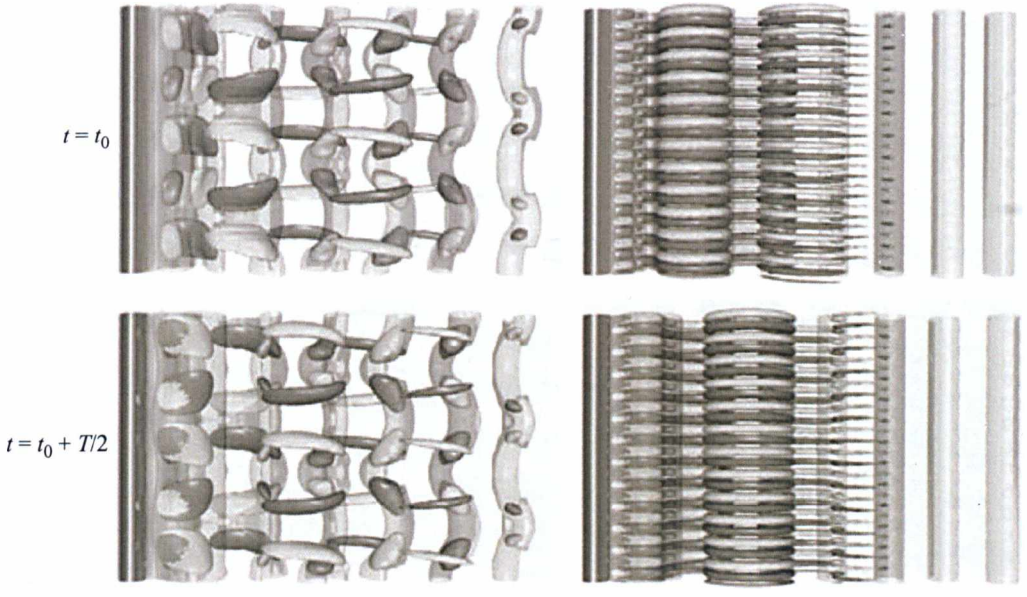


Figure 2.5: Vorticity isosurfaces for the two wake modes A (*left*) and B (*right*). Translucent isosurfaces are for the spanwise vorticity component, solid isosurfaces are for the streamwise component (Blackburn *et al.* (2005)).

sites of vortex loop and then evolve spontaneously in the wake.

The reduced spanwise coherency in the primary vortex causes a decrease of base suction and Reynolds stresses, as well as an increase of the formation length and the jump in the Strouhal number mentioned above. Interestingly, the Floquet analysis conducted by Barkley & Henderson (1996) showed that no new temporal frequency is introduced at the secondary instability: the discontinuity in the Strouhal number is hence to be directly related to the presence of non-linear phenomena such as vortex dislocations, rather than to a linear effect of the instability. This is an important feature of this regime and will be discussed further in section 2.2.2.2.

The nature of Mode B is markedly different, as can be noticed in figure 2.5 *right*. It takes place through a gradual shift of energy from Mode A over a wider range of Reynolds numbers (from 230 to 260 approximately) and the transition is not hysteretic. Williamson (1996a) suggested that during this interval of Re there is an intermittent swapping between Mode A and B, rather than the coexistence of the two. As shown in figure 2.7, Mode B involves an in-phase symmetry of the streamwise vortex array, which results in an in-line arrangements of streamwise vortices with a

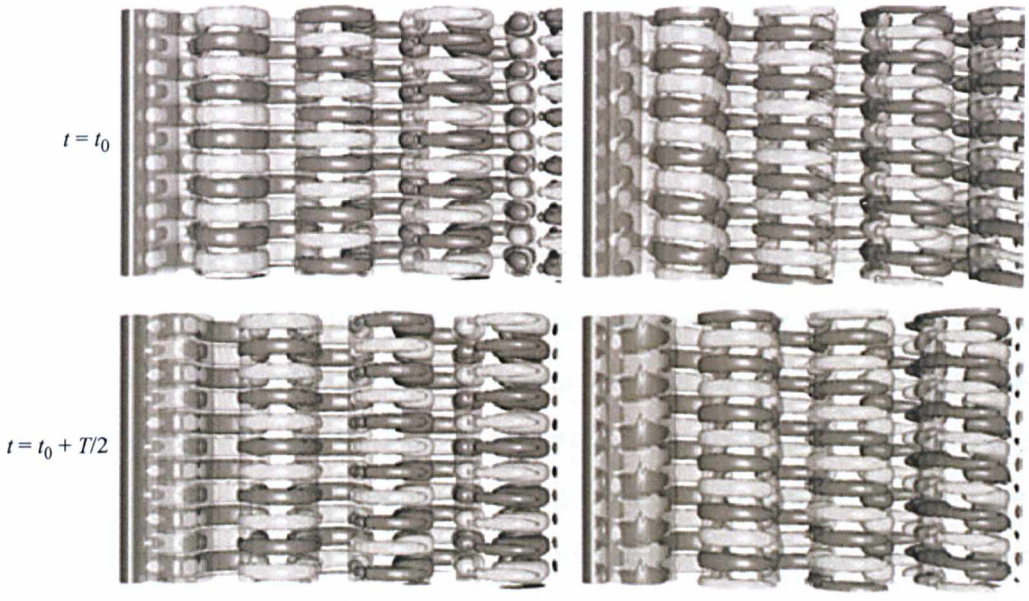


Figure 2.6: Vorticity isosurfaces for the two quasi-periodic modes with standing waves (*left*) and travelling waves *right*) at $Re = 400$. Translucent isosurfaces are for the spanwise vorticity component, solid isosurfaces are for the streamwise component (Blackburn *et al.* (2005)).

spanwise wavelength of about 1 diameter, as opposed to the out-of-phase symmetry of Mode A. Therefore, Mode B scales on flow structures like the braid shear layer: it entails finer streamwise vorticity in the braid region that connects the Karman vortices, as opposed to Mode A, in which the concentration of vorticity occurs in the primary cores. This observation was also supported by the experimental work of Brede *et al.* (1996), who studied the different modes of vortex shedding at Reynolds numbers between 160 and 500.

Another important result concerning the symmetry of the two modes was obtained by Blackburn *et al.* (2005) (see figure 2.5). They found that Mode A preserves the spatio-temporal symmetry of the wake, while Mode B breaks it. Full details of the Floquet stability analysis can also be found in Elston *et al.* (2006). When only one parameter is varied (i.e. the Reynolds number), three different bifurcations are possible in the passage from two-dimensional to three-dimensional flow: the long and short wavelength instabilities in the wake, Modes A and B respectively, are synchronous with real Floquet multipliers and represent a primary and secondary bifurcation. The third mode is a quasi-periodic state, which is not critical in this

range of Reynolds numbers (up to 280 approximately) but becomes unstable at $Re \approx 377$ and gives rise either to a modulated travelling wave or to a modulated standing wave, as illustrated in figure 2.6 (see also Blackburn & Henderson (1999)).

On the computational side, a complete investigation of the onset of Mode A and Mode B was carried out by Barkley & Henderson (1996), who performed a highly accurate global stability analysis of the wake past a circular cylinder for Reynolds numbers between 140 and 300. The two-dimensional wake was found to become absolutely linearly unstable to three-dimensional perturbations at $Re = 188.5 \pm 1.0$, when a secondary instability corresponding to Mode A developed in the wake with a critical wavelength of 3.96 ± 0.02. The critical Reynolds number for the secondary bifurcation to Mode B coincided with $Re = 259$ and the corresponding wavelength was 0.822 diameters. If the linear stability theory could give a description of Mode A bifurcation in excellent agreement with experimental findings, the transition to Mode B appeared more problematic to compare with experiments, since at this second critical Reynolds number the flow is already unstable to Mode A: this bifurcation cannot reach an equilibrium consisting solely of Mode B because it is also unstable to longer wavelength perturbations. Barkley & Henderson (1996) suggested that the two modes coexisted in the wake over this range of Reynolds numbers, supporting the conclusions of Thompson *et al.* (1996) and Williamson (1996a).

In order to understand which modes are intrinsic to the shedding in this regime and which are artifacts of experimental conditions, Leweke & Provansal (1995) studied the flow past a ring, which can be considered as a body without ends. They found that Mode B does not appear in this configuration and the lower $St-Re$ curve is continuous. Therefore they concluded that only Mode A is an intrinsic feature of three-dimensional shedding. This view is not supported by Williamson (1992), who reached opposite conclusions observing that the second discontinuity can be removed by altering the end condition to artificially induce dislocations: in this case the experimental curve was found to closely match the data obtained by Leweke & Provansal (1995).

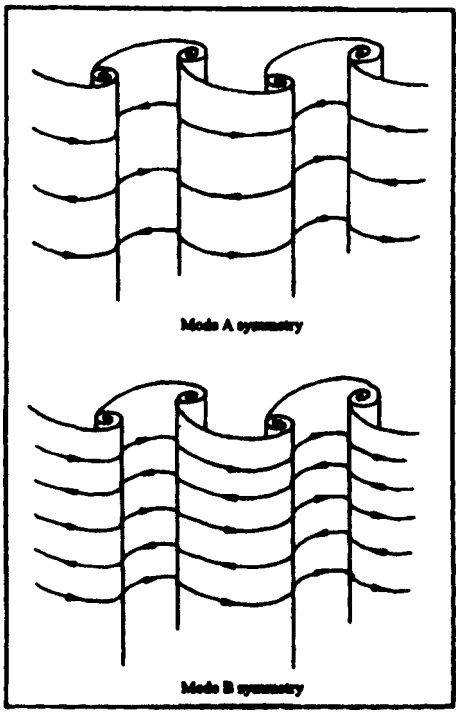


Figure 2.7: Sketches of the two types of symmetry in Mode A and Mode B (Williamson (1996a)).

2.2.2.2 Vortex dislocations in the near wake

As mentioned in the previous section, the wake transition regime is characterised by the presence of vortex dislocations in the flow states corresponding to the curve A in figure 2.4. This phenomenon was observed by Eisenlohr & Ecklemann (1989), who described it as a 'vortex splitting' process where "vortex filaments of one core split apart to merge into the offset cores of other vortices": this implied a spanwise variation of the shedding frequency and subsequently the onset of oblique shedding modes: when the oblique angle became too large or the cores too bent, vortex splitting was observed in the wake.

Although vortex dislocations are an inherent feature of the three-dimensional wake transition, their presence has also been observed in the laminar vortex shedding regime, where they appeared in a more ordered and periodic fashion than in the transition regime. As noted by Eisenlohr & Ecklemann (1989) and Williamson (1988, 1989), this phenomenon is associated with the presence of oblique shedding and is hence strictly related to the end conditions of the experiments. Williamson (1992) analysed the natural and forced formation of vortex dislocations in the laminar

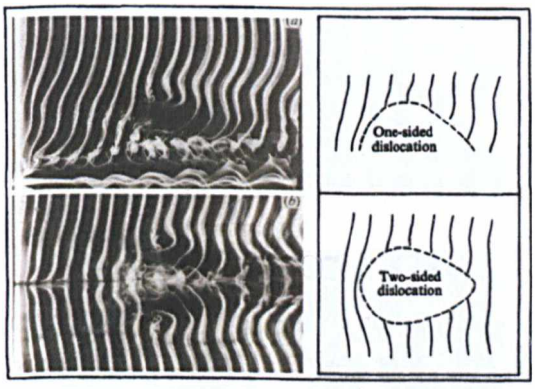


Figure 2.8: One-sided dislocations, due to a lower frequency cell near the end, and two-sided dislocations, due to a lower frequency cell in the centre, (Williamson (1992)).

regime using a small ring disturbance to trigger this mechanism at a local spanwise position. He provided experimental evidence that dislocations appear between cells of different frequency and involve vortex splitting, whereby a vortex of one sign in one cell is divided and linked to two vortices of the same sign in the other cell: this mechanism occurs at a beat frequency $f_1 - f_2$, where f_1 and f_2 are the shedding frequencies in the two cells, and involves helical twisting of the vortex lines within a vortex, inducing an axial core flow outwards from the dislocation. Interestingly, the dislocation frequency was found to decrease with decreasing ring diameter. The downstream growth of the dislocations caused large velocity fluctuations at low frequency and was associated with the relatively slow decay of fluctuation energy, as compared with the laminar wake without dislocations. Williamson (1992) also observed that two types of disturbances may occur in the wake (see figure 2.8). When the growth of the loops causes a local delay in the primary core shedding, that falls out of phase with the rest of the vortex at each spanwise side, a 'two-sided' dislocation occurs naturally and independently of the end conditions. This type of dislocation is symmetric and should not be confused with the asymmetric one observed by Eisenlohr & Ecklemann (1989) and Gerich & Ecklemann (1982), which is due to the cellular shedding near the ends and is thus labelled 'one-sided': being associated with the presence of end effects, this latter type has also been observed in the laminar shedding regime, as opposed to the two-sided dislocations, whose natural occurrence is encountered more often in the wake transition regime.

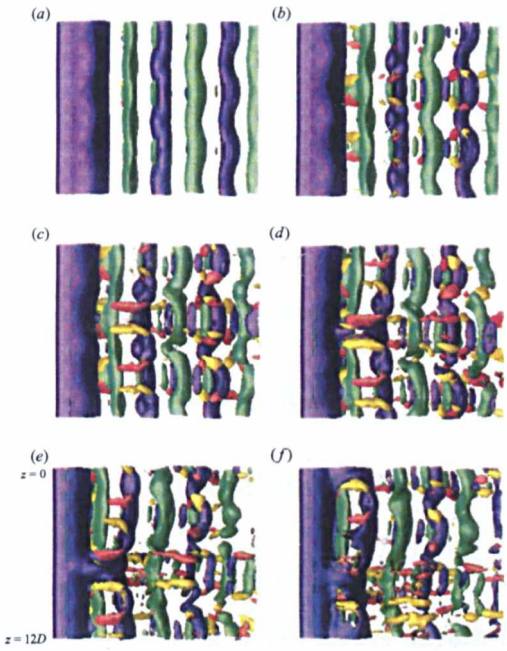


Figure 2.9: Formation of vortex dislocations visualised through isosurfaces of spanwise and streamwise vorticity (Braza *et al.* (2001)).

The role of dislocation in the three-dimensional wake transition was also investigated by Braza *et al.* (2001), who numerically simulated the transition features of the flow past a straight cylinder at $Re = 220$. Their study showed the existence of a transitional stage that was initiated by the amplification of the spanwise velocity component and its distribution into distinct regular cells along the cylinder span. The subsequent creation of streamwise and normal vorticity resulted in a regular spanwise undulation that was related to the passage of vortex dislocations in the near wake. This phenomenon was associated with a drastic fundamental frequency reduction and occurred long after the full development of Mode A pattern, as shown in figure 2.9. Braza *et al.* (2001) confirmed that the existence of vortex dislocation is an inherent feature of flow transition, as previously suggested by Williamson (1992). As a result of the formation mechanism described above, vortex dislocations may be triggered also by non-uniform flows (i.e. shear flows) past uniform cylinders and by uniform flows past non-uniform geometries, such as tapered cylinders or cones. This is a relevant point to this work and will be considered in section 2.5 and 2.6.1.

2.2.3 Shear layer and boundary layer transition regimes

The flow state after point C in figure 2.3 was defined by Roshko (1954) as the 'irregular' regime. A closer analysis reveals the existence of three different sub-regimes, outlined as follows:

- $260 < Re < 2 \times 10^5$: sub-critical regime (C-E)
- $2 \times 10^5 < Re < 10^6$: critical regime (E-H)
- $Re > 10^6$: super-critical regime (beyond H)

In the sub-critical regime, the wake is fully turbulent and the transition occurs in the shear layers, leaving the attached boundary layers laminar. In this regime, the formation length is found to increase between point C and D and to decrease between points D and E.

As the Reynolds number reaches the critical value at point E, the base suction and drag coefficients decrease drastically: the transition to turbulence occurs in the free shear layers and is associated with the formation of thin separation-reattachment bubbles on either side of the cylinder (with the only exception of point F, at which the bubble forms on only one side of the body, resulting in a non-zero mean lift coefficient, see Bearman (1969)). This causes the turbulent boundary layers to separate much further downstream, at an angle from the stagnation point $\theta \approx 140°$, giving rise to a much narrower wake than in the previous regime and generating the so-called 'drag crisis'.

Finally, the transition points move further upstream into the boundary layers, which separate at $\theta \approx 120°$; this results in a narrow wake and in a new increase in the base suction coefficient.

2.3 Flow past oscillating cylinders

One of the most important effects of the interaction between body motion and vortex shedding occurs when the fluid and structural systems respond at the same frequency: this complex non-linear phenomenon is generally referred to as 'lock-in'.

In this condition the loading on the surface of the cylinder may be critical, as a result of the stronger coupling of the flow in the spanwise direction and of the subsequent increase in the fluctuating forces acting on the body.

Several simulations have demonstrated that two-dimensional stationary bodies in steady flows are unlikely to shed two-dimensional vortices due to the spanwise variation of unsteady quantities such as fluctuating surface pressure or sectional lift force (see Bearman & Obasaju (1982); Bearman (1984)). An accurate measure of the degree of three-dimensionality present in the near wake is given by the correlation length: if the body oscillates, either freely or due to an imposed motion, this parameter increases and the coupling of the flow in the spanwise direction becomes stronger, resulting in a more nearly two-dimensional form of shedding. This is particularly evident at lock-in, when the longer correlation length leads to an increase in the unsteady forces and the contraction of the formation region causes the vortices (whose strength is now larger compared to its value for a stationary body) to be shed closer to the cylinder. On this ground, a large number of numerical simulations in the lock-in range has been performed using two-dimensional codes. Their reliability in the presence of three-dimensionality is however open to question, as it is not yet fully understood to what extent the effect of motion can suppress the three-dimensional structures in the near wake; an interesting comparison of the predictions from two-dimensional, three-dimensional and Fourier computations can be found in Blackburn (1998); Blackburn & Karniadakis (1993); Blackburn *et al.* (2000).

The common occurrence of VIV in typical engineering bluff body applications and its potentially dangerous consequences make the understanding of this phenomenon extremely important. The following sections outline the principal features of vortex shedding in Vortex-Induced Vibrations and forced oscillation problems.

2.3.1 Vortex-Induced Vibrations for flexibly mounted rigid cylinders

In this section we restrict our attention to the problem of transverse vibration of an elastically supported rigid body. This can be modelled using a single degree of freedom cylinder with linear spring and damping placed normal to an inflow with free-stream velocity U_∞. The equation of motion is given by:

$$m\ddot{y} + c\dot{y} + ky = F_y(t) \tag{2.6}$$

where y is the displacement of the cylinder of mass m per unit span, c is the coefficient of viscous damping and k denotes the stiffness of the spring. The right hand side represents the time-dependent fluid force acting on the body per unit length of span and embodies fluid inertia and damping forces. Recalling the definition in (2.3), the fluid force can be expressed through the lift coefficient. Hence this equation can be non-dimensionalised using three additional parameters: the mass ratio, the structural damping ratio and the reduced velocity. These are given by:

$$m^* = \frac{m}{\pi\rho D^2/4} \qquad \zeta = \frac{c}{c_0} \qquad V_r = \frac{U_\infty}{f_n D} \tag{2.7}$$

where $c_0 = 2\sqrt{km}$ is the critical damping and $f_n = \frac{\sqrt{k/m}}{2\pi}$ the natural frequency of the body in vacuo. The mass ratio represents the ratio between the inertial forces of the body and the hydrodynamic forces of the fluid. For VIV problems in water m^* is very low, while in air it is usually one or two orders of magnitude larger. The excitation frequency in air has generally a value similar to the frequency of the cylinder's response, close to the body natural frequency f_n. In the case of vibrations in water (small mass ratio) the frequency of excitation can be markedly different from f_n, because the implied additional inertia of the fluid system is able to drive the cylinder response away from its natural frequency. This different behaviour has been proved in several experiments, such as Feng (1968) and Khalak & Williamson (1999), that will be presented in section 2.3.3. The synchronisation of vortex shedding and the body frequency takes place over a range of reduced velocities, whose width is proportional to the oscillation amplitude. This range always encompasses the resonant

point, where the amplitude of oscillations is maximum. In transverse vibration motions, the maximum oscillation amplitude occurs when $V_r \approx 1/St$: considering (2.1) and the definition of the reduced velocity in (2.7), this means that the body's natural frequency, f_n, is approximately equal to the vortex shedding frequency f_s, provided that $m^* >> 1$. Similarly, in the case of in-line vibration the resonant point occurs at $V_r \approx 1/2St$, as the excitation frequency for this case is twice the value of f_s.

Going back to equation (2.6) and substituting the definitions given in (2.7), we obtain:

$$m\ddot{y} + 4\pi f_n \zeta m\dot{y} + 4\pi^2 f_n^2 my = \frac{1}{2} C_y \rho U_\infty^2 D \tag{2.8}$$

As described in Sarpkaya (2004), for large amplitude vortex-induced oscillations in a steady state, $F_y(t)$ and $y(t)$ oscillate at a common frequency, f', and the fluid force leads the cylinder response by a phase angle ϕ: in the lock-in region both quantities can be approximated by sinusoidal functions:

$$y = \hat{y}\sin(2\pi f' t) \qquad C_y = \hat{C}_y \sin(2\pi f' t + \phi) \tag{2.9}$$

The force coefficient can then be written as:

$$C_y = (\hat{C}_y \cos\phi)\sin(2\pi f' t) + (\hat{C}_y \sin\phi)\cos(2\pi f' t) \tag{2.10}$$

Equation (2.10) highlights the part of C_y in phase with the velocity (which in forced oscillations predicts whether the body is excited or damped) and the one in phase with the acceleration. Substituting (2.9) in (2.8) and equating the sine and cosine terms, we obtain the following equations:

$$\frac{f_n}{f'} = \left[1 - \frac{\hat{C}_y}{4\pi^2}\cos\phi\left(\frac{\rho D^2}{2m}\right)\left(\frac{U_\infty}{f_n D}\right)^2\left(\frac{\hat{y}}{d}\right)^{-1}\right]^{-\frac{1}{2}} \tag{2.11}$$

$$\frac{\hat{y}}{D} = \frac{\hat{C}_y}{8\pi^2}\sin\phi\left(\frac{\rho D^2}{2m\zeta}\right)\left(\frac{U_\infty}{f_n D}\right)^2 \frac{f_n}{f'} \tag{2.12}$$

Equation (2.12) can be expressed in terms of reduced mass and reduced velocity:

$$\frac{\hat{y}}{D} = \frac{\hat{C}_y}{4\pi^3}\sin\phi\left(\frac{1}{m^*\zeta}\right)V_r^2 \frac{f_n}{f'} \tag{2.13}$$

This expression shows that the amplitude of the cylinder's oscillations is dependent on several parameters, such as the part of C_y in phase with the velocity, the reduced velocity, the mass-damping parameter $m^*\zeta$ and the ratio between the natural frequency and the lock-in frequency. However, this analysis is based on the assumption that force and displacement are composed of a single frequency without including the effect of higher order harmonics: therefore this model is a linear approximation of the VIV dynamics. Despite being a simplified model, equation (2.13) illustrates the complex relationship between the governing parameters and provides a mathematical justification for many physical observations of VIV dynamics.

2.3.2 Force decomposition

Sarpkaya (2004) repeated a series of free and forced vibrations experiments on a rigid cylinder oscillating in a uniform inflow, originally done in 1978. For a body oscillating sinusoidally with velocity U he separated the lift coefficient into two components, one depending on the added mass coefficient, C_a, and one dependent on the drag coefficient, C_D. This is based on the hypothesis that the hydrodynamic force exerted on a body undergoing sinusoidal oscillations is the linear sum of a velocity-dependent drag force and an acceleration-dependent inertial force, the added mass force. The mathematical model for this assumption is given by the equation proposed by Morison *et al.* (1950):

$$F(t) = \frac{1}{2}\rho C_D D|U|U + \rho C_a \frac{\pi D^2}{4}\dot{U} \tag{2.14}$$

Note that if the flow is oscillating the problem is kinematically equivalent but the inertial force comprises also a buoyancy force arising from the pressure gradient required to accelerate the flow past the body and hence the added mass coefficient needs to be replaced by $1 + C_a$. Considering again equation (2.10), the added mass and drag coefficient can be written as:

$$C_a = -\hat{C}_y \cos\phi \qquad C_D = \hat{C}_y \sin\phi \tag{2.15}$$

The phase angle depends on these parameters and is given by the following expres-

sion:

$$\phi = \arctan\left(\frac{-C_D}{C_a}\right) \tag{2.16}$$

Similar expressions can be written for forced sinusoidal oscillations, where the lock-in frequency of the combined fluid-structure system must be replaced by the imposed excitation frequency, f_e, with the caveat pointed out by Sarpkaya (2004) that "the larger the amplitude of VIV oscillations, the more non-linear the dependence of the lift and inertial forces on A/D, particularly at mode changes, phase jumps, hysteresis, intermittent switching". Therefore, in these conditions a non-linear force equation is needed for a correct comparison of the results obtained from forced oscillations tests with the data found for self-excited cylinders.

In his forced vibration experiments Sarpkaya (2004) noted that, during the synchronisation range, the drag coefficient increased constantly from a negative value to a positive one, while the added mass coefficient rapidly decreased, resulting in a change of phase during the lock-in. The increase in C_D in this regime means that the drag is in phase with the motion of the cylinder and acts to excite its vibrations: there is a positive energy transfer from the fluid to the body to overcome the dissipation through the mechanical damping.

2.3.3 Response branches

In order to establish a clear relationship between the numerous parameters that govern VIV, two fundamental experiments were performed by Feng (1968) and Khalak & Williamson (1999), in air and water respectively.

In Feng's test a single-degree of freedom circular cylinder was free to vibrate in the transverse direction with $m^* = 248$, $\zeta = 0.00103$ and $m^*\zeta = 0.255$; the reduced velocity was based on the natural frequency of the body in air, f_n^{air}, and was varied by progressively increasing the free-stream velocity. The flow speed was also gradually decreased to investigate possible hysteretic effects. The variations in shedding frequency and response amplitude with the reduced velocity are plotted in figure 2.10.

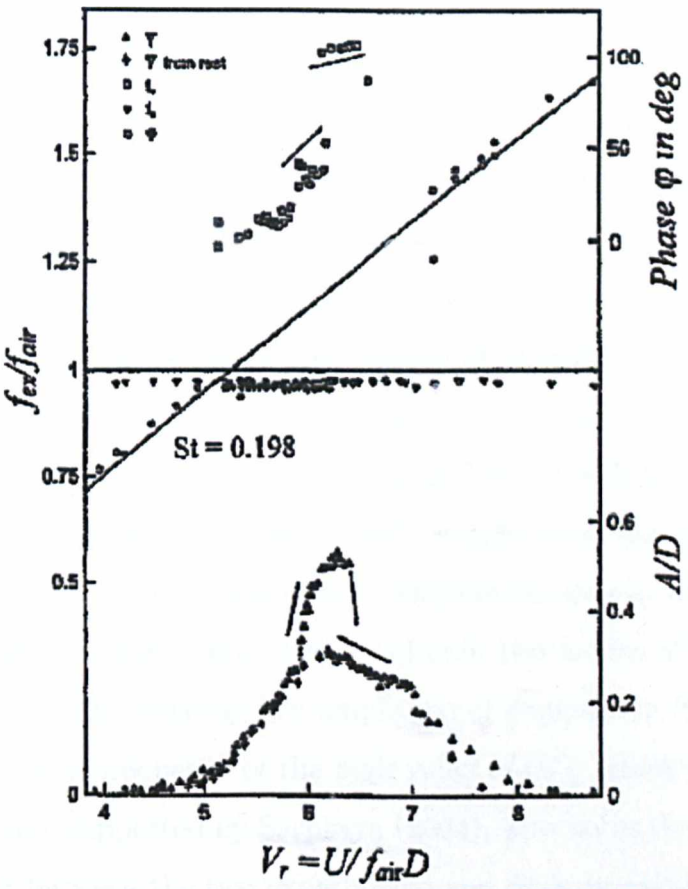


Figure 2.10: Wake characteristic of an elastically mounted cylinder freely vibrating in air ($m^* = 248$, $\zeta = 0.00103$ and $m^*\zeta = 0.255$). The Reynolds number varies from 10^4 to 5×10^4 (Feng (1968)).

At $V_r \approx 4$ the cylinder started to vibrate at a frequency close to f_n^{air} and the fluid system shed vortices at the Strouhal frequency (i.e. $f_v \approx f_s$, where f_v denotes the shedding frequency of a vibrating cylinder). The synchronisation occurred at $V_r \approx 5$, when both fluid and structure systems locked onto the cylinder's natural frequency in air; at this point, the oscillation amplitude started to increase and reached a maximum for $V_r = 6.3$, which was found to be the resonant value. This was accompanied by a phase jump and a change of vortex shedding timing, whose dynamic will be discussed later in this section. A further increase in the reduced velocity led to a progressive decrease in the oscillation amplitude and to the return of the shedding frequency to the Strouhal value.

Khalak & Williamson (1999) conducted a similar experiment in water using an elastically mounted cylinder with a much smaller mass ratio and mass-damping pa-

rameter ($m^* = 10.1$, $\zeta = 0.0013$ and $m^*\zeta = 0.013$). In their experiment, the reduced velocity was based on the natural frequency of a body vibrating in water and the Reynolds number ranges from 3×10^3 to 3×10^4. These results show some striking differences from the ones obtained by Feng, as illustrated in figure 2.11. The cylinder's response in water exhibits three modes, named initial, upper and lower branch; in Feng's experiments the upper branch does not appear and the peak amplitude is much lower. In addition, the regime of synchronisation occurs over a wider range of reduced velocity when the body is oscillating in water: this can be explained considering the concept of added mass, which will be further discussed in section 2.3.4. Khalak & Williamson (1999) suggest that the peak amplitude is dependent on the mass-damping parameter, whereas the lock-in width is associated primarily with the mass ratio: the presence of only two modes of response - initial and lower branch - with relatively low amplitude of response in Feng's experiment could therefore be a consequence of the high value of $m^*\zeta$. However, this interpretation is not entirely supported by Sarpkaya (2004), who notes the difference in the Reynolds number between the two experiments and cites an earlier observation by Zdravkovich (1990) as a proof that the presence of the upper branch is to be related to the Reynolds number rather than to the mass-damping parameter. Khalak & Williamson (1999) showed also that the first transition between the initial and upper branch is hysteretic, whereas the change from the upper to the lower branch involves an intermittent switching. In his experiments in air, Feng found hysteresis in the transition between the two response branches.

The value of A/D obtained in the numerical simulations of freely vibrating cylinders is far smaller than the data presented by Feng (1968); Khalak & Williamson (1999). Blackburn & Karniadakis (1993) and Newman & Karniadakis (1996) performed a numerical comparison of free and imposed motion on a flexible cable at $Re = 100$ and $Re = 200$ and compared their results with the set of experimental data compiled by Griffin (1985): for low values of the mass-damping parameter the numerically computed amplitude is considerably lower than the corresponding experimental value and the upper branch is not reproduced. For higher mass-damping parameters, the numerically simulated amplitude is closer to the experimental data.

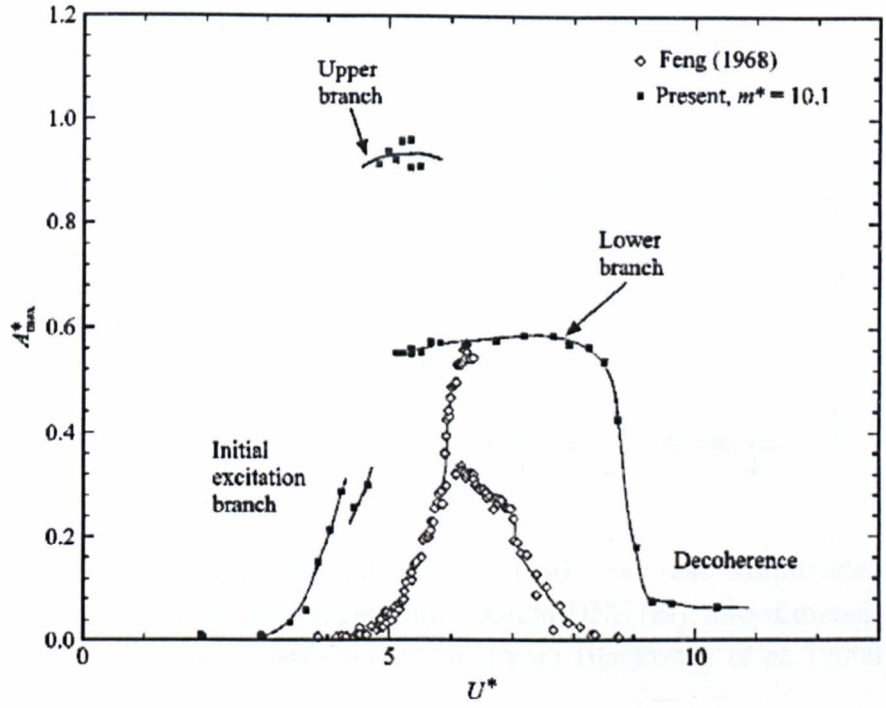


Figure 2.11: Comparison between the amplitude of response of a circular cylinder undergoing VIV obtained by Feng (1968) in air (○: $m^* = 248$, $\zeta = 0.00103$, $m^*\zeta = 0.255$ and Re from 10^4 to 5×10^4) and Khalak & Williamson (1999) in water (■: $m^* = 10.1$, $\zeta = 0.0013$, $m^*\zeta = 0.013$ and Re from 3×10^3 to 3×10^4).

However, none of these numerical simulations could predict the maximum value of $A/D \approx 1$ found in Khalak & Williamson (1999); this is primarily related to the large difference in the Reynolds number value, as DNS is limited by the high computational cost of high Reynolds number computations. This hypothesis is supported by the work of Blackburn *et al.* (2000), who compared the results obtained using three-dimensional and two-dimensional simulations with experimental data at a similar Reynolds number of approximately 556; figure 2.12 shows that the maximum amplitude in the simulations is somewhat smaller than the experimental data, although their values are now much closer. The amplitude response computed using three-dimensional DNS shows a behaviour qualitatively similar to the experimental results: these results show also that two-dimensional computations are unable to correctly reproduce the extension and the location of the three response branches, suggesting that a sectional approach is inadequate for this kind of problem.

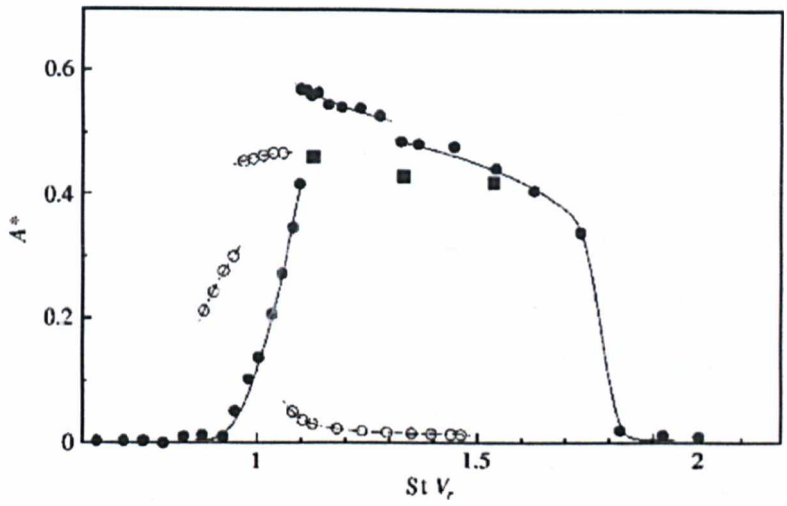


Figure 2.12: Non-dimensional average peak response amplitude, A^*, obtained from three-dimensional DNS (■), two-dimensional DNS (○) and experiments (•) (from Blackburn *et al.* (2000)).

2.3.4 The concept of added mass

The different frequencies arising in the previous results can be explained by a fundamental concept: the added mass due to the inertia forces that act on the accelerating body and add inertial resistance to its motion. In an inviscid flow the fluid particles pushed aside by the body's motion do not return to their original position: this permanently displaced fluid mass represents the added mass Δm and depends on the geometry only for this type of flow (Sarpkaya (2004)). The corresponding coefficient is given by:

$$C_a = \frac{\Delta m}{\rho V} \tag{2.17}$$

where ρ is the fluid density and V the volume of the body. For a unit length of circular cylinder, $C_a = \Delta m / \frac{1}{4}\pi\rho D^2$ where D is the cross-sectional diameter. However, as Sarpkaya (2004) stated, "in unsteady [viscous] flows neither the drag is equal to its steady state value nor is the added mass equal to its inviscid flow value; both are affected by viscosity and acceleration". In water the added mass coefficient reaches very small values and can also become negative (Vikestad *et al.* (2000)): this explains the initial findings in Bishop & Hassan (1964) that the transverse force

necessary to vibrate a cylinder to a certain amplitude is greater than that induced by vortex shedding. The fluctuations of C_a lead also to a variation of the synchronised frequency that characterises the lock-in region: by eliminating these fluctuations, it is possible to simulate free vibration by sinusoidal forced oscillations. Therefore the virtual mass of a moving cylinder immersed in a fluid is made by the real mass of the body plus the contribution due to the added mass: the natural frequency of the combined fluid and structural system, f_{com}, is then different from the cylinder's in vacuo natural frequency, f_n, and is given by:

$$f_{com} = f_n\left(\frac{1}{1+C_a}\right)^{\frac{1}{2}} \tag{2.18}$$

Therefore, positive values of C_a will make the body vibrate below its natural frequency, i.e. $f_{com} < f_n$ at lock-in, and conversely negative values of C_a will lead to lock-in at a frequency above the body's natural one, i.e. $f_{com} > f_n$. The added mass coefficient in freely vibrating cylinders is the cycle-averaged value of the fluid masses transported during the periods of acceleration (motion toward the mean position) and deceleration (motion toward the maximum amplitude). If $C_a < 0$, the mass drifted during the deceleration periods is larger than the mass displaced during the acceleration periods. This parameter is clearly dependent on the near wake topology and varies according to the vortex shedding and to the forces generated in this process.

The concept of added mass can also explain why the range of reduced velocity where lock-in occurs is much wider for low mass ratios. Since the fluid added mass influences also the natural frequency of the body and hence the reduced velocity, one needs to fix the definition of natural frequency, i.e. using the value in still water; if the reduced velocity is defined using a constant f_n, the added mass coefficient decreases monotonically with V_r and its reduction leads to an increase of the true natural frequency of the body, which is not fixed and is proportional to V_r. Consequently, in low mass cylinders, the lock-in regime occurs over a wider range of reduced velocity; this is not particularly evident for high mass ratio cylinders, which are clearly less influenced by the added mass effect: in these cases a relevant increase of the true natural frequency with decreasing C_a results in a much narrower lock-in range. As

noted in Vikestad *et al.* (2000), "if reduced velocity were defined in terms of the true natural frequency, then cylinders with different mass ratios would appear to have similar width of the lock-in regions". Further, if the added mass coefficient has a large negative value and the mass ratio is small, during the excitation phase (positive energy transfer from the fluid to the body) the amplitude of oscillation will be higher than that of high mass ratio cylinders: Khalak & Williamson (1999) showed that the data for a set of response amplitude plots over a wide range of mass ratios collapsed onto one curve when the true natural frequency was used to normalise the velocity.

2.3.5 Modes of shedding

2.3.5.1 Fundamental modes: 2S, 2P, P+S

Williamson & Roshko (1988) studied the wake of a circular cylinder forced to move along a sinusoidal path in the range $300 < Re < 1000$. Their aim was to identify the main features of vortex formation throughout the lock-in region: by varying the imposed amplitude of oscillation and the excitation frequency (through variations of the wavelength $\lambda/D = U_\infty/f_e D$), they compiled a map in the parameter plane $(\lambda/D,\ A/D)$ and identified different shedding regimes.

They observed three principal types of vortex patterns, which characterised different regions of the map illustrated in figure 2.13. In the 2S mode the wake topology is the typical Von Karman street, with two oppositely signed single vortices shed per cycle; the 2P mode is associated with the shedding of two pairs of vortices per cycle, while the P+S mode is a combination of the two previous regimes and consists of an asymmetric shedding mode in which a single vortex and a pair of vortices are formed per cycle. In the dashed region of figure 2.13 the vortices coalesce in the near wake, forming larger scale structures. Williamson & Roshko (1988) found that in the 2P region the out-of-phase component of the lift was small and the phase angle was close to π. Approaching the critical curve, i.e. along a line of constant amplitude, the out-of-phase component of the lift started to increase, as a result of the energy transfer from the fluid to the cylinder, until a maximum value was

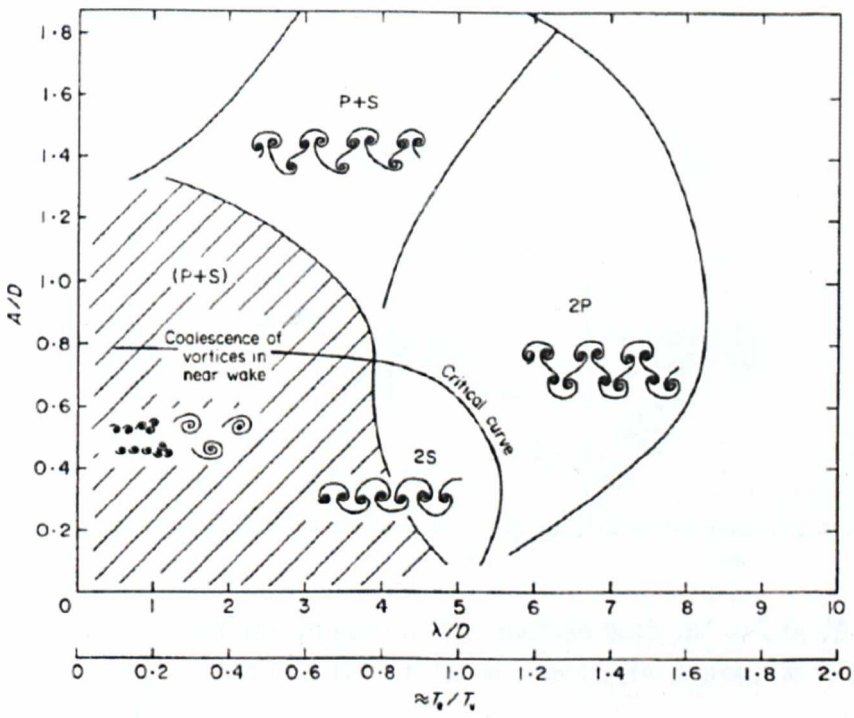


Figure 2.13: Map of vortex patterns for a circular cylinder forced to oscillate sinusoidally in the range $300 < Re < 1000$; three different modes of shedding are identified, namely 2S, 2P and P+S, and the corresponding wake topologies are sketched (Williamson & Roshko (1988)).

reached on the critical curve. Simultaneously the phase angle decreased and the added mass coefficient achieved its minimum, corresponding to the minimum value of the virtual mass of the body. On the critical curve, the 2P mode switched to a 2S form of shedding: the authors found that this rather abrupt change was accompanied by a sudden jump in the phase angle and in the lift coefficient, in agreement with the earlier observations of Bishop & Hassan (1964). There is evidence that the 2S shedding mode can lead to a more organised and correlated wake structure: this is consistent with the increase in the lift force observed by Williamson & Roshko (1988) and emphasises the fact that a 2S type of shedding leads to the most severe condition of fluid dynamic loading and therefore should be avoided in practical applications.

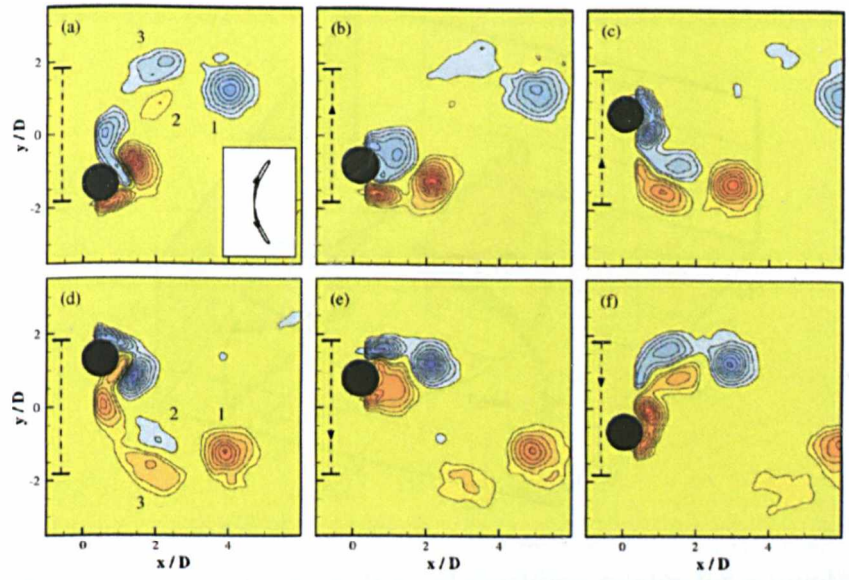


Figure 2.14: 2T shedding mode for XY motion with $m^* = 2.6$, $Re = 5300$, $A_y = 1.33$ and $(U^*/f^*)S = 1.48$ (from Jauvtis & Williamson (2004b)).

2.3.5.2 Other types of shedding modes: XY-motion and pivoted cylinders

Interestingly, Jauvtis & Williamson (2004b,a) discovered a third mode of shedding, consisting of three vortices shed per half cycle of transverse body motion and thus named "2T". The triplet resembles the 2P mode with the addition of a third vortex formed when the cylinder is close to the extremities of its transverse motion (see figure 2.14). This type of shedding occurs only when a cylinder is allowed to vibrate in both the transverse and the in-line direction and exhibits a remarkably high amplitude of response ($A_y/D = 1.5$); it is associated with a super-upper branch where vibrations are markedly stable and periodic. The 2T mode exists only for bodies with $m^* < 6$, the so-called "light bodies", as for higher mass ratios the freedom to oscillate in-line with the flow does not affect the transverse vibration dynamics. Therefore for $m^* > 6$ the vortex shedding analysis based on $y-$direction motion remains of strong relevance also in the case of two degrees of freedom.

The same experiment but with the cylinder pivoted at one side yields the appearance of a different mode, named "2C" and characterised by two couples of

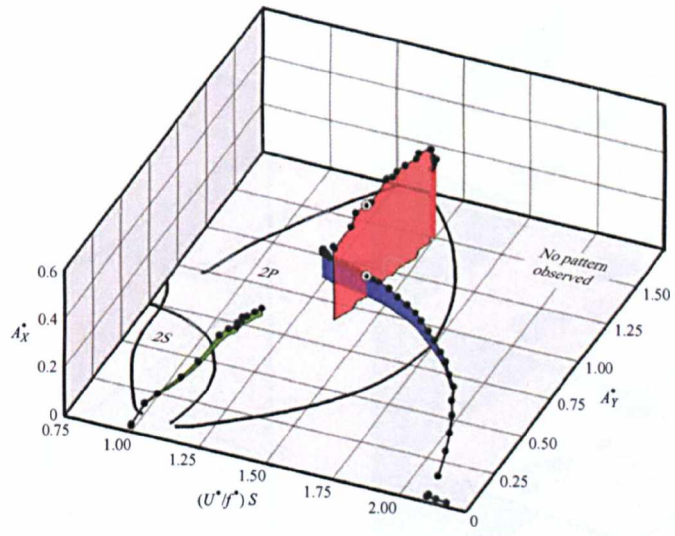


Figure 2.15: Three-dimensional map of shedding modes for a pivoted cylinder in $XY-$motion overlaid on the Williamson-Roshko map (Flemming & Williamson (2005)).

co-rotating vortices shed per motion cycle (Flemming & Williamson (2005)). Like in the previous case, for sufficiently low inertial-damping products, the principal dynamics of the pivoted body are transverse to the flow and three response branches are observed. In the case of sufficiently light bodies, the upper branch is associated with significant streamwise motion and a remarkable departure from the original Williamson & Roshko (1988) map of shedding modes is found. A three-dimensional extension of the Williamson & Roshko (1988) plot, which includes the effect of the in-line motion on the cylinder response, is shown in figure 2.15: two of the response branches that cross over each other exist in different parameter spaces, depending on the amplitude of in-line vibrations.

In the case of limited streamwise motion and for tip amplitudes below the 2S-2P threshold in figure 2.15, a 2S mode is observed in the initial branch, while the lower branch shows a 2P mode of shedding; both compare favorably with the modes found for a cylinder in uniform amplitude transverse vibration. However, when the tip amplitude lies in the 2P mode regime for the initial branch the shedding mode depends on the spanwise location: a 2P mode is found close to the tip, while the pivot region sheds vortices in a 2S mode, giving rise to the 2S-2P hybrid mode illustrated in figure 2.16 (*left*). This change involves the occurrence of vortex splitting: however,

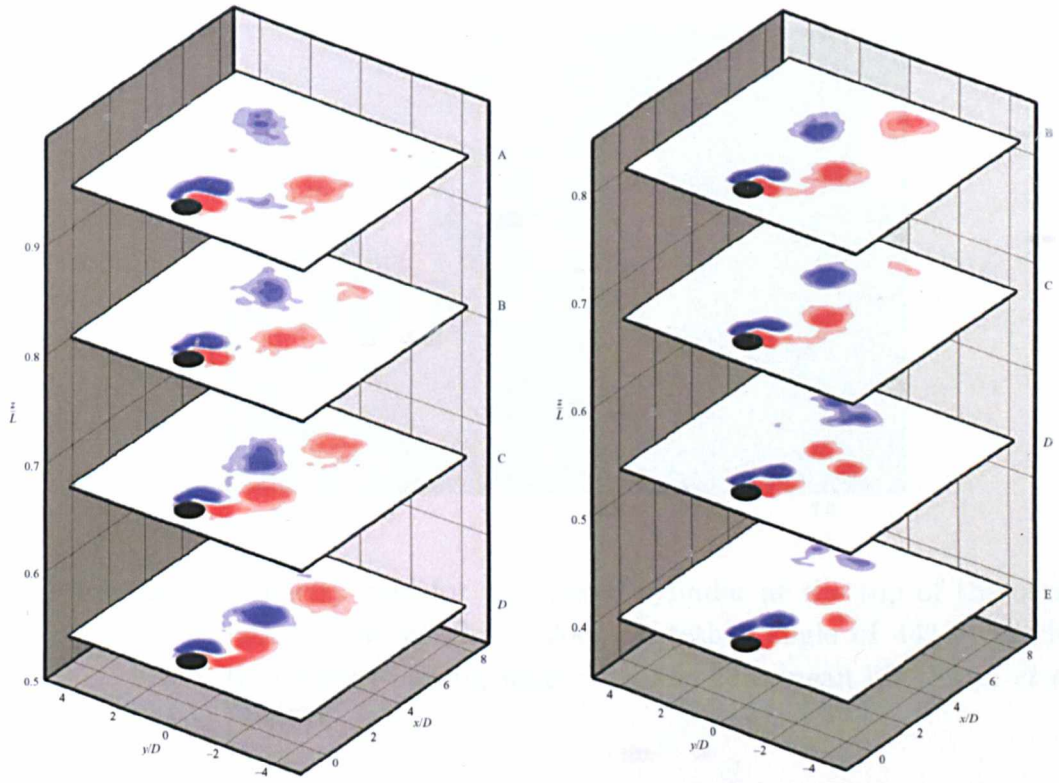


Figure 2.16: Pivoted cylinder in $XY-$motion (Flemming & Williamson (2005)): 2S-2P hybrid mode of shedding at low amplitude of streamwise motion (*left*) and 2C mode of shedding at high amplitudes of streamwise motion (*right*).

unlike the vortex dislocations observed by Williamson (1992), which occur at a beat frequency, this vortex splitting is locked to the frequency of oscillation of the cylinder. A similar hybrid mode of shedding was also observed by Techet *et al.* (1998) past a tapered cylinder, which spanned the 2S and 2P regimes in the Williamson & Roshko (1988) map, and by Lucor & Karniadakis (2004) in the case of straight cylinder forced to transversely vibrate under sheared inflow. In the latter case, a vortex split was found to connect 2S and 2P vortical patterns, giving rise to a periodic and repeatable hybrid mode. When the streamwise vibration is higher, a new 2C mode, consisting of two co-rotating vortices per half cycle, is observed: this mode is associated with larger amplitude of transverse vibration and the presence of vortex dislocations and vortex merging in the wake (see figure 2.16 (*right*)).

A different type of vortex pairing was observed by Ryan *et al.* (2007) past a tethered body at low Reynolds number: this pairing was associated with the action

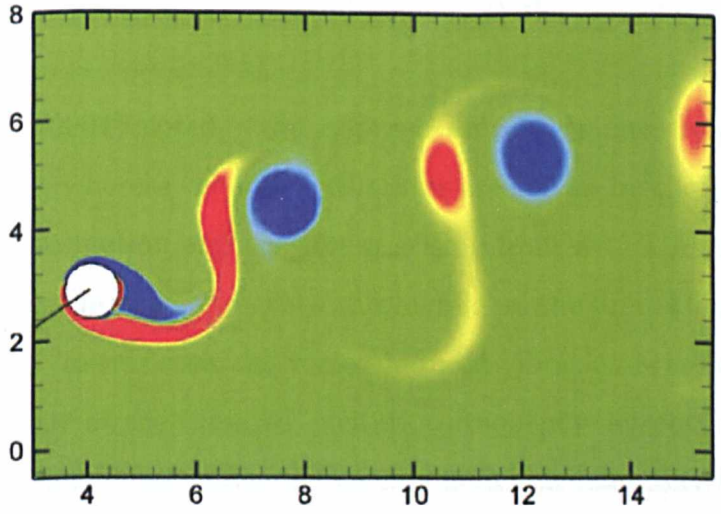


Figure 2.17: Vorticity field for a tethered cylinder at the top of the oscillation cycle at $Re = 200$. A tether angle of 44° gives rise to a vortex-pairing wake with non-zero mean lift (Ryan *et al.* (2007)).

of the tethered cylinder oscillating at an angle to the flow and produced a non-zero (negative) mean lift coefficient. The resulting wake structure is shown in figure 2.17. Ryan *et al.* (2007) related the vortex pairing to the delay of the shedding of the negative vortex from the lower shear layer and to the production of a jet flow between the two cores that formed the pair.

2.3.6 Forced and free oscillations

Feng's (1968) experiment shows that the prediction of the forces acting on a body in free vibration is extremely difficult: the structure responds very rapidly to changes in the reduced velocity and the resulting shedding depends on a significant number of independent parameters. The relationship between virtual mass, forces and body acceleration is non-linear and not yet fully understood. Therefore, a useful approach to understand and eventually predict such a complex problem is represented by forced vibrations simulations, in which the amplitude and the frequency of motion can be varied independently. However, even if this allows a close control of the input parameters in the simulation and the conditions of simulation, the range of imposed

amplitudes and frequencies (or reduced velocities) that can be relevant to a free vibrations problem is very limited.

As Sarpkaya (2004) noted, "the imposed amplitude and frequency drive the forced oscillations, whereas the free oscillations are driven by the past and the prevailing state of the motion and the forces arising from it". This is a fundamental difference between the two approaches and highlights the limitations of forced oscillation simulations: in this case, the vortex-induced vibration is controlled externally and forced to occur at the imposed excitation frequency, amplitude and Reynolds number. In self-excited vibration, the motion is driven internally by the wake and occurs at an average frequency which is the final outcome of the complex, non-linear, wake evolution and is strongly dependent on the Reynolds number. Although forced oscillation experiments represent an idealisation of most features of VIV problems, the investigations conducted so far show encouraging agreement with data from free oscillations tests.

The results obtained by Williamson & Roshko (1988) with forced oscillations found confirmation in several studies on freely vibrating cylinders. Govardhan & Williamson (2000) demonstrated that the initial and lower branches correspond respectively to a 2S and 2P mode. The upper branch exhibited a weak form of 2P mode, as the strength of second vortex in each pair appeared to be much lower than the one in the classical 2P regime.

However, numerical computations were not able to reproduce the 2P mode of shedding, probably due to the limitations on the Reynolds number dictated by the computational cost. In their two-dimensional numerical simulations, Meneghini & Bearman (1995) established the lock-in boundary for vortex shedding of a cylinder forced to oscillate in the transverse direction at $Re = 200$. For small amplitude of oscillation, i.e. $A/D < 0.6$, they identified a 2S shedding mode and labelled this kind of synchronisation "primary lock-in". As the amplitude was increased to higher values, the wake presented a P+S mode of shedding, but no evidence of the 2P mode was found for frequencies close to the shedding frequency. Similarly, the results obtained by Blackburn & Henderson (1999) at $Re = 500$ could successfully reproduce only 2S and P+S modes.

One of the first numerical simulations of the 2P mode in the lower branch was performed by Blackburn *et al.* (2000), who found this mode associated with a double-peaked form in the time-series of the lift coefficient. By comparison with two-dimensional calculations, Blackburn *et al.* (2000) demonstrated that three-dimensional computations are required to reproduce the response envelope observed experimentally: two-dimensional simulations in absence of a turbulence model are inadequate to predict the full nature of the vortex shedding mechanics, even at relatively low Reynolds numbers.

Carberry *et al.* (2004) performed an interesting and encouraging comparison between forced and free vibrations of a circular cylinder, in the attempt to establish the capability of imposed motion tests to replicate the features of vortex-induced vibrations cases. They confirmed the findings from a previous paper, Carberry *et al.* (2001): if the cylinder is forced to oscillate at relatively low amplitudes two different wake states are observed (low and high frequency) and the transition between these two regimes corresponds to a jump in the amplitude and to a phase shift of the order of π in the total and vortex lift forces. This resulted in an alteration in both the near wake topology and the timing of vortex shedding, providing evidence that the mode change and the phase shift are intrinsically linked: the low-frequency state exhibited a 2P shedding mode, while the high-frequency state presented a 2S mode, consistent with the plot obtained by Williamson & Roshko (1988) (figure Williamson & Roshko (1988)). Carberry *et al.* (2004) compared the forced vibrations test at $Re = 2300$ of her previous study with free oscillations at $3000 < Re < 3700$ and established a relation between the forced low-frequency state and the lower branch at high mass-damping; similarly, the high-frequency state corresponded to the initial branch. A transition between initial and lower branches involves a jump in the lift phase of similar magnitude to the jump observed in the transition from low- to high-frequency states described above. The free response branches at low mass-damping highlighted a clear shift in the vortex phase in the passage from the upper to the initial branch, corresponding to the change from 2P to 2S, whereas the jump in the total lift phase occurs between the lower and upper branches. The latter does not involve a significant change in the vortex shedding phase but can be related

to the weakening of the 2P mode in the upper branch observed by Williamson & Roshko (1988). When the amplitude of the forced oscillations was increased to $A/D = 0.5 - 0.6$, a third wake state appeared. Although the general mode for this intermediate state was found to be 2S, like in the high-frequency case, the phase of vortex shedding was markedly different between the two states and the wake much wider. This indicates that the forced oscillation tests are capable of simulating many of the important features of flow-induced motion, such as the variation in the phase of vortex shedding and in the total lift. Obviously the phase values for the forced oscillations cases can lie outside of the positive energy region, that is $0 < \phi > \pi$, as in this case the sign of the energy is not constrained like in free vibrations. Values of the phase angle in the range $[-\pi, 0]$ are not possible in free vibration: the energy transfer must be from the fluid to the structure to overcome the dissipations due to the mechanical damping and therefore some of the simulations in forced oscillations cannot be used for predictions of flow-induced cases.

Newman & Karniadakis (1996) also performed numerical simulations of a flexible cable in free and forced vibration at $Re = 100, 200$ and 300. They observed relatively similar responses in terms of energy transfer, force distribution and wake structures only at $Re = 100$, corresponding to a standing wave response: the differences increased at higher Reynolds number, at which a travelling wave response occurred in the case of flow-induced vibration, with the breakdown of time-periodic cable dynamics. To explain this discrepancy, the authors suggested that transition in the near wake might occur at lower Reynolds numbers in the case of flow-induced vibration, whereas forced vibration appears to delay the transition.

The same authors further studied the flow-induced vibration of a flexible pipe at $Re = 100$ and 200 (Newman & Karniadakis (1997)). They found that the lock-in response can have the form of a standing wave or travelling wave, although the travelling wave tended to prevail for longer times: this type of response was associated with oblique vortex shedding, while the standing wave response generated an interwoven pattern of vorticity with symmetric vortex shedding occurring at the nodes of the standing waves. The results showed that towards the nodes of the transversely vibrating cable the fluid acted to excite the pipe's vibration, whereas towards the

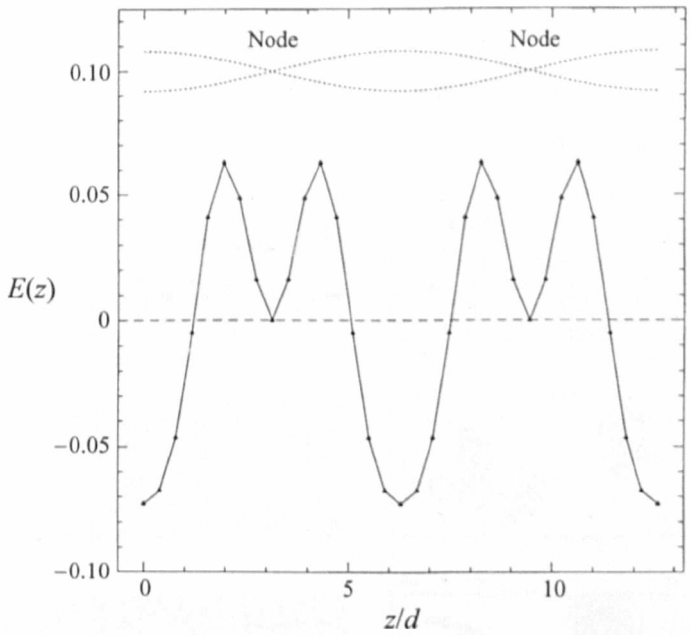


Figure 2.18: Time averaged value of the standing wave response energy E versus the spanwise coordinate z at $Re = 100$ (Newman & Karniadakis (1997)).

anti-nodes the fluid provided hydrodynamic damping (see figure 2.18).

Therefore, two regions of damping and one region of excitation were observed over each half wavelength of cable oscillation.

2.3.7 Phase and timing of vortex shedding

The experiments conducted by Feng (1968); Khalak & Williamson (1999) show that during lock-in the wake dynamic past a bluff body in VIV can change very quickly with reduced velocity variations. In particular, as V_r is increased, an abrupt jump in the phase between lift force and displacement occurs. This change in phase of about π is associated with the variation of the vortex shedding timing, as has been pointed out by many authors, Zdravkovich (1982); Gu *et al.* (1994); Lu & Dalton (1996) among the others; more recent studies have also shown that the switch occurs gradually over several cycles of cylinder oscillations (see Krishnamoorthy *et al.* (2001)).

Zdravkovich (1982) found that two different modes of vortex shedding occur during

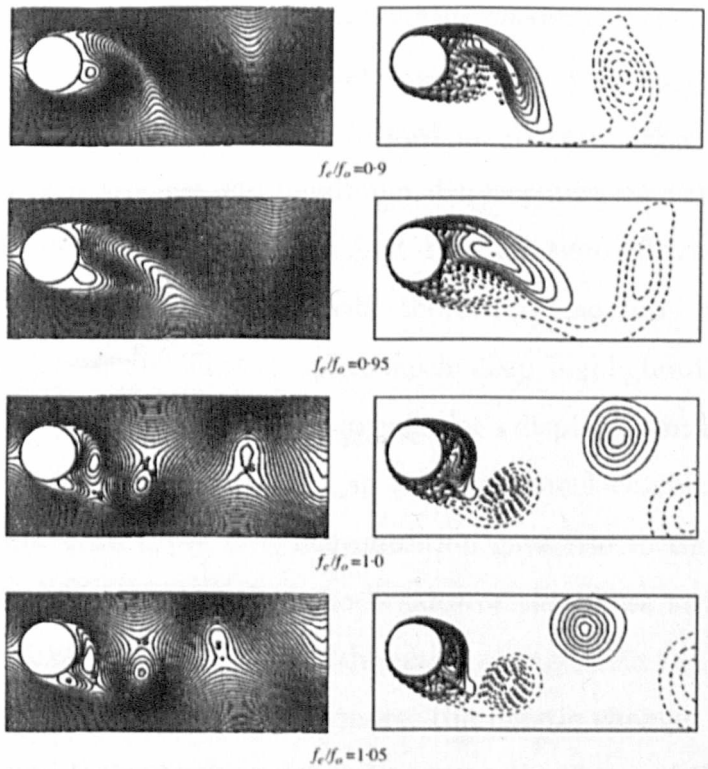


Figure 2.19: Instantaneous streamlines (*left*) and vorticity contours (*right*) for $A/D = 0.4$, $Re = 1000$ and various frequencies of excitation; the dashed lines represent positive vorticity, the solid line negative values. In all frames the cylinder is at its extreme upper position (Lu & Dalton (1996)).

the lock-in range. In the first part of the synchronisation regime, the vortex is shed from one side of the cylinder when the body reaches its maximum displacement on the opposite side; when the system reaches the maximum amplitude (i.e. the reduced velocity is close to the resonance value) the phase jump occurs and the cylinder starts to shed vortices when it is at its maximum displacement on the same side.

Zdravkovch's results were based mainly on the observation of freely vibrating cylinders. Ongoren & Rockwell (1988) conducted numerous tests on cylinders with different cross-section shape forced to oscillate in the transverse direction. By varying the excitation frequency and the Reynolds number, Ongoren & Rockwell (1988) found two basic forms of synchronisation. In the subharmonic synchronisation, which occurred when the excitation frequency was equal to half of the natural shed-

ding frequency of the stationary body, the vortex shedding appeared phase-locked such that it was alternatively in-phase and out-of-phase with the cylinder's motion. In this regime the initial vortex always formed on the same side of the body, regardless of whether it reached the maximum displacement on this side or on the opposite one. If the two frequencies merged a classic type of synchronisation occurred, involving alternating shedding from the side of the body corresponding to its maximum displacement. This complex mechanism highlights that there is not only one admissible phase relation between cylinder's displacement and vortex shedding that gives phase locking. However, in the experiment conducted by Ongoren & Rockwell (1988), both types of synchronisation gave rise to the same shedding mode, as Kármán wakes occurred on both sides of the phase switch; conversely, Williamson & Roshko (1988) associated the phase change with the jump from a 2S mode of shedding to a 2P one. Furthermore, the drastic changes in the phase of shedding were found to be strongly dependent upon the shape of the cross-section, but in all the cases analysed the necessary condition for the phase switch was the attainment of a minimum formation length.

To answer the question of which physical mechanisms determines the change of phase, Gu *et al.* (1994) used particle imaging to investigate the timing of vortex formation in cylinders with circular cross-section; Lu & Dalton (1996) examined computationally the same phenomenon and reached similar conclusions. Their results are illustrated in figure 2.19, which highlights the contraction of the formation length and the change in timing. These studies confirm Zdravkovich's initial observation: as the frequency of excitation over the Strouhal frequency (f_e/f_o in their notation) increases, the concentration of vorticity moves closer to the body until it reaches a limiting position, where it suddenly switches to the opposite side of the cylinder. The contraction of the formation region prior to the phase switch is due to interaction of the shear layer with a region of base vorticity, generated by the motion of the cylinder: the sign of this vorticity always opposes the sign of the shear layer towards which it advects. Therefore, it diminishes the supply of vorticity available for roll-up and weakens the forming vortex. As the frequency of excitation grows, the vortex on the other side becomes dominant until the phase switch occurs.

This mechanism is not substantially altered at higher Reynolds numbers (i.e. in the shear layer transition regime) where the base pressure and the formation length are markedly different. Gu *et al.* (1994) showed that the switching phenomenon was not modified by the presence of small-scale Kelvin-Helmoltz vortices, even though they observed a dependence on the excitation frequency: the value of f_e/f_o at which the switching occurred was found to decrease with increasing Reynolds numbers. These results are supported by the numerical calculations of Lu & Dalton (1996), who showed that the growth of the amplitude of oscillation had the same effect: a reduction in the value of f_e/f_o at which switching occurred.

Blackburn & Henderson (1999) performed numerical simulations of the forced oscillation of a two-dimensional cylinder at $Re = 500$; they suggested that the change of phase is due to a competition between two different mechanisms of vorticity production. The pressure gradient associated with the roll up of the main shear layer induces a basal concentration of vorticity bearing opposite sign, which weakens the growing vortex as described above (Lu & Dalton (1996)). However also the surface acceleration generates vorticity in the basal region, opposing the pressure gradient vorticity production. These two mechanisms compete to govern the vortex shedding and are supposed to be responsible for the switch in phase of the forces. At lower excitation frequencies the effect of the pressure gradient is dominant and the shear layers roll up first on the side of the wake towards which the cylinder is moving. Conversely, at higher frequencies the motion induced vorticity takes control of the vortex formation and induces an earlier rolling up of the shear layer on the opposite side, overriding the effect of the pressure gradient. Blackburn & Henderson (1999) also demonstrated that the phase switch is associated with a change in sign of the mechanical energy transferred between the cylinder and the flow.

2.4 Yawed cylinders and the Independence Principle

The need to understand and predict the wake dynamics in real applications has directed many investigations towards more complex geometries and flow profiles. This section presents a brief overview of the fundamental findings on the effect of oblique cylinders and sheared currents on the vortex shedding process. These results can be discussed in the light of the "Independence Principle" (or "Cosine Law"). The basic idea stems from the observation that, for moderate values of shear and yaw angle, the near wake region is dominated by vortex structures parallel to the cylinder and the flow field appears to be independent of the axial flow: the Independence Principle asserts that the forces and the vortex shedding frequency of a yawed cylinder (or of a straight cylinder in a sheared inflow) are the same of those past a cylinder with no yaw, provided that only the component of the onset flow normal to the body's axis, $U_N = U_\infty \cos\theta$, is considered. The component of the flow tangential to the cylinder can therefore be neglected in the force computations: however, if the oblique angle is too large, the axial wake convection cannot be ignored and the Independence Principle is not valid anymore.

In their experiments on a transversely vibrating yawed cylinder at $8 \times 10^3 < Re < 2 \times 10^4$, Nakagawa *et al.* (1998) found a critical value of $\theta = 45°$ for the inclination angle. As noticed by Marshall (2003) using a quasi-two-dimensional flow approximation, the process that leads to the destabilisation of the vortex street for large yaw angles, and therefore to the breakdown of the Independence Principle, is based on two mechanisms: the Kelvin-Helmoltz-type instability of the cross-flow vorticity component and the presence of axial velocity deficit within the vortex cores, which results in the instability of the Karman vortices. Marshall (2003) provided an estimate value of 61° for the critical angle based on this latter mechanism at $Re = 300$: however, being the vortex axial velocity deficit proportional to the Reynolds number, the critical angle for this instability to develop is expected to be smaller at higher Reynolds numbers.

Ramberg (1983) performed several experiments on cylinders with yaw angles

between 0° and 60° in the Reynolds number range $150-1000$. The results appeared very sensitive to end conditions, especially at low Reynolds numbers. When the end effects could be discarded, oblique shedding at angles smaller than the yaw value appeared to be an intrinsic feature of stationary yawed cylinders: in this case, the shedding frequency predicted by Independence Principle was lower than the real one, while the expected shedding angle, the wake width, the formation length and the base pressure were greater than the measured ones. However, when the cylinder was forced to oscillate, parallel shedding was observed and the locked-in wake states were correctly described by the Independence Principle, restricting the critical yaw angle in this Reynolds number range to values larger than 60°.

The experimental results of Ramberg (1983) for a fixed cylinder were confirmed by the numerical simulations of Lucor & Karniadakis (2003) at $Re = 1000$. Their freely oscillating yawed cylinder simulations with $\theta = -70°$ and $-60°$ showed that Ramberg's result in forced vibration could be extended to free vibration cases. For $\theta = -70°$ the flow structures appeared more contorted than in the stationary case and exhibited strong streamwise vortices winding up in helical paths around the spanwise vortices, as shown in figure 2.20. In disagreement with the Independence Principle, the free-stream flow direction was found to have a strong influence on the distorted cores at this large angle of attack.

2.5 Uniform bluff bodies under shear flow

Griffin (1985) summarised the key-findings from experiments performed on cylinders of various cross-section shape (i.e. circular, rectangular and D-section) under shear flows. To identify the different levels of shear in the flow profile, a general "steepness or shear parameter", $\overline{\beta}$, was defined as:

$$\overline{\beta} = \frac{D}{\overline{V_{ref}}} \frac{d\overline{V}}{d\overline{z}} \tag{2.19}$$

where D is the cylinder diameter, $\overline{V_{ref}}$ the midspan incident velocity and $\frac{d\overline{V}}{d\overline{z}}$ the velocity gradient. In highly turbulent inflows, a large shear parameter was found to decrease the critical Reynolds number for the drag crisis by a factor of 10, compared

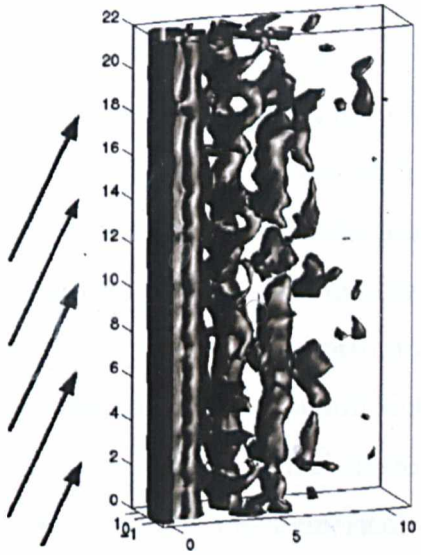


Figure 2.20: Freely oscillating yawed cylinder with $\theta = -70°$ at lock-in ($Re = 1000$). Pressure isocontours at -0.025 (Lucor & Karniadakis (2003)).

to the uniform flow conditions. The number of cells and the base pressure and drag variation along the cylinder span were related to the different aspect ratios and end conditions. In the case of short aspect ratios, cellular vortex shedding patterns were observed in the wake of a cylinder even with small values of $\overline{\beta}$; whether this occurs also in the case of large aspect ratios is still a controversial point. This observation was confirmed by several investigations: on the experimental side, Maull & Young (1973) reported the presence of spanwise cells in the wake of bluff bodies in shear flows and associated the division between these cells to changes in slope of the base pressure coefficient and to the occurrence of longitudinal vortices at the cells boundaries.

Mukhopadhyay *et al.* (1999a) and Mukhopadhyay *et al.* (1999b) performed three-dimensional numerical simulations of a sheared flow past circular cylinders of aspect ratio $L/D = 24$ and 48 at $Re = 131.5$. Several cells with spanwise length between three and seven diameters, as well as vortex dislocations, were identified in the wake. The Strouhal number based on the local velocity was found to be constant in each cell, whereas the Strouhal number based on the mean velocity varied linearly along the span, with discontinuities at the cells boundaries. Mukhopadhyay *et al.* (1999b) also observed changes in the slope of the base pressure coefficient at the cell

boundaries, in agreement with Maull & Young (1973). When the aspect ratio was increased to 48, multiple dislocations appeared along the span and the frequencies of the cells were found to be lower than in the case with $L/D = 24$.

Willden & Graham (2001) performed quasi-three-dimensional numerical simulations of a long cylinder with aspect ratio of 100 exposed to a sheared flow whose Reynolds numbers ranged between 100 (at the bottom of the sheared inflow) and 200 (at the top). Despite the sheared inflow, significant spanwise correlation was observed over a large portion of the body; cellular shedding was found in the wake in agreement with previous experimental and numerical observations.

Newman & Karniadakis (1997) also performed numerical simulations at $Re = 100$ and 200 of different types of inflow past a freely vibrating cable: a mixed standing wave/travelling wave cable response and chevron-like patterns with vortex dislocations in the wake were observed as a direct consequence of the sheared inflow profile.

Vandiver *et al.* (1997) studied the occurrence of lock-in in realistic Reynolds numbers ranges: their experiments showed that non lock-in response behaviour could be found when the shear in the flow was high. Different spanwise shedding frequencies were found to be responsible for the disruption of the vortex shedding patterns and led to a multi-modal vibration response where the degree of shear determined the number of modes that were excited.

Lucor *et al.* (2001) presented DNS results of VIV of flexible cylinder with large aspect ratio subject to linear and exponential sheared flows. The linear shear led to a standing wave pattern for the structure response where only a low mode (mode 3) was excited; the exponential shear produced a multi-mode response with modes as high as 12 and 14 participating and a mixed standing-travelling wave pattern. In the linear inflow case, cells of constant shedding frequency were obtained; their length appeared to be greater than the one measured for stationary cylinders. Further, the nodes were not exactly located at the boundary between the cells and moved in time, with a slight shift to the side of the low inflow in the sheared profile. Vortex dislocations were also observed: their presence was strictly related to low frequency modulation of the forces on the body.

The idea that for a straight constant diameter pipe a sheared onset flow profile

is required to excite simultaneously different modes was discussed by Willden & Graham (2004), who performed two-dimensional simulations using a strip theory CFD model at a realistic Reynolds number: multi-modal VIV was observed past a straight uniform cylinder subject to a uniform current profile and all the excited modes were found to vibrate at the same excitation frequency (corresponding to the Strouhal frequency). At low mass ratio the flow was dominant over the structure and controlled the response frequency.

2.6 Bluff bodies with spanwise geometric variations

2.6.1 Tapered cylinders

Vortex shedding past tapered cylinders has similar features to the wake dynamics of uniform bluff bodies in shear flows. The experiments performed by Gaster (1969) on cones with taper ratio of 36:1 and 18:1 highlighted some of the fundamental characteristics of the tapered cylinder shedding: low frequency modulation was found along the whole length of the body and the shedding frequency at a specific position appeared to be a function of the local diameter. The resulting vortex shedding occurred in cells with different frequencies.

The presence of discrete shedding cells, each with a constant frequency, as well as constant spanwise modulation frequencies, was also observed by Piccirillo & Van Atta (1993), who conducted experiments in the laminar vortex shedding regime (for a non-tapered cylinder) on four cylinders with taper ratios varying from 50:1 to 100:1. Vortex shedding was found to begin at a local Reynolds number of 60. The number of cells were a linear function of the cylinder's aspect ratio and scaled inversely with the taper ratio. Vortex splits and dislocations were also observed in the wake, as a result of a secondary instability that led to a kink in the shed vortex lines. This process was directed towards the small-diameter end of the cylinder, suggesting the presence of a pressure gradient along the span.

Techet *et al.* (1998) studied the vortex shedding past a linearly tapered cylinder

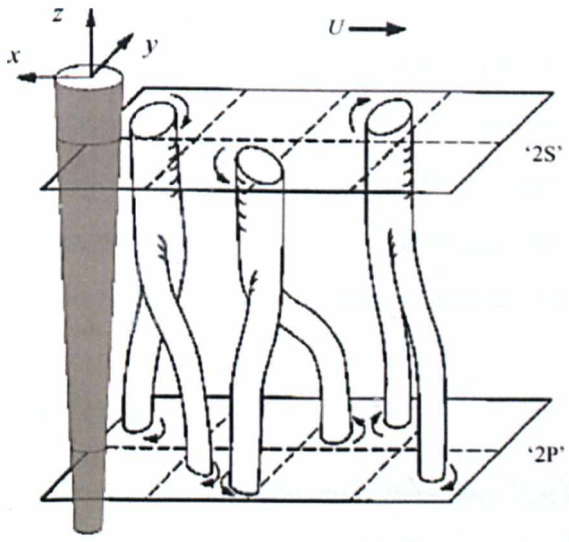


Figure 2.21: 2S-2P hybrid mode of shedding past a tapered cylinder in streamwise motion (Techet *et al.* (1998)).

with taper ratio 4:1 and Reynolds numbers in the range $400-1500$. They discovered a 2S-2P hybrid mode with the 2S and 2P modes occurring at different spanwise locations along the span of the tapered cylinder (2S at the larger diameter and 2P at the smaller diameter). Figure 2.21 shows a sketch of the subsequent vortex split and can be compared to the hybrid mode found by Flemming & Williamson (2005) and illustrated in figure 2.16 (*right*). This study showed excellent correlation with the map of modes presented by Williamson & Roshko (1988).

More recently Balasubramanian *et al.* (2001) performed experiments on VIV past a pivoted tapered cylinder in uniform and shear flow. One of the main effects of the shear in the flow was to increase the width of the lock-in region, which was proportional to the degree of non-uniformity in the flow (ratio of the frequencies at the pivoted and free end). However, the structural response amplitudes were still governed by the structural properties (i.e. reduced damping of the structure and diameter of free end); in particular, the maximum amplitude of oscillation occurred when the cylinder was pivoted at the small diameter. The behaviour of the tapered cylinder in uniform flow was found to be similar to the one of the uniform cylinder in sheared flow, with vorticity normal to the plane of the flow. The wake topology of tapered cylinders in sheared flow was found to depend on the relative orientation

taper/shear and subsequently on the interaction between the vorticity normal to the flow plane (generated by the shear) and the vorticity stemming from the geometrical three-dimensionality (introduced by the taper). In the case where the shear opposed the taper direction, a partial cancellation of the variation in the shedding frequency was observed, while a large spanwise variation of shedding frequency occurred in the configuration where the shear had the same orientation of the taper.

2.6.2 Wavy cylinders

If the external flow dynamics past straight cylinders has been broadly studied, the vortex shedding in the wake of wavy geometries has received limited attention in literature and curved cylinders even less. The most interesting effect of introducing a wavy trailing edge is a consistent drag reduction that has been achieved in many numerical simulations and experiments.

Bearman & Tombazis (1997) studied the uniform flow past a model with half-elliptical nose and a blunt trailing edge in the form of a sinusoidal wave. They measured the spanwise distribution of the mean base pressure and the Strouhal number. From the pressure measurements in model with different waviness, it was evident that steeper waves were associated with the greater drag reductions. They observed a significant difference between the value of the base pressure at a valley and at a peak, with the latter exhibiting a higher (less negative) C_{pb} and a larger drag reduction. Surprisingly, the vortex formation length was found to be longer at the valley, where the base pressure was lower. This was explained by considering "the fraction of the shed vorticity that survives vortex formation and arguing that mixing and cancellation must be greater at a valley". The velocity spectra showed the presence of two different shedding frequencies, the lower one dominant at the peak and the higher one at the valley. The authors postulated the presence of two cells in the spanwise region corresponding to a half-wavelength of the trailing edge and associated each shedding frequency with a certain level of base pressure, so that a dislocation could be identified by a jump in base pressure.

Similarly, Bearman & Owen (1998) studied the effect of wavy separation lines on the flow around a common bluff body at $Re = 40000$. They found that the waviness

fixed the dislocation positions and led to a drag reduction of at least 30% compared to the equivalent straight body; vortex shedding suppression was achieved for values of wave steepness (defined as the ratio between the peak-to-peak wave height and the wavelength) in excess of $0.06 - 0.09$.

Lam *et al.* (2004) studied a similar wavy geometry. Their spectral analysis of hot wire and load cell signals showed that only one predominant shedding frequency took place at every spanwise location: the Strouhal number in all the wavy cylinders tested was equal to the value for a straight body. The authors suggested that the "the re-organization of the wake structure due to the surface geometry variation may be the main reason for the drag and lift reduction", which is thus independent of the shedding behaviour.

Lam *et al.* (2004) performed Digital Particle Image Velocimetry on a circular cylinder where the waviness was applied to the whole surface and not only to the trailing edge; in the Reynolds number range from 3000 to 9000, they achieved a longer averaged formation length compared to the straight cylinder case and a consistent drag reduction, as the geometrical disturbance resulted in the vortex rolling up with a weaker strength at a further downstream position. In addition to this, the formation region was found to be longer behind a saddle point (corresponding to a valley in Bearman & Tombazis (1997) terminology), which exhibited also a wider wake: the authors observed a deceleration of the flow in the saddle plane, leading to an earlier vortex separation. This reverse flow speed within the vortex formation region is also responsible for the hook-like structure of the vorticity. Overall, the effect of the wavy geometry is to distort a two-dimensional vortex rolling into a three-dimensional process, by inducing a significant axial flow from the saddle to the nodal points: consequently the shear layers are stretched in the spanwise direction behind the saddle points and contracted behind the nodal points.

Numerical studies on wavy cylinders have been conducted by Darekar & Sherwin (2001b,a) for Reynolds numbers from 10 to 150. Unlike Bearman & Tombazis (1997), they considered a body with a wavy leading edge. Once again a sufficiently high wave steepness stabilised the near wake in a time-independent state. In particular, a moderate waviness corresponded to an anti-symmetric form of shedding, similar to

the straight cylinder with mild three-dimensionalities in the wake, which was named regime I. As the waviness was increased, three-dimensional structures appeared in the form of streamwise vorticity connecting adjacent spanwise vortices and the shear layers exhibited a large spanwise curvature: in this transitional regime, for non-dimensional wavelength below threshold value $\lambda/D = 5.6$, a time periodic state with a single dominant frequency was observed (regime II type A). Above the threshold value, two distinct shedding frequencies appeared, with a beating phenomenon in which the wake topology alternated from a nearly two-dimensional state similar to regime I (associated with the higher frequency) to a highly three-dimensional one (associated with the lower frequency). This can explain the discrepancy between the results obtained by Bearman & Tombazis (1997) and Lam *et al.* (2004), although the former studied a wavy-trailing-edge body and the latter a circular cylinder with an omni-directional waviness. A significant drop in the drag and lift forces was achieved as the waviness was further increased and the near wake became completely steady (regime III type A, for $\lambda/D \leq 5.6$). As for regime II, for $\lambda/D > 5.6$ a sub-regime B was observed with hairpin vortices shed periodically from the near base region.

The total suppression of the vortex shedding could not be achieved by Bearman & Tombazis (1997) on a wavy-trailing-edge body, probably due to the fact that in this configuration the three-dimensional effects are introduced later than in the wavy-leading-edge one and the bodies are consequently less sensitive to wave steepness. From a physical point of view the spanwise waviness of the leading edge sets up an axial flow that is believed to lead to a redistribution of the vorticity by generating streamwise and vertical vorticity. These additional vorticity components are stronger in the region near the inflection points, where the velocity component axially aligned to the body reaches a maximum; this process weakens the spanwise vorticity, leading to the breakdown of the unsteady Karman vortex street into a steady and symmetric near wake structure. The observation that the wake is wide behind the geometrical minimum and narrow behind the maximum can be related to the appearance of the streamwise vorticity, which is responsible for the sinusoidal displacement of the near wake illustrated in figure 2.22, and to the change in the vertical velocity distribution within the shear layer. Behind a geometrical minimum the vertical velocity reaches

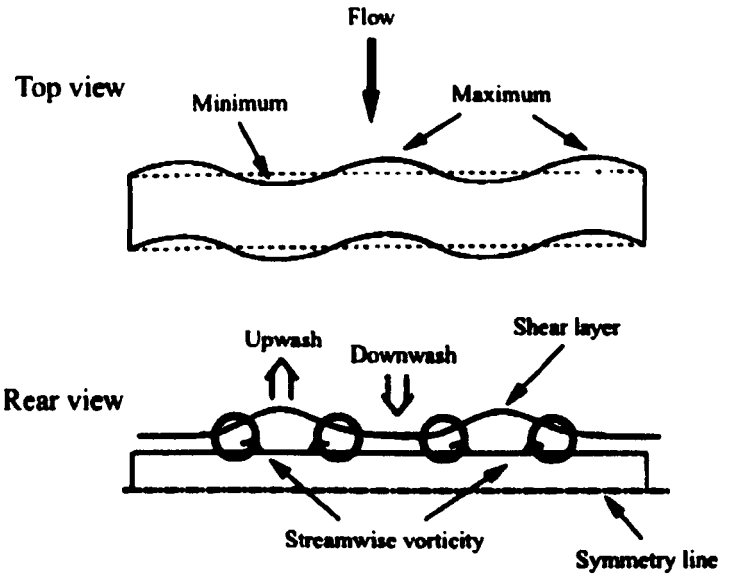


Figure 2.22: Relation between the streamwise vorticity at the inflection points and the wake width variation along the span (Darekar & Sherwin (2001b)).

its maximum and contributes to push the shear layers apart, preventing them from interacting in the classical vortex street. This process is associated with an increase in the mean base pressure and with a total drag reduction, which reaches a maximum value of 16% for regime III type A (compared with the straight cylinder results).

Numerous tests have been performed to suppress vortex shedding using passive control devices, such as strakes, bumps and wired cylinders. Strakes are particularly effective in wind engineering and for high mass ratio bodies: they can suppress VIV by preventing the shedding from becoming correlated along the span, as the introduction of three-dimensionalities in the separating flow disrupts the vortex formation mechanism in a similar fashion to that of wavy cylinders. However, this is associated with an increase of the drag and hence of the base bending moment, so that the structures need to be strengthened; in addition to this, in water these devices are not as successful as in air. Considering again (2.13) we note that the amplitude of oscillation depends on the inverse of the mass-damping parameter, which is generally low for bodies vibrating in water. Therefore, even if strakes are able to reduce the transverse force coefficient (as proved also by DNS on wired cylinders performed by Sirisup *et al.* (2004)), they are less successful in suppressing VIV in

water compared to air, although the amplitude of oscillation is smaller than that of a bare pipe.

These findings are confirmed by the experiments conducted by Bearman & Brankovic (2004) on circular cylinder covered with strakes and bumps in a uniform free-stream: for a fixed straked body VIV could not be fully suppressed, although its amplitude was consistently reduced. However, if the cylinder was free to respond, a strong vortex shedding was generated and VIV built up. The response in this case was similar to the plain cylinder one and modes of shedding were close to 2S and 2P, depending on the reduced velocity. Similar results were obtained using bumps instead of strakes.

Trim *et al.* (2005) performed a complete set of experiments on two different types of triple -start helical strakes. One of these configurations had a $5D$ pitch/$0.14D$ height design, which is quite close to the model tested by Bearman & Brankovic (2004) ($5D$ pitch/$0.12D$ height); the other had a pitch of $17.5D$ and a height of $0.25D$. The authors conducted several tests to determine the degree of VIV mitigation at different percentage of strake coverage over the length of the riser: in sheared currents both geometries were effective in suppressing VIV only if a coverage of more than 82% of the total length was used, while in uniform flow the $5D$ pitch/$0.14D$ height configuration was much less effective than the $17.5D/0.25D$ one. Further, in-line fatigue damage proved to be as severe as cross-flow fatigue damage.

Chapter 3

Problem definition

This chapter describes the computational grid, boundary conditions and post-processing tools used in the present numerical analysis of flow past a curved body of circular cross-section. As described in section 3.1, the relative complexity of the geometry poses a challenge in terms of grid generation, as the curvature of the body requires a high number of elements and a hybrid mesh. Therefore a compromise solution had to be achieved to perform efficiently the numerical simulations, as section 3.1.1 outlines.

Another challenge is represented by the imposition of the boundary conditions for the different types of motion analysed, especially on the upper and inflow plane of the computational domain. Section 3.1.2 presents the mathematical formulation of the different boundary conditions and motivates the choices made in the simulations, which are to be discussed in more details in the result chapters.

Finally, section 3.2 concludes this chapter illustrating the post-processing tools used to analyse the data, with special focus on the λ_2 criterion for the visualisation on vortical structures.

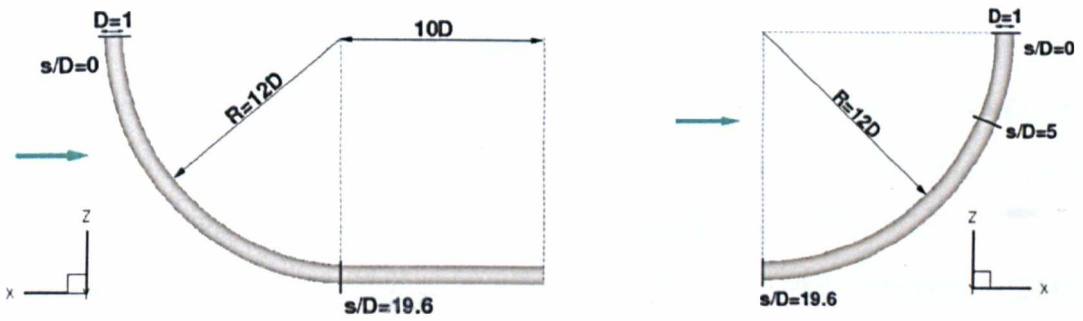


Figure 3.1: Convex configuration (*left*) and concave configuration (*right*); the arrows indicate the free-stream direction, whereas s/D is the non-dimensional arc-length.

3.1 Computational domain and geometrical models

Two different curved configurations have been studied: in both cases, the main component of the geometry is a "cylinder" of circular cross-section, whose centreline axis is prescribed by a quarter ring. The non-dimensional radius of curvature is defined as the ratio of the radius R of the curved axis of the deformed cylinder to its cross-section diameter, D. Most of the present computations have been performed using a non-dimensional radius of curvature $R/D = 12.5$. This value has been chosen very close to the limit curvature for flexible marine riser pipes used in the offshore industry and therefore the cases analysed represent a critical configuration from the point of view of the fluid dynamic loading on the structure.

In all the simulations, the plane of curvature of the body is aligned with the free-stream direction and the inflow velocity profile is uniform, with a Reynolds number $Re = \frac{U_\infty D}{\nu}$ of 100. As illustrated in figure 3.1, two different configurations can be identified depending on the orientation of the curved leading edge. In the "convex configuration", the body is oriented such that the outer part of the ring is the stagnation face, whereas in the "concave configuration" the free-stream is applied on the inside of the quarter ring. In the "convex configuration" a horizontal straight extension of 10 diameters has also been added to the end of the curved part

of the body, to allow a full development of the wake. A non-dimensional arc-length s/D is used to parametrise the geometries, with $s/D = 0$ and $s/D = 19.6$ denoting the top and the end of the quarter ring, respectively. In the convex configuration, the total body length is therefore $s/D = 29.6$, while the concave one (which consists of the quarter ring only) has a total non-dimensional length of 19.6.

In all the three-dimensional simulations the order of the polynomial expansion has been increased from $P = 4$ to $P = 6$, in order to save computational time and refine the solution only after the flow has reached a stabilised state. A first order time integration scheme was used in all the cases and the time step was chosen equal to 0.001: this allowed the CFL condition to remain bounded and below 0.6, ensuring the numerical stability.

3.1.1 Mesh generation

The meshes utilised in all the three-dimensional computations have been accomplished by *Felisa*, a software developed by Peiro' *et al.* (2004). The surface triangulation and the generation of the 3D tetrahedral mesh are based on a variant of the advancing front method, as described by Peraire *et al.* (1993); the boundary layer mesh on the body's walls is achieved through a modified advancing layer method, whereby the nodes of the prismatic elements are generated along lines approximately normal to the surface. A more rigorous explanation of this method can be found in Peiro' & Sayma (1995).

In the present studies, the mesh is generated over three sub-steps. First, the triangulation of the surface is accomplished, then a structured layer of prisms is built with each prism orientated such that one of the two triangular faces is attached to the body's surface; finally the rest of the computational domain is filled with an unstructured tetrahedral mesh. The surface triangulation stage and a detail of the boundary layer mesh are illustrated in figure 3.2. The combination of prisms in proximity of the body and tetrahedra in the rest of the domain allows a compromise between an improved resolution in the boundary layer region and the efficiency of the space filing with tetrahedra.

Given the features of the spectral/*hp* element method a simultaneous refinement



Figure 3.2: Surface triangulation (*left*) and detail of the three-dimensional grid showing the prismatic boundary layer mesh on the body's surface (*right*).

of the solution could be achieved by increasing the polynomial order and refining the grid. In the present work, the mesh resolution has been kept fixed and the necessary refinement has been achieved by increasing the polynomial order: the meshes are based on the ones tested by Miliou (2004), which were proved to be free from blockage effects. However, given the motion of the body in the present simulations, a grid refinement in the near-wake region has been performed to correctly reproduce the wide Von Karman street observed in some cases.

The convex configuration mesh consists of 12688 elements in total, out of which 1156 are prisms; in the concave geometry the total number of elements is 14874, with 1574 prisms in the boundary layer. The number of local degrees of freedom in the case of a prism is given by $\frac{(P+1)^2(P+2)}{2}$, whereas for a tetrahedron it is $\frac{(P+1)(P+2)(P+3)}{6}$, where P is the polynomial order. Therefore, at $P = 6$ the mesh for the convex geometry accounts for 1195264 local degrees of freedom per variable, whereas the mesh for the concave geometry has 1425704 local degrees of freedom per variable. These figures provide an estimate of the computational cost involved in each simulation. The computations have been carried out in parallel on 32 processors, using the computing resources provided by the Imperial College High Performance Computing Service and by the Department of Aeronautics.

These data highlight the greater challenge of performing a parametric study using a fully three-dimensional approach; on the other side, as discussed in section 6.2, the two-dimensional codes currently available for VIV calculations rely on assumptions

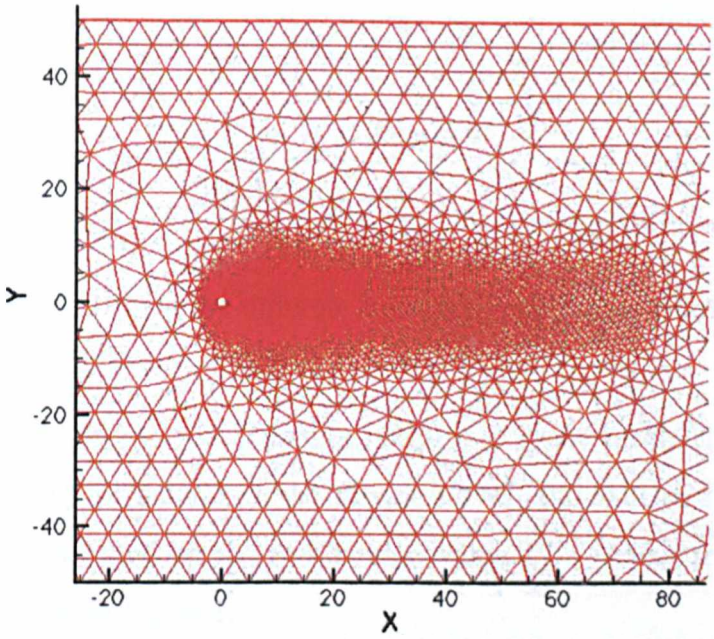


Figure 3.3: Two-dimensional mesh used in the VIVIC computations.

that discard some of the physical features of the curved geometries. However, the considerable reduction of computational effort allowed by strip theory models makes this approach attractive to industry research. The unstructured triangular grid obtained with *Felisa* for the two-dimensional simulations is shown in figure 3.3.

3.1.2 Boundary conditions

This section will provide a brief description of the boundary conditions utilised in the simulations. A summary of all the boundary conditions is given in table 3.1.

In both configurations, a velocity inlet boundary condition is specified on the inflow plane of the computational domain, as well as on all the side planes (with the exception of the top plane of intersection with the body). In the concave geometry, since the cylinder intersects the inflow plane, an exponential term has been added to the inflow to achieve exponential decay of the velocity inside the boundary layer. Therefore, the following no-slip conforming boundary condition is applied:

$$u(x,y,z) = 1 - e^{-\beta(\sqrt{x^2+y^2+(z+12.5)^2}-0.5)}, \qquad v(y,z) = w(y,z) = 0$$

Description	Mathematical formulation	Computational Plane
Velocity	$\mathbf{u} = f(\mathbf{x}, t) \vee \mathbf{u} = const., \frac{\partial p}{\partial n} = 0$	Inflow and side planes
Symmetry	$w = 0, \frac{\partial u}{\partial n} = \frac{\partial u}{\partial z} = 0, \frac{\partial v}{\partial n} = \frac{\partial v}{\partial z} = 0, \frac{\partial p}{\partial n} = 0$	Upper plane (z axis)
Outflow	$\frac{\partial u}{\partial n} = \frac{\partial v}{\partial n} = \frac{\partial w}{\partial n} = 0, p = 0$	Outflow plane
Wall	$u = v = w = 0$	Body's surface

Table 3.1: Overview of the different boundary condition imposed in the simulations.

where $\beta = 50$ is a constant determining the rate of decay inside the boundary layer, whose thickness δ_{99} is defined as the distance from the wall to the point at which the velocity reaches 99% of the free-stream value U_∞. Away from the body, the free-stream velocity is $U_\infty = 1$.

In all the cases examined, the outflow plane of the domain corresponds to a fully developed zero stress condition and the surface of the body is represented by a wall boundary condition, which ensures that the velocity field on the cylinder is zero by enforcing a no-slip condition.

As mentioned above, the upper plane of the domain contains the intersection of the computational boundary and the top section of the body. The imposition of a specific boundary condition on this plane has a strong effect on the vortex shedding dynamics and therefore must be considered carefully. A symmetry boundary condition has been chosen to approximate the flow features on this plane: this involves that no flow can be directed normally to the plane $z = 0$ and thus $w = 0$. The effect of this constraint on the resulting vortex shedding is particularly relevant in the concave configuration, which generates axial flow directed towards the top sections due to the leading edge orientation, and will be further discussed in the light of the computational results in section 6.1.2 and 6.3.2.2.

A final remark concerns the forced vibration simulations with uniform cross-flow translation and rotation about the bottom end of the quarter ring. In these cases, an oscillatory velocity profile is imposed on the inflow and side planes and the cylinder is kept fixed in the frame of reference; to model this flow condition, the velocity inlet

boundary condition has been modified and a velocity profile dependent on the spatial coordinates and on the time has been imposed ($\mathbf{u} = f(\mathbf{x}, t)$ in table 3.1). Therefore, the inertia is increased by the Froude-Krylov force, a buoyancy force due to the pressure gradient imposed on the fluid to generate the oscillating inflow; to estimate the forces on the surface of the oscillating body, this additional force contribution is taken into account in the pressure gradient term in the Navier-Stokes equations. This ensures the fluid dynamic equivalence between an oscillating cylinder moving in a uniform flow and a cylinder at rest in an oscillatory flow.

3.2 Data analysis and post-processing tools

The analysis of the main flow features has been conducted along two lines of investigation. From a physical point of view the wake topology in the computed flow is presented using vorticity, velocity and pressure isocontours, whereas the effect of the fluid dynamics on the body is discussed considering the sectional force distribution, the frequency of vortex shedding and the energy transfer mechanism. However, a rigorous mathematical method for the identification of vortical structures is also required to provide a clear description of the mechanics of vortex shedding: in this work we limit ourselves to the λ_2 criterion proposed by Jeong & Hussain (1995).

3.2.1 The λ_2 criterion

A coherent structure could be defined as a localised region within a flow where the vortical and swirling motions are significant compared to the surrounding fluid: the vortex is then one of the most visible and stable coherent structures in fluid mechanics. The need of a clear identification method has led to the formulation of several criteria: in this study, the vortical structures are captured and visualised through the λ_2 criterion developed by Jeong & Hussain (1995). This method is based on the existence of a local pressure minimum in a swirling flow, in the absence of unsteady and viscous contributions. This condition is essential, since unsteady straining can create a pressure minimum without involving a vortical motion; on the other hand, the effect of viscosity can balance the pressure gradient term in

the Laplace equation and thus eliminate a pressure minimum from a vortical flow. Therefore, the presence of a pressure minimum in itself is neither a necessary nor a sufficient condition for the vortex identification, unless these two terms are discarded. By taking the gradient on both sides of the Navier-Stokes equation, one obtains the following expression for the Hessian of pressure:

$$-\frac{\partial^2 p}{\partial x_i \partial x_j} = \frac{DS_{ij}}{Dt} - \nu \frac{\partial^2 S_{ij}}{\partial x_k \partial x_k} + S_{ik}S_{kj} + \Omega_{ik}\Omega_{kj} \tag{3.1}$$

where the velocity gradient tensor $\nabla \mathbf{u}$ has been decomposed in a symmetric and an anti-symmetric part, respectively given by:

$$S_{ij} = \frac{1}{2}\left(\frac{\partial u_i}{\partial x_j} + \frac{\partial u_j}{\partial x_i}\right); \qquad \Omega_{ij} = \frac{1}{2}\left(\frac{\partial u_i}{\partial x_j} - \frac{\partial u_j}{\partial x_i}\right) \tag{3.2}$$

The first two terms in the RHS of equation (3.1) must be neglected since the unsteady straining and the viscous effect affect the presence of a pressure minimum. Jeong & Hussain (1995) demonstrated that the Hessian of pressure must have two positive eigenvalues in order to have a local pressure minimum. Since the tensor $S^2 + \Omega^2$ is symmetric and has only positive eigenvalues, i.e. $\lambda_1 > \lambda_2 > \lambda_3$, this condition is satisfied by requiring that $\lambda_2 < 0$ within a vortex core, hence the name of the criterion. The vortex core can then be defined as "a connected region in space with two negative eigenvalues of the velocity gradient tensor" (Jeong & Hussain (1995)).

3.2.2 Filtering the λ_2 isosurfaces

Due to the computational cost dictated by the large three-dimensional hybrid mesh, the polynomial order $P = 6$ could not be further increased to allow a better approximation of the flow in the region of the wake where the grid becomes coarser. Further, in the spectral element discretisation, the lack of a C^1 continuous expansion basis implies that derivatives of velocity may not be continuous at the boundaries between elements. Since the λ_2 criterion is based on the evaluation of the eigenvalues of the matrix containing terms with the square of the velocity derivatives, any error at the element boundaries will be magnified: this will in turn lead to localised discontinuities in the isosurfaces of constant λ_2. These considerations highlight the

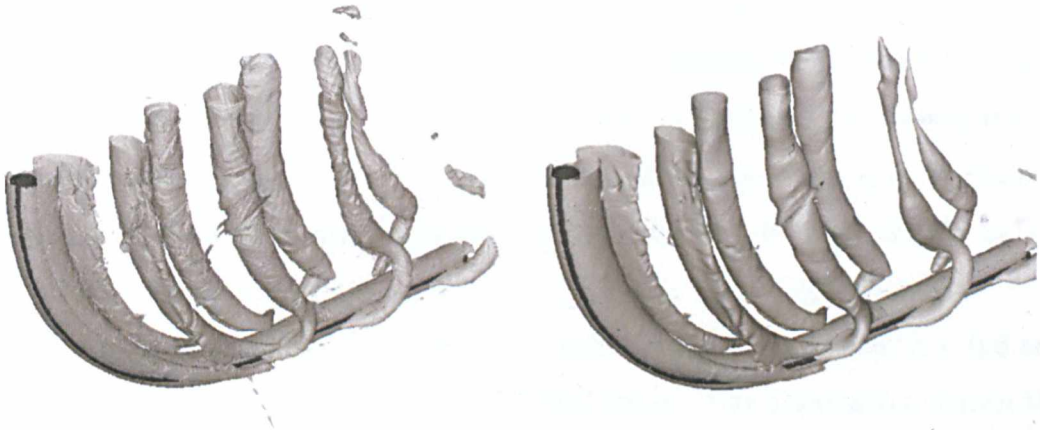


Figure 3.4: Filtering algorithm applied to isosurfaces at $\lambda_2 = -0.1$ visualising vortex shedding past the convex configuration: unfiltered (*left*) and filtered (*right*) results.

need for a refinement of the isosurfaces in the post-processing operations in order to obtain unambiguous visualisations of the cores: for this reason, a two-stage filtering algorithm has been applied to the data sets to remove spurious structures.

First, the isosurface is filtered depending on the number of elements that contribute to a single surface: if this number is lower than a chosen threshold value, the corresponding coherent structure is discarded. The isosurface is then smoothed using a non-shrinking low pass filter. This operates by first moving a vertex i from a coordinate $\mathbf{x}_i$ to a new location $\mathbf{x'}_i$ such that:

$$\mathbf{x'}_i = \mathbf{x}_i + \lambda \Delta \mathbf{x}_i \tag{3.3}$$

$$\Delta \mathbf{x}_i = \frac{1}{2}(\mathbf{x}_{i-1} - \mathbf{x}_i) + \frac{1}{2}(\mathbf{x}_{i+1} - \mathbf{x}_i) \tag{3.4}$$

where λ is a scale factor that has to be chosen between 0 and 1 to attenuate high frequencies, and $\Delta \mathbf{x}_i$ is the discrete Laplacian of $\mathbf{x}$. This latter variable represents the discrete surface signal and can be written as a summation of weighted averages over all the N_i neighbouring vertices connected to the $i-$th vertex:

$$\Delta \mathbf{x}_i = \sum_{j=1}^{N_i} w_{ij}(\mathbf{x}_j - \mathbf{x}_i) \tag{3.5}$$

where the weights w_{ij} are positive numbers whose sum is equal to one. However, as the smoothing described in equation (3.3) generates shrinkage, the vertex is displaced again using a new scale factor μ for $\Delta \mathbf{x}_i$: this time, μ is chosen to be negative to compensate the shrinkage produced by the initial step. Its value is a function of λ and of the bandwidth of the unfiltered low frequencies. Further details on the mathematical formulation of this filter can be found in Taubin (1995, 2001).

In the present work, all the λ_2 isosurfaces have been obtained using $\lambda = 0.6$ and $\mu = 0.6$ and iterating the smoothing process 1000 times. The difference between the unfiltered and the filtered λ_2 isosurfaces in the case of the vortex shedding past the convex configuration is illustrated in figure 3.4.

3.2.3 Lift force decomposition and phase angle

When the body is subjected to sinusoidal oscillations, its motion introduces in the wake an additional frequency that competes with the Strouhal frequency. According to the choice of input amplitude and frequency of oscillation, the body's response may be locked-in, so that the imposed motion takes control of the vortex shedding and the Strouhal frequency disappears. A formula for the lift force, which in the current notation is directed in the $y-$direction, based on the Strouhal and oscillation frequencies f_s and f_o and on the corresponding phase angles can be written as:

$$F_y(t) = F_{yo} \sin(2\pi f_o t + \phi_o) + F_{ys} \sin(2\pi f_s t + \phi_s) \tag{3.6}$$

Similarly the drag force, which operates in the $x-$direction, can be expressed as:

$$F_x(t) = F_{xm} + F_{xo} \sin(2\pi(2f_o)t + \psi_o) + F_{xs} \sin(2\pi(2f_s)t + \psi_s) \tag{3.7}$$

where F_{yo} and F_{xo} are the magnitude of the sinusoidal lift and drag forces respectively, while f_o and $2f_o$ represent the corresponding oscillation frequencies; F_{ys}, F_{xs} and f_s refer to the Strouhal component of the signal. In the hypothesis of a locked-in state, the Strouhal components in equations (3.6) and (3.7) can be neglected: further, since the body will not oscillate at the Strouhal frequency, these components do not affect the energy transfer from the fluid to the structure and vice versa. How-

ever, if the Strouhal component of the lift force exists and has a sufficient magnitude, it is possible that the body starts to respond at both frequencies, giving rise to a beating vibration or vortex dislocations.

Once the Strouhal component has been discarded, the forces from equations (3.6) and (3.7) can be non-dimensionalised against the cross-sectional diameter D, the free-stream velocity U_∞ and the density ρ. The resulting lift and drag coefficients are given by:

$$C_L(t) = \frac{F_{yo}}{\frac{1}{2}\rho D^2 U_\infty^2} \tag{3.8}$$

$$C_D(t) = \frac{F_{xo}}{\frac{1}{2}\rho D^2 U_\infty^2} \tag{3.9}$$

As the present investigation focuses on cross-flow motion, information on the lift force distribution is of great importance. Further insight can be gained from the analysis of the integrated unsteady forces acting on the body's surface. The pressure and shear stresses values are extracted at a number of discrete surface points in circular cross-sections located at constant intervals along the span and perpendicular to the body's centreline: the forces at each section are then obtained by integrating over the cross-section's line in the two-dimensional plane. The variation of the integrated lift coefficient along the span is plotted against the non-dimensional time to understand its different contribution in each section of the cylinder, as shown in figure 3.5.

The lift coefficient analysis is crucial in determining whether the hydrodynamic forces act to excite or dampen the body's motion. The mechanical energy transferred between the body and the fluid can be expressed via the following relationship:

$$E = \frac{2}{\rho U_\infty^2 D^2} \int_0^T \dot{y} F_y dt \tag{3.10}$$

A positive value of E indicates that work is done by the fluid on the structure, which is subsequently excited. Conversely, a negative value of E means that the body's motion is damped by the hydrodynamic forces. In forced oscillation, the motion is driven externally and the sign of E is not constrained: therefore the energy

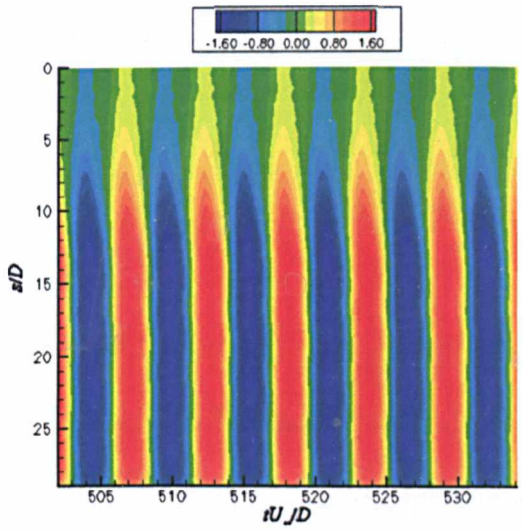


Figure 3.5: Spanwise variation of the integrated sectional lift coefficient against non-dimensional time. Convex configuration at $f_o = 1.1f_s$, $A/D = 0.5$ and $Re = 100$.

transfer can occur in both directions. In free vibration instead, the time-averaged value of E integrated along the whole span of the body must remain positive to overcome energy dissipated through structural mechanical damping, if present, and to allow vortex-induced vibrations to be excited. The sign of the energy transfer is related to the phase angle between the body's displacement and the fundamental harmonic of the lift force, so that positive values of E correspond to a phase angle in the interval $[0°; 180°]$ and negative values of E to phase angle in the interval $[-180°; 0°]$.

Quantitative determination of the phase angle is made via Fourier coefficient analysis. The lift coefficient can be represented as a Fourier series:

$$C_L(t) = a_0 + \sum_{n=1}^{\infty} a_n \cos\left(\frac{2\pi nt}{T}\right) + \sum_{n=1}^{\infty} b_n \sin\left(\frac{2\pi nt}{T}\right) \tag{3.11}$$

where the Fourier coefficients are as follows:

$$a_0 = \frac{1}{T}\int_0^T C_L(t)dt \tag{3.12}$$

$$a_n = \frac{2}{T}\int_0^T C_L(t)\cos\left(\frac{2\pi nt}{T}\right)dt \tag{3.13}$$

$$b_n = \frac{2}{T}\int_0^T C_L(t)\sin\left(\frac{2\pi nt}{T}\right)dt \tag{3.14}$$

After discarding the Strouhal component in the RHS of equation (3.6), the lift coefficient can be written as:

$$C_L(t) = C_{L_o}\cos(\phi_o)\sin(2\pi f_o t) + C_{L_o}\sin(\phi_o)\cos(2\pi f_o t) \tag{3.15}$$

where C_{L_o} is the magnitude of the oscillating lift coefficient. Considering the imposed sinusoidal trajectory of amplitude $\hat{y}_o$:

$$y(t) = \hat{y}_o\sin(2\pi f_o t) \tag{3.16}$$

the part of the lift coefficient in phase with the body velocity, CL_v, and the one in phase with the body's acceleration, CL_a, are given by:

$$CL_v = C_{L_o}\sin\phi_o; \qquad CL_a = C_{L_o}(-\cos\phi_o) \tag{3.17}$$

Equation (3.15) can therefore be re-written as:

$$C_L(t) = -CL_a\sin(2\pi f_o t) + CL_v\cos(2\pi f_o t) \tag{3.18}$$

Comparing this expression to equation (3.11) where $a_0 = 0$ (due to the sinusoidal nature of the signal), $n = 1$ and $T = 1/f_o$ yields the following definitions:

$$a_1 = \frac{2}{T}\int_0^T C_L(t)\cos(2\pi f_o t)dt = CL_v \tag{3.19}$$

$$b_1 = \frac{2}{T}\int_0^T C_L(t)\sin(2\pi f_o t)dt = -CL_a \tag{3.20}$$

Subsequently, the phase angle ϕ_o can be obtained from the above relationships as:

$$\phi_o = \arctan\left(\frac{a_1}{b_1}\right) = \arctan\left(\frac{CL_v}{-CL_a}\right) \tag{3.21}$$

Hence, when $CL_v > 0$ the energy is transferred from the fluid to the structure and positive excitation is achieved ($0° < \phi_o < 180°$). Likewise, $CL_v < 0$ corresponds

to hydrodynamic damping and to phase angles in the range $180° < \phi_o < 0°$. To simplify the notation, in the next chapters the subscript will be dropped and the phase angle will be referred to as ϕ.

Chapter 4

Computational framework

This chapter presents the fundamentals of the numerical methods used for the simulations performed. As the two- and three-dimensional simulations have been carried out using two different numerical codes, this chapter is divided into two parts.

First, the fundamentals of spectral element methods are introduced in section 4.1, with details on the matrix formulation, local expansions and global assembly. The method of weighted residuals in the Galerkin formulation is presented in section 4.1.1, with an example solution of the Poisson equation in one dimension. Section 4.1 concludes with an overview of the advantages of applying a $p-$type extension to the spectral element approach, in terms of accuracy of the solution and error convergence. Section 4.2 presents the three-dimensional Navier-Stokes algorithm in the form solved by the *Νεκταr* code: the temporal discretisation of the system of PDE is described in section 4.2.1, whereas the algorithm implemented in the three-dimensional code for predicting the fluid/structure interaction in free vibration is described in section 4.2.2.

The second part of this chapter is devoted to the two-dimensional sectional approach: the strip theory model and its application to VIV problems is discussed in section 4.3, which also provides a brief overview of the strip theory based methods. Finally, section 4.4 concludes this chapter with a description of the VIVIC code and its implementation.

4.1 Spectral/*hp* element methods

In finite element methods, the computational domain is divided in contiguous elemental sub-domains and the solution is approximated by a linear combination of basis functions of low polynomial order, defined over a standard element; the algebraic error decay is then ensured by the $h-$convergence, where h represents the size of the mesh: the number of elements is increased and their size decreased, while the polynomial order is kept fixed. On the other hand, spectral element methods make use of high order polynomial or trigonometric expansion basis functions that are defined globally on the whole computational domain. In these methods, exponential convergence is achieved by increasing the order of the basis functions keeping the size of the mesh constant, in the so-called $p-$type refinement. The basic concept of the spectral/*hp* finite element scheme is to combine the attributes of both these approaches and develop an $hp-$type of convergence: this consists in the simultaneous increase of the mesh refinement and of the polynomial order in the expansion basis. Before introducing the implementation of this method in the numerical code, the fundamentals of finite elements are illustrated through the solution of the one-dimensional Poisson equation: this allows us to introduce the Galerkin formulation and to discuss the construction of a suitable expansion basis.

4.1.1 Galerkin weighted residual method

The method of weighted residual can be illustrated considering a linear differential problem in the form:

$$\mathbf{L}(u(\mathbf{x},t)) = f(\mathbf{x},t) \tag{4.1}$$

where $\mathbb{L}$ is a linear differential operator, applied to a function u defined over the domain Ω and subject to suitable boundary and initial conditions. The solution to this problem can be approximated by a linear combination of basis functions of the form:

$$u^{\delta}(x,t) = u_0(x,t) + \sum_{i=1}^{N} \hat{u}_i(t)\phi_i(x) \tag{4.2}$$

where $\phi_i(x)$ are analytic functions, generally referred to as *trial functions*, $\hat{u}_i$ are N unknown coefficients and $u_0(x,t)$ is a function satisfying the initial and boundary conditions. The substitution of an approximated solution u^{δ} in the linear differential operator generally results in a non-zero residual $R(u^{\delta})$, since $\mathbf{L}(u^{\delta}(\mathbf{x},t)) \neq f(\mathbf{x},t)$. The method of weighted residuals is based on the assumption that the inner product of the residual with a weight function v^{δ} over the solution domain is equal to zero. Since the Legendre inner product of two functions f and g over the domain Ω is defined as:

$$(f,g) = \int_{\Omega} f(x)g(x)dx \tag{4.3}$$

the above restriction can be written as:

$$\int_{\Omega} v_i^{\delta} R(u^{\delta})d\mathbf{x} = 0 \qquad i = 1,2,...,N \tag{4.4}$$

This yields a set of N algebraic equations that can be solved for the unknown coefficients $\hat{u}_i$ at a given time.

The choice of the weight functions determines the type of sub-method in the weighted residual framework. The Navier-Stokes solver used in this work is based on the Galerkin methods, whereby the weight, or test, functions coincide with the trial functions $\phi_i(x)$. In the remainder of this section, the Galerkin formulation of the weighted residual method will be illustrated through the example solution of the Poisson equation in one dimension.

4.1.1.1 Solution of the one-dimensional Poisson equation

The general form of the Poisson equation in one dimension can be written considering a linear differential operator $\mathbf{L}$ applied to a function u in the domain $\Omega = \{x \mid 0 \leq x \leq L\}$:

$$\mathbf{L}(u) \equiv \frac{\partial^2 u}{\partial x^2} + f = 0 \tag{4.5}$$

where λ is a real positive constant and f is a forcing function.

Appropriate boundary conditions are imposed at both ends of the domain and are of Dirichlet and Neumann type:

$$u(0) = g_D, \qquad \frac{\partial u}{\partial x}(L) = g_N \tag{4.6}$$

The weak formulation for the problem can be obtained by taking the Legendre inner product of equation (4.5) using a test function $v(x)$, which by definition is zero on all Dirichlet boundaries. This yields the equality:

$$(v, \mathrm{L}(u)) = \int_0^L v\Big(\frac{\partial^2 u}{\partial x^2} + f\Big)dx = 0 \tag{4.7}$$

Equation (4.7) can be integrated by parts to obtain the following:

$$\int_0^L \frac{\partial v}{\partial x}\frac{\partial u}{\partial x}dx = \int_0^L vf dx + \Big[v\frac{\partial u}{\partial x}\Big]_0^L \tag{4.8}$$

This weak formulation naturally includes the Neumann boundary condition and also reduces the order of the maximum derivative of the discrete problem: the second-order differential equation (4.5) has been transformed into a first-order differential equation and thus the solution space includes now functions that are C^0 continuous. When the exact solution is approximated by an appropriate expression such as equation (4.2) and the test functions are also replaced by a finite expansion, the discrete form of equation (4.8) is obtained:

$$\int_0^L \frac{\partial v^\delta}{\partial x}\frac{\partial u^\delta}{\partial x}dx = \int_0^L v^\delta f dx + v^\delta(L)g_N \tag{4.9}$$

where the homogeneous Dirichlet boundary condition has been imposed on the test functions and the Neumann boundary condition has also been incorporated into the formulation.

To enforce the Dirichlet boundary condition, the solution $u(x,t)$ is "lifted". This is equivalent to decomposing it into a known function $u^{\mathcal{D}}$, which satisfies the Dirichlet boundary condition, and an unknown homogeneous function $u^{\mathcal{H}}$, which is zero on the Dirichlet boundaries:

$$u^{\delta} = u^{\mathcal{D}} + u^{\mathcal{H}} \tag{4.10}$$

where

$$u^{\mathcal{H}}(\partial\Omega_{\mathcal{D}}) = 0, \qquad u^{\mathcal{D}}(\partial\Omega_{\mathcal{D}}) = g_{\mathcal{D}} \tag{4.11}$$

By substituting equation (4.10) into the weak formulation given by equation (4.9), one obtains:

$$\int_0^L \frac{\partial v^{\delta}}{\partial x}\frac{\partial u^{\mathcal{H}}}{\partial x}dx = v^{\delta}(L)g_N + \int_0^L v^{\delta} f dx - \int_0^L \frac{\partial v^{\delta}}{\partial x}\frac{\partial u^{\mathcal{D}}}{\partial x}dx \tag{4.12}$$

As all the terms on the RHS of equation (4.12) are known functions that satisfy the boundary conditions, this problem can be solved as a finite linear algebraic system once the homogeneous solution $u^{\mathcal{H}}$ and the test function v^{δ} have been replaced by the appropriate finite expansions, respectively:

$$u^{\mathcal{H}}(x,t) = \sum_{i=1}^{N_{dof}} \hat{u}_i(t)\phi_i(x) = \mathbf{\Phi}^t\hat{\mathbf{u}} \tag{4.13}$$

$$v^{\delta}(x,t) = \sum_{i=1}^{N_{dof}} \hat{v}_i(t)\phi_i(x) = \mathbf{\Phi}^t\hat{\mathbf{v}} \tag{4.14}$$

Hence, upon substitution of the definitions in (4.13) and (4.14), equation (4.12) can be written in matrix form as:

$$\hat{\mathbf{v}}^T[\mathbf{M}\hat{\mathbf{u}}] = \hat{\mathbf{v}}^T\mathbf{f} \quad \Rightarrow \quad \mathbf{M}\hat{\mathbf{u}} = \mathbf{f} \tag{4.15}$$

where $\mathbf{M}$ is a constant matrix equivalent to the LHS of equation (4.12), $\hat{\mathbf{u}}$ is the vector of unknown coefficients $\hat{u}^{\mathcal{H}}$ and $\mathbf{f}$ is a force vector that embodies both the Dirichlet and Neumann boundary conditions, as well as the forcing contributions from the RHS of equation (4.12).

4.1.2 Expansion basis and global assembly

The example above describes a single domain approximation of the Poisson equation. To implement the $h-$type method, the solution domain Ω has to be divided into N_{el}

non-overlapping elements such that:

$$\Omega = \bigcup_{e=1}^{N_{el}} \Omega^e, \qquad \bigcap_{e=1}^{N_{el}} \Omega^e = \emptyset \tag{4.16}$$

Each element Ω^e can be mapped onto a standard element $\Omega_{st} = \{\xi \mid -1 \leq \xi \leq 1\}$ by applying a coordinate transformation $\mathcal{X}^e(\xi)$ so that:

$$x = \mathcal{X}^e(\xi) = \phi_0(\xi) x_{e-1} + \phi_1(\xi) x_e, \qquad \xi \in \Omega_{st} \tag{4.17}$$

This transformation uses a local expansion basis that can be written as:

$$\phi_0(\xi) = \begin{cases} \frac{1-\xi}{2} & \xi \in \Omega_{st} \\ 0 & \xi \notin \Omega_{st} \end{cases} \quad \text{and} \quad \phi_1(\xi) = \begin{cases} \frac{1+\xi}{2} & \xi \in \Omega_{st} \\ 0 & \xi \notin \Omega_{st} \end{cases} \tag{4.18}$$

Consequently, the approximate solution u^δ, originally defined in equation (4.13) using the global expansion modes Φ_i, can now be expressed in terms of the local expansion modes, i.e.:

$$u^\delta(x) = \sum_{i=1}^{N_{dof}} \hat{u}_i \Phi_i(x) = \sum_{e=1}^{N_{el}} \sum_{p=0}^{P} \hat{u}_p^e \phi_p^e(\xi) \tag{4.19}$$

where P is the polynomial order of the expansion in each element.

Figure 4.1 shows the partitioning of the one-dimensional domain described in the previous section into a three-element domain and the corresponding passage from local to global expansion basis. This transformation is based on the hypothesis that the solution at a global point between two elements must be the same on both sides, which is mathematically satisfied by requiring that the solution $u^\delta(x)$ is C^0. In the three element domain of figure 4.1, this implies that the number of local degrees of freedom is equal to 6, whereas the number of global degrees of freedom is equal to 4 once the C^0 continuity requirement is satisfied.

The matrix form of the Poisson equation (4.15) can be inverted and written as:

$$\hat{\mathbf{u}} = \mathbf{M_G}^{-1} \mathbf{f_G} \tag{4.20}$$

where:

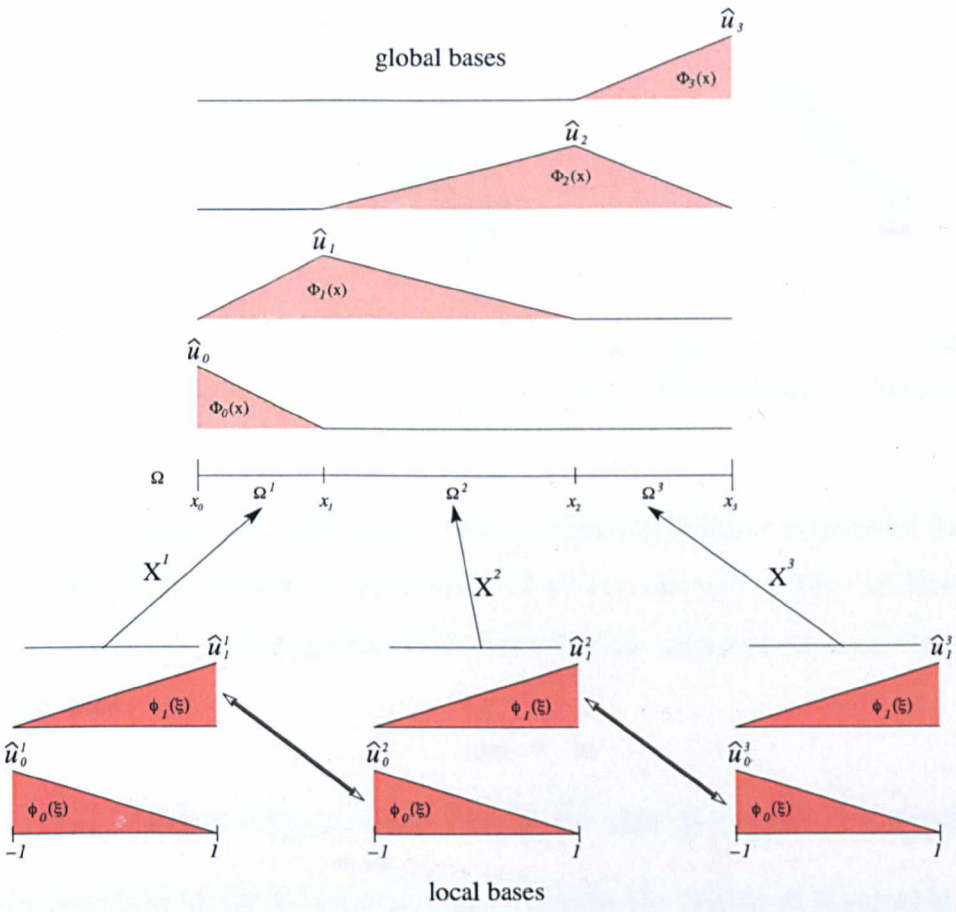


Figure 4.1: Local and global expansion basis on a three-element domain Ω (from Karniadakis & Sherwin (2005)).

$$\mathbf{M_G}[i][j] = (\mathbf{\Phi}_i, \mathbf{\Phi}_j), \quad \hat{\mathbf{u}} = [\hat{u}_1, \ldots, \hat{u}_{N_{dof}}]^T, \quad \mathbf{f_G}[i] = (\mathbf{\Phi}_i, f) \tag{4.21}$$

The global mass matrix $\mathbf{M_G}$ is obtained from the evaluation and the assembly of the local mass matrices $\mathbf{M}^e[p][q] = (\phi_p, \phi_q)$ for each element. Likewise, the global force vector $\mathbf{f_G}$ is obtained by assembling the local force vectors $f^e[p] = (\phi_p, f)$. The process of global assembly can be interpreted as an assembly matrix, $\mathbf{A}$, which leads to the following relations between global and local vectors:

$$\begin{bmatrix} \hat{\mathbf{u}}^1 \\ \vdots \\ \hat{\mathbf{u}}^{N_{el}} \end{bmatrix} = \mathbf{A} \begin{bmatrix} \hat{u}_1 \\ \vdots \\ \hat{u}_{N_{dof}} \end{bmatrix}, \qquad \mathbf{f_G}[i] = \mathbf{A}^T \begin{bmatrix} f^1[p] \\ \vdots \\ f^{N_{el}}[p] \end{bmatrix} \tag{4.22}$$

where $\hat{\mathbf{u}}^e = [\hat{u}^e_0, ..., \hat{u}^e_P]^T$. The enforcing of the continuity of the solution at the ele-

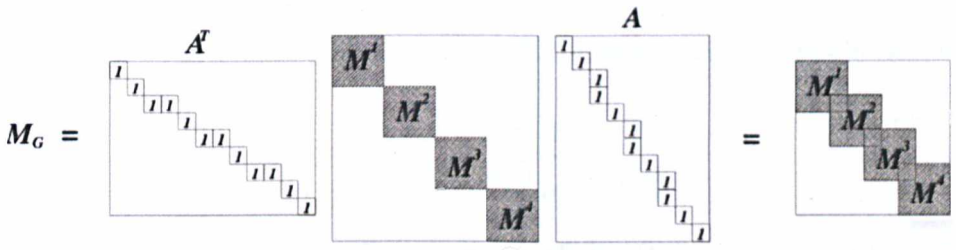


Figure 4.2: Global assembly procedure to obtain the mass matrix $\mathbf{M_G}$ from the element mass matrices (from Karniadakis & Sherwin (2005)).

ment boundaries, yields a global system that has generally fewer degrees of freedom than the combined local degrees of freedom of all the elements. This is illustrated in figure 4.2 by the global assembly of elemental mass matrices to form the global mass matrix $\mathbf{M_G}$.

4.1.3 High-order expansion basis in the $p-$type extension

The implementation of the $p-$type method requires the choice of a suitable set of local expansion modes, ϕ_p. One of the main requirements to obtain well-conditioned matrices, is that the set of functions are orthogonal. The basis functions are generally divided into two categories, modal or nodal, according to their properties. A modal expansion basis is a hierarchical set of functions, where the expansion set of order $P-1$ forms a sub-set contained within the set of order P; therefore, higher order expansions can be built on lower order function sets. On the other hand, a nodal expansion is non-hierarchical and has to be completely redefined if the polynomial order is increased; however, it has the advantage that the value of the expansion coefficient at its corresponding nodal point represents the approximate solution, facilitating the physical interpretation of the problem. Conversely, in a modal basis the value at the point is given by the combination of the contribution from each mode.

The implementation of a polynomial basis involves the performance of mathematical operations such as integration and differentiation at an elemental level. Numerical integration is carried out using Gaussian quadrature, which is particu-

larly accurate when integrating smooth functions. Within the standard elemental interval, the integral is approximated by a finite summation in the following form:

$$\int_{-1}^{1} u(\xi)d\xi \approx \sum_{i=0}^{Q-1} w_i u(\xi_i) \tag{4.23}$$

where the w_i are the weights and ξ_i the $i-$th of the Q quadrature points. The exact location of these points depends on the choice of gaussian quadrature, i.e. Gauss (whereby the zeros are al internal to the element), Gauss-Radau (which includes one end point) and Gauss-Lobatto (which includes both end points). In all the cases the spacing of the Q quadrature points is optimally chosen to exactly integrate polynomials of order $2Q-1$.

Similarly differentiation is performed using Lagrange polynomials to approximate the solution:

$$u^\delta(x) = \sum_{p=0}^{P} \hat{u}_p \phi_p(\mathcal{X}(\xi)^{-1}) \tag{4.24}$$

In this case, only the values of the derivative at the quadrature points are required. For a more comprehensive description of the elemental operations within the standard domain the reader is referred to Karniadakis & Sherwin (2005).

4.1.3.1 One-dimensional expansion basis

The present code uses a modal expansion basis formed from Jacobi polynomials $P_p^{\alpha,\beta}(x)$ with $\alpha = \beta = 1$, which allows to obtain a high degree of orthogonality in the mass matrix. These polynomials are a family of solutions to the singular Sturm-Liouville problem, which in the region $-1 < x < 1$ is written as:

$$\frac{d}{dx}\left[(1-x)^{1+\alpha}(1+x)^{1+\beta}\frac{d}{dx}P_p^{\alpha,\beta}(x)\right] = \lambda_p(1-x)^\alpha(1+x)^\beta P_p^{\alpha,\beta}(x) \tag{4.25}$$

where $\lambda_p = -p(\alpha+\beta+p+1)$. These polynomials exhibit the property of orthogonality, so that $P_p^{\alpha,\beta}(x)$ is orthogonal to all polynomials of order less than p when integrated with respect to $(1-x)^\alpha(1+x)^\beta$. A considerable advantage of this family of Jacobi polynomials is the boundary/interior decomposition, where the boundary

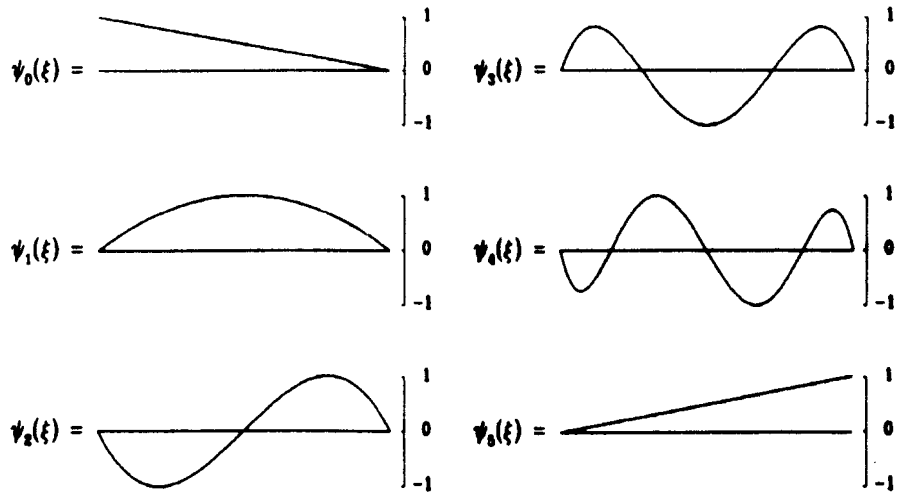


Figure 4.3: Shape function of the modal expansion of order $P = 5$ defined in equation (4.26) (from Karniadakis & Sherwin (2005)).

modes are unity at the element boundaries and zero in the interior and, likewise, the interior modes have contribution only in the interior. This guarantees C^0 continuity of the solution across element boundaries. A $p-$type modal expansion $\phi(\xi)$ can therefore be defined in the standard element as:

$$\psi_p(\xi) = \begin{cases} \left(\frac{1-\xi}{2}\right) & p = 0 \\ \left(\frac{1-\xi}{2}\right)\left(\frac{1+\xi}{2}\right) P_{p-1}^{1,1}(\xi) & 0 < p < P \\ \left(\frac{1+\xi}{2}\right) & p = P \end{cases} \tag{4.26}$$

In this expansion only the boundary modes $p = 0$ and $p = P$ have a non-zero value at the ends of the domain and the resulting mass matrix is penta-diagonal for the interior modes. Figure 4.3 illustrates the shape of the normalised modes with a polynomial order of 5.

4.1.3.2 Multi-dimensional expansion basis

The construction of a multi-dimensional basis is based on the same principles of the one-dimensional basis. First, a standard element Ω_{st} is defined as a quadrilateral of triangular element in two-dimensions; in three-dimensional it can be a hexahedron,

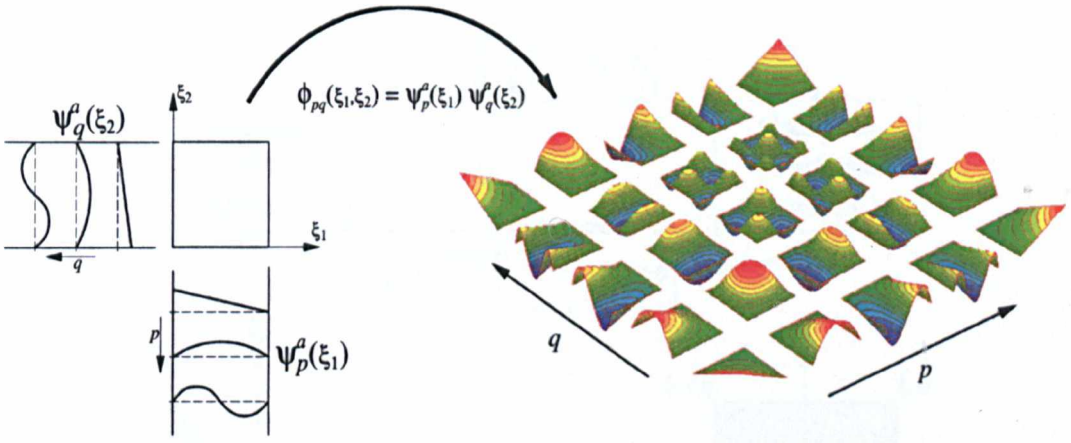


Figure 4.4: Construction of a two-dimensional quadrilateral expansion of order $P = 4$ (from Karniadakis & Sherwin (2005)).

a prism, a tetrahedron or a pyramid. Then, the expansion basis is constructed: in the case of quadrilateral or hexahedral regions, this can be built directly from the tensor product of a one-dimensional basis.

The standard region for a two-dimensional quadrilateral element is given by:

$$\Omega_{st} = \{\xi \mid -1 \leq \xi_1, \xi_2 \leq 1\} \tag{4.27}$$

The corresponding expansion basis $\phi_{pq}(\xi_1, \xi_2)$ can be written as a tensor product in the form:

$$\phi_{pq}(\xi_1, \xi_2) = \psi_p^a(\xi_1)\psi_2^a(\xi_2) \quad 0 \leq p, q; p \leq P_1, q \leq P_2 \tag{4.28}$$

where P_1 and P_2 represent the maximum polynomial order in the ξ_1 and ξ_2 directions respectively. Figure 4.4 illustrates a fourth-order quadrilateral expansion basis obtained from the tensor product of two one-dimensional expansions of order $P = 4$. It is also possible to chose a different polynomial order in the two coordinate directions ξ_1 and ξ_2, although in spectral element methods it is generally the same. Similarly, a three-dimensional expansion basis $\phi_{pqr}(\xi_1, \xi_2, \xi_3)$ can be defined over the standard cuboid $\Omega_{st} = \{\xi \mid -1 \leq \xi_1, \xi_2, \xi_3 \leq 1\}$ as:

$$\phi_{pqr}(\xi_1, \xi_2, \xi_3) = \psi_p^a(\xi_1)\psi_2^a(\xi_2)\psi_r^a(\xi_3) \quad 0 \leq p, q; p \leq P_1, q \leq P_2, r \leq P_3 \tag{4.29}$$

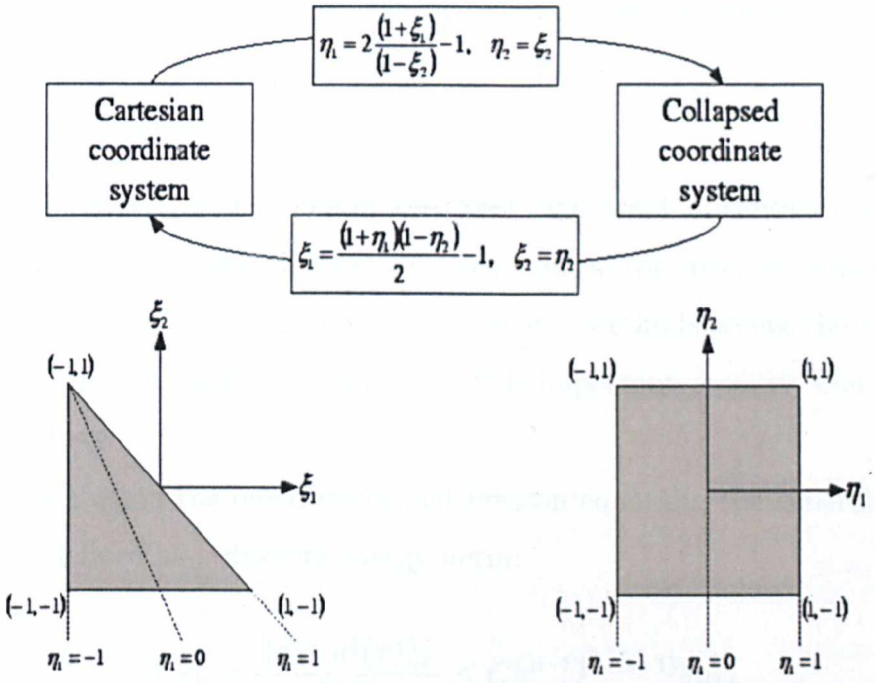


Figure 4.5: Coordinate transformation to form an expansion basis on a triangular region (from Karniadakis & Sherwin (2005)).

Analogous to the one-dimensional basis, multi-dimensional expansions are also conducive to a boundary/interior decomposition and to a global assembly procedure, where C^0 continuity is ensured by constricting the vertex and edge modes to have the same value at the elemental boundaries.

Conversely, the formation of an expansion basis on triangular and tetrahedral elements is not straightforward: the triangular elements can be related to the quadrilateral ones by a coordinate transformation from a Cartesian coordinate system to a collapsed coordinate system, as shown in figure 4.5. This transformation collapses the unit square of coordinates (η_1, η_2) onto a unit triangle of coordinates (ξ_1, ξ_2). An expansion basis for the triangular element can be constructed from the tensor product of a one-dimensional basis , $\psi_p^a(\eta_1)$, and a two-dimensional tensor $\psi_{pq}^a(\eta_2)$:

$$\psi_{pq}(\xi_1, \xi_2) = \psi_p^a(\eta_1)\psi_{pq}^a(\eta_2) \tag{4.30}$$

where $\psi_p^a(\eta_1)$ and $\psi_{pq}^a(\eta_2)$ are known as modified principal functions. A more detailed

description of the construction of a multi-dimensional basis, as well as the exact form of the modified principal functions, can be found in Karniadakis & Sherwin (2005).

4.1.4 Error convergence

As mentioned in section 4.1, one of the most significant advantages of the spectral methods is that the solution exhibits exponential (or spectral) convergence for smooth functions, unlike traditional finite element methods where the error in the approximate solution decays algebraically. This important property can be demonstrated as follows.

Considering again the one-dimensional Poisson equation, the general error estimate can be defined as a discrete energy norm:

$$\|\epsilon\|_E = \frac{\|u - u^\delta(x)\|_E}{\|1\|^1} \leq Ch^{\mu-1}P^{-(k-1)}\|u\|_k \tag{4.31}$$

where h is the element size, P is the polynomial order, k is the differentiability of the solution, $\mu = min(k, P+1)$ and C is a constant independent of the previous parameters. In the case of infinitely differentiable solutions, this yields:

$$\epsilon \propto h^P \tag{4.32}$$

In the $h-$convergence the polynomial order is constant with respect to the number of degrees of freedom N_{dof}, and thus $h \propto \frac{1}{N_{dof}}$. Hence, by taking the natural logarithm of equation (4.32) one obtains:

$$\ln\epsilon \propto P\ln h \quad \Rightarrow \quad \ln\epsilon \propto -P\ln N_{dof} \tag{4.33}$$

This demonstrates that in the $h-$convergence the error decays linearly with increasing N_{dof} on a log-log axis.

In the case of $p-$convergence, h remains constant and P varies; considering that $N_{dof} = N_{el}P + 1$, equation (4.32) leads to:

$$\ln\epsilon \propto P \quad \Rightarrow \quad \ln\epsilon \propto N_{dof} \tag{4.34}$$

In the case of complex solutions, the minimum error for a given number of degrees of freedom is typically achieved with both a local mesh improvement where the solution gradients are large ($h-$convergence) and an increase of the polynomial order through a $p-$type refinement.

4.2 The Nektar code

The three-dimensional simulations presented in this thesis have been performed using a spectral/*hp* element method based code named *Νεκταρ*, originally developed by Sherwin & Karniadakis (1996) and Karniadakis & Sherwin (2005) for unstructured triangular and tetrahedral meshes and then extended by Warburton (1998) to hybrid domains. This code uses the spectral/*hp* element method described in the previous sections for the spatial discretisation of the incompressible three-dimensional Navier-Stokes equations. The temporal discretisation employs a high-order stiffly stable splitting scheme based on Karniadakis *et al.* (1991) that accounts for enhanced stability properties.

4.2.1 The time-stepping scheme

To illustrate the time stepping scheme, we first introduce the incompressible Navier-Stokes and continuity equations in the form:

$$\frac{\partial \mathbf{u}}{\partial t} = -\nabla p + \mathbf{N}(\mathbf{u}) + \nu \mathbf{L}(\mathbf{u}) \tag{4.35}$$

$$\nabla \cdot \mathbf{u} = 0 \tag{4.36}$$

where $\mathbf{u}$ represents the velocity vector and $\mathbf{N}(\mathbf{u})$ and $\mathbf{L}(\mathbf{u})$ are the non-linear convection and the linear diffusion operators, respectively given by:

$$\mathbf{N}(\mathbf{u}) = -(\mathbf{u} \cdot \nabla)\mathbf{u} \tag{4.37}$$

$$\mathbf{L}(\mathbf{u}) = \nabla^2 \mathbf{u} \tag{4.38}$$

The stiffly stable splitting scheme propagates the velocity and the pressure over the time interval Δt in three sub-steps; this scheme allows to treat the primitive variables independently and thus the pressure term is decoupled from the convective and diffusive terms. Equation (4.35) can be integrated over Δt to obtain:

$$\mathbf{u}^{n+1} - \mathbf{u}^n = -\int_{t_n}^{t_{n+1}} \nabla p dt + \int_{t_n}^{t_{n+1}} \mathbf{N}(\mathbf{u}) dt + \nu \int_{t_n}^{t_{n+1}} \mathbf{L}(\mathbf{u}) dt \tag{4.39}$$

where the pressure contribution can be written using the mean pressure field $\bar{p}^{n+1}$ (i.e. averaged over the time step) which ensures that the final velocity field satisfies the continuity equation and is thus incompressible at the time t_{n+1}. The pressure term is then given by:

$$\int_{t_n}^{t_{n+1}} \nabla p dt = \Delta t \nabla \bar{p}^{n+1} \tag{4.40}$$

The three sub-steps of the high order splitting scheme by Karniadakis *et al.* (1991) utilise the intermediate velocity fields $\hat{\mathbf{u}}$ and $\hat{\hat{\mathbf{u}}}$ to separately treat the convection, diffusion and pressure gradient term, and can be written as:

$$\frac{\hat{\mathbf{u}} - \sum_{q=0}^{J_e-1} \alpha_q \mathbf{u}^{n-q}}{\Delta t} = \sum_{q=0}^{J_e-1} \beta_q \mathbf{N}(\mathbf{u}^{n-q}) \tag{4.41}$$

$$\frac{\hat{\hat{\mathbf{u}}} - \hat{\mathbf{u}}}{\Delta t} = -\nabla \bar{p}^{n+1} \tag{4.42}$$

$$\frac{\mathbf{u}^{n+1} - \hat{\hat{\mathbf{u}}}}{\Delta t} = \nu \sum_{q=0}^{J_i-1} \gamma_q \mathbf{L}(\mathbf{u}^{n+1-q}) \tag{4.43}$$

where α_q, β_q and γ_q are the stiffly stable splitting coefficients, while J_e and J_i are the integration order in the Adams-Bashforth family scheme and in the Adams-Moulton family scheme respectively. The Dirichlet boundary condition is imposed on the boundary of the domain in the form $\mathbf{u}^{n+1} = u_0$.

In equation (4.41) the non-linear term is approximated by an explicit scheme. The pressure gradient term is treated in the second step: taking the divergence of equation (4.42) and imposing the incompressibility constraint on the second intermediate velocity field (i.e. $\nabla \cdot \hat{\hat{\mathbf{u}}} = 0$) yields a Poisson equation for the pressure:

$$\nabla^2 \bar{p}^{n+1} = \nabla \cdot \left(\frac{\hat{\mathbf{u}}}{\Delta t} \right) \tag{4.44}$$

This equation is then subjected to the Neumann boundary condition on $\partial\Omega$:

$$\frac{\partial \bar{p}^{n+1}}{\partial n} = -\frac{u_0 \cdot \mathbf{n} - \hat{\mathbf{u}} \cdot \mathbf{n}}{\Delta t} \tag{4.45}$$

Finally, in the third sub-step the linear term is treated implicitly, yielding a Helmholtz equation for the final velocity field. Overall, one Poisson equation for the pressure term and three Helmholtz equations for each of the velocity components are solved at every time step. Further details on the splitting scheme can be found in Karniadakis *et al.* (1991) and Guermond & Shen (2003).

4.2.2 Application of the *Νεκταr* code to VIV problems

In the past years numerous numerical algorithms have been developed to meet the needs of fundamental research and engineering applications in the filed of fluid/structure interaction. Finite element methods based on Arbitrary Lagrangian-Eulerian formulation (ALE) and deformable grids (Nomura & Hughes (1992)) and spectral element methods with coordinate transformations (Newman & Karniadakis (1997)) represent some possible approaches to model the free response of a vibrating body, whose governing equations are the incompressible Navier-Stokes equations (4.35) and (4.36) with moving boundary conditions, i.e. $\mathbf{u} = \mathbf{u}_b(t)$ on the interface between the flow and the body $\Gamma(t)$. However, these methods are generally confined to transverse or in-line motions and have not been applied to rotational motions, which play an important role in vortex-induced vibration problems. Furthermore, in the ALE methods the computational grid is continually deformed: the Navier-Stokes solver must therefore construct a new solution matrix at each time step and smooth the mesh when it becomes highly deformed.

To avoid this extra computational cost, Li *et al.* (2002) developed an alternative formulation for solving the two-dimensional moving-boundary flow problems for a rigid body: this approach involves the implementation of a loosely coupled algorithm, in which the coordinate system is attached to the body and the solution of

the flow and structural equations is carried out in the moving frame of reference. At each time step the Navier-Stokes equations are solved to provide the hydrodynamic forces acting on the body; these forces are then used as input for the structural equation. The structural solver predicts the displacement of the body due to these forces at the next time step: the resulting velocities are subsequently used to advance the fluid solver.

A three-dimensional loosely coupled algorithm based on this formulation has been implemented in the spectral element code for the solution of the free vibration problems presented in this work. The next sections provide the coordinate transformation and the mathematical formulation of the Navier-Stokes equations for a moving frame of reference fixed to a rigid body undergoing cross-flow and rotational motions.

4.2.2.1 Coordinate transformation

We assume that the body moves instantaneously in the absolute inertial frame of reference of coordinates $\mathbf{x}' = [x', y', z']$ with translation $\mathbf{d} = [d_x(t), d_y(t), d_z(t)]^T$ and rotation angle $\theta = [\theta_x(t), \theta_y(t), \theta_z(t)]$, defined positive clockwise. A corresponding moving frame of reference attached to the body, (x, y, z), is defined by the following coordinate transformations:

$$\mathbf{x}' = \mathbf{d} + \mathbf{A}\mathbf{x}, \qquad \mathbf{x} = \mathbf{A}^{-1}(\mathbf{x}' - \mathbf{d}) \tag{4.46}$$

where the general rotation matrix $\mathbf{A}$ describes the rotation about the x, y or z axis depending on the type of motion considered.

4.2.2.2 Mathematical model for the flow and structure equations in three dimensions

To simplify the notation, in the following formulation we will consider only a motion in the yz plane and the rotation angle θ_x about the x axis (i.e. $\theta_y = \theta_z = 0$): this formulation models the types of motion presented in chapters 5 and 6 and the corresponding notation can be visualised in figure 4.6. The transformation matrix in the yz plane then is given by:

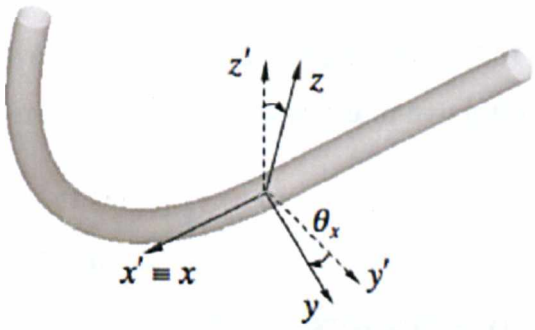


Figure 4.6: Coordinate transformation from the absolute frame of reference to the moving frame of reference in the case of rotation about the x axis.

$$\mathbf{A}_x = \begin{pmatrix} 1 & 0 & 0 \\ 0 & \cos\theta_x & \sin\theta_x \\ 0 & -\sin\theta_x & \cos\theta_x \end{pmatrix} \tag{4.47}$$

In this case $\mathbf{A}_x^T = \mathbf{A}_x^{-1}$ and thus by differentiating equation (4.46) with $\mathbf{A} = \mathbf{A}_x$, one obtains the velocity in the moving frame of reference as:

$$\mathbf{u} = \dot{\theta} I_0 \mathbf{x} + \mathbf{A}_x^T(\mathbf{u}' - \dot{\mathbf{d}}) \tag{4.48}$$

where

$$I_0 = \begin{pmatrix} 0 & 0 & 0 \\ 0 & 0 & -1 \\ 0 & 1 & 0 \end{pmatrix} \quad \text{and} \quad \dot{\mathbf{A}}_x^T \mathbf{A}_x = \dot{\theta}_x I_0 \tag{4.49}$$

From equation (4.46) the spatial and temporal derivatives in the moving frame of reference can be derived from the following expressions:

$$\nabla' = \mathbf{A}_x \nabla, \qquad (\nabla')^2 = \nabla^2 \tag{4.50}$$

$$\left(\frac{\partial}{\partial t}\right)_a = \frac{\partial}{\partial x}\frac{\partial x}{\partial t} + \frac{\partial}{\partial y}\frac{\partial y}{\partial t} + \frac{\partial}{\partial z}\frac{\partial z}{\partial t} + \left(\frac{\partial}{\partial t}\right)_r \tag{4.51}$$

where the subscripts a and r refer to the absolute (fixed) and relative (moving) frames of reference respectively.

Substituting the above relationships into equations (4.35) and (4.36) leads to the formulation of the Navier-Stokes equations in the moving frame of reference:

$$\nabla \cdot \mathbf{u} = 0 \tag{4.52}$$

$$\frac{\partial \mathbf{u}}{\partial t} + (\mathbf{u} \cdot \nabla)\mathbf{u} = -\nabla p + \nu \nabla^2 \mathbf{u} + \mathbf{G}(\mathbf{u}, t) \tag{4.53}$$

$$\mathbf{G}(\mathbf{u}, t) = 2\dot{\theta} I_0 \mathbf{u} + \dot{\theta}^2 I_0 I_0 \mathbf{x} + \ddot{\theta} I_0 \mathbf{x} - \mathbf{A}_x^T \ddot{\mathbf{d}} \tag{4.54}$$

The forcing term $\mathbf{G}(\mathbf{u}, t)$ in equation (4.54) includes the deflecting Coriolis force ($2\dot{\theta} I_0 \mathbf{u}$), the centrifugal force ($\dot{\theta}^2 I_0 I_0 \mathbf{x}$) and the contribution due to unsteady translation ($\mathbf{A}_x^T \ddot{\mathbf{d}}$) and rotation ($\ddot{\theta} I_0 \mathbf{x}$). The Coriolis and centrifugal contributions have not been included in the pressure field: indeed, leaving the pressure unaltered simplifies the implementation of the pressure boundary condition for the splitting scheme in the moving frame of reference and is also convenient in the coupling with the structural equation, which is based on the pressure forces in the fixed frame of reference.

4.2.3 Transformation of boundary conditions

In the far-field the Dirichlet boundary condition for the Navier-Stokes equations (4.53) can be expressed as:

$$\mathbf{u} = \dot{\theta} I_0 \mathbf{x} + \mathbf{A}_x^T (\mathbf{u}' - \dot{\mathbf{d}}) \tag{4.55}$$

where $\mathbf{u}'$ is the far-field velocity in the absolute frame of reference. The Neumann boundary condition in the moving frame of reference can be derived from the boundary conditions in the absolute frame of reference:

$$\underline{\nabla' \mathbf{u}'} \mathbf{n}' = \mathbf{g}'_{\mathbf{N}} \tag{4.56}$$

where $\underline{\nabla' \mathbf{u}'} \mathbf{n}' = \mathbf{A}_x [\underline{\nabla \mathbf{u}} \mathbf{n} - \dot{\theta}_x I_0 \mathbf{n}]$ and $\mathbf{g}'_{\mathbf{N}} = [g_N^{u'}, g_N^{v'}, g_N^{w'}]^T = \mathbf{A}_x \mathbf{g}_{\mathbf{N}}$. Consequently, the Neumann boundary conditions for a motion of translation/rotation in the yz

plane in the moving frame of reference will be:

$$\nabla u \cdot \mathbf{n} = g_N^{u'} \tag{4.57}$$

$$\nabla v \cdot \mathbf{n} = g_N^{v'} - \dot{\theta}_x n_z \tag{4.58}$$

$$\nabla w \cdot \mathbf{n} = g_N^{w'} + \dot{\theta}_x n_y \tag{4.59}$$

$$\tag{4.60}$$

4.2.4 Structural equation

In the case of a rigid body free to translate and rotate, the planar motion is described by the following structural equation:

$$\mathbf{M}\ddot{\mathbf{x}} + \mathbf{C}\dot{\mathbf{x}} + \mathbf{K}\mathbf{x} = \mathbf{F} \tag{4.61}$$

$$\mathbf{I}_\theta \ddot{\theta} + \mathbf{C}_\theta \dot{\theta} + \mathbf{K}_\theta \theta = \mathbf{M}_\theta \tag{4.62}$$

In equation (4.61) $\mathbf{M}$, $\mathbf{C}$ and $\mathbf{K}$ are the mass, damping and stiffness matrices respectively and $\mathbf{x}$ is the vector of the displacements in the three directions. In equation (4.62) $\mathbf{I}_\theta$, $\mathbf{C}_\theta$ and $\mathbf{K}_\theta$ are the matrices for the mass moments of inertia, the torsional damping and the torsional stiffness respectively. $\mathbf{F}$ and $\mathbf{M}_\theta$ are the vectors of the external hydrodynamic forces and moments acting on the body: these are the output of the Navier-Stokes solver in the loosely coupled algorithm. All the matrices in equations (4.61) and (4.62) are diagonal with constant coefficients. In the numerical code both these equations are solved using a Newmark scheme.
The loosely coupled algorithm can be summarised in the following steps:

- The Navier-Stokes equation (4.53) is solved to obtain the vector of fluid dynamic loading at t_n.
- The force and moment at t_{n+1} are extrapolated from the previous time steps values via a relaxation approximation.
- The structural equations (4.61) and (4.62) are solved using a Newmark scheme, yielding the vector of displacements, velocities and accelerations at t_{n+1}.

- These vectors are then substituted into equation (4.53) and the boundary conditions are updated for the next time level.

4.3 Strip Theory model

The strip theory model solves the Navier-Stokes equation in multiple two-dimensional planes positioned at intervals along the span of the body and perpendicular to its axis. The flow evolution and the resulting forces are computed in each plane; the forces are then used to determine the body's response via a structural dynamics model of the flexible pipe. This response is then fed back to the two-dimensional CFD planes, so that the simulation proceeds in a loosely coupled staggered approach, where the flow evolution and the body response are alternately computed.

One important feature of strip theory models is that the only three-dimensional linkage between the CFD planes exists through their effect on the structure and its subsequent response: no three-dimensional hydrodynamic linkage is normally taken into consideration and hence strip theory codes are not suitable for the simulation of fully three-dimensional problems. However, the correlating effect of the lock-in allows one to consider the flow locally two-dimensional and therefore provides a justification for the use of strip theory based codes in three-dimensional problems. In particular, the axial flow convection due to the curvature of the flexible pipe undergoing vortex-induced vibration is considered to be sufficiently gradual to induce three-dimensional changes in the flow that can be neglected without severe implications. Only the normal component of the onset flow is considered to be responsible for the generation of hydrodynamics forces on the body, including axial flows due to the obliqueness of the cylinder locally to the incident flow: the velocity component tangential to the body's axis, as well as any spanwise flow convection, is neglected in this approach. Although strip theory computations are less accurate than fully three-dimensional CFD, the codes based on this approach are typically many orders of magnitude faster and allow to perform parametric studies than would be too demanding in terms of computational cost in three-dimensions; further, the discrete

representation of the flow domain via multiple two-dimensional planes makes these codes ideal for parallelisation on multiprocessor machines.

4.3.1 The strip theory and its application to three-dimensional problems

As anticipated, in the case of curved bodies the flow direction in each two-dimensional CFD plane is orientated to be normal to the cylinder's local axis and hence only the normal component of the inflow velocity is taken into consideration when the hydrodynamic forces are calculated. However, the axial flow convection is significant in the case of highly curved bodies such as the ones considered in this thesis, and neglecting its contribution towards VIV may therefore lead to wrong results. This was shown in the work done by Miliou (2004) and Miliou *et al.* (2007), where the wake topology past a concave and a convex body with the same radius of curvature was found to be radically different due to the different mechanism of axial flow convection. Similarly, the application of strip theory models to the curved geometries of the present investigation has highlighted some severe limitations, such as the impossibility of identifying the in-plane curvature orientation: their effect on the overall flow approximation will be further discussed in the relevant result sections.

4.4 The VIVIC code

The strip-theory based code VIVIC was developed by Willden (2003) from a pre-existing Cloud in Cell method (Graham (1988)) that employed finite difference approximations and Fast Fourier Transforms on a structured grid. Later Arkell (1995) extended this method to allow the use of the finite element technique on unstructured grids. The current version of VIVIC uses velocity and vorticity as the primary variables for the solution of the two-dimensional Navier-Stokes equations. The treatment of the vorticity boundary condition on the surface of the body represents the most important difference with respect to its predecessors, as in the present method

the vorticity generated by the surface is related to the streamfunction flux at the wall: this new formulation allows the vorticity boundary condition to be set without the expensive iterative procedures that have been previously used to preserve the spatial accuracy.

4.4.1 Mathematical formulation

VIVIC uses a first order in time hybrid Eulerian-Lagrangian scheme based on both the velocity-vorticity formulation and the streamfunction-vorticity formulation of the Navier-Stokes equations, combining the accuracy of the former with the low computational cost of the latter. By taking the curl of equation (4.35) and enforcing mass conservation, an alternative form of the Navier-Stokes equation for incompressible flows can be derived:

$$\frac{\partial \omega}{\partial t} + (\mathbf{u} \cdot \nabla)\omega = (\omega \cdot \nabla)\mathbf{u} + \nu \nabla^2 \omega \tag{4.63}$$

where $\omega = \nabla \wedge \mathbf{u}$ and $\nabla^2 \mathbf{u} = -\nabla \wedge \omega$. The above relationship is the vorticity transport equation, in which the terms from left to right represent respectively: the change of vorticity in time, the convection of vorticity, the stretching and tilting of vorticity and the diffusion of vorticity. The two-dimensional form of the velocity-vorticity equation may be obtained from equation (4.63); in the xy plane, where the only vorticity component is in the spanwise direction z, the vortex stretching and tilting term is equal to zero and equation (4.63) becomes:

$$\frac{\partial \omega_z}{\partial t} + (\mathbf{u}.\nabla)\omega_z = \nu \nabla^2 \omega_z \tag{4.64}$$

$$\nabla^2 u = -\frac{\partial \omega_z}{\partial y} \tag{4.65}$$

$$\nabla^2 v = \frac{\partial \omega_z}{\partial x} \tag{4.66}$$

with u and v being the components of the velocity vector in the x and y direction, respectively. The streamfunction-vorticity formulation employs the streamfunction ψ which is related to the velocity field by the following equations:

$$u = \frac{\partial \psi}{\partial y} \qquad v = -\frac{\partial \psi}{\partial x} \tag{4.67}$$

Substituting (4.67) in (4.64) and using the definition of vorticity, the two-dimensional Navier-Stokes problem can be written in terms of ψ and ω_z:

$$\frac{\partial \omega_z}{\partial t} + \frac{\partial \psi}{\partial y}\frac{\partial \omega_z}{\partial x} - \frac{\partial \psi}{\partial x}\frac{\partial \omega_z}{\partial y} = \nu \nabla^2 \omega_z \tag{4.68}$$

$$\nabla^2 \psi = -\omega_z \tag{4.69}$$

Vorticity based formulations do not provide direct information on the pressure field and therefore the hydrodynamic forces must be established by other means. An additional equation to relate the pressure to the velocity field is given by:

$$\nabla^2 p = -\rho \nabla \cdot [(\mathbf{u} \cdot \nabla)\mathbf{u}] \tag{4.70}$$

Therefore the two-dimensional equation for the pressure can be written as:

$$\nabla^2 p = -2\rho\left(\frac{\partial u}{\partial y}\frac{\partial v}{\partial x} - \frac{\partial u}{\partial x}\frac{\partial v}{\partial y}\right) \tag{4.71}$$

4.4.2 Streamfunction-velocity-vorticity method

The temporal derivative of the vorticity in equation (4.64) is discretised using a first order forward Euler approximation. The vorticity transport equation is then split into two sub-steps:

$$\frac{\hat{\omega}_z - \omega_z^n}{\Delta t} = \nu([1-\alpha]\nabla^2 \omega_z^n + \alpha \nabla^2 \hat{\omega}_z) \tag{4.72}$$

$$\frac{\omega_z^{n+1} - \hat{\omega}_z}{\Delta t} = -(\hat{\mathbf{u}} \cdot \nabla)\hat{\omega}_z \tag{4.73}$$

where $\hat{\mathbf{u}}$ and $\hat{\omega}_z$ are the velocity and vorticity fields at an intermediate time level. The use of these intermediate field variables introduces errors of $O(\Delta t)$. First the diffusive term is computed to find the intermediate vorticity field from the data at t_n: an explicit, Crank-Nicholson or implicit diffusion scheme can be selected in this sub-step and the resulting computational cost mainly arises in the solution of

two Poisson equations. The vorticity boundary condition at the solid surfaces is specified by generating vorticity at the walls in such a way as to enforce the no-slip condition: vortex sheet elements, positioned about the body's surface, are employed to generate a potential flow that is then added to the velocity field in order to satisfy the impermeability condition on the outer surface and the no-slip condition on the inner surface. The no-slip condition is satisfied on the wall side of the vortex sheet, which may be considered to be an infinitesimal distance into the flow. The vorticity flux through the wall is then used as a Neumann boundary condition in the solution of the diffusion equation.

The convection of vorticity is accomplished by assigning the post-diffusion intermediate vorticity to the point vortices as circulation: each is then convected by the local velocity and its new position is calculated, the velocity at the vortex position being evaluated using the finite element shape functions. After the convection, the circulation is assigned to the nodes of the element in which each point vortex lies: this is done using the same shape functions of the previous algorithm to distribute correctly the point vortex circulation to the new element nodes. Finally, the point vortices whose circulation falls below a cut-off value are removed and their circulation is redistributed amongst the neighbouring vortices.

Chapter 5

Convex configuration

5.1 Background studies: fixed cylinder in uniform flow

This section presents an overview of the computations carried out on a stationary cylinder in a uniform flow and aims at providing a reference case for the free and forced vibration simulations performed on the same geometry. A more comprehensive investigation on the fixed cylinder configuration can be found in Miliou (2004) and Miliou *et al.* (2007).

The following results are obtained at $Re = 100$ with a uniform free-stream velocity profile in the plane of curvature of the body, which is kept fixed in the computational domain. The low Reynolds number and the absence of complex flows allow the simulation of the basic vortex shedding features, thus enabling assessment of the effect of curvature on the wake dynamics and force distribution. This will provide a comparison basis for the investigation of the more complex flow field arising from the body's motion.

5.1.1 Effect of curvature: a three-dimensional problem

Three-dimensional simulations of the vortex shedding past the steady convex configuration were performed using first order time integration at a polynomial order

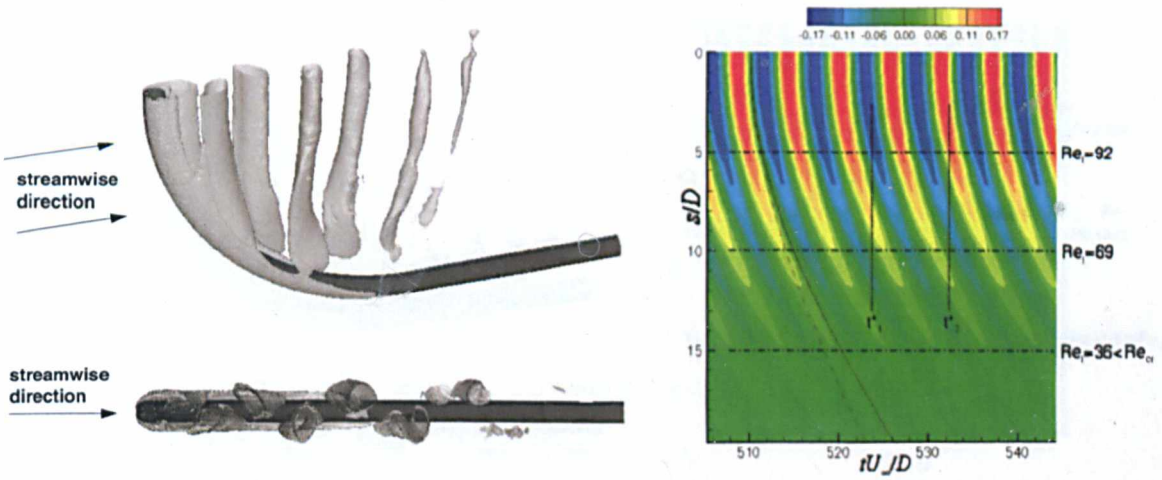


Figure 5.1: Convex configuration at $Re = 100$, isosurfaces at $\lambda_2 = -0.1$ (*left*); sectional lift coefficient distribution in time along the span (*right*).

$P = 8$. Figure 5.1 (*left*) shows the qualitative features of the wake at a non-dimensional time $t_1^* = 524$, at which the top shear layer is rolling up. This corresponds to a minimum in the integrated lift coefficient and hence to suction in the negative $y-$direction. The cores are visualised through isosurfaces at $\lambda_2 = -0.1$ and the view from the top ($xy-$plane) highlights the anti-symmetric nature of the wake, with staggered arrays of vortices (2S type of shedding). In the proximity of the body, the vortical structures appear to be straight, with their axis perpendicular to the free-stream: the cores start to distort in the near-wake, as they are convected downstream. Under these inflow conditions, the horizontal extension does not affect the shedding dynamics and generates virtually zero forces.

The evolution in time of the lift coefficient isocontours in every section perpendicular to the cylinder's axis is shown in figure 5.1 (*right*). At $t_1^* = 524$ we observe a decrease in the magnitude of the lift coefficient as s/D increases, eventually resulting in a sign change. This can be interpreted by considering the effect of the body's curvature: as displayed by the λ_2 isosurfaces, the distance between the straight cores and curved cylinder decreases along the span, leading to a gradual phase shift which can be modelled by the following relationship:

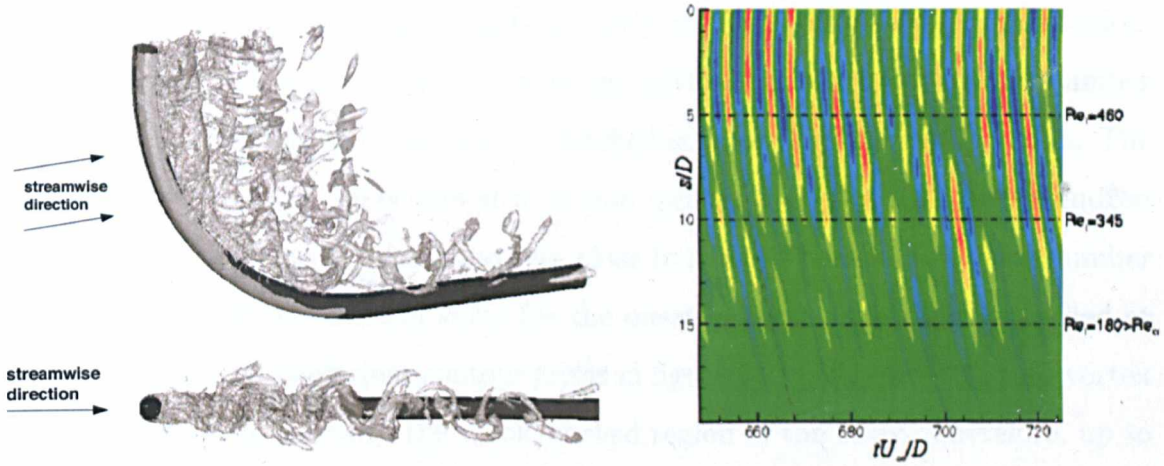


Figure 5.2: Convex configuration at $Re = 500$, isosurfaces at $\lambda_2 = -0.8$ (*left*); sectional lift coefficient distribution in time along the span (*right*).

$$\frac{tU_\infty}{D} = 13 - 13cos(s/R) \tag{5.1}$$

The dashed line in figure 5.1 (*right*) represents a model for the phase variation of the sectional lift force along the quarter ring based on the free-stream velocity $U_\infty = 1$, whereas the continuous line is based on the convective velocity of the vortices. The out-of-phase shedding is an intrinsic feature of this type of geometry in the absence of oscillations and persists also at higher Reynolds numbers, as shown in figure 5.2 (*right*), although the magnitude of sectional lift coefficient does not decrease uniformly along the span. At $Re = 500$, which is greater than the critical value for three-dimensional transition for a straight cylinder, the λ_2 isosurfaces in figure 5.2 (*left*) highlight the presence of braids and streamwise vorticity connecting the spanwise rollers: these features may be associated with Mode A and Mode B transition, as observed in the case of a straight cylinder in this Reynolds number range.

On the right-hand side of figure 5.1 (*right*), the local normal Reynolds number corresponding to different spanwise sections is shown to decrease as the body turns to lower angles to the flow, i.e. the non-dimensional arc-length s/D increases. The reduction of the normal component of the incoming flow vector is a direct conse-

quence of the body's curvature: from the point of view of a sectional argument, whose fundamental hypothesis is that the body responds only to the normal velocity component, this reduction implies that the critical value of the Reynolds number for the vortex shedding to be initiated is reached at a specific spanwise position. The critical value $Re = 47 - 49$ occurs at a section located at $s/D \approx 13.2$, which indeed corresponds to a lift coefficient value very close to zero. When the Reynolds number is increased to 500, the critical value for the onset of vortex shedding is reached at $s/D \approx 18.4$: the lift coefficient contour levels in figure 5.2 (*right*) indicate that vortex shedding is present in nearly the whole curved region of the body. Therefore, up to this point the sectional approximation would seem to hold. From a two-dimensional sectional perspective, we would also expect to see a variation of the Strouhal number along the span as the local normal Reynolds number changes. However, the Fourier analysis of the lift coefficient signal over ten cycles of vortex shedding shows that there is only one dominant frequency in the $y-$direction: for the range of Reynolds number considered St decreases with Re, and thus with the normal velocity component, leaving the Strouhal frequency constant in every spanwise section. Unlike the shedding past non-uniform geometries or inflows, this configuration does not exhibit neither cellular flow patterns nor discrete frequencies at different spanwise locations: in fact, the upper cylinder shedding drives the shedding from the lower end without frequency variation along the span. The Strouhal number in the $y-$direction is constant and equal to 0.1761: this value is slightly larger than the one for straight axis cylinders, which is approximately 0.164 at $Re = 100$ (Williamson (1989)).

5.1.2 Two-dimensional simulations of the fixed cylinder case

Two-dimensional simulations were also performed in the fixed body case, using a total of 16 sectional planes equi-spaced along the quarter ring part. As anticipated in section 5.1.1, a sectional argument based on the local normal component of the incoming velocity would predict a gradual decrease of the Reynolds number as the non-dimensional arc-length s/D increases, i.e. at lower sections along the span. This is consistent with the observation that the vortex shedding is not present at sectional locations corresponding to a local Reynolds number below the critical value

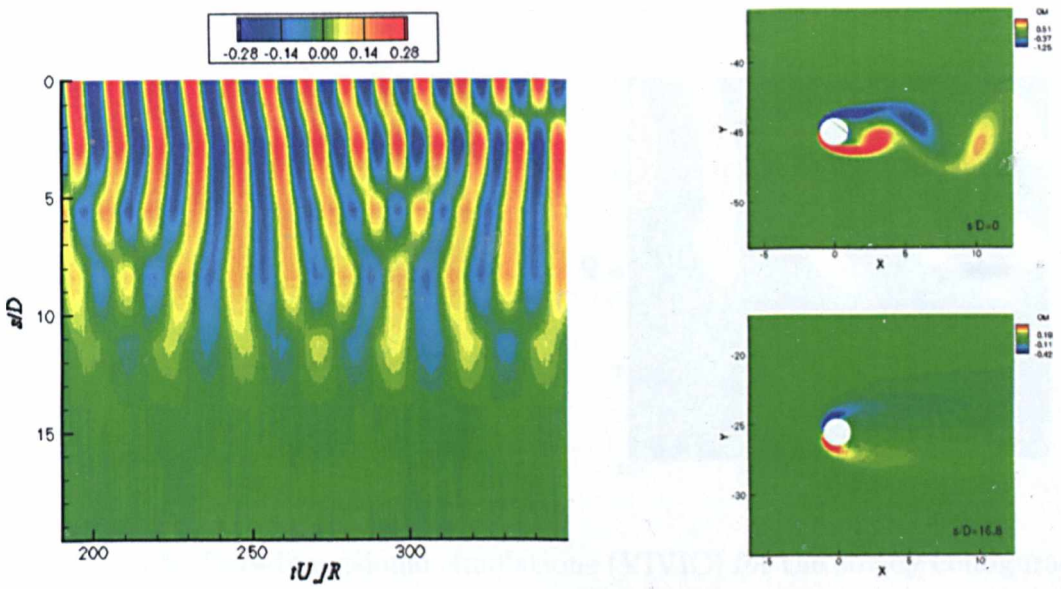


Figure 5.3: Two-dimensional simulations for the steady convex configuration at $Re = 100$: spanwise variation of sectional lift coefficient against non-dimensional time (*left*) and streamwise vorticity isocontours at $s/D = 0$ and $s/D = 16.8$ (*right*).

for the onset of shedding. However, this would also suggest that different shedding frequencies would take place at every sectional plane: this has been shown to be untrue by the three-dimensional computations presented in the previous section, where only one dominant frequency was observed for the whole body in all the cases tested, highlighting a possible shortcoming of a two-dimensional analysis.

Figure 5.3 (*left*) shows the spanwise distribution of the lift coefficient in time at $Re = 100$: consistent with the plot in figure 5.1 (*right*), the magnitude of the lift coefficient is close to zero for $s/D > 13$ and vortex shedding does not take place below this position, as shown by the vorticity isocontours in figure 5.3 (*right*). The spanwise lift distribution plot also shows the presence of phase jumps at $s/D = 1.5$, 5 and 7.5, which are related to vortex dislocations and cellular shedding. The lack of a constant phase change along the span could be partially compensated by including a model for the phase shift based on equation (5.1) (which is in turn based on the curvature of the body). The resulting isocontours for the lift coefficient are shown in figure 5.4. However, this model provides only an approximation for the gradual spanwise phase change and is not able to correct the phase jumps that occur at the

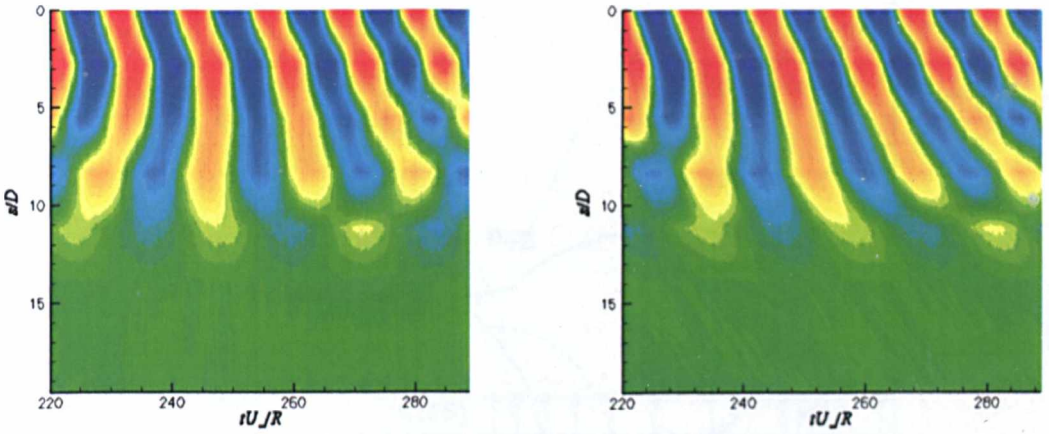


Figure 5.4: Two-dimensional simulations (VIVIC) for the steady configuration at $Re = 100$: spanwise variation of sectional lift coefficient against non-dimensional time without phase shift model (*left*) and with phase shift model (*right*).

boundaries between cells shedding at different frequencies.

Finally, it should be noted that the period of shedding in these plots appears to be twice the period found in the three-dimensional computations: this is due to the different non-dimensionalisation of the time units in the two-dimensional code, which is based on the radius instead of the diameter.

5.2 Forced cross-flow vibration

This section presents a set of simulations investigating the effect of an imposed sinusoidal motion on the wake behind the convex configuration. Figure 5.5 illustrates the pairs of non-dimensional input parameters $(f_s/f_o, A/D)$ simulated in the case of transverse translation at $Re = 100$, overlaid on the parameter plane obtained by Willden *et al.* (2008) with two-dimensional simulations at the same Reynolds number. The dashed line corresponds to the map of modes for $300 < Re < 1000$ originally obtained by Williamson & Roshko (1988), whose terminology is also used to identify the different flow states; the solid line was obtained by Willden *et al.* (2008) with two-dimensional computations at $Re = 100$ and represents the part of the lock-in region where a positive energy transfer from the flow to the cylinder takes

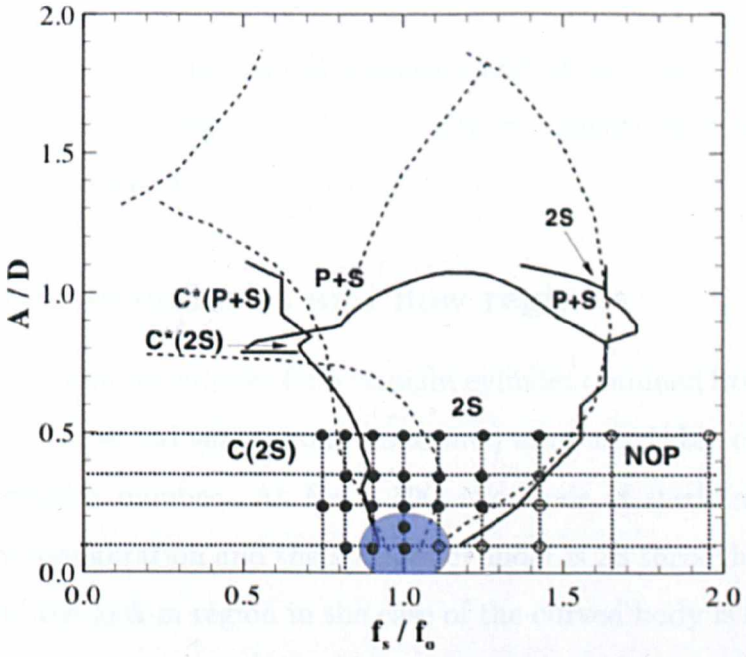


Figure 5.5: Flow states simulated for the convex configuration in the case of forced vibration at Re=100, overlaid on the Willden *et al.* (2008) map obtained with two-dimensional simulations at the same Reynolds number. The grey circles refer to type A shedding and the hollow circles to type B shedding. The shadowed area indicates the fluid excitation region.

place. In the cases presented, the amplitude of oscillation ranges from a minimum value of $0.1D$ to a maximum of $0.5D$, whereas the input frequency f_o varies from $0.5f_s$ to $1.3f_s$, where f_s is the Strouhal number for a fixed straight cylinder at $Re = 100$.

The next section presents a description of the types of shedding found in different regions of the parameter space analysed, using the wake topology and force distribution on the surface as a criterion for the categorisation. Section 5.2.2 analyses a case of vortex shedding outside the two-dimensional lock-in region for a straight cylinder, while section 5.2.3 focuses on low amplitude states, where dislocations occur spontaneously in the near-wake at regular intervals and fixed positions, even at a Reynolds number equal to 100. Sections 5.2.4.1 and 5.2.4.2 investigate the influence of the imposed amplitudes and frequencies on the energy transfer mechanism to identify the flow regimes that are positively excited and to predict where VIV

is likely to take place. Two modified geometries are presented in section 5.2.5 to investigate the effect of the horizontal extension and of the radius of curvature on the wake dynamics and energy transfer. Finally, a comparison with selected free vibration cases is provided in section 5.4.

5.2.1 Lock-in boundaries and flow regimes

In figure 5.5, the lock-in boundaries for a straight cylinder obtained from experiments (dashed line) and numerical simulations (solid line) are remarkably close, albeit the difference in Reynolds number. At $Re = 100$, the mode of shedding observed for both the convex configuration and the straight cylinder is 2S throughout the lock-in region. However, the lock-in region in the case of the curved body is larger than the two-dimensional one, as the vortex shedding syncronisation takes place over a wider range of input frequencies.

In particular, the lower lock-in boundary appears shifted towards higher values of input frequency f_o (i.e. lower values of the ratio f_s/f_o in figure 5.5). Flow states corresponding to input parameter pairs such as $(0.77, 0.5)$ and $(0.83, 0.1)$, which would normally give rise to de-synchronised wakes, result in globally locked-in vortex shedding over the whole span. This suggests that the introduction of a geometrical non-uniformity can shift the lower boundary of the lock-in region in figure 5.5 to include higher excitation frequencies that resulted in non-synchronised flow patterns in the case of a uniform cylinder. This observation is also supported by the outcome of the study conducted by Nuzzi *et al.* (1992) on a cylinder with a mild diameter variation: their experiment shows that the lock-in region for the flow past the geometrical disturbance reaches higher excitation frequencies compared to the uniform cylinder case.

Close to the upper boundary of the lock-in region (lower excitation frequencies), the flow appears only locally locked-in, with two distinct frequencies measured in different spanwise regions: a higher frequency, close to the Strouhal value for the steady convex configuration, is found to drive the shedding in the upper part of the body, while a lower frequency, equal to the excitation frequency, is dominant in the lower half. In this regime, the Strouhal component of the lift force is therefore non

negligible compared to the force contribution generated by the body's oscillation: this component would disappear if the cylinder's response was locked-in everywhere. However, the Strouhal contribution does not participate in any energy transfer between the body and the fluid, since there is no oscillation at the Strouhal frequency. In the region of the two-dimensional parameter plane with no observable flow patterns (NOP in figure 5.5), the vortex shedding results in a complex wake dynamics where a mix of 2S and 2P modes of shedding is observed; this hybrid mode shows similarities with the 2P-2S mode found by Flemming & Williamson (2005) in the wake of pivoted cylinders and by Techet *et al.* (1998) past a tapered cylinder. Inside this extended lock-in region, two regimes could be identified: type A (grey circles) and B (hollow circles). Although both cases give rise to a 2S type of shedding, the force and phase angle distribution change significantly along the span of the body, as will be described in the next sections.

5.2.1.1 Type A

At high excitation frequencies and relatively high amplitudes of oscillation the vortices are shed in-phase with the cylinder's motion: the resulting lift distribution is shown in figure 5.6 together with the wake topology visualised through $\lambda_2 = -0.1$ isosurfaces. The shedding at the top exhibits the features of a 2S mode, with two oppositely signed single vortices shed per oscillation cycle. Due to the three-dimensionality of the model, the vortex cores in the near-wake are bent according to the curvature of the body and start to distort further downstream. In the lower part of the quarter ring they become weaker and deform in a wavy fashion, developing lateral arms of vorticity that reconnect to the main vortex core around the horizontal extension.

This wake dynamics is significantly different from the one past the fixed convex cylinder illustrated in section 5.1.1, where the straight vertical vortices give rise to out-of-phase shedding along the span and virtually no vortical motion is detected in the horizontal extension. As a consequence of the imposed translation, the cores and the body's axis are nearly parallel and the main vortex detaches from the trailing edge at the same time in every spanwise location, as shown in figure 5.7: conse-

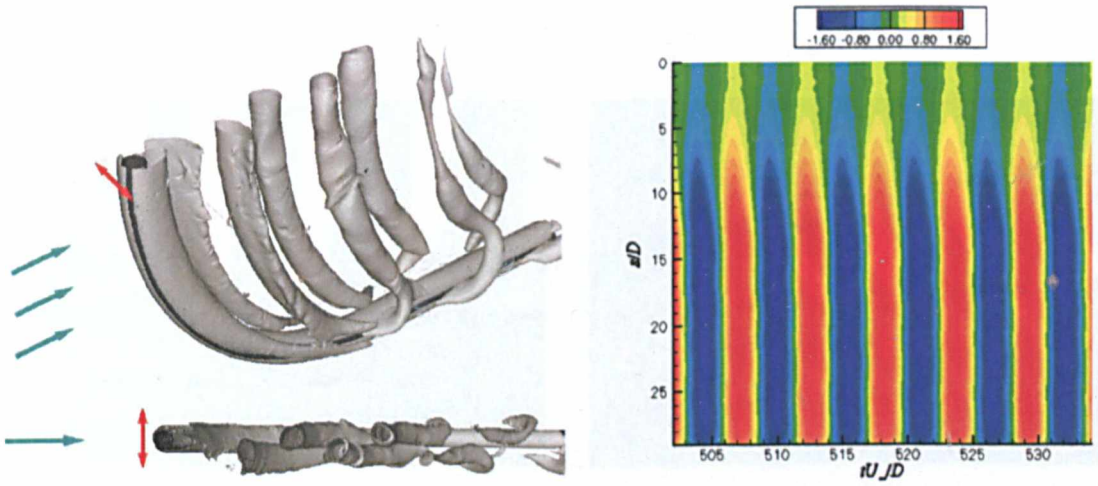


Figure 5.6: *Left*: Wake topology for the flow past the convex configuration at $f_o = 1.1f_s$, $A/D = 0.5$ ($Re = 100$); isosurfaces at $\lambda_2 = -0.1$ and $\frac{tU_\infty}{D} = 524.5$. *Right*: Time evolution of the sectional lift coefficient along the cylinder's span.

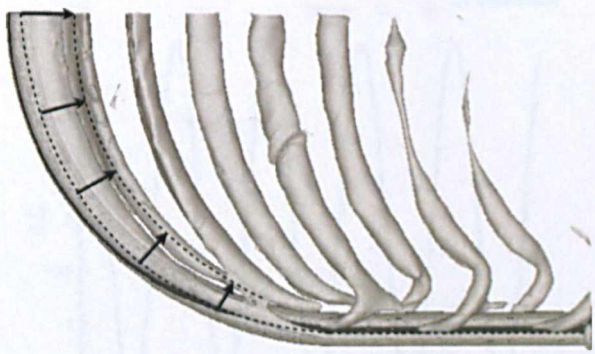


Figure 5.7: Shedding mechanism at $\frac{tU_\infty}{D} = 524.5$ for the case at $f_o = 1.1f_s$, $A/D = 0.5$. Isosurfaces at $\lambda_2 = -0.1$.

quently, at a fixed time instant, no change in the sign of the force exerted on the body takes place and the lift coefficient isocontours in figure 5.6 appear straight.

The effect of motion on the force distribution can be deduced also from the vertical velocity isocontours plotted in figure 5.8 for the steady and oscillatory case. In the former the velocity component in the $y-$direction is negative for the first vortex shed, whereas in the latter it is positive (hence directed out of the paper). These plots show how the distance of the first vortex from the body decreases as the cylinder is forced to oscillate in the transverse direction; this is consistent with this case exhibiting higher forces on the body's surface.

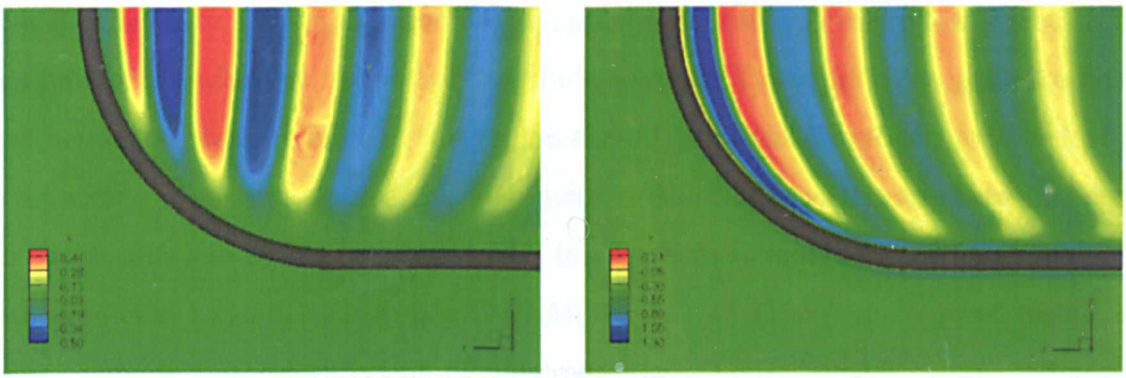


Figure 5.8: Isocontours of the v velocity component in the $y-$direction (positive out of paper) at $Re = 100$. *Left*: steady case at $\frac{tU_\infty}{D} = 523.8$ (set of data from Miliou (2004)). *Right*: oscillating case at $f_o = 1.1 f_s$, $A/D = 0.5$ and $\frac{tU_\infty}{D} = 524.5$.

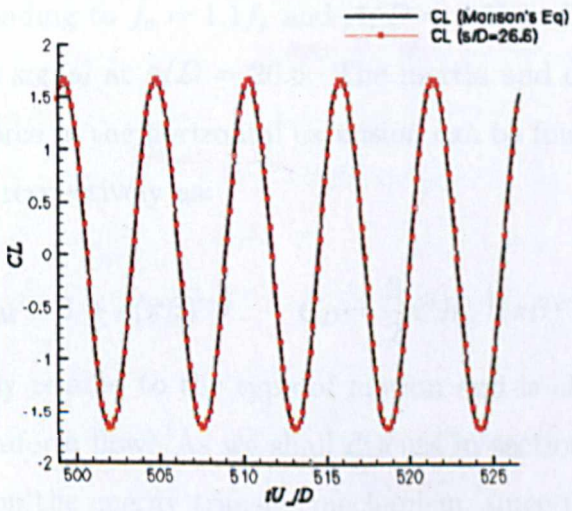


Figure 5.9: Lift signal for $A/D = 0.5$ and $f_o/f_s = 1.1$ at a section $s/D = 26.6$ (horizontal extension) and force signal given by the Morison's equation (Morison *et al.* (1950)).

The fact that the sectional forces do not decrease with increasing s/D may appear in contrast with the weakening of the shedding in the lower part of the pipe shown by the λ_2 isosurfaces in figure 5.6 (*left*). In the region where the cylinder is parallel to the inflow the body responds only to the force due to the cross-flow, since the inflow is parallel to its axis and does not generate vortex shedding. For $\theta > 45°$ (corresponding to $s/D \approx 10$), the axial component of the incoming velocity is

significantly greater than the normal one and therefore this region shows similarities to a slender body, eventually becoming completely parallel to the inflow direction in the horizontal addition: following the "Independence Principle", the pressure field and hence the pressure force in this region should be insensitive to the axial velocity component. However, due to the alignment of the body with respect to the flow direction, this is a spanwise "drag-type" force, whose magnitude and frequency are well predicted by equation proposed by Morison *et al.* (1950) (5.2) based on mean force coefficients in the direction of the cross-flow.

$$F(t) = \frac{1}{2}\rho U|U|DC_D + \frac{1}{4}\pi\rho D^2\frac{dU}{dt}C_M \tag{5.2}$$

The force given by equation (5.2) for an oscillating cylinder in a stationary flow with Keulegan-Carpenter number $KC = \frac{U_{max}T}{D} = \pi$ and Stokes parameter $\beta = \frac{D^2}{\nu T} = 18.04$ (corresponding to $f_o = 1.1f_s$ and $A/D = 0.5$) is displayed in figure 5.9 together with the lift signal at $s/D = 26.6$. The inertia and drag coefficients used to calculate the lift force in the horizontal extension can be found in Bearman *et al.* (1985) and are given respectively as:

$$C_M = 1 + 4(\pi\beta)^{-\frac{1}{2}} \qquad C_D = \frac{3}{2}\pi^3 K_c^{-1}(\pi\beta)^{-\frac{1}{2}} \tag{5.3}$$

This feature is strictly related to the type of motion and is absent when the body is kept fixed in an uniform flow. As we shall discuss in section 5.2.4.1, this has an important influence on the energy transfer mechanism, since the transverse oscillation of the horizontal extension provides a significant hydrodynamic damping to the whole structure.

As expected from theoretical considerations, the transverse motion within the lock-in region enhances the spanwise correlation of the vortices and generates a more two-dimensional form of shedding. The correlating effect of lock-in, often used to justify the use of two-dimensional simulations for predicting the flow behaviour, allows a better approximation of the force distribution in forced vibration through the strip theory based code. Figure 5.10 shows the lift coefficient distribution along the span of the body: unlike the steady case, where the phase shift due to the leading

edge curvature could not be accurately modelled, in the oscillating configuration the sectional approach provides a correct approximation of the in-phase vortex shedding. The maximum value of the sectional lift coefficient obtained through two-dimensional simulations agrees remarkably well with the three-dimensional results, especially in the lower part of the quarter ring ($s/D > 10$), where the force distribution is predicted by equation (5.2). Figure 5.11 and 5.12 show the spanwise vorticity distribution in the near wake obtained with three and two-dimensional simulations respectively. As discussed in chapter 4, in the strip theory based code the sectional planes are perpendicular to the cylinder axis and therefore correspond to the sections of the three-dimensional domain illustrated in figure 5.11. The three-dimensional results show that the wake topology remains nearly unaltered in the upper half of the quarter ring (up to $s/D = 10.4$), exhibiting a 2S type of shedding with progressive contraction of the shear layers as the non-dimensional arc-length increases. This is consistent with the gradual increase in the magnitude of the lift force from the top to the bottom of the body shown in plot 5.6 (*right*). However, the wake topology in figure 5.12 shows good agreement with the three-dimensional counterpart only for $s/D = 0$: further down along the span, i.e. at $s/D = 5.2$, which corresponds to a section inclined of 24° approximately, the cross-flow influence strongly interferes

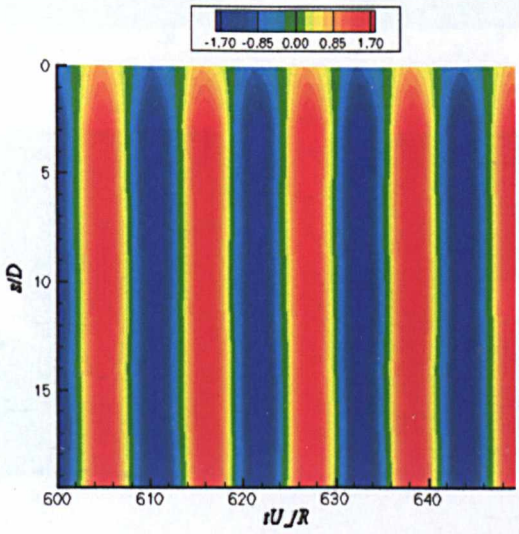


Figure 5.10: Spanwise variation of sectional lift coefficient against non-dimensional time for $f_o = 1.1f_s$ and $A/d = 0.5$ at $Re = 100$ (two-dimensional simulations).

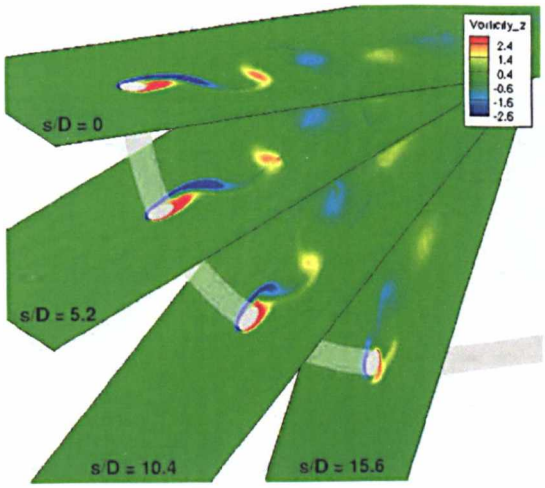


Figure 5.11: Spanwise vorticity component at four different sections ($s/D = 0$, $s/D = 5.2$, $s/D = 10.4$ and $s/D = 15.6$), three-dimensional simulations at $f_o = 1.1f_s$, $A/D = 0.5$ and $Re = 100$. The non-dimensional time corresponds to a minimum in the lift force.

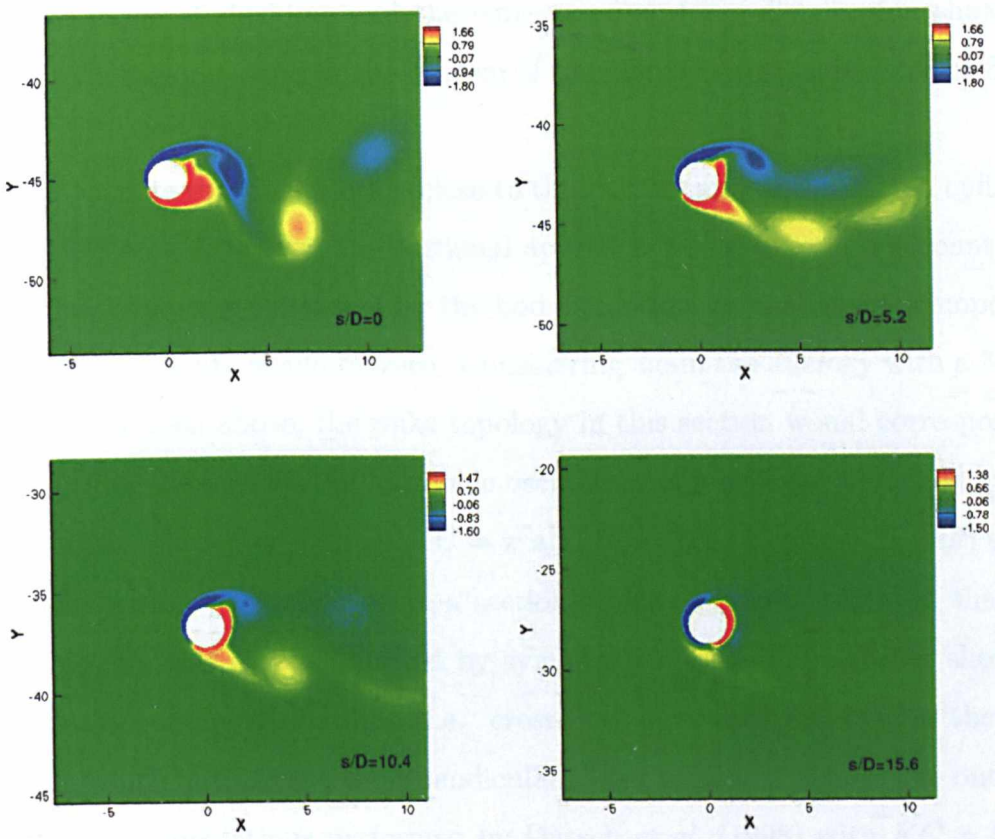


Figure 5.12: Spanwise vorticity component in four different sections, two-dimensional simulations at $f_i = 1.1f_s$, $A/D = 0.5$ and $Re = 100$. The non-dimensional time corresponds to a minimum in the lift force.

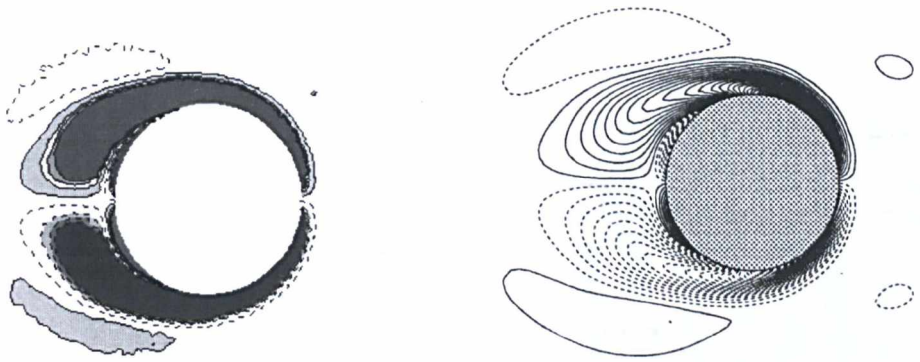


Figure 5.13: Spanwise vorticity in a section perpendicular to the inflow direction, corresponding to $s/D = 19.6$ (bottom end of the quarter ring). The dashed lines represent negative vorticity. *Left*: present two-dimensional simulation with $KC = \pi$ and $Re = 100$. *Right*: vorticity isolines with $KC = 5$ and $Re = 100$ from Dutsch *et al.* (1998).

with the 2S mode of shedding and the corresponding force distribution shows no difference with the one found at the bottom of the quarter ring, as depicted in figure 5.10.

Finally, we note that in a section close to the bottom end of the curved cylinder, approximately at $s/D = 19.6$, the sectional approach would take into account only the cross-flow component dictated by the body's motion, as the normal component of the incoming velocity would be zero. Considering again the analogy with a "drag-type" force described above, the wake topology in this section would correspond to the laminar flow induced by the harmonic oscillation of a cylinder in a fluid at rest with Keuleugan-Carpenter number $KC = \pi$ and $Re = 100$. Figure 5.13 (*left*) shows the spanwise vorticity distribution in a sectional plane inclined $\pi/2$ from the free-stream direction; this is characterised by symmetric and periodic vortex shedding in the direction of the oscillations (i.e. cross-flow direction) and not in the free-stream one, which in this case is perpendicular to the sectional plane. The outcome of the numerical simulations performed by Dutsch *et al.* (1998) with $KC = 5$ and $Re = 100$, which corresponds to the same flow regime of the present case according to the definition given by Tatsuno & Bearman (1990), is also shown for comparison.

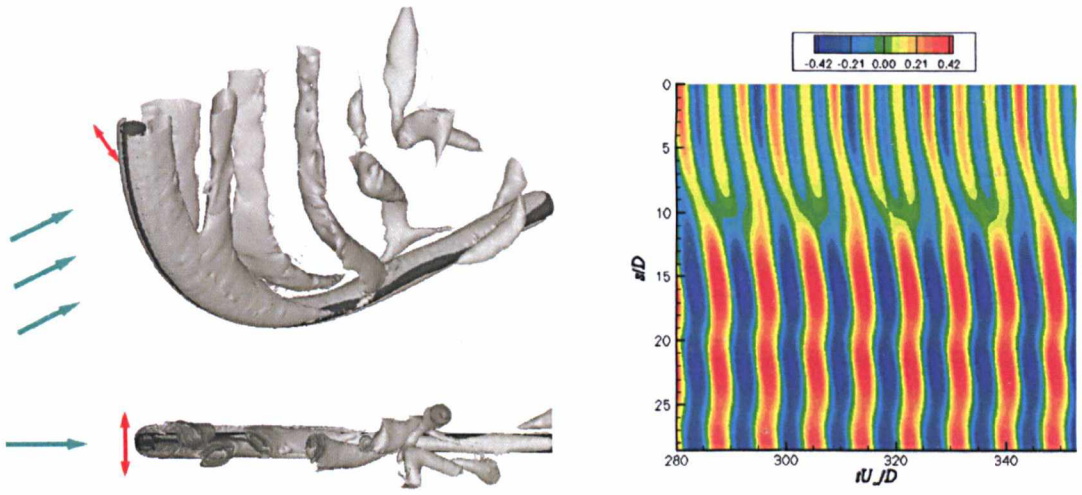


Figure 5.14: *Left*: Wake topology for the flow past the convex configuration at $f_o = 0.7f_s$ and $A/D = 0.25$ ($\frac{tU_\infty}{D} = 353.6$); isosurfaces at $\lambda_2 = -0.08$. *Right*: Time evolution of the sectional lift coefficient along the cylinder's span.

5.2.1.2 Type B

When the excitation frequency is decreased to values below the Strouhal frequency, a second frequency higher than the imposed one appears in the vortex shedding from the top region of the body. This flow state is identified by the hollow circles in the shedding map of figure 5.5. The spanwise extension of the region where the vortex shedding occurs at this higher frequency depends on the input parameters choice, becoming larger with decreasing amplitude and frequency of excitation (see figure 5.21 in section 5.2.3).

This section will discuss the case at $f_o = 0.7f_s$ and $A/D = 0.25$, which represents a point just outside the two-dimensional lock-in region in figure 5.5; this may be regarded as a transition from the steady to the oscillating configuration, as it presents features common to both cases.

Figure 5.14 illustrates the wake topology through $\lambda_2 = -0.08$ isosurfaces, as well as the corresponding lift coefficient evolution in time along the span. The vortex cores in the upper part of the curved cylinder are straight and the shedding process occurs in a similar fashion to the one in the stationary case, shown in figure 5.1.

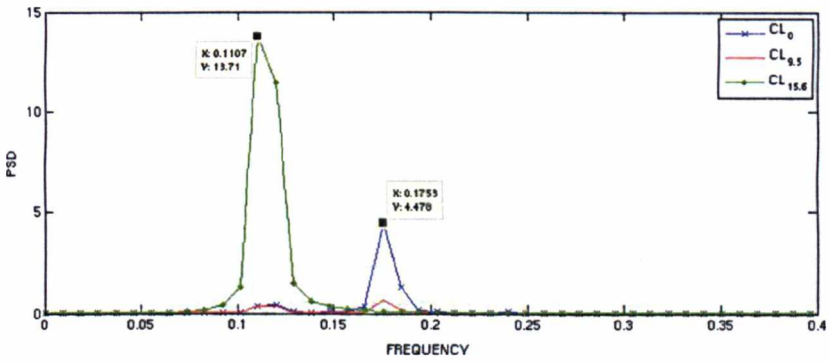


Figure 5.15: Dominant frequencies in the lift coefficient in the top section (CL_0), at the dislocation position ($CL_{9.5}$) and in the bottom part of the quarter ring ($CL_{15.6}$). Transverse oscillation at $f_o = 0.7f_s$, $A/D = 0.25$.

Consequently, a gradual phase shift takes place in this region, due to the different timings of the vortex shedding in each spanwise location. However, when the cylinder is forced to vibrate in the cross-flow direction, the contribution from the lower part of the body to the overall force is significant: as for type A, the analogy with the flow around a slender body forced to vibrate in a fluid at rest and the validity of the equation by Morison *et al.* (1950) in predicting the resulting force in the horizontal extension holds in this case as well. Therefore, for $s/D > 10$, the flow behaviour presents similar features in the two regimes. Nevertheless, the simultaneous presence in two regions along the span of cells characterised by different shedding frequencies results in the occurrence of vortex dislocations where the two cells are connected. This was not observed in the non-oscillating case, since the vortex shedding was not present in the lower part of the body.

Figure 5.15 shows the Fourier analysis of the lift coefficient signal in three sections corresponding to the top of the body, the position at which the dislocations occur and the lower half of the quarter ring ($s/D = 0$, $s/D = 9.5$ and $s/D = 15.6$ respectively). This plot shows that only one frequency is dominant at the top and at the bottom of the body, while at the dislocation position both frequencies are detected, although the power spectra density is considerably smaller than in the other spanwise regions. This highlights the presence of a beat frequency, which results in modulations in the time evolution of the integrated lift coefficient as shown in figure 5.16. The higher

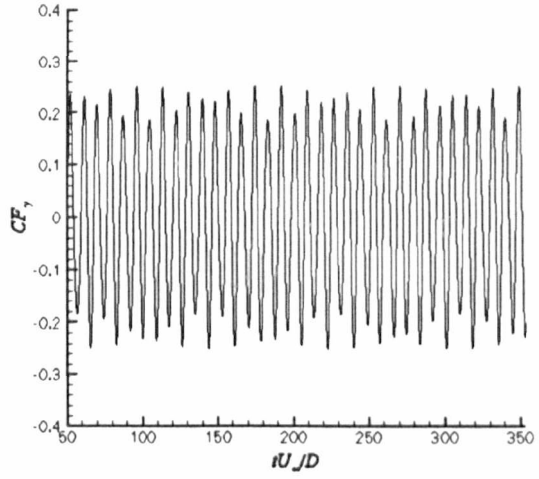


Figure 5.16: Time evolution of the integrated lift coefficient in the case of transverse oscillation at $f_o = 0.7f_s$, $A/D = 0.25$ and $Re = 100$.

frequency at the top sections is equal to 0.1753; this value is very close to the Strouhal frequency measured in the fixed cylinder case, which was equal to 0.1761. This observation lends support to the idea that in the type B shedding the Strouhal component of the lift force cannot be neglected as it generally happens in globally locked-in states under forced vibrations.

In type B the vortex dislocations occur at a fixed spanwise position and are periodically formed in the near wake when the cylinder reaches the maximum amplitude. This phenomenon is also observed at very low amplitudes of oscillation: for $A/D = 0.1$ and excitation frequencies below the Strouhal value, two distinct shedding frequencies take place along the span of the cylinder and vortex splitting is found to occur at the boundary between the cells. A more complete overview of the dislocation formation mechanism within this shedding regime will be given in section 5.2.3.

5.2.2 Vortex shedding outside the two-dimensional lock-in region

Simulations of the vortex shedding at very low frequencies were performed at $A/D = 0.5$ and $Re = 100$. The pair of input parameters $(f_e/f_s = 0.6, A/D = 0.5)$ lies

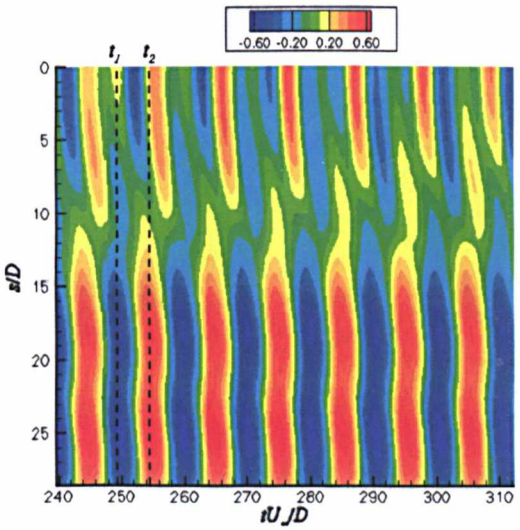


Figure 5.17: Time evolution of the sectional lift coefficient along the convex body's span at $f_e = 0.6f_s$ and $A/D = 0.5$.

outside of the "conventional" two-dimensional lock-in region depicted in figure 5.5. The lift distribution along the span in figure 5.17 highlights the presence of vortex dislocations at $s/D = 10$, which result from the competition between the frequencies at the top and at the lower half of the cylinder as described in the previous section: the region $0 < s/D < 10$ tends to shed vortices with a straight core at the higher frequency f_{top}, whereas for $s/D < 10$ the effect of curvature prevails and the cores are bent and shed at the imposed frequency (f_{bottom}).

The λ_2 isosurfaces and the spanwise distribution of the sectional lift coefficient are presented in figure 5.18. In this case, the shedding at the top is not as well established as in the type B shedding and the main vortex morphology changes from cycle to cycle, giving rise to an alternation of curved and straight cores. At t_1 in figure 5.18 *(right)*, f_{top} is prevailing and the cylinder sheds a straight vortex that detaches from the shear layer at about $s/D = 10$, generating dislocations. At t_2 in the following cycle, when the influence from the bottom part is predominant, a pair of curved vortices is shed from the top region in the fashion described in 5.2.1.1.

However, these two types of cores do not have the same strength, as the level of vorticity in the curved core is significantly higher: the vorticity in the straight core is not sufficiently concentrated to cut off the supply of circulation to the forming vortex on the opposite side and this weaker core detaches once the cylinder's motion

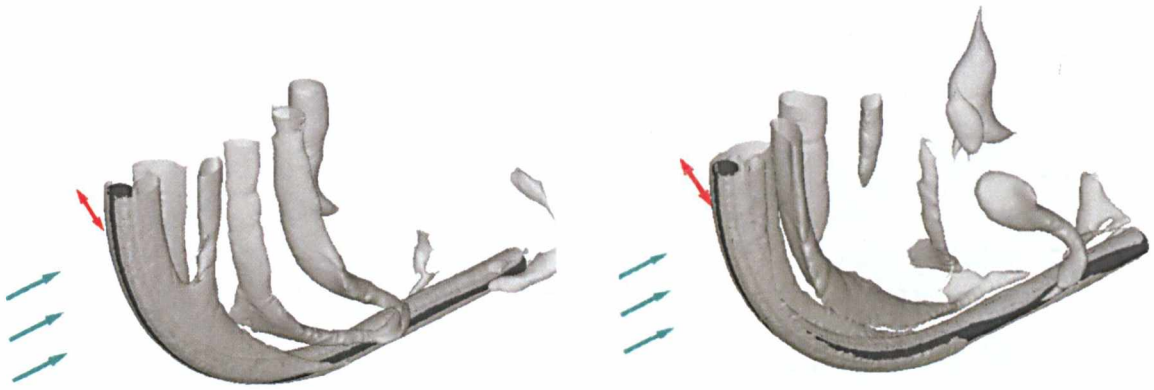


Figure 5.18: Wake topology for the flow past the convex configuration at $f_e = 0.6f_s$ and $A/D = 0.5$. *Left*: isosurfaces at $\lambda_2 = -0.07$ and $\frac{tU_\infty}{D} \approx t_1$. *Right*: isosurfaces at $\lambda_2 = -0.07$ and $\frac{tU_\infty}{D} \approx t_2$.

changes direction, without interaction with the opposite shear layer. This weak form of shedding is illustrated through isocontours of spanwise vorticity in figure 5.19 (*left*), while the curved vortex shedding dynamics is visualised in figure 5.19 (*right*). The wake topology past the top sections is similar to a 2P mode, with two counter-rotating vortex pairs shed per cycle, as described by Williamson & Roshko (1988). However, a closer analysis reveals that the vorticity distribution in this 'weak' type of shedding is different from the one in the 2P mode: in this case the two vortices that form the pair maintain the same vorticity sign in each shed couple (i.e. the first is positive and the second is negative in every pair, as shown in figure 5.19 (*left*)). This is consistent with the idea that the Strouhal frequency f_s is trying to re-assert itself in this region of the cylinder, which therefore tends to shed vortices at a frequency that is nearly double the frequency imposed. The absence of synchronised wake patterns observed for the two-dimensional cylinder is therefore not present in the case of the convex geometry. The three-dimensionality of this configuration and the effect of motion enhance the correlation of the vortex cores, although the competition of two frequencies in the upper part of the body prevents the vortex shedding from being globally locked-in along the whole span.

A measure of the degree of three-dimensionality in the wake is given by the correlation coefficient of the lift force acting on the body's surface in every spanwise location, which can be calculated as:

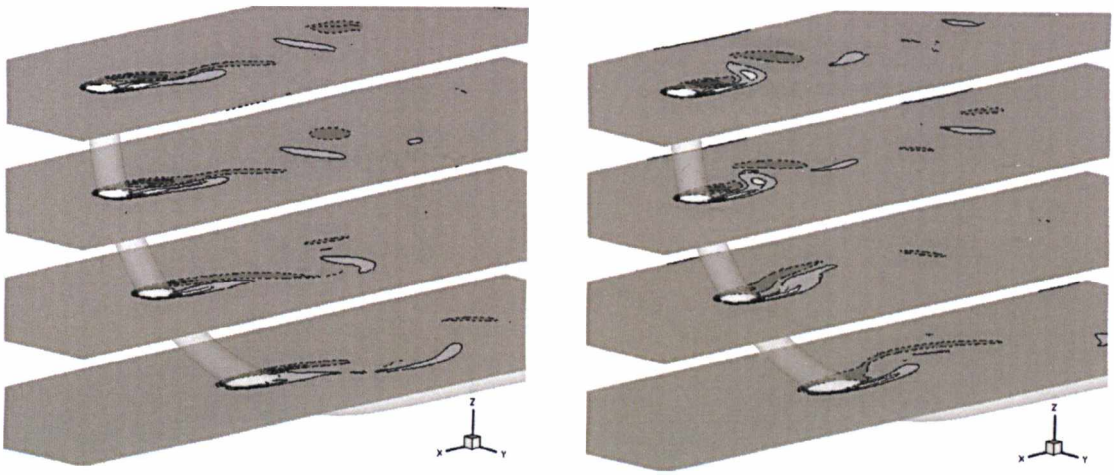


Figure 5.19: Case at $f_o/f_s = 0.6, A/D = 0.5$: spanwise vorticity at $t_1 = 249.2$ ($y = 0.5$), when the straight vortex core is shed (*left*), and at $t_1 = 254$ ($y = -0.5$), when the curved vortex core is shed (*right*). Dashed lines for negative vorticity.

$$\mathrm{R_{ff}} = \frac{\sum_{i=1}^{n}(C_{L_0} - \overline{C_{L_0}})(C_{L_i} - \overline{C_{L_i}})}{\left[\sum_{i=1}^{n}(C_{L_0} - \overline{C_{L_0}})^2 \sum_{i=1}^{n}(C_{L_i} - \overline{C_{L_i}})^2\right]^{1/2}} \tag{5.4}$$

where n denotes the number of slices. Figure 5.20 shows the spanwise variation of R_{ff} in case $f_o = 1.3f_s$ and $A/D = 0.5$ (type A), in case $f_o = 0.8f_s$ and $A/D = 0.1$ (type B) and in case $f_o = 0.6f_s$ and $A/D = 0.5$ (shedding outside the two-dimensional lock-in region). A value of R_{ff} close to unity implies strong correlation and suggests uniform condition in the primary vortex, while a value near 0 corresponds to regions with poor spanwise correlation. Clearly, the degree of correlation in type A is very high, resulting in a more severe hydrodynamic loading and in a uniform 2S type of shedding with phase angle close to 0°. On the other side, type B exhibits a drastic loss of correlation in the upper region of the body: this is associated with phase jumps and a sharp reduction in the magnitude of the lift coefficient in the top sections. A more detailed description of the vortex shedding phasing will be given in section 5.2.4.1.

Finally, in the case with input parameters outside of the two-dimensional lock-in region ($f_o = 0.6f_s$ and $A/D = 0.5$), the loss of correlation occurs more gradually

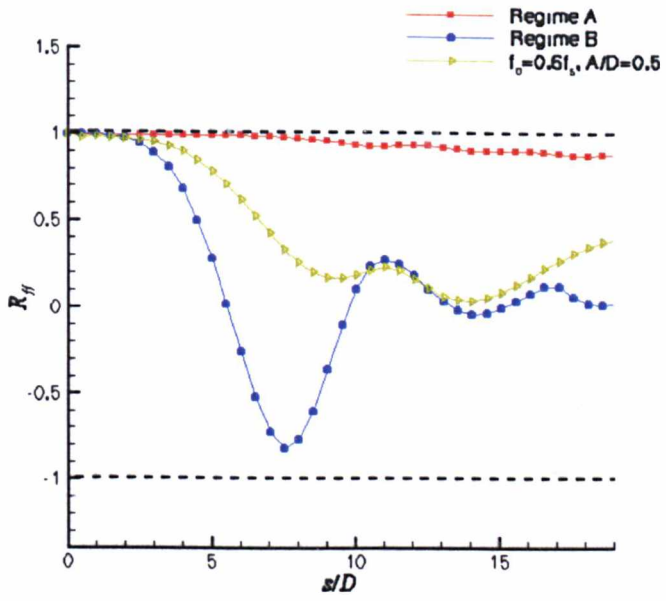


Figure 5.20: Spanwise lift correlation coefficient in type A, B and outside the two-dimensional lock-in region (i.e. at $f_o = 0.6f_s$ and $A/D = 0.5$).

over a wider range of non-dimensional arc-length s/D, until R_{ff} reaches a value close to 0 for $s/D = 9.7$. This phenomenon is associated with the coexistence of a 2S and a 2P mode along the span (as suggested by Hover *et al.* (1998) in the case of the 2S-2P hybrid mode of shedding past a tapered cylinder).

5.2.3 Vortex dislocations at low frequencies and amplitudes

As discussed in sections 5.2.1.2 and 5.2.2, the three-dimensional effects introduced by the body's curvature may lead to the occurrence of vortex dislocations in the wake: this is particularly evident at low excitation frequencies, in regions of the $(A/D, f_o/f_s)$ plane outside the lock-in boundaries. This phenomenon was also observed at low amplitudes of oscillation: for $A/D = 0.1$ and excitation frequencies below the Strouhal value, two distinct shedding frequencies were found along the span of the cylinder, i.e. a higher frequency in the top part of the body (f_{top}) and a lower frequency always corresponding to the imposed frequency of oscillation in the lower region (f_{bottom}). Vortex dislocations form periodically in the wake as these cells

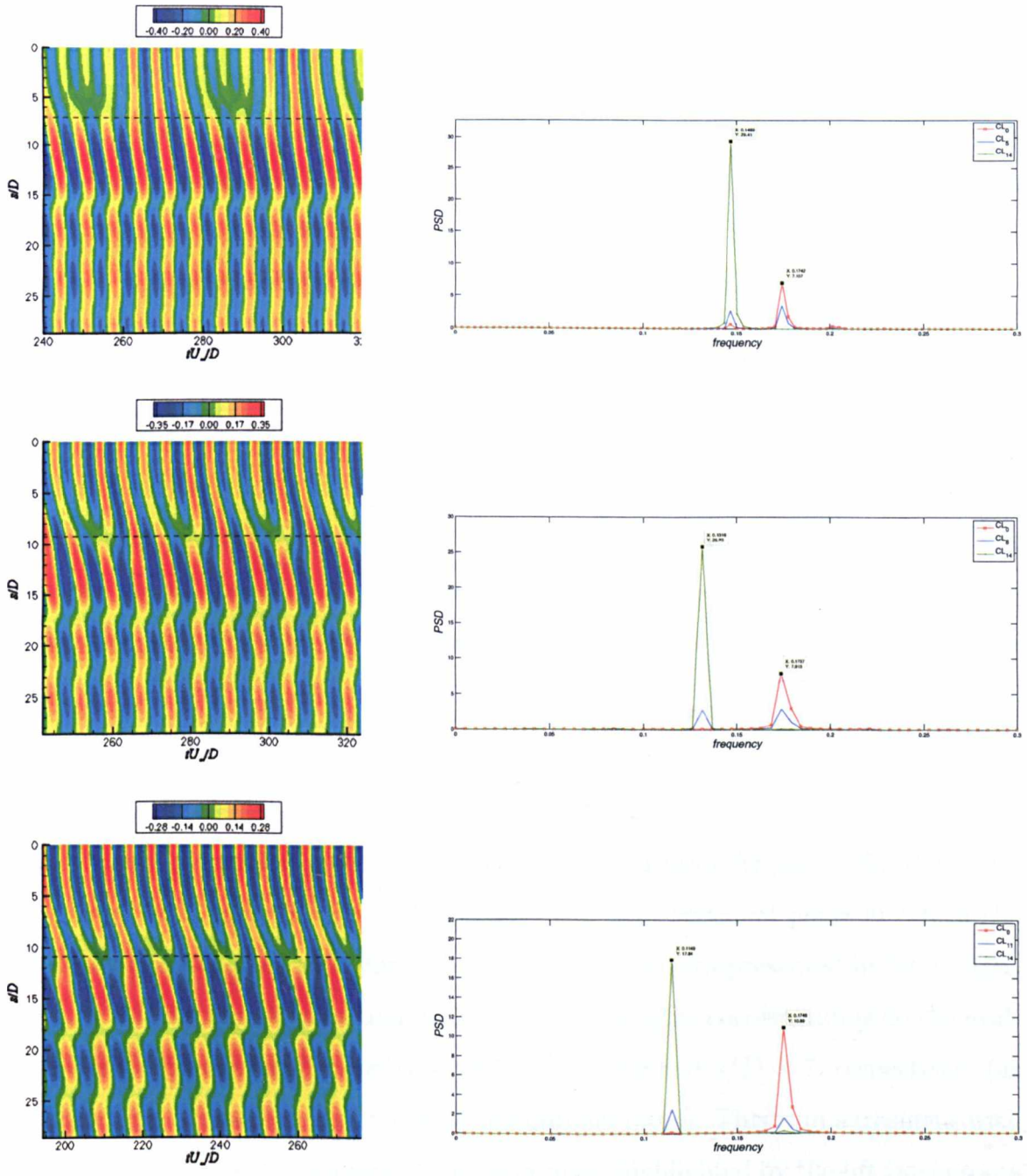


Figure 5.21: *Left*: spanwise distribution of the total lift coefficient at $A/D = 0.1$ and $f_o/f_s = 0.9$, $f_o/f_s = 0.8$ and $f_o/f_s = 0.7$ (top to bottom). *Right*: dominant frequencies in the top and bottom part, and at the dislocation position.

move out of phase with each other. Consistent with findings in past literature on shedding at low Reynolds numbers (Williamson (1992)), their occurrence is periodic in time and at fixed spanwise positions. Similarly, in all of these three cases illustrated in figure 5.21 the dislocation occurs at a beat frequency $f_D = f_{top} - f_{bottom}$. When the imposed frequency is increased from $0.7f_s$ to $0.9f_s$, the dislocation position shifts towards the top of the body and its frequency f_D decreases.

Williamson (1992) analysed the natural and forced formation of vortex dislocations in the laminar regime and used a small ring disturbance to trigger this mechanism at a local spanwise position; the dislocation frequency was found to decrease with decreasing ring diameter. In the curved cylinder there is no such disturbance; however, if we consider two-dimensional sections in the plane (x, y) placed at different spanwise locations, the local cross-section of the body is an ellipsis whose greater diameter is larger than the cylinder diameter D: similar to the ring diameter in Williamson's experiments, this introduces a different length-scale in the problem. An approximate relationship between the ratio of the dislocation frequency to the primary vortex shedding frequency and the greater diameter of the elliptical cross-section D_e was found to hold for the cases presented in figure 5.21. This is given as:

$$\frac{f_D}{f_o} = \frac{D_e}{D} - 1 \tag{5.5}$$

Substituting the oscillation frequency f_o and the dislocation frequency f_D, this equation provides a value for D_e that identifies the cross-sectional plane at which the dislocation is expected to occur: for the three frequencies presented in figure 5.21, $f_o/f_s = 0.7$, 0.8 and 0.9, the non-dimensional arc-lengths corresponding to the evaluated elliptical diameter are $s/D = 10.6$, $s/D = 8.9$ and $s/D = 7$, respectively (as indicated by the dashed line in the lift isocontours plots). This is in agreement with the value at the lower boundary of the dislocation highlighted by the lift isocontours in figure 5.21 (*left*), where the vortex splitting takes place.

The exact spanwise position at which the jump in frequency occurs can also be obtained from the Fourier analysis of the lift coefficient signal: figure 5.22 shows the frequency variation with the normal velocity component, $U_n = U_\infty \cos(\theta)$, which is related to the non-dimensional arc-length via the following relationship:

$$s/D = R^* \cos^{-1}\theta \tag{5.6}$$

where R^* is the non-dimensional radius of curvature of the quarter ring. The spanwise locations for the frequency jump, obtained using equation (5.6), are

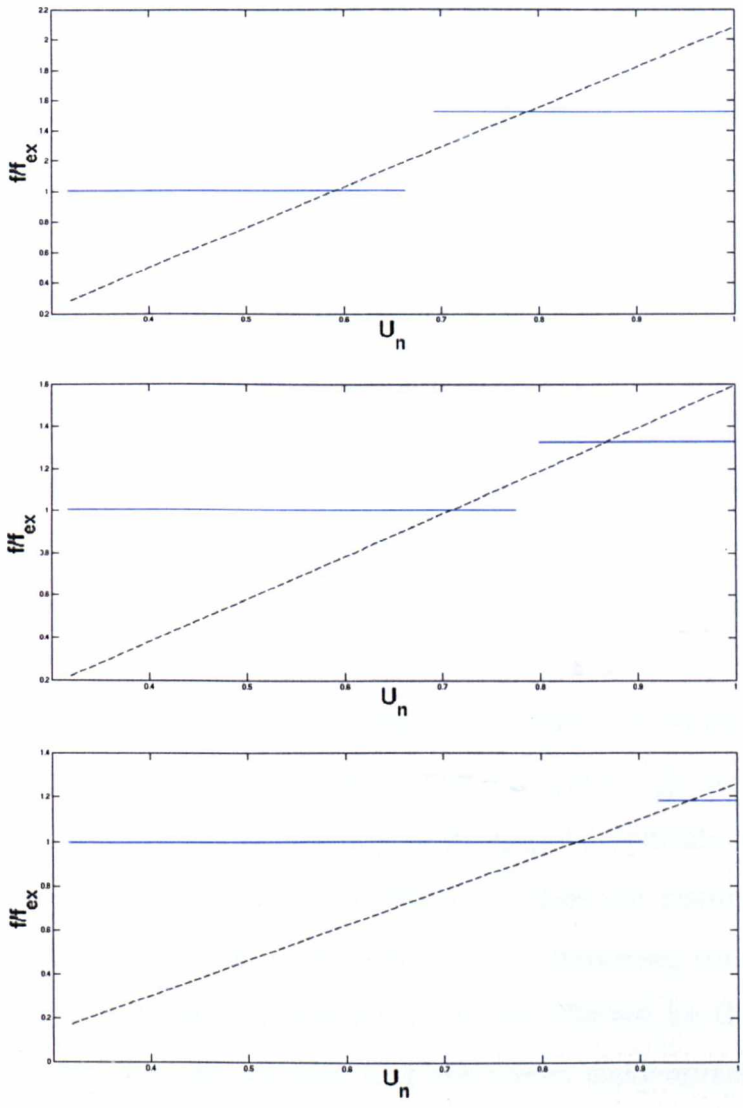


Figure 5.22: Spanwise distribution of the vortex shedding frequency in the three cases with imposed frequency $f_o/f_s = 0.9$, $f_o/f_s = 0.8$ and $f_o/f_s = 0.7$ (top to bottom) and oscillation amplitude $A/D = 0.1$.

$s/D = 10.57$, $s/D = 8.55$ and $s/D = 5.9$ for input frequencies $f_o/f_s = 0.7$, 0.8 and 0.9 respectively. Figure 5.22 highlights also that the frequency in the lower part of the body is equal to the imposed frequency of vibration ($f/f_{ex} = 1$), while the shedding from the top part takes place at a higher frequency.

A further observation which supports this interpretation may be derived from the existence of a mathematical relationship that allows the oblique-shedding Strouhal data St_θ to collapse onto the parallel-shedding Strouhal curve St_o, hence giving rise

to an universal St/Re curve. Williamson (1989) provides experimental evidence that such a relationship exists in the form $St_o = St_\theta/\cos\theta$, where θ is the angle of oblique shedding. If we consider the shedding from the top of the body to be nearly parallel to the cylinder's axis in the upper half of the quarter ring and the bent cores in the lower part to be at an oblique angle θ dependent on the non-dimensional arc-length at which the dislocation occurs, a similar relationship can be given as:

$$f_{top} = f_{bottom}/\cos\theta \tag{5.7}$$

Substituting the value of the frequencies found by means of the spectral analysis (see figure 5.21), equation (5.7) leads to a value for θ which identifies the same spanwise positions for the dislocation given by the argument of the elliptical cross-sections illustrated above.

These observations suggest that the spanwise position at which vortex dislocations occur is primarily a function of the imposed frequency f_o: as shown in figure 5.14, in the case with imposed frequency $f_o = 0.7f_s$ and amplitude $A/D = 0.25$, the dislocation takes place at $s/D \approx 10$ and this value does not change when the amplitude of oscillation is decreased to $0.1D$ keeping the frequency constant (see figure 5.21). Similarly the dislocation frequency f_D is not affected by the change in the oscillation amplitude. Finally, we note that the vortex dislocations exhibit a clear periodicity at lower frequencies and amplitudes of oscillation because in these cases the velocity and acceleration of the body are smaller and hence the weak shedding of straight vortices from the top is less disrupted by the change of direction in the sinusoidal trajectory. In fact the straight core shedding implies a gradual detachment of the core from the shear layer and therefore occurs only for long periods of vortex shedding. As f_o/f_s is increased and A/D is kept constant, the change in the direction of the body close to the extremes of the trajectory is more abrupt and there is not enough time for the straight cores to form.

As illustrated in figure 5.23, at this very low amplitude of oscillation the force distribution in the upper part strictly resembles the one for the steady case presented in figure 5.1, with a similar phase shift along the span. This feature disappears as the frequency is increased above the Strouhal value, in type A. Figure 5.24 (*left*)

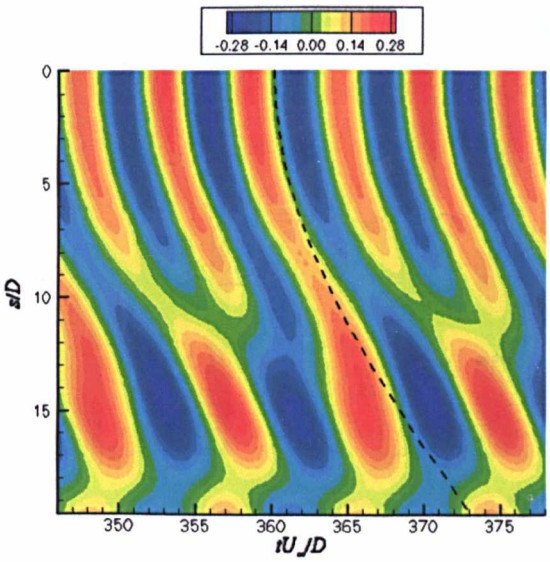


Figure 5.23: Detail of the lift coefficient distribution in time along the span of the curved part only in the case with $f_o/f_s = 0.7$ and $A/D = 0.1$. The dashed line represents the phase shift based on the free-stream velocity $U_\infty = 1$.

shows the time evolution of the lift coefficient in the case ($f_o/f_s = 1.1$; $A/D = 0.1$): as a direct consequence of the frequency increase, the dislocations have disappeared in the wake and the lift force is gradually reaching the same phase of the cylinder's motion. Although the lift coefficient isocontours are still bent in the upper region of the body, the phase line that approximates the spanwise shift is now based on a velocity $U = 0.5U_\infty$. A further increase in the oscillation frequency ultimately leads to in-phase shedding, as shown in figure 5.24 (*right*).

Finally, a closer view of the near-wake in the case with $f_o = 0.9f_s$ and $A/D = 0.1$ is shown in figure 5.25; the dashed line t_3 in the plot of the sectional lift coefficient isocontours indicates the time instant at which the λ_2 isosurfaces are extracted, $\frac{tU_\infty}{D} = 253.8$, a position corresponding to the maximum displacement in the positive direction and in the middle of the vortex splitting process. This picture may be compared to the results presented in sections 5.2.1.2 and 5.2.2: since the dislocation position has moved to the top region, the vortex splitting is less evident than in the other two cases, presented in figures 5.14 and 5.18 respectively. The time instants t_1 and t_2 refer to the shedding of straight cores before the occurrence of a dislocation,

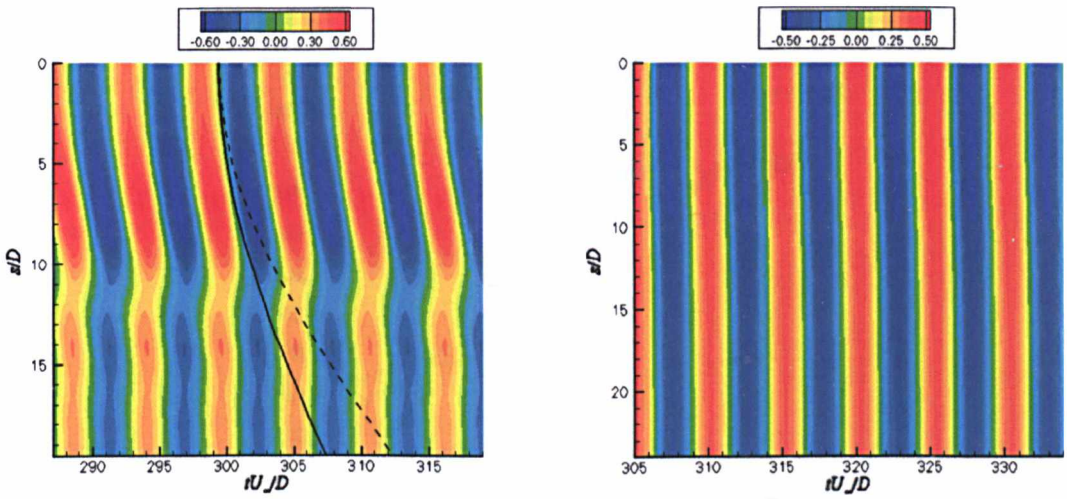


Figure 5.24: Detail of the lift coefficient distribution in time along the span of the quarter ring. *Left*: case with $f_o/f_s = 1.1$ and $A/D = 0.1$. The dashed line represents the phase shift based on the free-stream velocity $U_\infty = 1$, while the solid line is based on $U = 0.5U_\infty$. *Right*: case with $f_o/f_s = 1.2$ and $A/D = 0.1$.

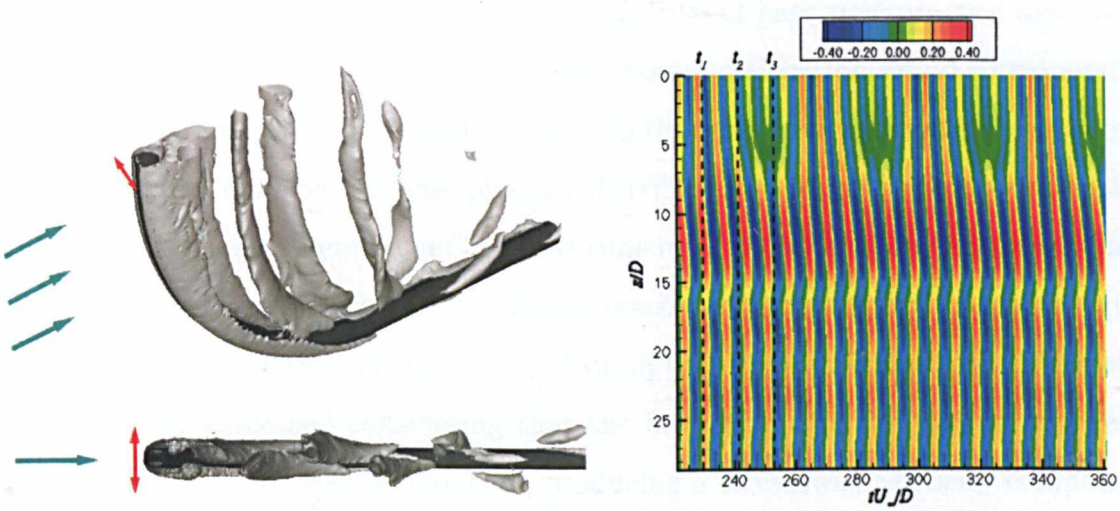


Figure 5.25: *Left*: Wake topology for the flow past the convex configuration with $f_o = 0.9f_s$ and $A/D = 0.1$ at t_3; isosurfaces at $\lambda_2 = -0.1$. *Right*: Time evolution of the sectional lift coefficient along the cylinder's span.

while t_3 has been chosen in the middle of the vortex splitting. The base pressure coefficient distribution along the span of the body at t_1, t_2 and t_3 is shown in figure 5.26: the presence of vortex dislocations involves a sharp increase in C_{pb} in the top region where the splitting takes place. In their experiments on wavy cylinders, Bear-

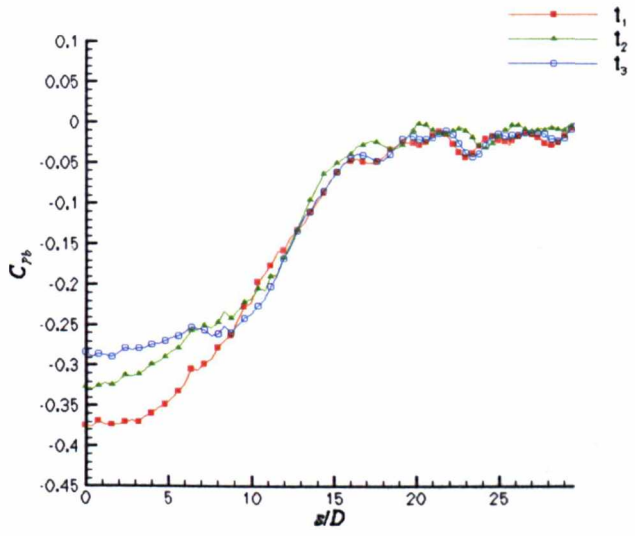


Figure 5.26: Base pressure coefficient for the convex configuration with $f_o = 0.9f_s$ and $A/D = 0.1$. The three time instants t_1, t_2 and t_3 refer to figure 5.25.

man & Tombazis (1997) found that a certain level of base pressure was associated with a different shedding frequency so that a vortex dislocation would correspond to a jump in the base pressure along the span. In the present simulation the occurrence of a dislocation modifies the base pressure distribution along the spanwise direction, generating a gradual increase in C_{pb} in the time instants prior to the vortex splitting, shortly before the base pressure coefficient reaches a maximum value at t_3 in figure 5.26, which also corresponds to a sharp drop in the drag coefficient C_D. This mechanism can be explained considering that the formation of a dislocation involves a sharp bending of the vortex filaments, producing a streamwise vorticity component able to sustain the pressure gradient. This trend has been found in all the cases that exhibited vortex dislocations.

5.2.4 Vortex shedding phase and energy transfer

5.2.4.1 Effect of the frequency's variation

The regimes so far analysed present similar features in the wake topology, with a 2S type of shedding dominant in the lock-in region. However, the lift force distribution changes considerably along the span with varying input frequencies and amplitudes,

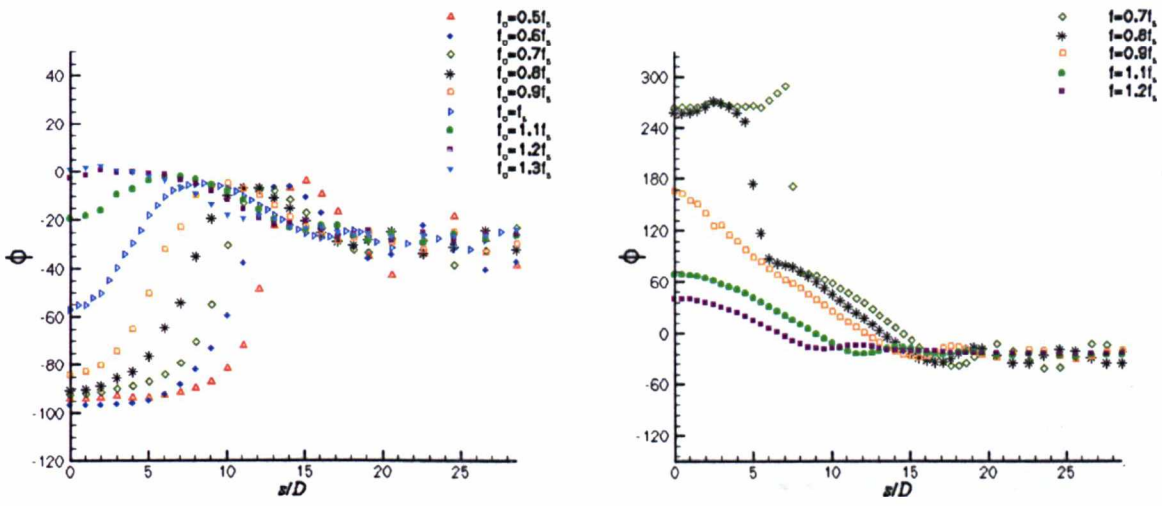


Figure 5.27: Spanwise variation of the time-averaged phase angle ϕ with the imposed frequency at a fixed amplitude $A/D = 0.5$ (*left*) and at $A/D = 0.25$ (*right*).

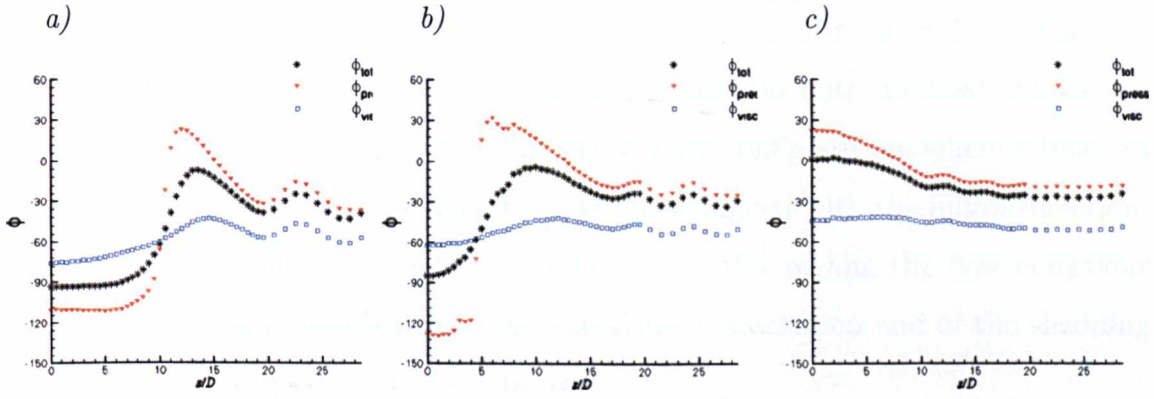


Figure 5.28: Phase angle of total lift, ϕ_{tot}, pressure lift ϕ_{press}, and viscous lift, ϕ_{visc} at $A/D = 0.5$ and $Re = 100$. *a)* $f_o = 0.6f_s$; *b)* $f_o = 0.9f_s$; *c)* $f_o = 1.3f_s$.

as the curvature of the body has a significant effect on the vortex shedding phase. The spanwise variation of the phase angle ϕ with the imposed frequency is shown in figure 5.27 for fixed amplitudes equal to $A/D = 0.5$ and $A/D = 0.25$: at the higher amplitude of oscillation, the phase angle lies in the range $[-180°; 0°]$ along the whole span of the body. Figure 5.27 (*left*) highlights the different behaviour of the top region in type A and B, as described in the previous section. At input frequencies above the Strouhal value ($f_o = 1.1f_s, 1.2f_s$ and $1.3f_s$), the phase shift is relatively small and the vortex shedding is in-phase along the entire span and locked onto the imposed frequency; this is associated with very high values of the

lift correlation coefficient R_{ff}, as shown in figure 5.20. At lower frequencies, such as $f_o = 0.8f_s$ and $0.9f_s$, the phase angle in the top part exhibits a sharp reduction of about 90°: this localised jump implies a gradual phase change in the central region of the quarter ring, in order to reach the value of ϕ in the horizontal extension, which is approximately constant at every frequency given the nature of the forces in this region (see section 5.2.1.1). As shown in figure 5.28, the phase change in the total lift is due to the jump in the phase of the pressure force component, as the viscous contribution ϕ_{visc} is constant along the body's arc-length. When the amplitude of oscillation is halved to 0.25 (figure 5.27 (*left*)), the spanwise variation of the phase angle is considerably different, as the values of ϕ are now higher and lie in the positive excitation region $[0°; 180°]$ for most of the frequencies tested. We shall describe the variation of the energy transfer with the oscillation amplitude later in this section, the important point concerning the phase angle illustrated in figure 5.27 being the common value $\phi \approx -30°$ in the lower part of the body at both imposed amplitudes of vibration: this feature is also found in the concave configuration, where ϕ tends to the same negative value as the curvature becomes aligned with the inflow direction, regardless of the input frequency or amplitude. In this region, the flow behaviour is found to be nearly insensitive to the curvature's orientation and of the shedding mechanism in the upper part of the body.

The time-averaged part of the lift coefficient in phase with the body's velocity, CL_v, is proportional to the energy transferred from the fluid to the structure: positive values of CL_v correspond to fluid excitation, while negative values indicate fluid damping. According to the plot in figure 5.29, CL_v is negative at every spanwise location, with the most negative values in the lower part of the geometry ($s/D > 15$), where the total lift coefficient reaches the highest magnitude. At high frequencies, the velocity and the acceleration of the cylinder are higher and, according to the equation given in (5.2), the force acting on the body as it oscillates transversely in the fluid is larger. This region acts as a hydrodynamic damper to the whole structure, preventing the top part to be excited by the vortex shedding, with the only exception the case at $f_o/f_s = 1.3$, where CL_v is mildly positive for $0 < s/D < 3$. As the frequency ratio is decreased from 1.3 to 0.5, the value of CL_v in the lower

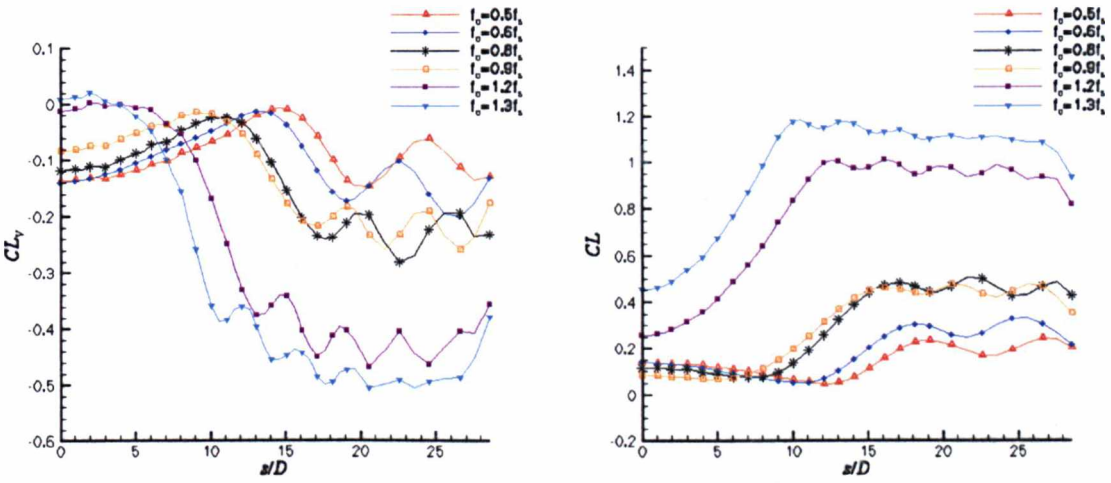


Figure 5.29: Spanwise variation of the time-averaged lift coefficient in phase with the cylinder's velocity CL_v (*left*) and of the total time-averaged lift coefficient CL (*right*) at a fixed amplitude $A/D = 0.5$ and $Re = 100$.

region increases, without however becoming positive; at the same time, the value at the top decreases slightly. Therefore, for all the frequencies tested at this amplitude, the integral of the energy transferred over the whole structure is negative.

For $\theta > 45°$ (corresponding to $s/D \approx 10$), the axial component of the incoming velocity is significantly greater than the normal one and thus this region shows similarities to a slender body, becoming entirely parallel to the inflow direction in the horizontal addition: following the "Independence Principle", the pressure field and hence the pressure force in this region appear to be insensitive to the axial velocity component. Figure 5.29 (*right*) clearly shows the predominance of the force contribution arising from this lower portion of the body; the force coefficient increases and its peak shifts to the middle region ($s/D = 10$) as the input frequency is increased.

Figure 5.29 (*left*) also shows that the spanwise location of the maximum value of CL_v shifts towards the upper part of the body as the imposed frequency is increased: at frequencies within type A shedding ($f_o = 1.2f_s$ and $f_o = 1.3f_s$) this takes place at $s/D = 2$, while within type B it occurs further down along the span, at $9 < s/D < 10$. Finally, for input frequencies outside of the two-dimensional lock-in regime (i.e. $f_o = 0.5f_s$ and $f_o = 0.6f_s$), the peak of CL_v occurs in the range $13 < s/D < 14$.

5.2.4.2 Effect of the amplitude's variation

At lower amplitudes, the influence of the horizontal extension is weakened and the shedding from the upper half of the cylinder is stronger. Two distinct trends for the lift coefficient are found to occur depending on the frequency ratio value. At input frequencies within type B, such as $f_o/f_s = 0.9$, the total lift coefficient still reaches its maximum value in the lower part of the body ($s/D > 15$), as shown in figure 5.30 (*right*): however, when the amplitude of oscillation is reduced, the peak in the total lift coefficient shifts further along the span, until for ($f_o/f_s = 0.9$; $A/D = 0.1$) it occurs at $s/D = 12$ and for ($f_o/f_s = 1.1$; $A/D = 0.1$) at $s/D = 7.1$, as illustrated in the right-hand side of figures 5.31 and 5.32.

At the same time, figure 5.31 (*left*) shows that CL_v in the range $0 < s/D < 12$ becomes positive for $A/D = 0.1$ and 0.25, with a maximum at $s/D = 9$. This shows that the region of the body's span that determines the direction of the energy transfer is located in the middle part of the quarter ring. The spanwise location of the maximum CL_v appears to be the same at all the amplitudes tested (see figure 5.31 (*left*)), suggesting that it may depend on the frequency only.

At $f_o/f_s = 1.1$, the part of the lift coefficient in phase with the velocity sharply increases: figure 5.32 shows that the maximum positive value for CL_v at $A/D = 0.1$ and 0.25 is now reached in the top sections ($0 < s/D < 6$), as opposed to type B where the peak in CL_v occurs in the middle part of the quarter ring. Similarly, at these lower amplitudes, the total lift coefficient attains a maximum for $s/D > 10$: the direction of the energy transfer is thus determined in the upper half of the body.

When the convex configuration is forced to oscillate in the cross-flow direction, the net energy transfer for the whole structure is positive for ($f_s/f_o = 0.9; A/D = 0.1$), ($f_s/f_o = 1.1; A/D = 0.1$), ($f_s/f_o = 1; A/D = 0.1$) and ($f_s/f_o = 1; A/D = 0.15$), as schematically shown in figure 5.5: although the exact boundaries in the parameter plane for the excitation region have not been determined, these results show that the excitation region for this configuration is considerably contracted when compared to its two-dimensional counterpart, which is delimited by the solid line. The plots of the CL_v distribution presented in this section show that the reduction of

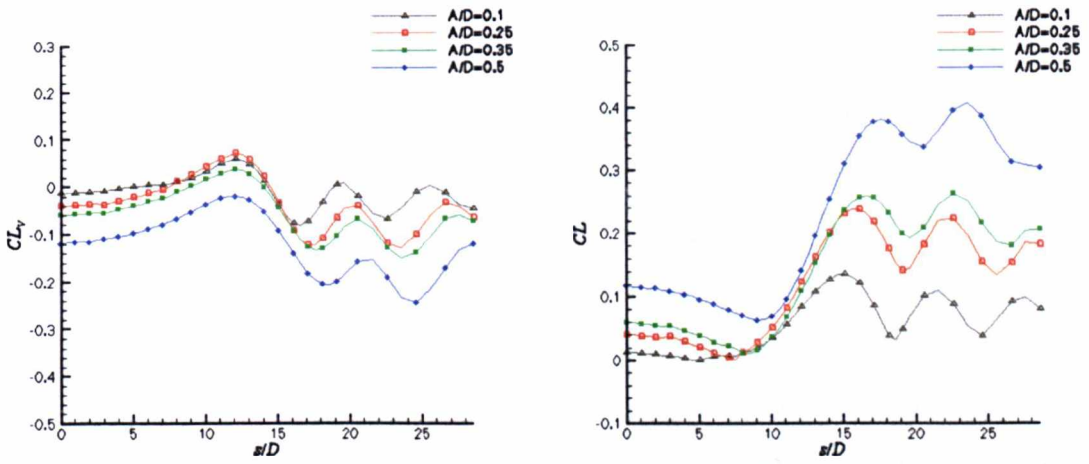


Figure 5.30: Effect of amplitude variation on the spanwise distribution of CL_v (*left*) and total CL (*right*) at $f_o = 0.7f_s$.

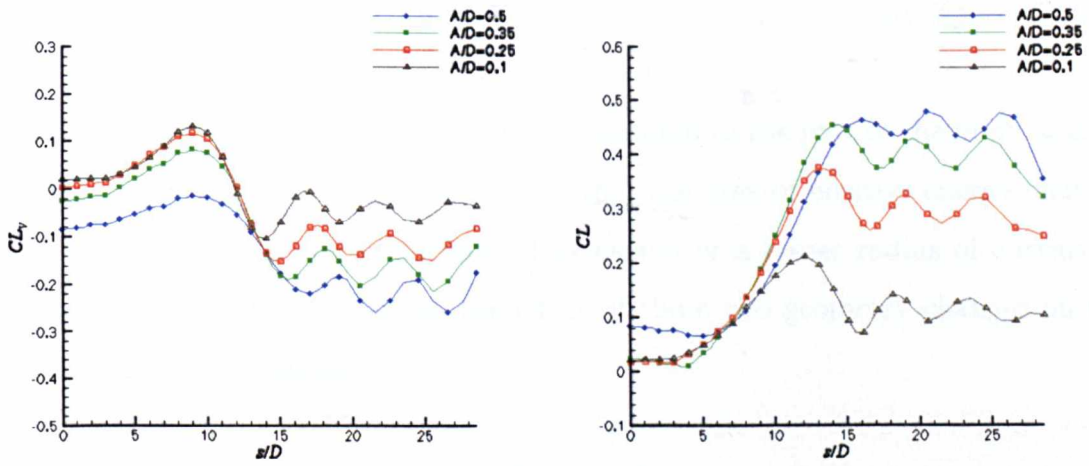


Figure 5.31: Effect of amplitude variation on the spanwise distribution of CL_v (*left*) and total CL (*right*) at $f_o = 0.9f_s$.

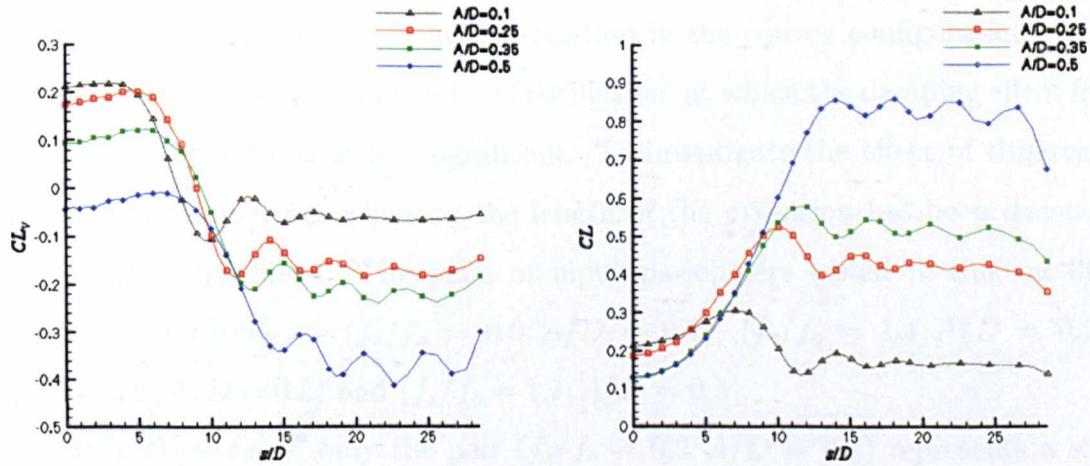


Figure 5.32: Effect of amplitude variation on the spanwise distribution of CL_v (*left*) and total CL (*right*) at $f_o = 1.1f_s$.

the excitation region in the parameter plane is a direct consequence of the horizontal extension presence: the high hydrodynamic damping in this lower region of the body prevents the top part, which is likely to shed vortices in a similar manner to the straight cylinder, from being excited by the flow. At $A/D < 0.15$ within type A, the top sections are subjected to positive energy transfer (see figure 5.32), since the force contribution from the horizontal extension is weaker due to the very low amplitude of oscillation. As observed in section 5.2.3, this type of shedding strictly resembles the one in the steady configuration, which exhibits straight cores and the spanwise lift distribution depicted in figure 5.1. This flow configuration is therefore likely to lead to excitation in the top sections, although the response amplitude expected in free vibration is considerably smaller than the one observed for straight cylinders; this point will be further discussed in section 5.4.

The presence of a strong fluid damping generated in the part of the body aligned with the inflow may lead to the hypothesis that the area of positive energy transfer could increase with a shorter horizontal extension or a larger radius of curvature. The following section will discuss the effect of these two geometry changes on the energy transfer mechanism.

5.2.5 Modified convex configurations

5.2.5.1 Effect of the horizontal extension

As discussed in section 5.2.4.2, fluid excitation in the convex configuration can be achieved only at very low amplitudes of oscillation, at which the damping effect from the horizontal extension is less significant. To investigate the effect of this region on the energy transfer mechanism the length of the extension has been decreased from 10 to 5 diameters. The pairs of input parameters tested in this modified convex configuration are $(f_s/f_o = 0.9; A/D = 0.1)$, $(f_s/f_o = 1.1; A/D = 0.25)$, $(f_s/f_o = 0.9; A/D = 0.5)$ and $(f_s/f_o = 1.1; A/D = 0.5)$.

Among these cases, only the pair $(f_s/f_o = 0.9; A/D = 0.1)$ represents a state where the structure is excited by the flow and the net energy integral is positive. As shown in figure 5.21, vortex dislocations appear at regular interval in the wake

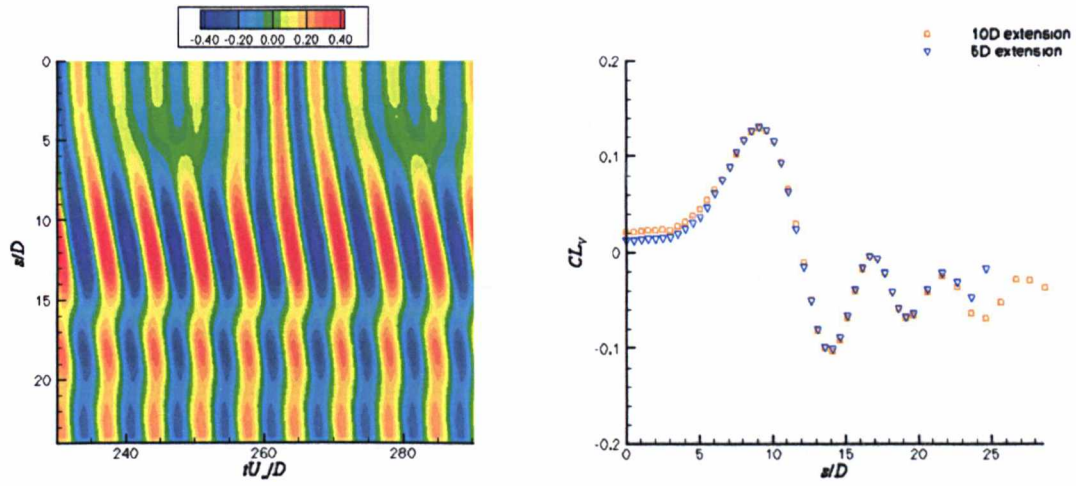


Figure 5.33: Modified convex geometry, $f_o = 0.9f_s$ and $A/D = 0.1$. *Left*: spanwise variation of sectional lift coefficient in the case with a 5-diameter long extension. *Right*: comparison of CL_v distribution with a 10− and a 5−diameter long horizontal extension.

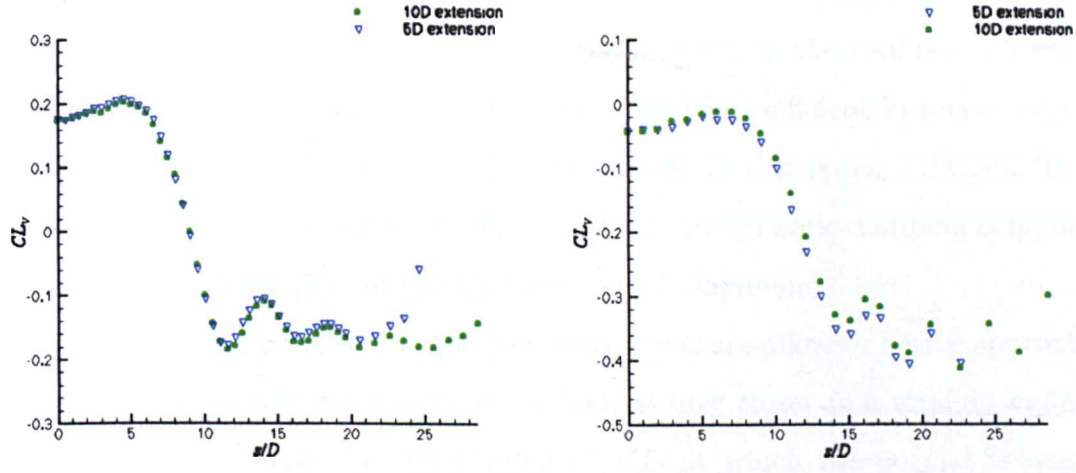


Figure 5.34: Modified convex geometry, $f_o = 1.1f_s$. Comparison of CL_v distribution with a 10− and a 5−diameter long horizontal extension. *Left*: $A/D = 0.25D$. *Right*: $A/D = 0.5D$.

of the original configuration, at a spanwise position in the range $4 < s/D < 7$. The reduction in the length of the horizontal extension has no effect on the frequency and position of vortex dislocations, as highlighted in figure 5.33. Consequently the CL_v distribution is not altered and the energy transfer has the same value of the geometry with a $10D$ long extension. This trend is confirmed at higher amplitudes of oscillation within type A shedding: figure 5.34 shows that the geometric modification

in the length of the horizontal addition has no effect on the energy distribution.

5.2.5.2 Effect of the radius of curvature

To investigate the effect of curvature, numerical simulations at $f_o = 1.1f_s$ and $A/D = 0.5$ have been performed on a second modified geometry with a double radius of curvature, $R = 25D$. To reduce the computational cost of this bigger mesh, the horizontal extension has been reduced to a length of 7 diameters, since the previous simulations demonstrated that this parameter has no relevant effect on the force distribution and on the energy transfer mechanism. Figure 5.35 shows the wake topology, while figures 5.36 and 5.37 (*right*) provide a comparison of the lift coefficient distribution in the case of the double radius of curvature geometry and in the original one. Although the maximum and minimum value of the fluctuating lift coefficient and its spanwise distribution are the same in the two cases, the energy transfer mechanism is modified by the increase in the radius of curvature: as shown in figure 5.37 (*left*), when $R = 25D$ the lift coefficient in-phase with the velocity becomes positive for $14° < \theta < 40°$. However this is not sufficient for the whole structure to be excited by the flow, as the hydrodynamic damping component generated in the lower part of the geometry is still dominant.

From a sectional perspective, the increased curvature allows a better approximation of the flow, as the upper part of the body is now closer to a straight cylinder: following the cosine law, the same value of s/D at which the normal velocity is smaller than the axial one in the original configuration would now account for a higher velocity contribution and hence it would give rise to a more "conventional" vortex shedding. This two-dimensionalising effect is shown in figure 5.38, where the variations of CL and CL_v along the span of the body are illustrated. The distribution of the total lift coefficient is remarkably similar to the one obtained with fully three-dimensional simulations (see figure 5.36): the magnitude of CL ranges from -1.789 to $+1.76$, when computed through the three-dimensional code, and from -1.76 to $+1.737$, when computed using the sectional approach.

However, the part of CL in phase with the velocity, shown in figure 5.38 (*right*), is in good quantitative agreement with its three-dimensional counterpart only in the

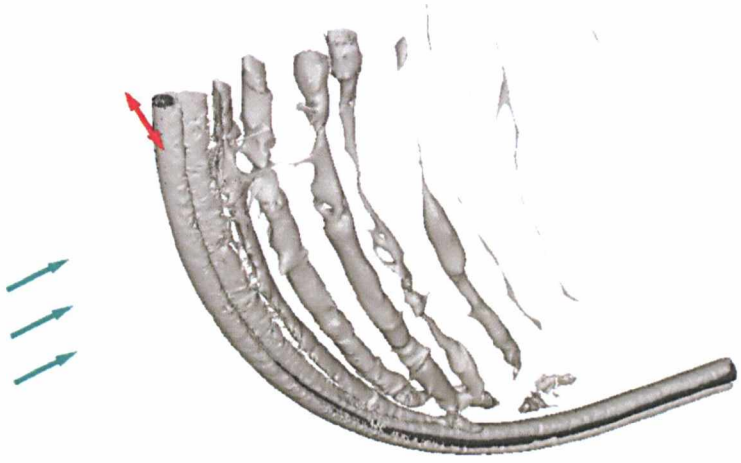
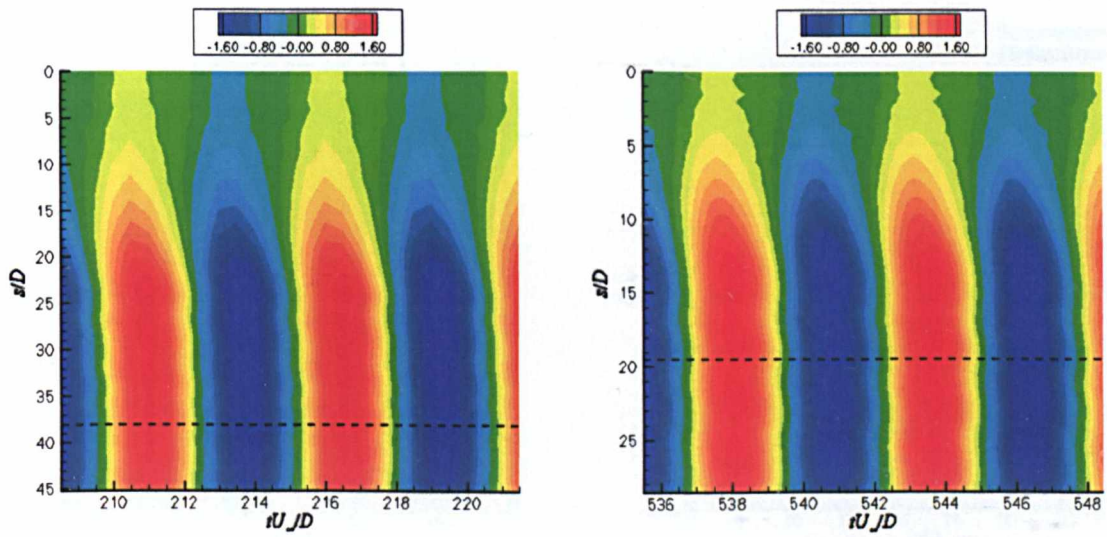


Figure 5.35: Wake topology for the flow past the convex configuration at $f_o = 1.1f_s$ and $A/D = 0.5$ visualised through isosurfaces at $\lambda_2 = -0.1$.



$R = 25D$ $R = 12.5D$

Figure 5.36: Lift coefficient distribution on the body's surface, in the case with $R = 25D$ (*left*) and $R = 12.5D$ (*right*). Both configurations are forced to oscillate at $f_o = 1.1f_s$ and $A/D = 0.5$. The dashed line identifies the end of the curved part.

top region $0 < s/D < 6$, where the maximum discrepancy in the values obtained with two and three-dimensional simulations is equal to 0.047. As the cylinder becomes progressively aligned with the inflow direction, the axial velocity component U_A increases until it reaches the same magnitude of the normal velocity component and

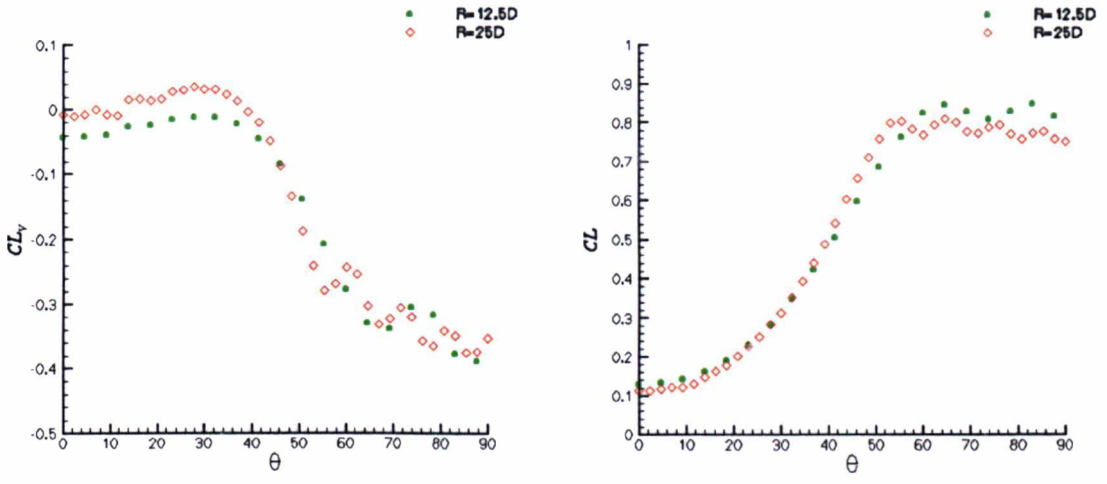


Figure 5.37: Spanwise distribution of the lift coefficient in phase with the velocity CL_v (*left*) and of the total lift coefficient CL (*right*) in the case with $R = 25D$ and $R = 12.5D$. Both configurations are forced to oscillate with $f_o = 1.1f_s$ and $A/D = 0.5$.

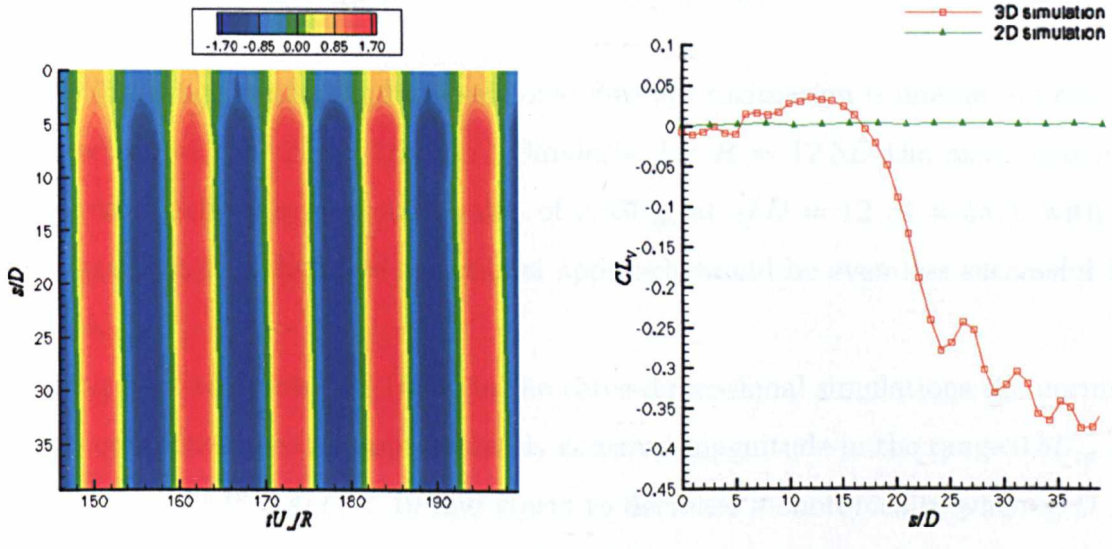


Figure 5.38: Two-dimensional sectional simulation of the modified geometry with double radius of curvature at $f_o = 1.1f_s$ and $A/D = 0.5$. *Left*: lift coefficient distribution on the body's surface. *Right*: spanwise distribution of the lift coefficient in phase with the velocity in two- and three-dimensional simulations.

cannot be neglected. Figure 5.39 (*left*) shows that U_A reaches a peak magnitude of $0.822U_\infty$ at $s/D = 18.7$ (corresponding to $\theta = 42.85°$): this non-dimensional arc-length corresponds to the point where the two and three-dimensional results in figure 5.38 start to diverge considerably. In these conditions, the strip theory fundamental

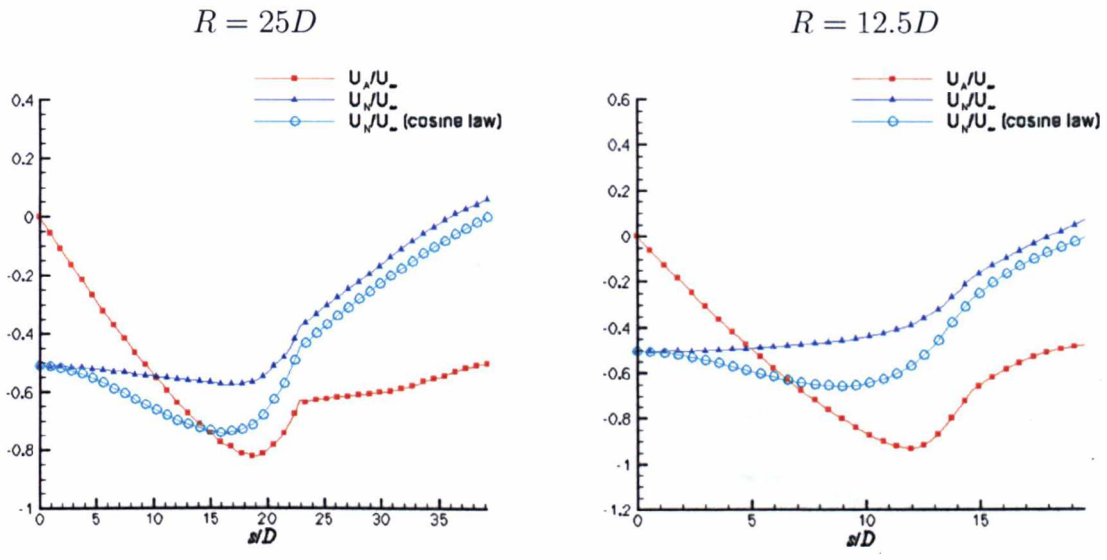


Figure 5.39: Spanwise distribution of the time-averaged values of the vertical, normal and axial velocity component extracted $0.3D$ upstream in the radial direction. Both configurations are forced to oscillate at $f_o = 1.1f_s$ and $A/D = 0.5$.

assumption is not verified and the sectional flow approximation is unable to predict the direction of the energy transfer. Similarly, for $R = 12.5D$ the axial velocity component reaches an maximum value of $0.93U_\infty$ at $s/D = 12$ ($\theta = 55°$), with a higher gradient and therefore a sectional approach would be even less successful in this case.

Going back to figure 5.39 (*left*), in the three-dimensional simulations the normal velocity component has an approximately constant magnitude in the range $0.5U_\infty < U_n < 0.58U_\infty$ for $0 < s/D < 19$ and starts to decrease monotonically when $s/D > 19$. The normal velocity component calculated using the cosine law is very close to the three-dimensional one for $0 < s/D < 6.1$, with a maximum difference of $\Delta U/U_n$ of 9.5%. In the case with $R = 12.5$ the condition $\Delta U/U_n < 10\%$ is fulfilled only for a much narrower range, $0 < s/D < 3.1$. This supports the conclusion that a sectional approach leads to a better flow approximation in the case with double radius of curvature, where the normal velocity upstream of the body is approximately constant and close to the value predicted by the cosine law.

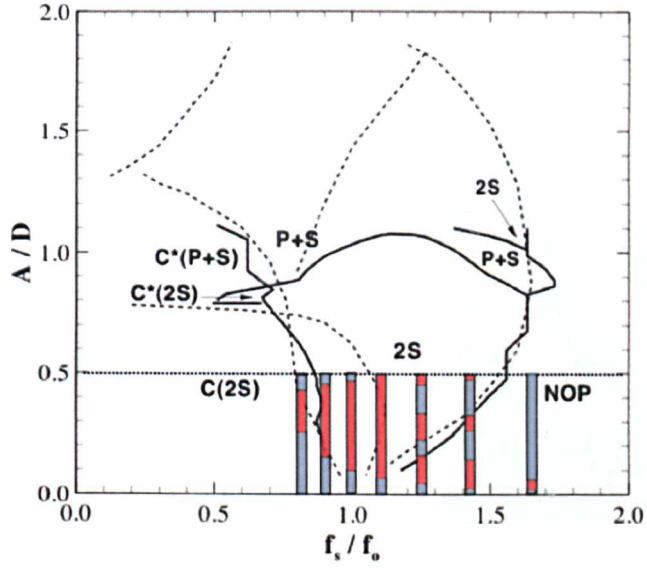


Figure 5.40: Flow states simulated for the convex configuration in the case of forced rotation about the horizontal extension axis, overlaid on the Willden *et al.* (2008) map (two-dimensional simulations).

5.3 Forced cross-flow rotation

When a uniform translation in the cross-flow direction is imposed to the convex configuration, the resulting vortex shedding is significantly influenced by the dynamics in the lower half of the body; in particular, the horizontal extension acts like a strong hydrodynamic damper, preventing the whole structure from being excited by the flow. For this reason, only the flow states generated at very low input amplitudes lie within the region of positive energy transfer and can be used to predict free vibration. This is an intrinsic feature of the convex configuration in uniform translation. To avoid this mechanism, an oscillatory roll motion about the horizontal extension axis has been imposed as an alternative: the maximum amplitude, equal to $0.5D$, is thus reached at the top section and decreases with decreasing distance to the roll axis. This value was chosen equal to $0.5D$ to span all the amplitudes considered in the forced transverse translation presented in section 5.2. The horizontal extension has no translational motion in this configuration. The oscillating rotation of this part will generate a damping effect due to skin friction, which in this case is so small as to be negligible. Figure 5.40 shows the amplitude spanned

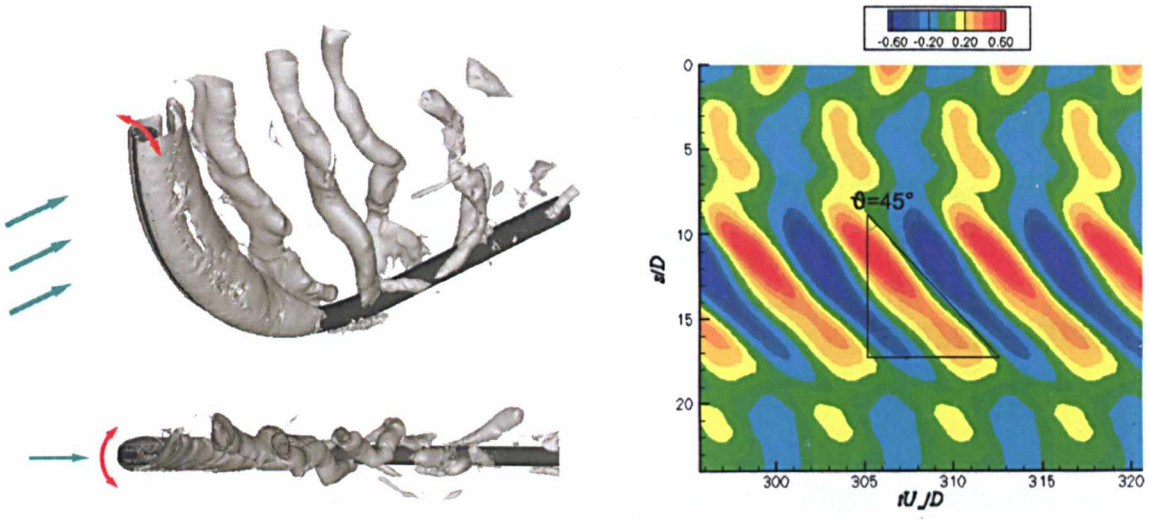


Figure 5.41: Forced rotation at $f_o = 0.9f_s$. *Left*: Wake topology for the flow past the convex configuration, isosurfaces at $\lambda_2 = -0.1$ and $\frac{tU_\infty}{D} = 302$. *Right*: Time evolution of the integrated lift coefficient along the cylinder's span.

for a fixed input frequency in each of the simulations. The oscillation amplitudes corresponding to the part of the cylinder undergoing a positive energy transfer are highlighted in red; similarly, the amplitudes corresponding to the regions where the structure is damped by the fluid are marked in blue.

The next section will present an overview of the wake dynamics and of the physical features related to this kind of motion. A quantitative analysis of the results will be provided in section 5.44, together with a comparison with the uniform translation motion.

5.3.1 Wake topology at $f_o = 0.9f_s$

As shown in figure 5.40, the input frequency at which the largest portion of the cylinder is excited by the flow is $f_o = 0.9f_s$ (corresponding to $f_s = 1.11f_o$ in the notation used in the plot).

The wake topology is presented in figure 5.41, together with the time evolution of the lift coefficient on the cylinder's surface. The $\lambda_2 = -0.1$ isosurfaces show that

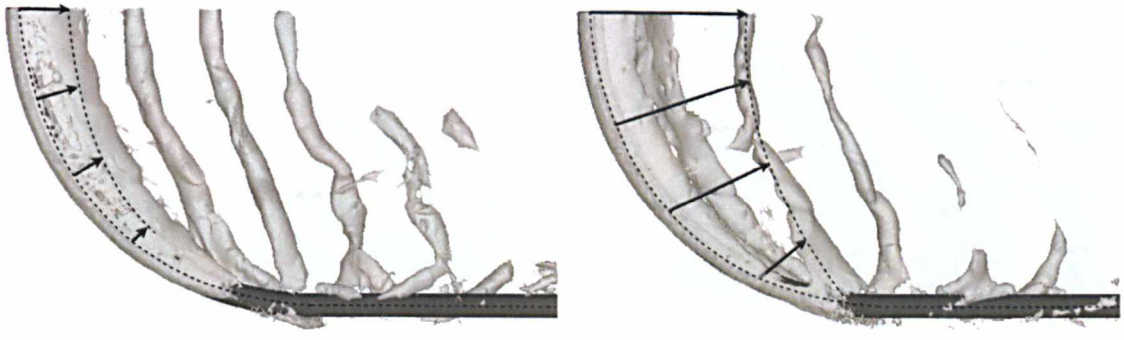


Figure 5.42: Forced rotation at $f_o = 0.9f_s$, isosurfaces at $\lambda_2 = -0.1$. *Left*: detachment at $s/D \approx 12$, $\frac{tU_\infty}{D} = 302$. *Right*: detachment at $s/D \approx 17$, $\frac{tU_\infty}{D} = 307.5$.

the shed cores twist around their axes and exhibit significant spanwise waviness. In contrast to the translational motion previously considered, the main vortex is weaker and does not envelop the horizontal extension, which is now fixed. The cores are only slightly bent according to the cylinder's curvature and detach from the main vortex at different spanwise locations for every time instant: the imposed rotation leads to out of phase shedding and thus to the non-uniform spanwise distribution of the sectional lift coefficient illustrated in figure 5.41 (*right*). The phase shift in the lift force takes place in the lower half of the body, for $8 < s/D < 18.5$, corresponding to inclination angles $41° < \theta < 85°$. However, this mechanism does not occur gradually like in the steady case or in the uniform translation motion (i.e. figure 5.1). In uniform translation, the curved line given by the phase model in equation (5.1) is based on the cylinder's curvature and is consistent with the morphology of the main vortex core, which is bent according to the geometry's shape and detaches from the body at the same time along the whole span. In rotation, the detachment occurs at the same time only in the top region; as s/D increases, the separation point shifts down along the span during one cycle, moving from $s/D \approx 10$ to $s/D \approx 18.5$, as displayed in figure 5.42. This mechanism gives rise to a constant phase shift in this range of non-dimensional arc-lengths: figure 5.41 shows that the lift coefficient isocontours have a constant inclination angle $\theta = 45°$ over the region of the cylinder

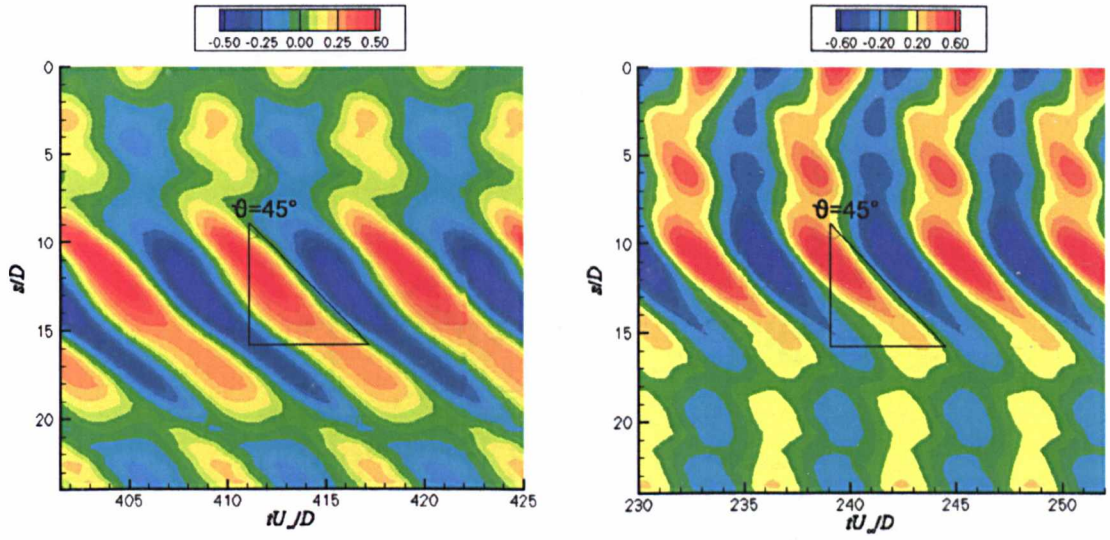


Figure 5.43: Forced rotation at two different imposed frequencies, sectional lift coefficient isocontours. *Left*: $f_o = 0.8f_s$. *Right*: $f_o = f_s$.

where the detaching point is moving.

5.3.2 Phase angle variation and energy transfer

As shown in section 5.3.1, the imposed rotation significantly influences the vortex shedding timing and the morphology of the cores. The variation of the imposed oscillation frequency f_o has highlighted that the value $\theta = 45°$ for the spanwise location of the phase shift is an intrinsic feature of the vortex shedding in this type of motion for input frequencies $f_o \leq f_s$. Figure 5.43 illustrates two examples of the lift coefficient distribution for input frequencies $f_o = 0.8f_s$ and $f_o = f_s$. In both cases θ has a value of 45°, although the spanwise location for the phase shift changes with the input frequency: at $f_o = 0.8f_s$ it corresponds to the region $9 < s/D < 19.6$, while at $f_o = f_s$ its extension shrinks to $9 < s/D < 16$ approximately. This is illustrated in figure 5.44, which shows the effect of the oscillation frequency variation on the phase angle ϕ between the lift and the displacement: for $s/D > 9$ and imposed frequencies $0.7f_s \leq f_o \leq f_s$, ϕ decreases monotonically with a constant slope and the curves are parallel.

At the same time, the shedding at the top becomes stronger and more correlated as the input frequency increases: the distribution of the maximum total lift in each section is displayed in figure 5.45 and shows that the location of the largest CL moves from the bottom to the top of the body as the input frequency is increased to values

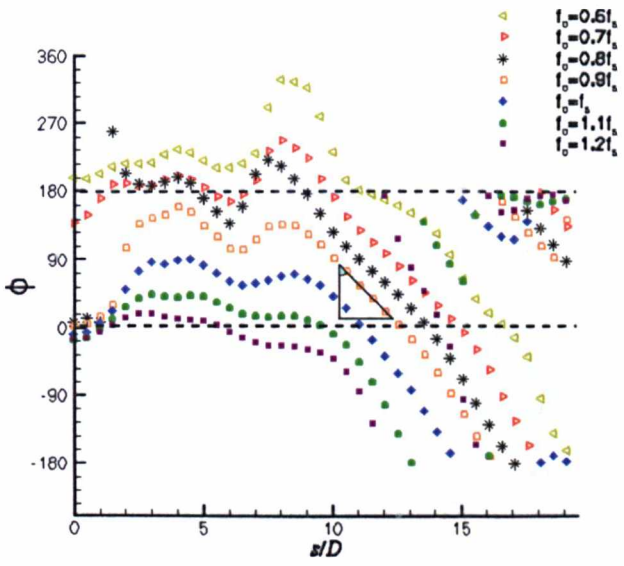


Figure 5.44: Effect of the oscillation frequency variation on the phase angle ϕ between lift force and displacement (forced rotation with fixed top amplitude $A/D = 0.5$).

larger than the Strouhal one. The case at $f_o = 0.9f_s$ exhibits $CL_{max,bottom} = 0.7$ at $s/D = 11$ and $CL_{max,top} = 0.32$ at $s/D = 0$, with a difference $\Delta CL_{max} = CL_{max,bottom} - CL_{max,top} = 0.38$. However, when the oscillation frequency is increased to $1.2f_s$, $CL_{max,top} = 0.61$ is achieved at $s/D = 6$, while $CL_{max,bottom} = 0.16$ occurs at $s/D = 13.6$. The total difference in this case is thus $\Delta CL_{max} = CL_{max,top} - CL_{max,bottom} = 0.45$.

The case at $f_o = f_s$ is a transition between the two states, without significant changes in the magnitude of CL along the geometry's span: the maximum value in the bottom region is equal to 0.36 (at $s/D > 10.6$), while in the top region it reaches a value of 0.23 (at $s/D = 6$), with a $\Delta CL_{max} = 0.13$ between the upper and the lower half of the geometry.

A measure of the energy transfer magnitude along the span of the body is given by the product of the part of the sectional lift coefficient in phase with the velocity and the distance of the relevant section from the axis of rotation. The resulting variable is the moment of the lift coefficient in the $i-$th section and can be written as:

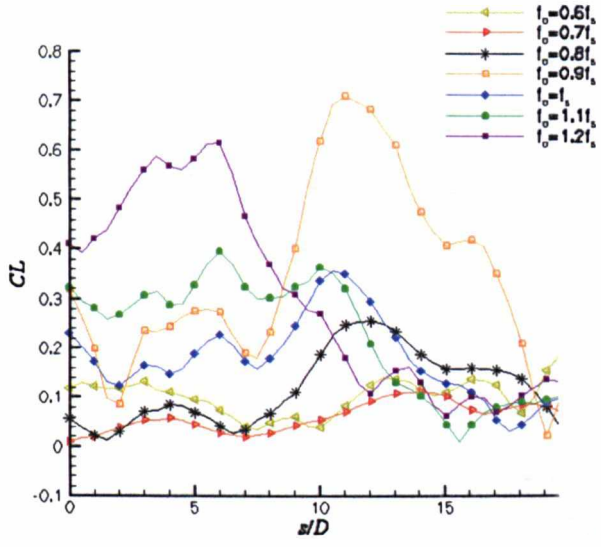


Figure 5.45: Effect of the oscillation frequency variation on maximum CL (forced rotation with fixed top amplitude $A/D = 0.5$).

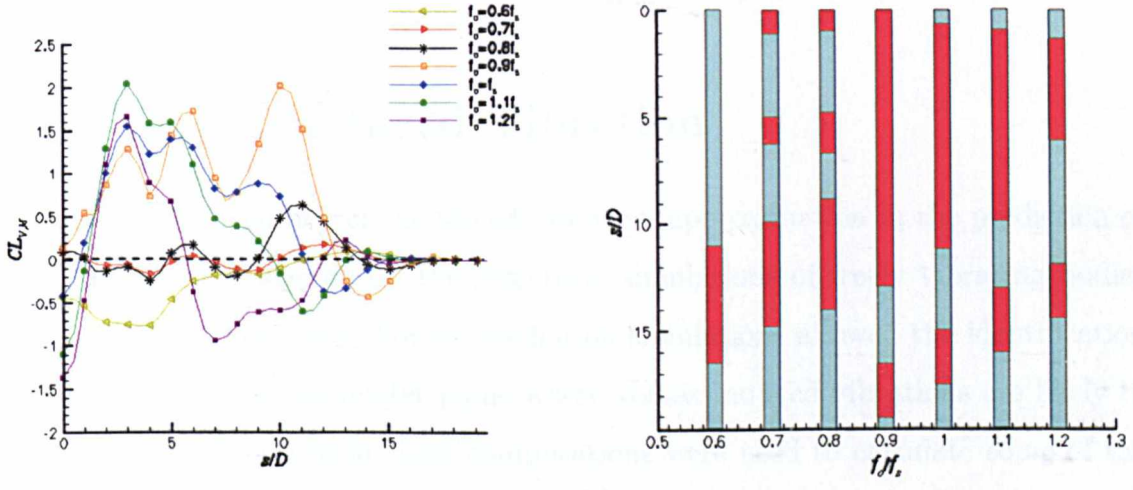


Figure 5.46: *Left*: moment of the lift coefficient in phase with the velocity. *Right*: spanwise location (and corresponding amplitude of oscillation) of the excitation (red) and damping (blue) regions for all the frequencies tested.

$$CL_{VM_i} = CL_{v,i}(z_i - z_{cr}) \tag{5.8}$$

where $(z_i - z_{cr})$ is the vertical distance between the centre of rotation and the centre of the $i-$th section along the span where CL_v is measured. Figure 5.46 shows

the behaviour of CL_{VM} for all the input frequencies tested: the regions along the cylinder's span that are excited or damped by the flow are highlighted in red and blue respectively. At low frequencies, only the sections oscillating with amplitudes $0.07 \leq A/D \leq 0.25$ are effectively excited by the vortex shedding forces, while the rest of the body is damped; this is consistent with the observation that in uniform cross-flow translation the cases with $f_o = 0.7f_s$ and $A/D = 0.1$ and 0.25 exhibits a positive maximum CL_v in the middle/lower region of the quarter ring, corresponding to the excitation region marked in red in figure 5.46 (*right*) at the same input frequency in forced rotation.

As f/f_s increases, the excitation region expands and includes sections vibrating at much higher amplitudes: at $f_o = 0.9f_s$ it reaches its maximum extent ($0 \leq s/D \leq 12.9$ corresponding to oscillation amplitudes $0.07 \leq A/D \leq 0.5$). After this point, a further increase in the imposed frequency leads to a gradual decrease in the area of the excitation region, which also shifts towards the top of the body.

5.4 Vortex-Induced Vibration

To validate the accuracy of the forced vibration approximation in the prediction of the fluid dynamic loading on the structure, simulations of freely vibrating bodies have also been performed. Forced oscillation simulations allowed the identification of the regions in the parameter plane where vortex-induced vibrations are likely to occur: the input data from these computations were used to calculate some of the parameters that govern vortex-induced vibrations.

The forced purely sinusoidal oscillations were able to reproduce the different wake structures observed for a freely vibrating cylinder. However, as highlighted by several previous investigations (see section 2.3.6), the lack of a complete understanding of the non-linear relationship between the structural parameters and the frequency and amplitude of oscillation poses caveats to the use of forced vibration to approximate VIV: in fact, when the cylinder is free to move and respond to the hydrodynamic forces, the resulting amplitude and frequency may correspond to regions of the parameter plane where the energy transfer in forced vibration is negative and vice

versa. Therefore, the purpose of the next section is to compare the results obtained in free vibration to the flow states where a positive energy transfer was found to occur in forced vibration. Given the high computational cost of these simulations, it has not been possible to obtain a complete response plot for the free vibration cases and thus it is not intended to establish to what extent forced vibration tests can be used in VIV prediction.

Selected cases with reduced velocity and spring and damping constants matching the forced vibration parameters will be presented in this section, together with the reference case at zero structural damping. In all the simulation presented the mass ratio was chosen equal to 3, a plausible value for vortex-induced vibration in water.

5.4.1 Free vibration simulations

5.4.1.1 Free translation in the cross-flow direction

Forced vibration simulations of uniform translation in the cross-flow direction showed that the excitation region in the parameter plane of figure 5.5 was significantly reduced compared to the one in the straight cylinder case and limited to very low amplitudes of oscillation. This was due to the strong component of hydrodynamic damping generated by the part of the body aligned with the inflow direction and could be considered as an intrinsic feature of this type of curvature.

As expected from these considerations, when the convex body is free to respond to the fluid forces, the resulting amplitude of motion is very small. Figure 5.47 shows the cross-flow displacement in the case with structural damping $\zeta = 0.012$, mass ratio $m^* = 3$ and reduced velocity is $V_r = 6.77$, which corresponds to a natural frequency $f_n \approx 0.9 f_s$. The maximum amplitude A/D for this value of structural damping is very low and the frequency of oscillation is $f_o = 0.94 f_s$. This flow configuration can be compared to the fixed cylinder wake illustrated in figure 5.1: the wake topology shown in figure 5.48 (*left*) exhibits straight cores and a gradual phase shift takes place along the spanwise direction, as illustrated by the lift coefficient time evolution in figure 5.48 (*right*). No significant vorticity is generated in the horizontal extension.

In the case with $\zeta = 0$, $m^* = 3$ and $V_r = 6.77$ the response of the cylinder takes

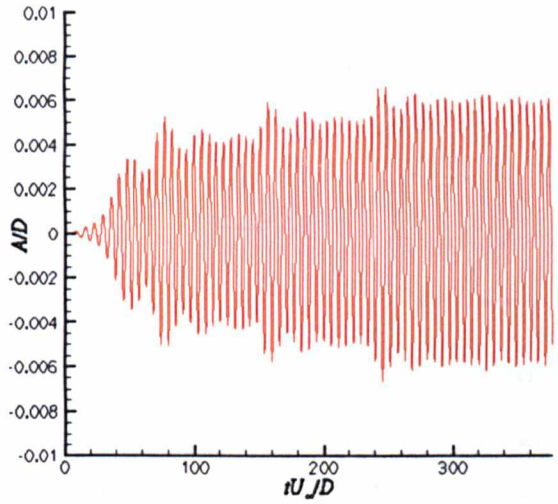


Figure 5.47: Maximum amplitude of the cross-flow vibration of the convex body with $V_r = 6.77$, $m^* = 3$ and $\zeta = 0.012$.

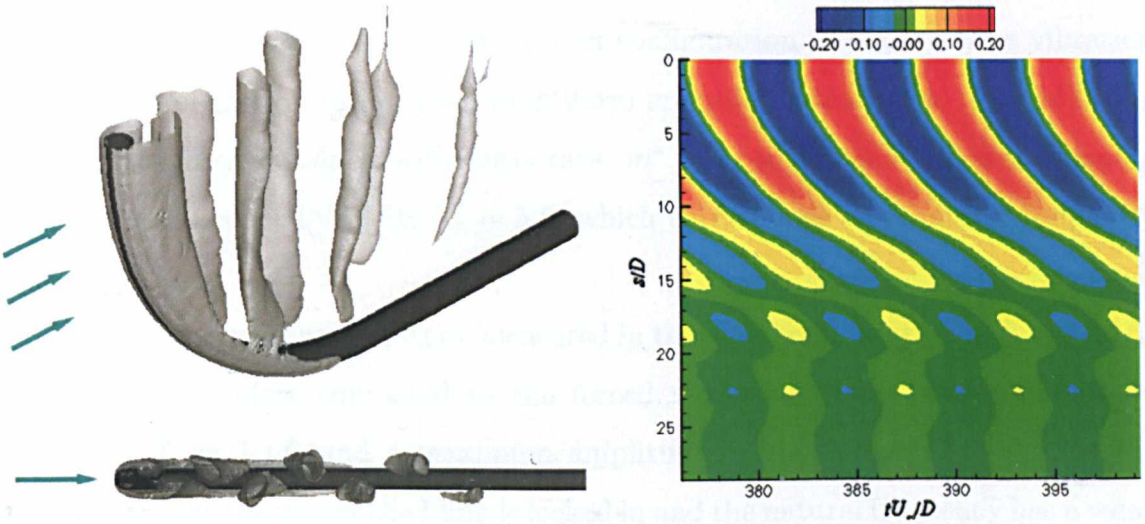


Figure 5.48: Free vibration with $V_r = 6.77$, $m^* = 3$ and $\zeta = 0.012$. *Left*: Wake topology, isosurfaces at $\lambda_2 = -0.1$. *Right*: Time evolution of the integrated lift coefficient along the cylinder's span.

the form illustrated in figure 5.49. The maximum amplitude is slightly increased and the displacement history in time exhibits low frequency modulations that are typically found in the lower branch in the straight cylinder case.

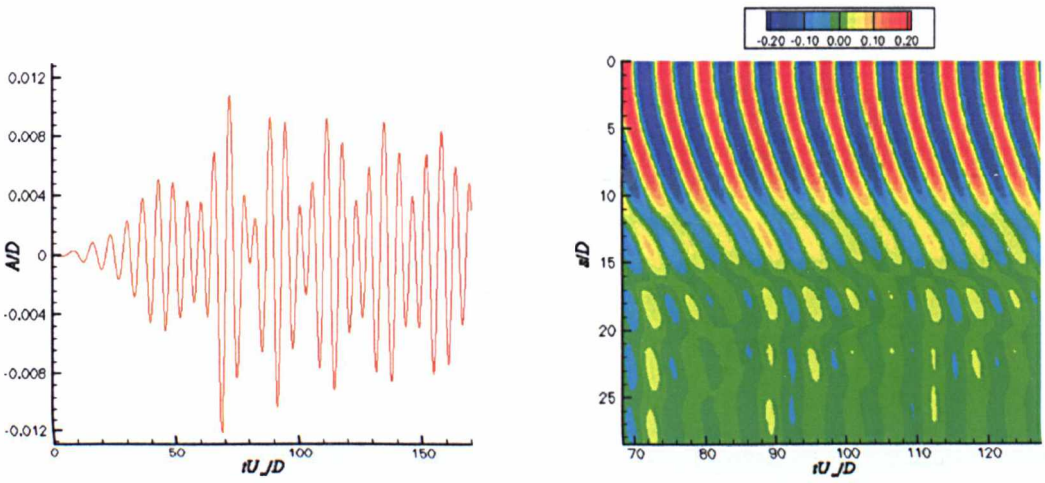
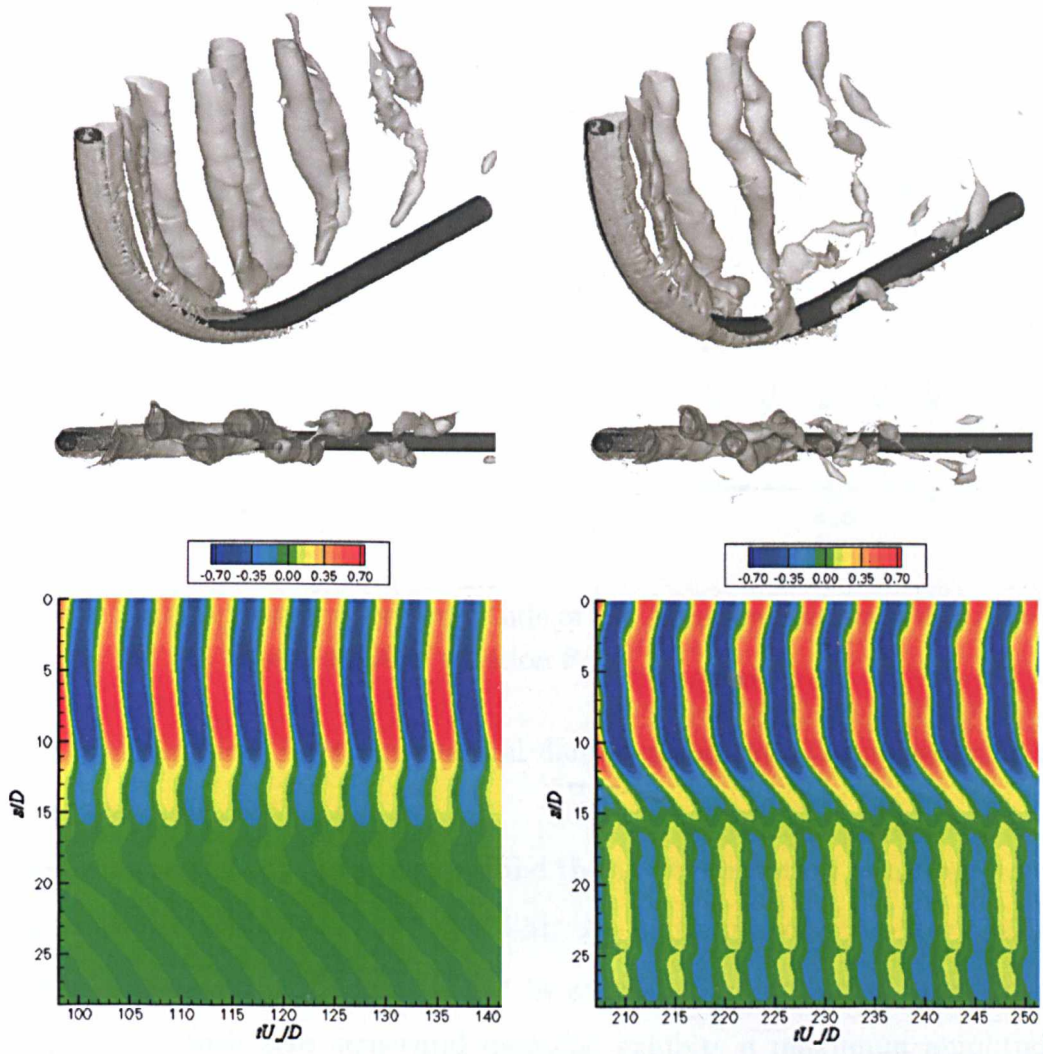


Figure 5.49: Maximum amplitude of the cross-flow vibration with $V_r = 6.77$, $m^* = 3$ and $\zeta = 0.0$.

5.4.1.2 Free rotation in the cross-flow direction

Forced vibration simulations of the uniform rotation about the horizontal extension showed that it is more likely for the convex configuration to undergo free vibration in this type of motion rather than in uniform cross-flow translation. The following results have been obtained with mass ratio $m^* = 3$, torsional structural damping $\zeta_T = 0.1$ and reduced velocity $V_r = 5.5$, which corresponds to a natural frequency $f_n \approx 1.1 f_s$.

The vortex shedding frequency measured in this flow configuration is $f_o = 1.14 f_s$; this case is therefore compared to the forced vibration results with an imposed frequency $f_o = 1.1 f_s$ and a maximum amplitude at the top $A/D = 0.5$, in the hypothesis that the vortex shedding is locked in and the natural frequency has a value similar to the shedding frequency. The wake topology and the sectional lift coefficient evolution in time are shown in figure 5.50: the forced vibration simulation could correctly reproduce the range of values for the sectional lift coefficient ($[-0.92; 0.92]$ in free rotation, $[-0.84; 0.87]$ in forced rotation) and its spanwise distribution in the region $0 < s/D < 15$. The λ_2 isosurfaces show that in the forced vibration case the cores twist along the spanwise direction and exhibit an elliptical instability; this waviness of the main vortex is absent in the results from free vibration. Further, the separation of the shed vortex from the shear layer occurs at a much lower spanwise



FREE VIBRATION FORCED VIBRATION

Figure 5.50: Wake topology isosurfaces at $\lambda_2 = -0.1$ and sectional lift coefficient distribution. *Left*: free rotation at $V_r = 5.5$ and $\zeta_T = 0.1$. *Right*: forced rotation at $f_o = 1.1 f_s$ and $A/D = 0.5$.

position in forced motion: the bottom end of the secondary core is still attached to the shear layer at a position close to the junction with the horizontal extension when the main vortex is about to be shed. This delay in the separation is responsible for the slanted distribution of the lift coefficient isocontours in the forced vibration results over the region $11 < s/D < 15$, which does not take place in free vibration. This behaviour is reflected in the constant slope in the spanwise distribution of the phase angle ϕ, shown in figure 5.52 and discussed in section 5.44: in free vibration the net energy transfer must be positive (from fluid to structure) in order to overcome

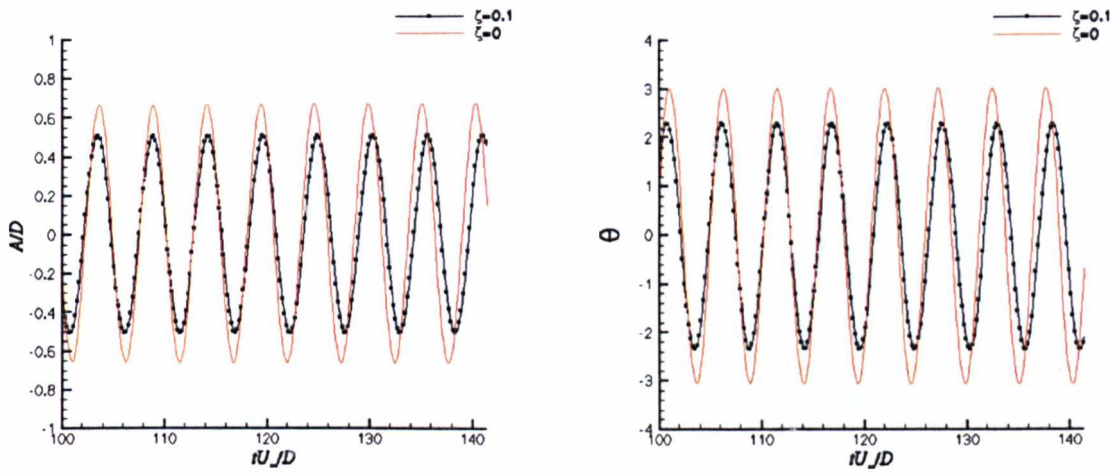


Figure 5.51: *Left*: maximum amplitude of the transverse rotation at $s/D = 0$. *Right*: angle of rotation θ.

the energy dissipation due to mechanical damping and thus the phase angle must lie in the region $[0°, 180°]$.

The displacement of the top section and the angle of rotation measured from the axis of rotation are displayed in figure 5.51. An amplitude of cross-flow oscillation at $s/D = 0$ equal to $0.5D$ corresponds to an angle of rotation of approximately 2.3°. The case with zero structural damping exhibits a maximum amplitude of oscillation equal to $0.67D$. To obtain the same amplitude of the forced vibration simulation at $f_o = 1.1f_s$, a structural damping $\zeta_T = 0.1$ has to be added to the system: the corresponding black dotted line in figure 5.51 (*left*) reaches in fact a maximum amplitude $0.51D$.

Figure 5.52 shows the effect of the structural damping on the phase angle and total lift coefficient. The phase angle in free rotation is close to 0° and a maximum discrepancy of 20.35° between free and forced vibration simulations is obtained in the range $0 < s/D < 10$. In the lower half of the quarter ring, $s/D > 10$, the phase angle in the two cases diverges significantly: this is due to the different shedding mechanism highlighted in figure 5.50 and to the shift of the separation point along the span discussed in section 5.3.1 for the forced vibration simulations. Finally we note that in the system with zero damping the density of energy is lower than

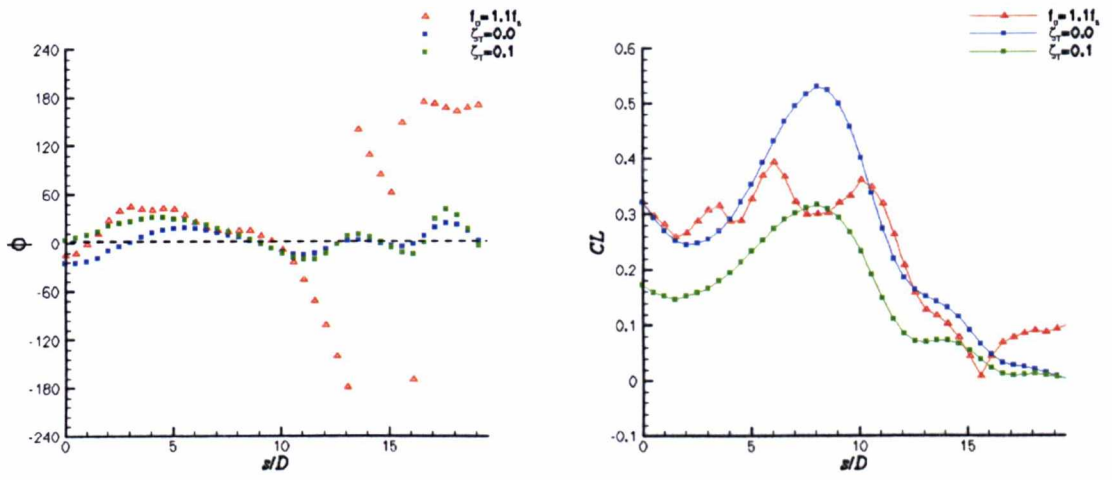


Figure 5.52: Spanwise variation of phase angle ϕ and total lift coefficient CL in forced rotation with ($f_o = 1.1f_s$; $A/D = 0.5$) and in free rotation with $\zeta_T = 0.1$ and $\zeta_T = 0$ (both at $V_r = 5.5$).

in the damped one as no structural dissipation has to be overcome in order to generate VIV. The total lift coefficient in free vibration with $\zeta_T = 0.1$ exhibits a considerable deviation from the one obtained in forced vibration; however, a similar magnitude could be reproduced in the undamped free motion case, although the spanwise location of the maximum value for CL is shifted down the span and occurs at $s/D = 8.1$ instead of $s/D = 6$.

Chapter 6

Concave configuration

6.1 Background studies: fixed cylinder in uniform flow

6.1.1 Vortex shedding suppression

This section presents some fundamental studies on the vortex dynamics past the stationary concave configuration carried out by Miliou (2004) and Miliou *et al.* (2007). When the concave configuration is exposed to an uniform inflow at $Re = 100$, the wake topology is markedly different than the one past the convex cylinder, as shown in figure 6.1: the most striking features are the absence of interaction between the two shear layers and the subsequent suppression of vortex shedding. The fluid-dynamic loading on the structure is thus significantly different in the two configurations: in the concave one the forces are steady, with a drag reduction of 12% compared to the opposite configuration, which exhibits vortex shedding. The completely different wake features observed for the convex and concave geometries can be related to the strong velocity component generated by the shape of the stagnation face and thus aligned to the cylinder's axis: its curvature deflects part of the approaching flow towards the top of the body (in the concave case) or the bottom (in the convex case). In analogy with the study conducted by Darekar & Sherwin (2001b,a) on vortex shedding past a wavy geometry (see 2.6.2), Miliou *et al.* (2007)

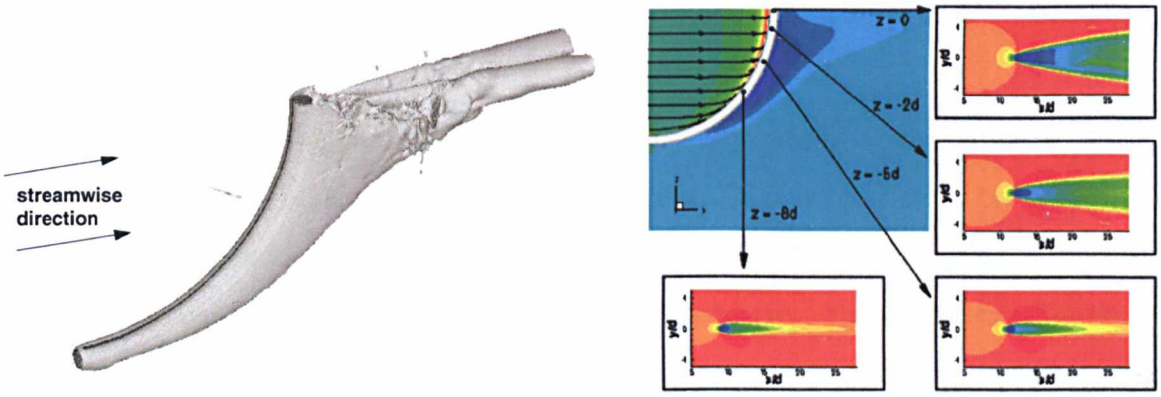


Figure 6.1: *Left*: concave configuration at $Re = 100$, $\lambda_2 = -0.01$. *Right*: streamwise velocity in the wake and pressure distribution along the span.

found that the axial flow generation can be associated with a redistribution of the spanwise vorticity along the span and with the presence of streamwise vorticity and vertical velocity. This additional vorticity component is believed to have a direct influence on the wake width, by pulling the shear layers apart and preventing them from interacting and forming vortical structures.

Figure 6.1 (*right*) shows the variation in the wake width at different spanwise locations: at $z = 0$ the wake is significantly wider than at lower positions. If we consider the concave configuration as an extreme case of the wavy cylinders investigated by Darekar and Sherwin, the top of the concave configuration would correspond to the 'geometrical minimum of the wavy cylinder', defined as the most downstream point, which indeed exhibits the wider wake. Similar to the present case, in the case of wavy cylinders the width of the wake decreases from the valley to the peak. Although the peak-to-peak height and the wavelength of the curved model lies outside the parameter space investigated by Darekar and Sherwin, an interesting comparison between the wake topology past the concave configuration and the one observed in Regime III type A can be drawn. The vortex shedding is absent also when the Reynolds number is increased up to 500, although the forces are not completely steady as in the low Reynolds number case.

6.1.2 Vortex shedding resumption and weak form of shedding

As outlined in section 3.1.2, a symmetry boundary condition is imposed on the top computational plane. To investigate the effect of this restriction on the vortex shedding suppression, a 6−diameter long vertical extension was added to the top of the concave configuration: in this modified geometry, the symmetry boundary condition is specified on a plane that has no intersection with the quarter ring, allowing to assess the effect of the axial flow on the classical mechanism of vortex formation in the wake of a nominally two-dimensional body.

The results demonstrate that the curved part influences the vertical extension and weakens the two-dimensional shedding expected for a straight circular cylinder at Re=100: the steady wake found for the concave configuration is not destabilised by the straight part and the wake at the end of the curved part (top of the quarter ring) appears narrow and nearly symmetric. Although periodic fluctuations in the lift coefficient are observed at the top of the vertical extension, their amplitude and frequency is considerably smaller than the values found for the convex configuration at the same Reynolds number, resulting in a 'weak' form of shedding where the vortex structures away from the body re-connect in loops (figure 6.2). In this case, the formation length is considerably longer and the vortex cores do not fully detach from the shear layers: the growing vortex is not sufficiently strong to fully draw the opposite shear layer across the wake and shed as would be expected in a regular von Kármán street. A similar wake was observed past the wavy cylinder studied by Darekar & Sherwin (2001c), where the spanwise vortex structures were found to re-orientate due to the streamwise vorticity in what they defined as regime IIA (which exhibited a milder geometrical disturbance compared to regime IIIA).

When the Reynolds number is increased from 100 to 500, rather than observing a stronger two-dimensional shedding past the vertical extension, the weak vortex shedding primarily occurs at the junction between the curved cylinder and the straight vertical extension. The magnitude of the streamwise vorticity generated in the shear layers is larger than at the value measured for $Re = 100$ and the vertical velocity

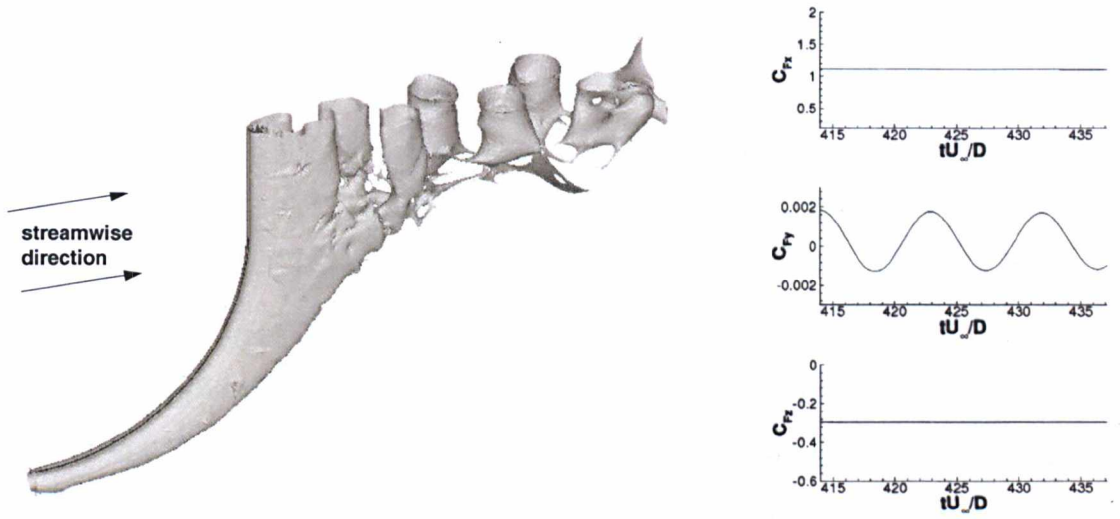


Figure 6.2: Concave configuration with a 6−diameter vertical extension at $Re = 100$, $\lambda_2 = -0.01$ (left); time distribution of the integrated force coefficients at $P = 6$ (right).

component in the wake reaches the same order of magnitude of the free-stream. It is suggested that shedding at the top of the vertical extension is weakened by the re-orientation of a significant portion of the axial flow at the rear of the body into the free-stream direction, as a result of the upper symmetry boundary condition: this process shows similarities to a base bleed mechanism and is also consistent with the longer formation length observed in this region of the cylinder (see Bearman (1967a)). However, it is postulated that a longer vertical extension would displace the numerical boundary condition further away from the top of the curved cylinder, allowing regular shedding to resume in the two-dimensional part.

6.2 A note on the two dimensional sectional approach

Given the nature of the sectional code, whereby the flow analysis is conducted in two-dimensional planes linked via a structural model, the fluid solver does not take into account the orientation of the curvature. From a fluid-dynamic point of view, there is no distinction between convex and concave configuration, since a two-dimensional

section does not provide any information on the type of curvature of the whole body.

A sectional argument based on strip theory would therefore predict the same hydrodynamic force distribution for both configurations, in contradiction with the outcome of the fully three-dimensional analysis, which has highlighted the key role played by the axial flow in the vortex shedding suppression. Consequently, the suppression mechanism found for the stationary concave configuration could not be reproduced by the two-dimensional simulations: this is an intrinsic limitation of the sectional approach and poses a severe restriction on its application to the analysis of steady configurations.

6.3 Forced cross-flow vibration

A parametric study of the flow states past the concave configuration in forced vibration will be presented in this section. As for the convex configuration, the reference frame for this investigation is the map obtained by Willden *et al.* (2008) for a two-dimensional circular cylinder at the same Reynolds number, $Re = 100$, and displayed in figure 6.3.

The next sections present a description of the shedding regimes observed in the near wake for different pairs of oscillation frequencies and amplitudes. First, each type of vortex shedding will be outlined in sections 6.3.1.1 and 6.3.1.2, followed by an example of vortex shedding outside the two-dimensional lock-in region presented in section 6.3.1.3, which will also discuss the process that leads to vortex shedding in the concave configuration as opposed to the one observed past the convex geometry with the same input parameters. Section 6.3.2 briefly summarises the results and discusses the most important features arising from this geometrical configuration. The phase angle distribution and the energy transfer mechanism for the different regions of the parameter space are illustrated in section 6.3.3, while free vibration simulations with different combination of structural damping and reduced velocity are presented in section 6.4.

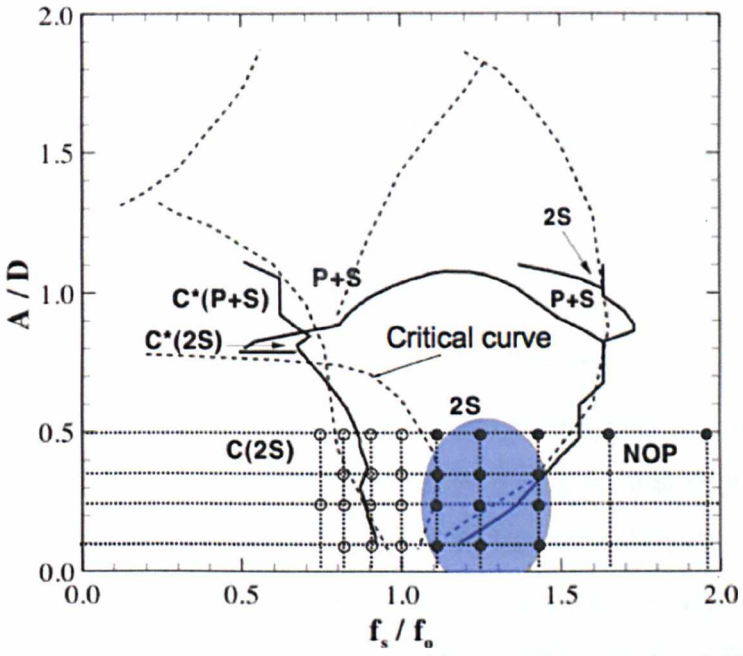


Figure 6.3: Flow states for the concave configuration in forced cross-flow vibration, overlaid on the Willden *et al.* (2008) map obtained with two-dimensional simulations at the same Reynolds number ($Re = 100$).

6.3.1 Lock-in boundaries and flow regimes

Similar to the convex configuration, the concave body exhibits a 2S mode of shedding throughout the parameter space considered. However, although two oppositely-signed vortices are shed per cycle, the resulting wake topology is considerably dissimilar from the 2S mode observed in two-dimensional simulations of forced motion with the same input parameters. The circles in figure 6.3 refer to different sub-regimes of the 2S shedding mode: the grey circles correspond to a shedding with a narrow wake, while the hollow circles indicate a wide wake state that, in some cases, exhibits a secondary core between the two shear layers and can therefore be assimilated to a very weak form of P+S shedding. In this geometry, the critical curve originally found by Williamson & Roshko (1988) in their forced vibration experiment separates the two wake states, with a threshold value for the input frequency $f_o \approx f_s$. All the flow configurations examined represent locked-in states, with only one dominant frequency for the whole structure. In the concave geometry, the lock-in region

encompasses the one for the two-dimensional cylinder on both sides, resulting in a significantly more extended area. This is an important effect of the curvature's orientation and introduces a key point that will be further discussed in section 6.3.2.

The shadowed area where a positive energy transfer from the fluid to the structure takes place is considerably larger than the one observed in the convex configuration, where the resulting excitation region was considerably reduced and limited to very low amplitudes of vibration: in the concave case the flow excitation is achieved at oscillation frequencies lower than the Strouhal value and at amplitudes up to $0.5D$, which is also the highest value tested. This region is thus shifted towards the right-hand side of the critical curve of figure 6.3. In particular, the highest density of energy occurs at oscillation amplitudes in the range $0.1 < A/D < 0.35D$ and increases with increasing oscillation frequencies, peaking at $f_o = 0.9f_s$: when the frequency ratio reaches unity, the density of energy drops drastically. This supports the hypothesis that the shedding mechanism changes for imposed frequencies above and below the Strouhal value, giving rise to different sub-regimes of the 2S type of shedding.

6.3.1.1 2S shedding with wide wake

In figure 6.4 (*left*) the vortices in the wake of the concave body with $A/D = 0.5$ and $f_o = 1.1f_s$ are visualised through λ_2 isosurfaces. As the free-stream velocity is now directed towards the inside of the curved cylinder and no horizontal extension is added to this geometry, the cores do not interact with the structure when they are convected downstream; however, similar to the wake dynamics observed in the convex configuration, they are bent according to the curvature of the leading edge and the shedding is in-phase along the whole length of the body. This is illustrated in figure 6.4 (*right*), which displays the lift coefficient distribution along the spanwise direction and its evolution in time: in a similar way to the force dynamics in the convex configuration, the lift coefficient isocontours at a fixed instant do not change sign along the span of the body and no switching in time is observed. The magnitude of the lift coefficient in this configuration ranges from -2.11 to +2.09 and is thus 22% higher than in the convex case with the same input parameters.

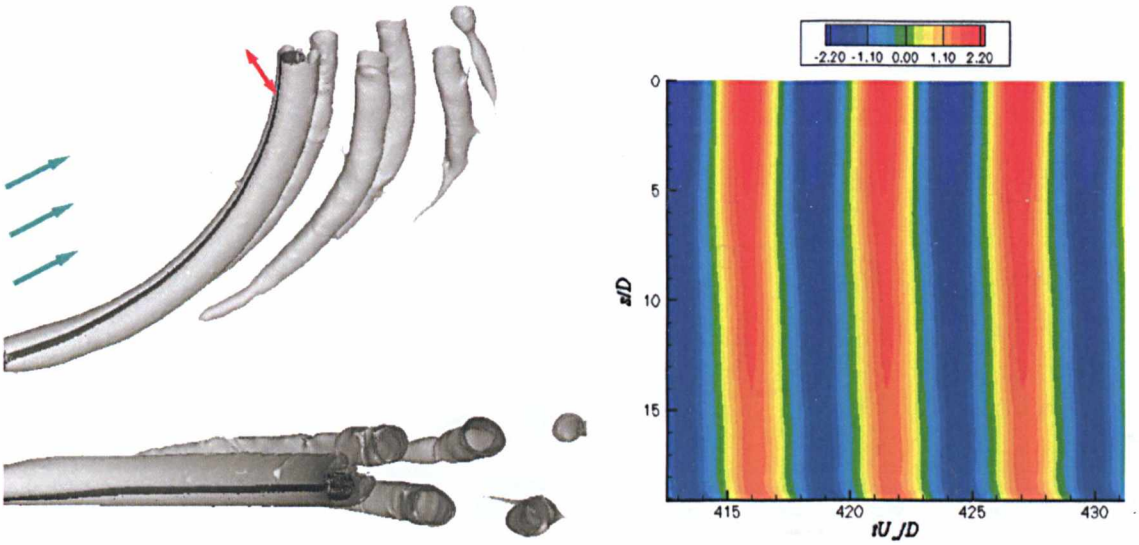


Figure 6.4: *Left*: wake topology past the concave configuration at $f_o = 1.1f_s$, $A/D = 0.5$ (wide wake 2S regime); isosurfaces at $\lambda_2 = -0.1$. *Right*: Time evolution of the sectional lift coefficient along the spanwise direction.



Figure 6.5: Forced translation of the concave body at $f_o = 1.1f_s$, $A/D = 0.5$: $\lambda_2 = -0.1$ isosurfaces overlaid on spanwise vorticity isocontours; the secondary core is visible between the two shear layers.

The near-wake topology also appears completely different from the one obtained in the convex configuration. Figure 6.5 shows that the shear layers are more contracted in the concave case: this is consistent with the higher forces generated on the body's surface. As we shall see in section 6.3.2, the shedding at these higher

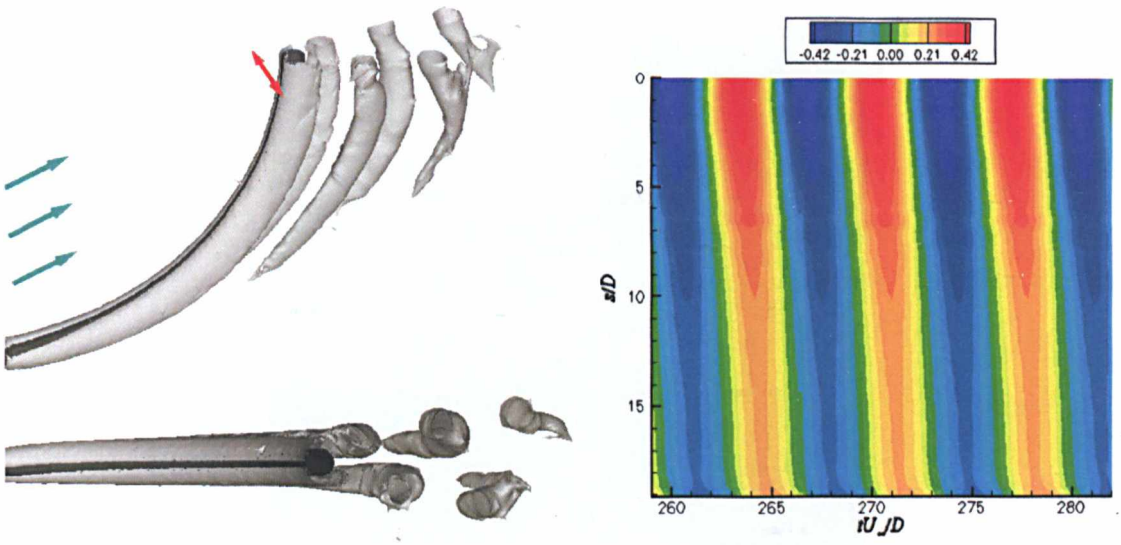


Figure 6.6: *Left*: wake topology past the concave configuration at $f_o = 1.1f_s$, $A/D = 0.1$ (wide wake 2S regime); isosurfaces at $\lambda_2 = -0.07$. *Right*: Time evolution of the sectional lift coefficient along the spanwise direction.

frequencies is the only case where the lift coefficient magnitude differs significantly in the convex and in the concave configuration with identical flow conditions. Further, in this geometry both the near and far wakes are much wider than the one in the reverse configuration shown in figure 5.6 (*left*). The similarities between the near wake topology in forced vibration and the steady shear layers found in the wake of the fixed body can be explained considering that the shear layers in forced vibration do not interact in the fashion described by Gerrard (1966) and outlined in section 2.1: the shedding of vortices appears to be a result of the change of direction in the imposed trajectory that occurs quite abruptly at these higher frequencies. The secondary core between the shear layers is also related to the high frequency of oscillation: it is generated from the vorticity in the base region, which separates when the body reaches the extremes of its trajectory and inverts the direction of oscillation. During one half cycle the strength of this vortex decreases until it fades out before reforming from the opposite-signed base vorticity in the remaining half of the motion. This resembles a very weak form of P+S type of shedding, where the second vortex of the pair is not strong enough to leave the base region and be convected downstream in the near wake.

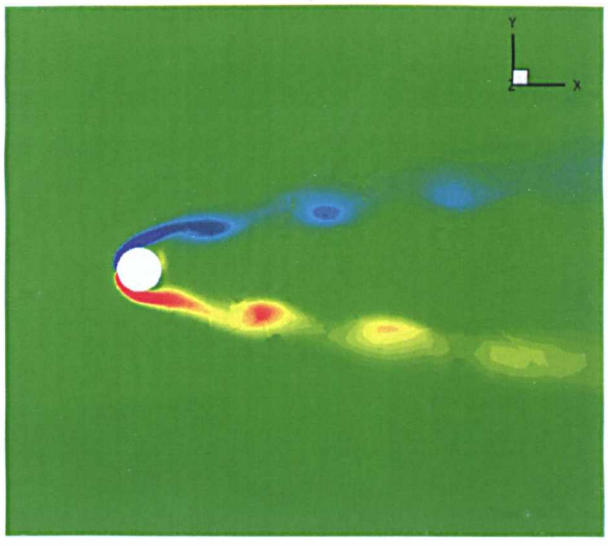


Figure 6.7: Spanwise vorticity distribution at the top of the concave body at $f_o = 1.1f_s$, $A/D = 0.1$.

This mode of shedding is absent at lower oscillation frequencies but still occurs at lower oscillation amplitudes. The case of forced vibration at $f_o = 1.1f_s$ and $A/D = 0.1$ is presented in figure 6.6 for comparison: at this lower oscillation amplitude, although the shear layers appear significantly elongated, the wake is still wide and the vortex cores are very well correlated in the spanwise direction, implying that this sub-regime of the 2S shedding is not considerably affected by changes in the imposed oscillation amplitude. A closer examination of the spanwise vorticity isocontours illustrated in figure 6.7 reveals that the shedding of the vortices is not caused by the mutual interaction of the two shear layers. Interestingly the wake topology at $f_o = 1.1f_s$ and $A/D = 0.1$ resembles more closely the steady wake found past the fixed body than the one observed at the same amplitude but lower frequency. Like in the concave case at $A/D = 0.5$, the shedding mechanism is governed by the abrupt change of direction in the trajectory and the corresponding spanwise distribution of the sectional lift coefficient also presents similarities, although its magnitude is considerably reduced in this case: in the wide wake 2S regime the lift force is higher in the top region and decreases with increasing arc-length s/D. This could be expected, since the λ_2 isosurfaces show how the vortex cores become progressively thinner as s/D reaches values in the lower half of the geometry. Therefore, in this regime it is the vortex shedding in the top sections that drives the one in the lower sections and

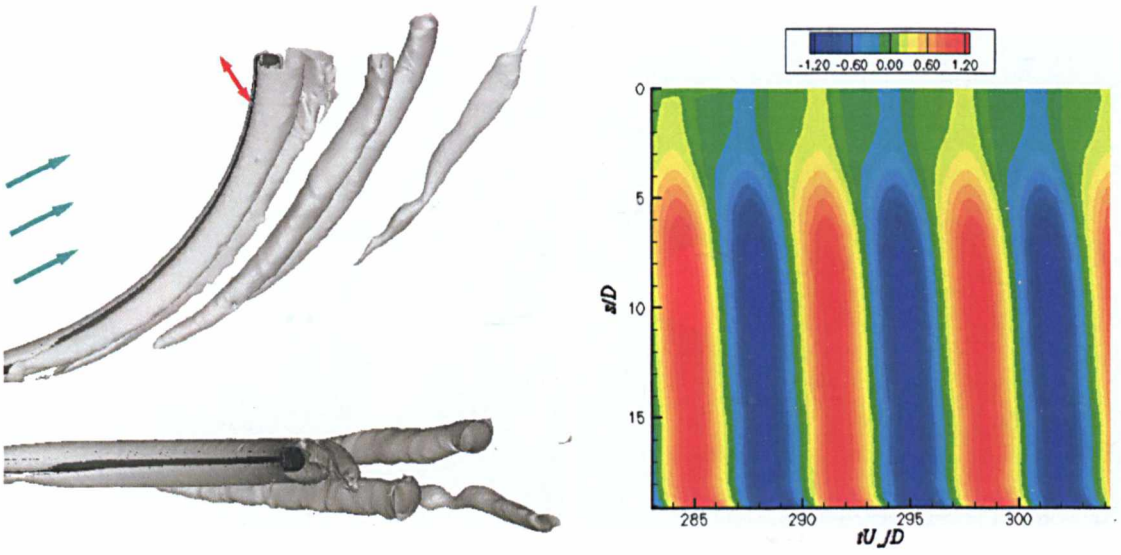


Figure 6.8: *Left*: wake topology past the concave configuration at $f_o = 0.9f_s$, $A/D = 0.5$ (narrow wake 2S regime); isosurfaces at $\lambda_2 = -0.1$. *Right*: Time evolution of the sectional lift coefficient along the spanwise direction.

not the opposite, as it is observed in the convex configuration: this can be partly explained considering that in the concave geometry the fluid/structure interaction is absent once the vortex is convected downstream, whereas in the convex case the lower part of the body interferes with the shed vortex.

6.3.1.2 2S shedding with narrow wake

When the oscillation frequency is reduced to values below the Strouhal one, the wake topology changes radically, becoming narrower and exhibiting longer shear layers in a similar fashion to the form of 2S shedding observed in the two-dimensional simulations. The wake topology for the case with $A/D = 0.5$ and $f_o = 0.9f_s$ is displayed in figure 6.8, together with the sectional lift coefficient isocontours. This plot highlights the wake width reduction and the increase in the formation length in the low oscillation frequency range. This is accompanied by a weakening in the lift forces generated by the vortex shedding in the top sections of the body; therefore, the sectional lift coefficient distribution in the spanwise direction takes the form illustrated in figure 6.8 (*right*), with a progressive reduction in the magnitude of the lift force in the top region of the body with decreasing oscillation frequency. The

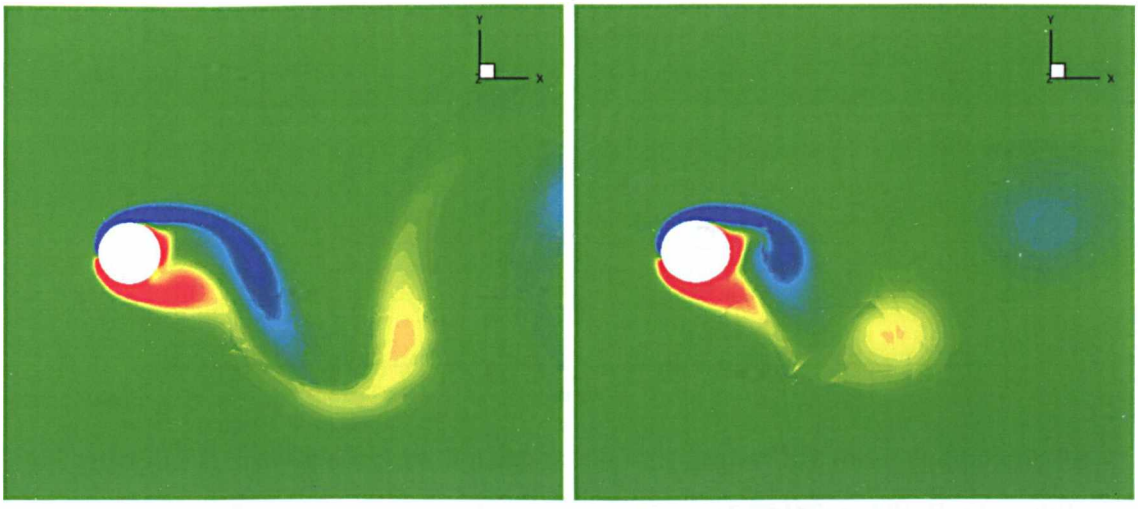


Figure 6.9: Forced translation of the concave body at $f_o = 0.9f_s$, $A/D = 0.5$: vorticity isocontours at $s/D = 0$ (*left*) and at $s/D = 7$ (*right*).

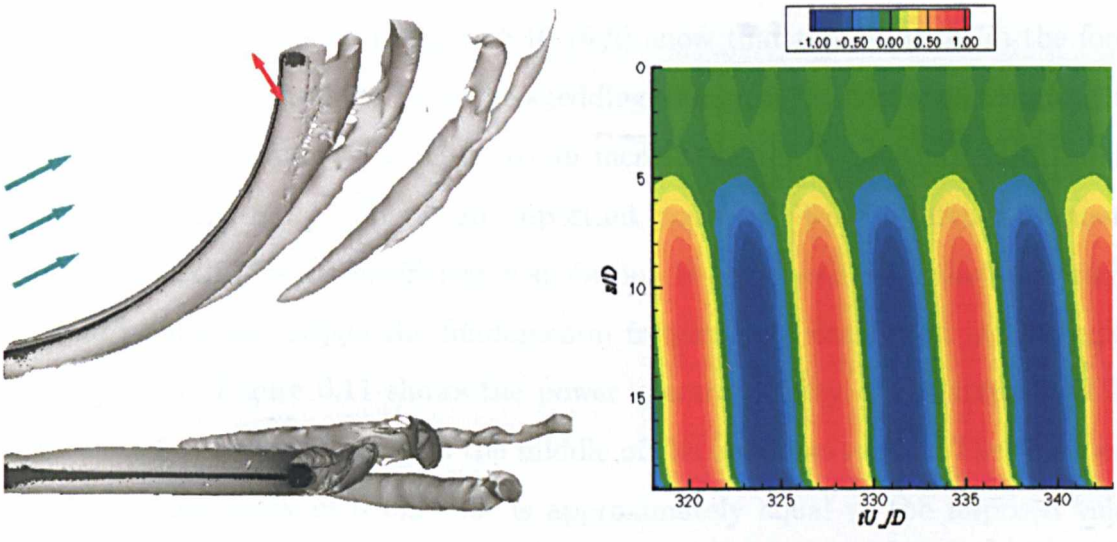


Figure 6.10: *Left*: wake topology past the concave configuration at $f_o = 0.8f_s$, $A/D = 0.5$; isosurfaces at $\lambda_2 = -0.1$. *Right*: Time evolution of the sectional lift coefficient along the spanwise direction.

formation length varies considerably along the span: the vorticity isocontours in figure 6.9 shows that at $s/D = 7$ the shear layer interaction occurs approximately at $1.5D$ downstream of the body and the wake resembles the wide wake 2S regime described in 6.3.1.1, whereas at $s/D = 0$ it takes place at $2.7D$ downstream and gives rise to the narrow wake 2S regime described above.

We note from figure 6.10 (*right*) that when the frequency is further reduced to

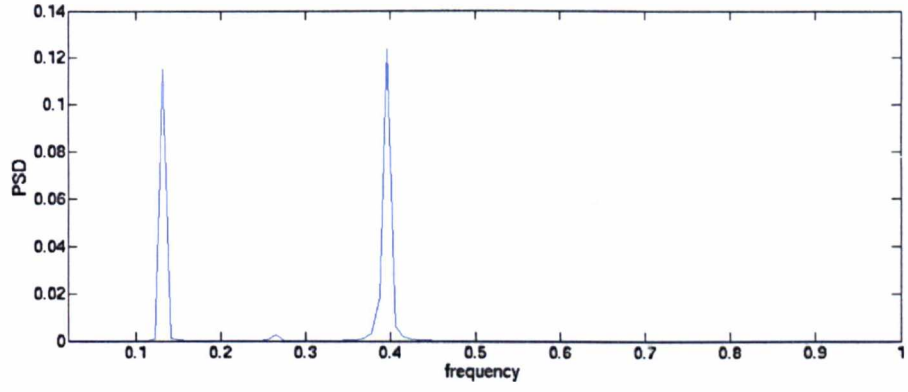


Figure 6.11: Power spectra density of the integrated lift force coefficient for the flow past the concave body at $f_o = 0.8f_s$ and $A/D = 0.5$.

$0.8f_s$ the lift coefficient distribution drops to very low values in the upper part of the ring, reaching a maximum absolute value of 0.11 in the range $0 \leq s/D \leq 5$. The $\lambda_2 = -0.1$ isosurfaces in figure 6.10 (*left*) show that this decrease in the force magnitude is related to a delay in the shedding along the span of the configuration and, like in the case at $f_o = 0.9f_s$, to an increase in the formation length in the upper part of the body. This is an important point and will be further discussed in section 6.3.2. This lift coefficient distribution is associated with the appearance of a third harmonic beside the fundamental frequency of oscillation in the region $0 < s/D < 5$. Figure 6.11 shows the power spectra density of the integrated lift coefficient at $s/D = 2.5$, hence in the middle of the low force region. The first peak occurs at a frequency of 0.132 that is approximately equal to the imposed value $f_o = 0.8f_s$; the second peak is a third harmonic and corresponds to a frequency of 0.3961. This is only present in the top part of the body, for $0 < s/D < 5$: below this region, the frequency of the imposed motion is predominant and the third harmonic disappear. A similar phenomenon, though less accentuated, was observed also when $f_o = 0.9f_s$ and appears to be an inherent feature of the narrow wake mode, being absent at input frequencies corresponding to the wide wake 2S regime. Furthermore, figure 6.12 shows that the Fourier decomposition of the lift signal in the top region gives rise to two phase angles, $172° < \phi_1 < 180°$ for the first harmonic and $0° < \phi_2 < 17°$ for the third harmonic. Subsequently in this region the lift force is made by two components in phase opposition, one due to the body's

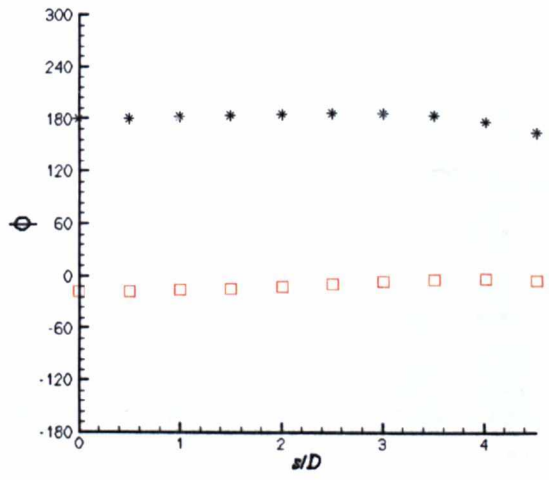


Figure 6.12: Power spectra density of the integrated lift force coefficient for the flow past the concave body at $f_o = 0.8f_s$ and $A/D = 0.5$.

motion and one due to the higher frequency: as a result, the magnitude of the total lift force for $0 < s/D < 5$ is very close to zero, as figure 6.10 (*left*) shows.

6.3.1.3 Forced vibration outside the lock-in region

The vortex shedding suppression is related to the axial flow generation and vorticity re-distribution described in section 6.1: once the stabilising effect of the axial flow is disrupted by the body's oscillation, the shedding resumes and the body is subjected to hydrodynamic forces on its surface. Figure 6.13 (*right*) shows that at imposed frequencies as low as $f_o = 0.6f_s$ the lift coefficient has the same magnitude of the corresponding case in the convex configuration (see figure 5.17 in section 5.2.2). Therefore the shedding outside the lock-in region may appear driven by a similar mechanism in both configurations, although the flow behaviour in the two geometries when the body is kept fixed is markedly different. However, a closer examination reveals that the process leading to vortex shedding originates from two distinct dynamics: in the convex case the shedding occurs for both the steady and the moving body and the effect of the imposed oscillation is to change the shape of the cores and enhance the spanwise correlation, whereas in the concave case the vortex shedding is due to the interaction between the shear layers induced by the motion of the body: at high amplitudes, i.e. $A/D = 0.5$, the imposed oscillation drives the

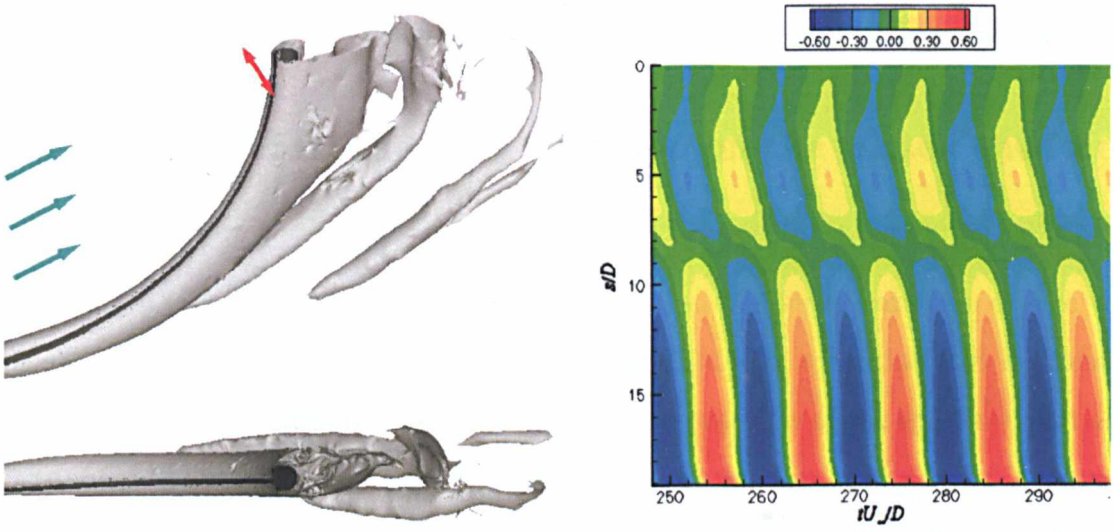


Figure 6.13: *Left*: wake topology past the concave configuration at $f_o = 0.6f_s$, $A/D = 0.5$; isosurfaces at $\lambda_2 = -0.06$. *Right*: Time evolution of the sectional lift coefficient along the spanwise direction.

shear layers across the centre-line and the vortex separation results in an interaction process similar to flutter. This mechanism is different than the one occurring in the wide wake 2S regime, where the shear layers separate as a result of the sharp change of direction due to the high oscillation frequency: as illustrated in figure 6.13 (*left*) by the λ_2 isosurfaces, at $f_o = 0.6f_s$ the shear layers are extremely elongated and thus their destabilisation and subsequent interaction appear to be a consequence of the high amplitude rather than of the frequency of oscillation.

Figure 6.13 also shows that the separation of the primary vortex from the shear layer is delayed in the top region of the body and the cores are subsequently bent with different inclinations in the upper and lower half of the quarter ring. This shedding mode gives rise to a phase shift of π in the region $7 \leq s/D \leq 10$, as displayed by figure 6.21 (*right*); however, no vortex splitting is observed and the shedding frequency does not change along the span, unlike the convex configuration shedding where the right-hand side of the lock-in region in the map 5.5 (type B) was characterised by the competition in the upper part of the body between two distinct frequencies. In the concave geometry only one dominant frequency is found along the whole body, even at very low input frequencies and amplitudes: this is in contrast with the convex case, where a decrease in the oscillation amplitude and frequency

involves the appearance of cells with different frequencies and vortex splitting.

6.3.2 Effect of frequency's variation on the vortex shedding mode

This section will focus on the effect of the oscillation frequency variation on the vortex shedding process and therefore only one amplitude of vibration will be considered, $A/D = 0.5$. Figures 6.14 and 6.15 provide an overview of the spanwise vorticity component at different input frequencies in the top section of the body, $s/D = 0$, and in a lower section, $s/D = 7$, respectively. The three types of shedding can be summarised as follows: at frequencies of oscillation outside the two-dimensional lock-in region, i.e. $f_o = 0.5f_s$ and $f_o = 0.6f_s$, the shear layers are significantly elongated and the vortex shedding appears to be a consequence of the relatively large amplitude of oscillation of the body's cross-flow motion that drags the shear layers across the wake centreline and forces them to interact. For oscillation frequencies within the lock-in region and on the left-hand side of the critical curve in figure 6.3, the wake topology strictly resembles the 2S shedding mode obtained using two-dimensional simulations and is characterised by a narrow wake. As the Strouhal frequency is approached, i.e. at $f_o = 0.9f_s$, the vortex shedding process changes along the span: at $s/D = 0$ (figure 6.14), it gives rise to the narrow wake described above, whereas at $s/D = 7$ (figure 6.15) the wake width increases and the vortex topology resembles the one observed in the wide wake 2S mode. As shown in figure 6.16, this non-dimensional arc-length corresponds to the point where the axial flow and the vertical velocity component curve for the case with $f_o = 0.9f_s$ reaches the value found in the simulations with $f_o > f_s$. On the right-hand side of the critical curve of figure 6.3, where the imposed oscillation frequency is greater than the Strouhal value, an atypical 2S shedding mode with wide wake and contracted shear layers is observed along the whole span of the body. This type of shedding is found to be rather insensitive to changes in the oscillation amplitude and appears to be primarily a function of the oscillation frequency.

The wake mode changes as the oscillation frequency is set equal to the Strouhal

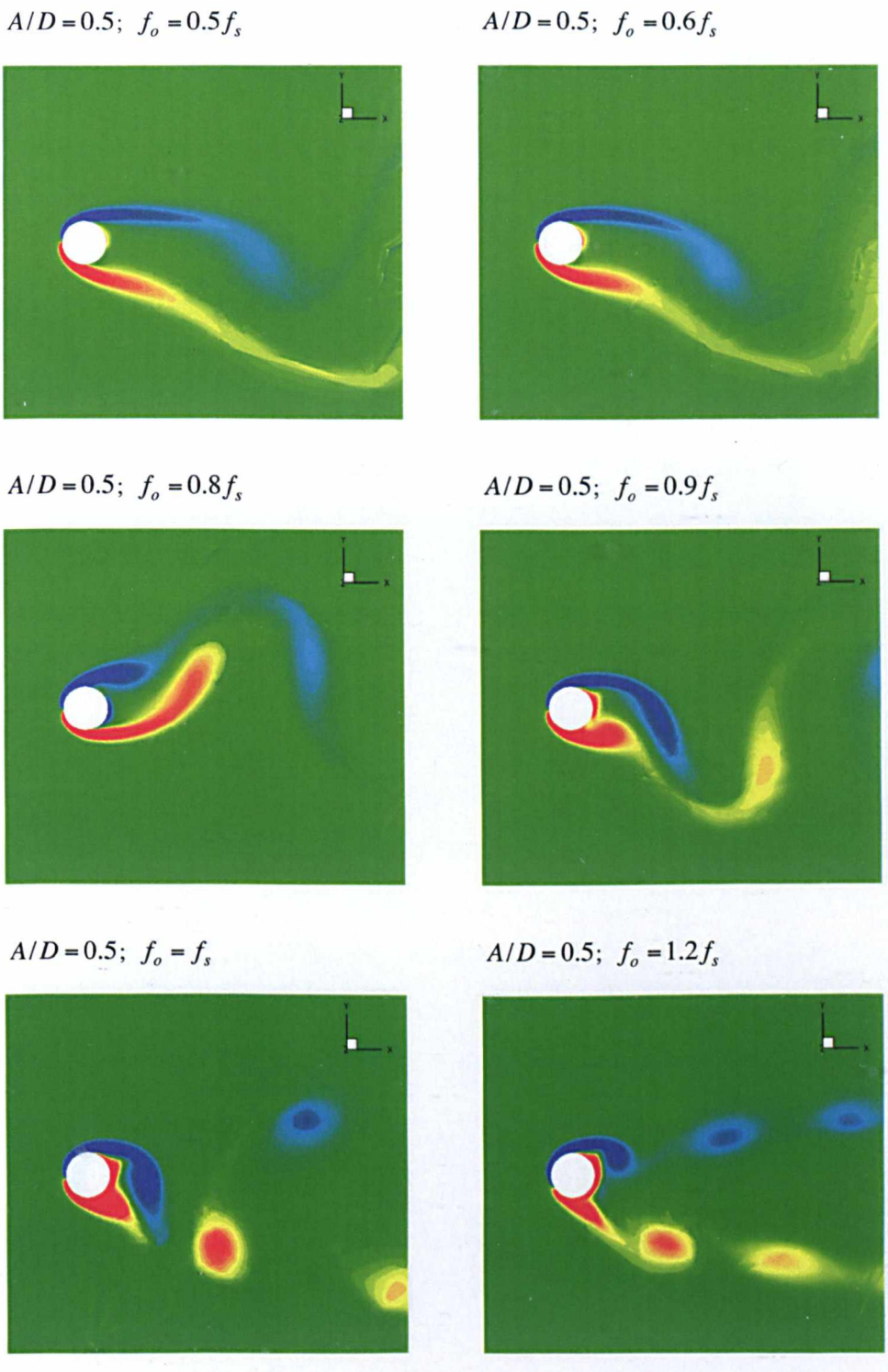


Figure 6.14: Spanwise vorticity component at $s/D = 0$ for the concave configuration with $A/D = 0.5$ and varying input frequency.

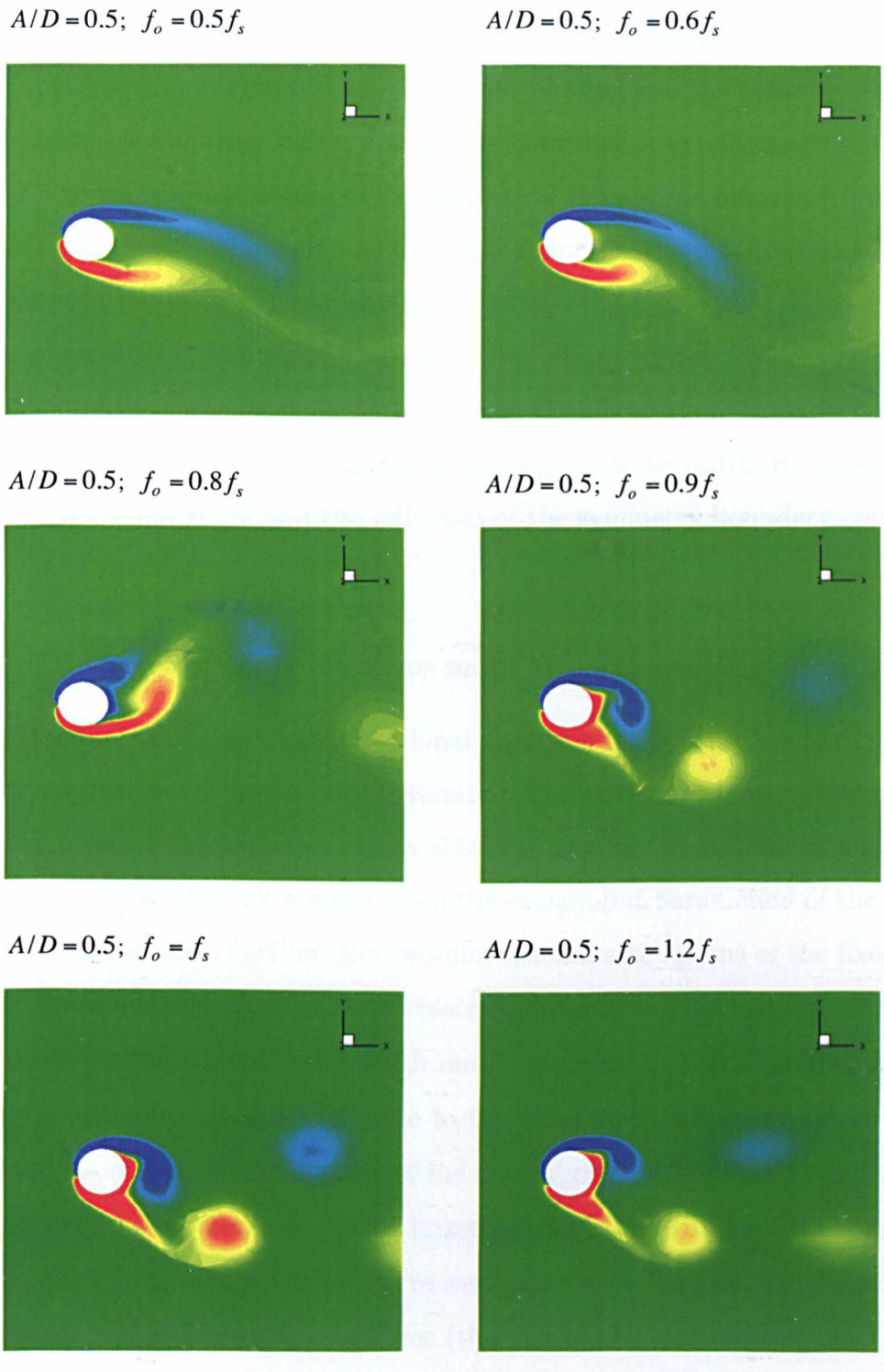


Figure 6.15: Spanwise vorticity component at $s/D = 7$ for the concave configuration with $A/D = 0.5$ and varying input frequency.

value f_s: this case can be considered as a transition between the narrow and the wide wake 2S shedding. The formation length is significantly reduced and the vortex topology in the near wake is similar to the one observed at higher input frequencies; however, the shedding mechanism has a different phasing and the shear layers interact as in the lower frequency cases, giving rise to a more "conventional" 2S type of shedding. The transitional nature of this flow state can also be inferred from figure 6.16, where the empty symbols follow the curve found for the low frequency regime before switching to the high frequency one at $s/D \approx 6$.

These observations pose some fundamental questions on the underlying physics that determines the wake topology in the concave configuration. In particular, the next sections will discuss the mechanism governing the wake width, its relationship with the vortex suppression and the influence of the symmetry boundary condition on this type of shedding.

6.3.2.1 The onset of the wide wake mode from the steady shear layers

As highlighted in section 6.2, in the sectional approach the orientation of the curvature has no influence on the flow approximation and therefore the two-dimensional simulations produce the same results as shown in chapter 5; in these simulations, the wide wake mode does not appear using the same input parameters of the three-dimensional simulations. Further, the two-dimensional simulations of the fixed concave body could not reproduce the suppression mechanism. This suggests that both the dynamics controlling the wake width and the vortex shedding suppression are related to a three-dimensional effect due to the axial flow convection, which is neglected by the sectional approximation of the flow. From the fixed body simulations, the vortex shedding suppression appears linked to the gradient of the vertical velocity and of the axial flow, with a steeper curve associated with a vorticity redistribution in the critical region for vortex shedding (the top of the curved part) and hence with vortex suppression, as described in section 6.1. In the forced vibration results, the width of the wake is found to be dependent on the sign of the axial flow in the upper region of the curved ring. These two features can be visualised in figure 6.16, which shows the time averaged value of the vertical and axial velocity component

extracted along a line $0.3D$ downstream of the body in the radial direction for both the stationary and the moving body.

In the fixed body case, the gradient of the axial velocity component along the spanwise direction is considerably higher than the one measured in all the forced vibration cases. As anticipated, this high gradient leads to the generation of additional vorticity components in the $x-$ and $y-$direction that prevent the shear layers from rolling up in a von Kármán street. The imposed motion causes a weakening of the axial flow production with a subsequent disruption of this suppression mechanism. Figure 6.16 shows that in forced vibration both the vertical and axial velocity components are considerably smaller and their gradient in the spanwise direction lower than the one in the steady cylinder configuration: the vertical velocity w/U_∞ at $f_o = 1.2f_s$ reaches a maximum value of 0.29, 62% smaller than the peak observed in the fixed body case, where $w/U_\infty = 0.47$. Further, the spanwise location of the maximum vertical velocity in the fixed body case takes place at $s/D = 6.4$, in the upper part of the quarter ring, whereas in forced vibration the maximum is reached at a lower spanwise position, $s/D = 9.5$. This corresponds to an inclination angle $\theta = 43.5°$ and hence to a region located in the middle of the curved part of the body. Therefore the additional vorticity components are generated too far away from the top region, where the vortex shedding is more likely to occur, and their stabilising effect on the shear layers is unable to suppress vortex shedding.

Figure 6.16 also reveals that at imposed frequencies corresponding to the wide wake mode the axial and vertical velocity components have a negative value in the top sections and become positive at $s/D = 3$, in a similar way to the fixed body case. In this region of the quarter ring, the vertical velocity and the axial flow directed towards the bottom of the geometry are associated with a wide wake, which may take the form of either an atypical 2S shedding (in forced vibration) or steady shear layers (in the stationary case).

Figure 6.17 shows a comparison of the different distribution of the streamwise vorticity component ω_x in a slice located $0.3D$ downstream of the body, at a time instant corresponding to the position $y = 0$ along the cross-flow trajectory. On the left-hand side is the case with narrow wake and on the right-hand side the one

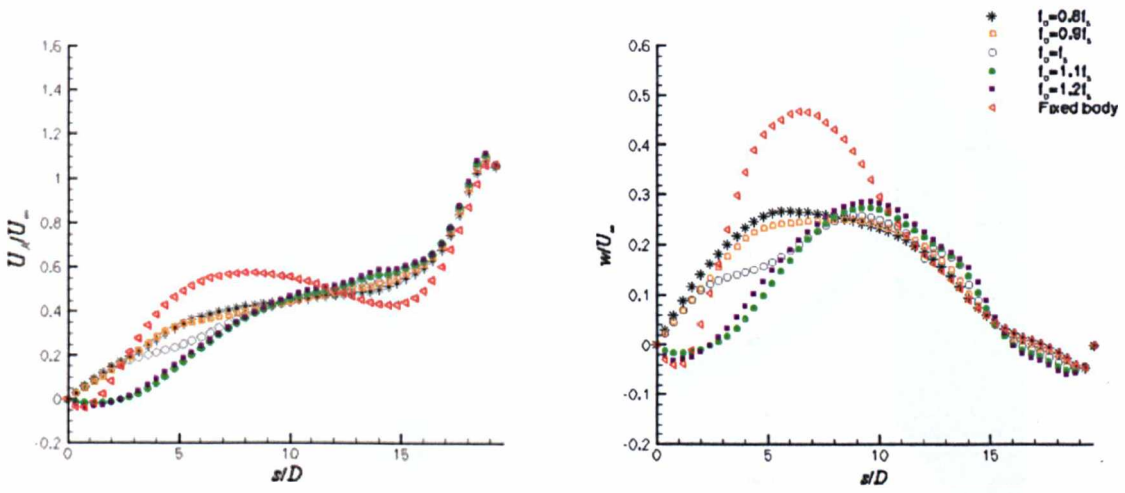


Figure 6.16: Time-averaged values of axial velocity (U_A/U_∞) and vertical velocity (w/U_∞) extracted along a line $0.3D$ downstream of the body in the radial direction. Fixed body case and forced vibration at $A/D = 0.5$ and varying oscillation frequencies.

with wide wake ($f_o = 0.9f_s$ and $f_o = 1.2f_s$ respectively). In the wide wake state, the ω_x distribution in the top sections is nearly symmetrical with respect to the centreline, similar to the results obtained in the fixed body case (see Miliou (2004)), although this symmetry is not completely preserved along the span: as anticipated, the maximum magnitude of ω_x is reached in the middle region and its intensity decreases close to the top of the body. On the other hand, in the narrow wake case the positive and negative ω_x isocontours do not appear simultaneously in the same location, but alternate along the spanwise direction. At the time instant depicted in figure 6.17 (*left*), the body is moving in the negative $y-$direction and the negative ω_x in the top part of the slice drives the shed cores towards the centre of the wake; on the contrary, in the wide wake mode illustrated on the right-hand side of figure 6.17, where the body is moving towards the positive extreme of its trajectory, the streamwise distribution tends to pull the vortices away from the centre of the wake.

The production of additional vorticity components is a consequence of the change in the direction of the cross-flow, normal and axial velocity components: figure 6.18 shows that in the wide wake state the cross-flow velocity (in the $y-$direction) extracted $0.3D$ downstream of the body is negative at $y = -0.25$ and positive at $y = 0.25$, hence directing the shed vortices away from the centreline. In the narrow

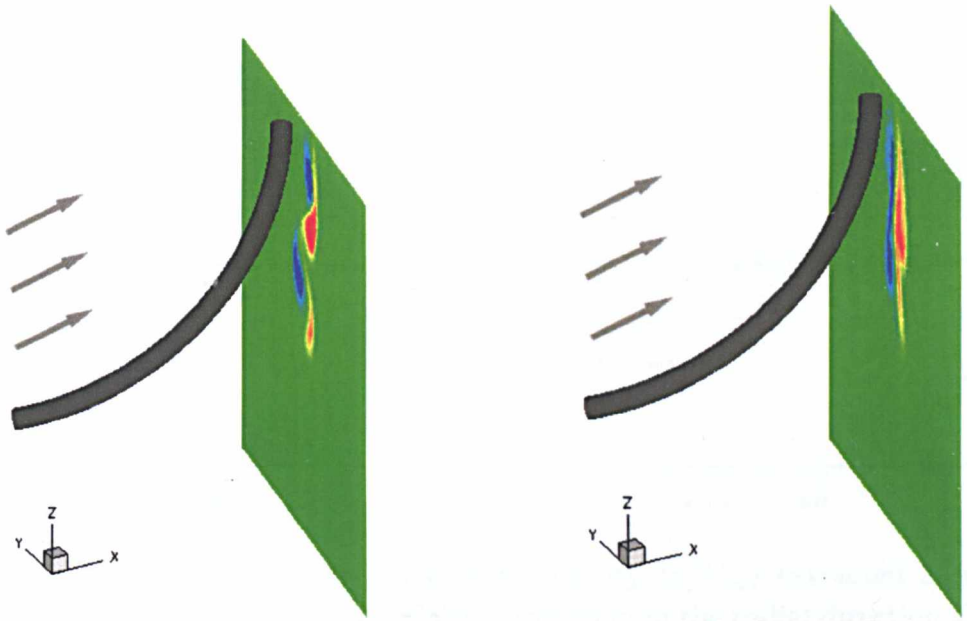


Figure 6.17: Isocontours of the streamwise vorticity component ω_x extracted at $0.6D$ downstream of the body, at a time instant corresponding to the position $y = 0$. Narrow wake state at $f_o = 0.9f_s$ and $A/D = 0.5$ (*left*) and wide wake state at $f_o = 1.2f_s$ and $A/D = 0.5$ (*right*).

wake state the cross-flow velocity direction is reversed, with a positive velocity occurring at $y = -0.25$ and a negative one at $y = 0.25$ and thus pointing towards the centreline. Further, in the wide wake state the time-averaged velocity component directed normal to the body, U_N/U_∞, extracted along the same lines is negative only at $y = 0$, while at both cross-flow positions $y = -0.25$ and $y = 0.25$ its value is positive: this suggests the presence of two counter-rotating 'bubbles" in the range $0 \leq s/D \leq 3.8$ where this change of sign takes place. This is not observed in the narrow wake state, where the normal velocity component is positive at every cross-flow position along the whole span of the body.

The isocontours of the vertical velocity in the wake are shown in figure 6.20, where the two different wake modes are compared: as anticipated, the wide wake is associated with a high vertical velocity in the middle/top region of the body, which moves the vortex cores away from the wake centreline, whereas in the narrow wake mode the vertical velocity component is considerably weakened in proximity of the top and thus the wake generated in this case is not significantly altered. The

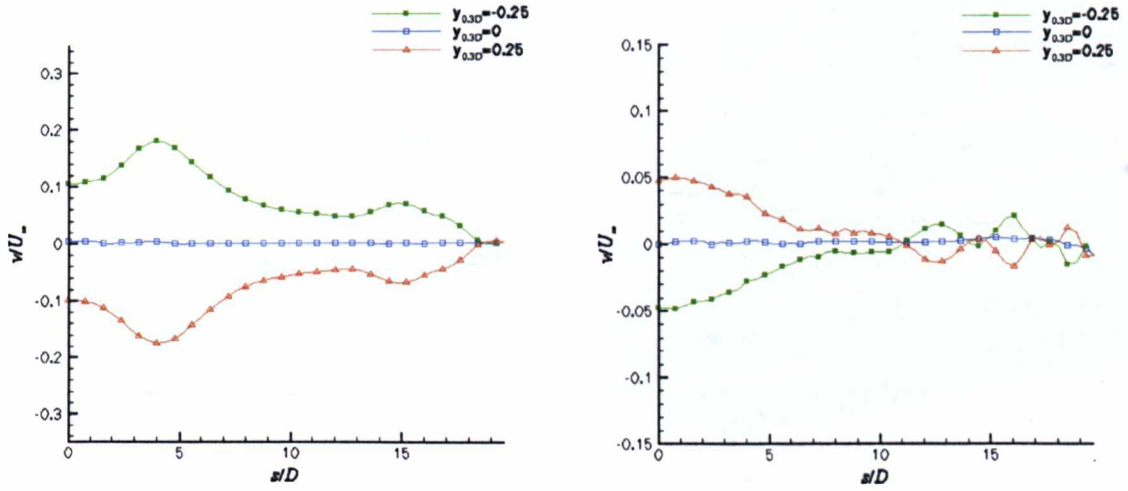


Figure 6.18: Time-averaged cross-flow velocity (v/U_∞) extracted along a line $0.3D$ downstream of the body in the radial direction. Narrow wake state at $f_o = 0.9f_s$ and $A/D = 0.5$ (*left*) and wide wake state at $f_o = 1.2f_s$ and $A/D = 0.5$ (*right*).

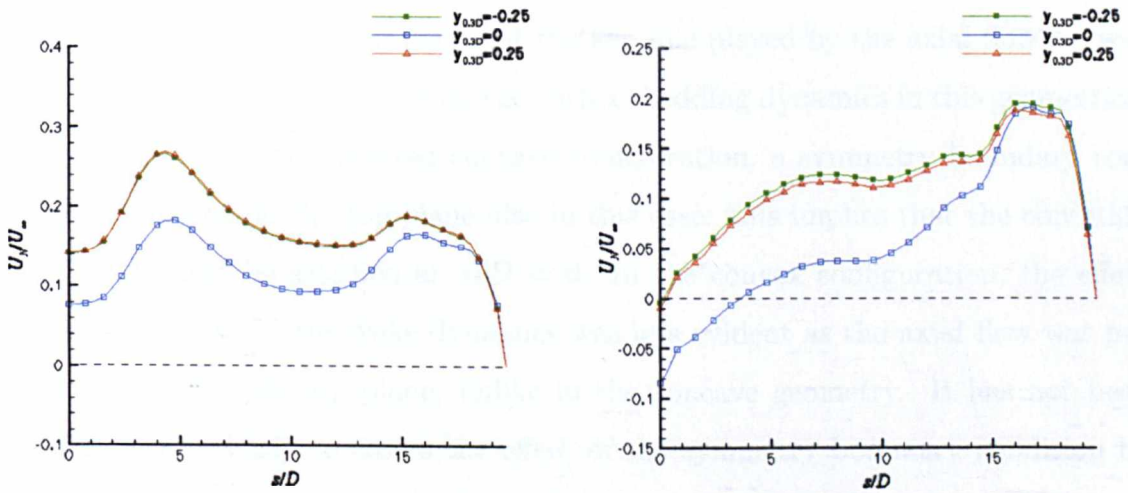


Figure 6.19: Time-averaged normal velocity (U_N/U_∞) extracted along a line $0.3D$ downstream of the body in the radial direction. Narrow wake state at $f_o = 0.9f_s$ and $A/D = 0.5$ (*left*) and wide wake state at $f_o = 1.2f_s$ and $A/D = 0.5$ (*right*).

presence of large vertical velocities downstream of the upper part of the body is also related to the persistence of a streamwise vortex pair in the wake.

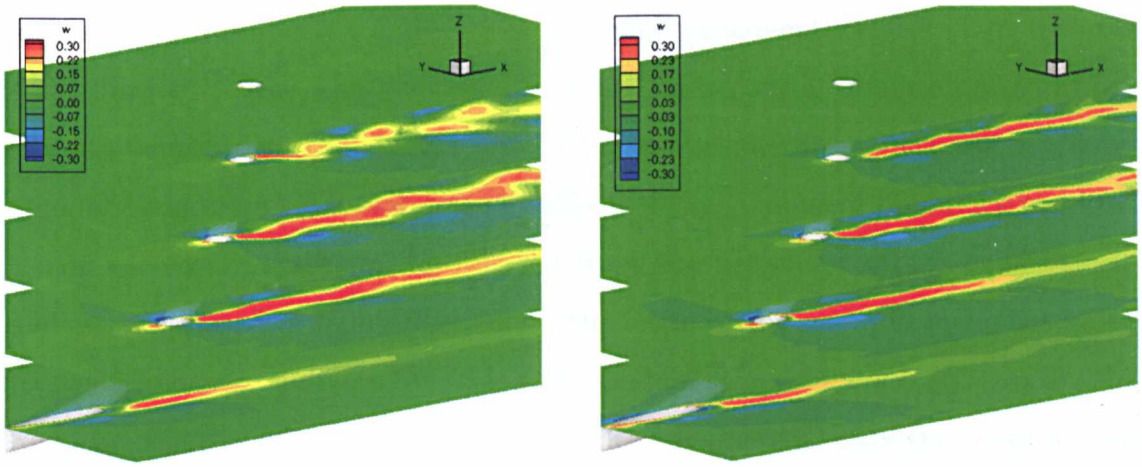


Figure 6.20: Vertical velocity w isocontours. Forced translation at $A/D = 0.5$: $f_o = 0.9f_s$ (*left*) and at $f_o = 1.2f_s$ (*right*).

6.3.2.2 Effect of the symmetry boundary condition on the vortex shedding mode

The results so far illustrated highlight the key role played by the axial flow convection and by the vertical velocity on the vortex shedding dynamics in this geometrical configuration. Like in the fixed concave configuration, a symmetry boundary condition is imposed on the top plane also in this case: this implies that the condition $w/U_\infty = 0$ must be satisfied at $s/D = 0$. In the convex configuration, the effect of this restriction on the wake dynamics was less evident as the axial flow was not directed towards the top plane, unlike in the concave geometry. It has not been possible in this study to assess the effect of the symmetry boundary condition by testing the modified concave configuration with a vertical extension on the top of the curved ring; however, some considerations on the physics of the wide wake state might provide a possible explanation on how this artificial zero vertical velocity condition imposed on the top plane may affect the vortex shedding.

A high oscillation frequency implies than the velocity of the moving body is also higher; therefore, the change of direction when the body reaches the extreme position of its trajectory has to occur over a shorter time. This prevents the cross-flow velocity and the axial velocity in the wake of the body from gradually adjusting to the change of direction: the resulting direction of the velocity vector downstream of the body may be in conflict with the requirement prescribed by the symmetry

boundary condition, $w = 0$ and $\frac{\partial u}{\partial z} = \frac{\partial v}{\partial z} = 0$, and consequently cause a redistribution of the fluid particles. This process ultimately leads to the formation of additional vorticity components that would not be present in the absence of the symmetry boundary condition. Another possible effect of the symmetry boundary condition on the wide wake state can be inferred from the behaviour of the axial velocity gradient illustrated in figure 6.16: here, the slope of the curve is such that at the frequencies corresponding to the wide wake shedding the values of U_A/U_∞ and w/U_∞ would be negative at the top of the body, if the symmetry boundary condition was not applied. The natural inclination of the vertical velocity curve (and subsequently of the axial flow one) is thus altered in order to comply with the restriction dictated by the condition $w/U_\infty = 0$ that has to be satisfied at $s/D = 0$. At the frequencies corresponding to the narrow wake state, the decreasing of the vertical velocity as the non-dimensional arc-length approaches the top plane appears to be more likely to satisfy the symmetry boundary condition without substantial alteration of its behaviour and, more importantly, without a change in the sign of its gradient.

6.3.3 Effect of amplitude and frequency variation on the shedding phase and energy transfer

Figures 6.21 and 6.22 provide an overview of the flow configurations where a positive phase angle ϕ (and hence flow excitation) takes place. At flow states corresponding to the narrow wake mode, the phase angle at the top is approximately 180° and the vortex shedding is out-of-phase with the motion. Since the lower part of the quarter ring is aligned to the inflow direction and behaves like a slender body, its phase angle has a common value close to zero for all the frequencies tested. Therefore, when the imposed frequency of oscillation is below the Strouhal value, a gradual phase shift occurs along the body's length and the phase angle ϕ spans the excitation region [0°; 180°].

In the case at $f_o = 0.9f_s$ and $A/D = 0.5$, the phase angle at $s/D = 7$ is very close to the one obtained in the wide wake 2S shedding mode, $\phi \approx 0°$: this spanwise position is where the change from the narrow wake to the wide wake topology occurs

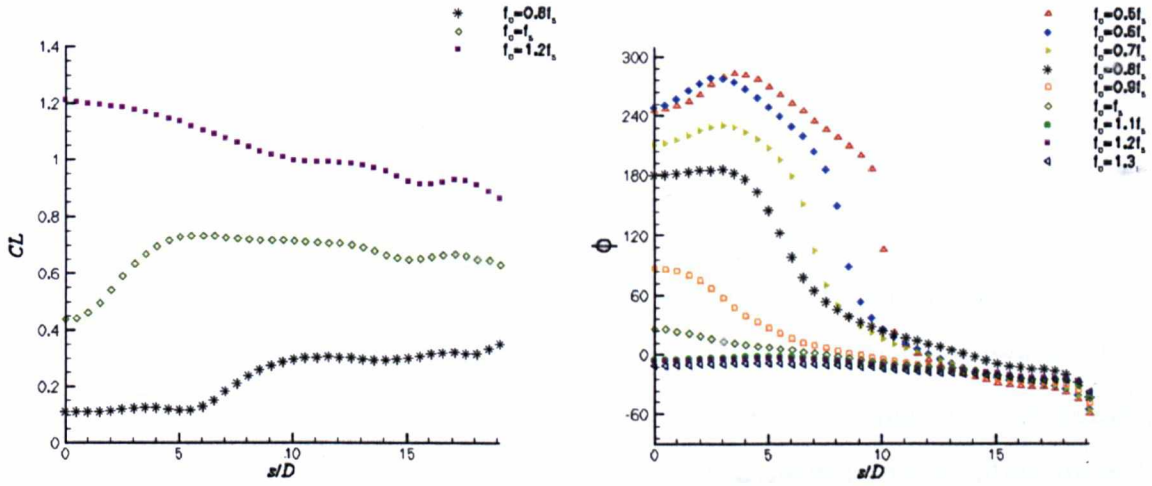


Figure 6.21: *Left*: Spanwise variation of the lift coefficient at three different imposed frequencies and $A/D = 0.5$, corresponding to the narrow wake state ($f_o = 0.8f_s$), the transitional state ($f_o = f_s$) and the wide wake state ($f_o = 1.2f_s$). *Right*: phase angle variation along the span for different input frequencies and $A/D = 0.5$.

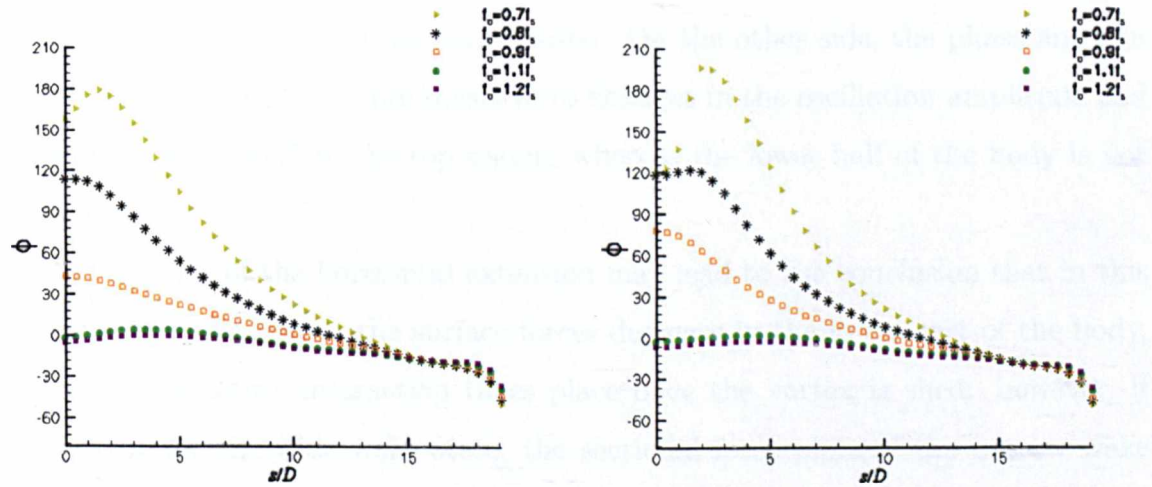


Figure 6.22: Phase angle variation for $A/D = 0.1$ (*left*) and $A/D = 0.25$ (*right*).

(see section 6.3.2, figure 6.15). This lends support to the idea that the wide wake mode takes place when the vortex shedding is approximately in-phase with the body's motion, with phase angles in the range $0° \leq \phi \leq -30°$. We shall discuss later in the light of the correlation coefficient that the inception of the wide wake mode is initiated in the lower part of the body and is related to the force generated by the imposed motion rather than to the one arising from the vortex shedding itself.

This wake mode propagates to the upper half of the geometry as the frequency is increased and the phase angle approaches values below zero over a progressively larger portion of the body's span: as mentioned in section 6.3.2, this process is completed at $f_o = f_s$, where a fully developed wide wake is observed at $s/D = 0$. The change in the wake mode along the span is not evident at $f_o = 0.8f_s$: in this case, the phase angle does not reach the wide wake value until a much lower spanwise position, where the inclination of the body is such that the vortices are not shed in the wake but follow the dynamic described by the Morison's equation (see section 5.2.1.1). The wake dynamics in the lower part of the curved ring exhibits indeed common features with the one in the convex body, where the phase angle value is also negative and close to zero, as illustrated in figure 5.27.

The observation that the vortex topology in the wide wake mode is not primarily influenced by the oscillation amplitude is confirmed by the findings on the phase angle distribution: figure 6.22 shows that at $f_o > f_s$, ϕ does not change significantly when the oscillation amplitude is decreased. On the other side, the phase angle in the narrow wake more is more sensitive to changes in the oscillation amplitude and ϕ decreases with A/D in the top region, whereas the lower half of the body is not influenced.

The absence of the horizontal extension may lead to the conclusion that in this geometrical configuration the surface forces decrease in the lower part of the body, as no fluid/structure interaction takes place once the vortex is shed: however, if this is true for the wide wake state, the sectional force plots of the narrow wake state in figures 6.8 and 6.10 seem to contradict this conclusion, showing a greater lift coefficient in the lower part of the geometry. Figure 6.21 (*left*) also illustrates the different lift coefficient spanwise distribution in the two sub-regimes and in the transitional case at $f_o = f_s$.

The spanwise vorticity displayed in figures 6.14 and 6.15 confirms this observation: in the narrow wake mode the formation length decreases from the top to the bottom, whereas the opposite behaviour is observed in the wide wake mode, with the corresponding decrease in the magnitude of the lift coefficient from top to bottom illustrated in figure 6.21. This can be related to the phase angle variation along

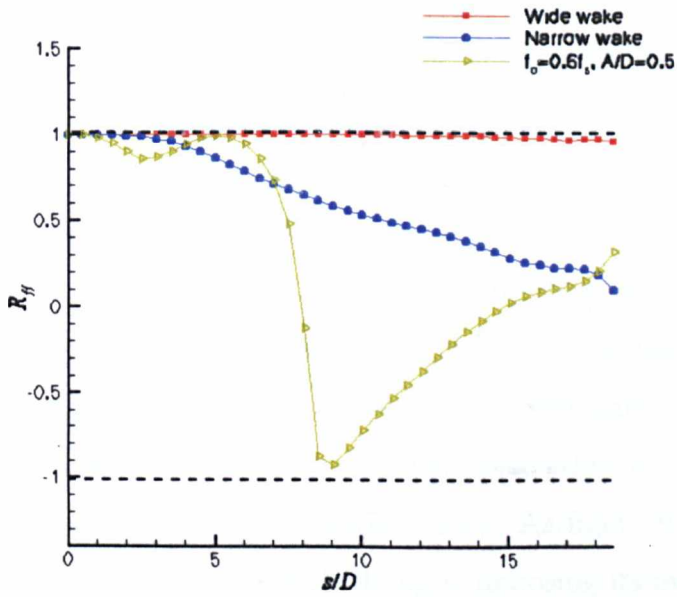


Figure 6.23: Spanwise lift correlation coefficient in the wide wake mode ($f_o = 1.2f_s$ and $A/D = 0.5$), narrow wake mode ($f_o = 0.9f_s$ and $A/D = 0.5$) and outside the two-dimensional lock-in region ($f_o = 0.6f_s$ and $A/D = 0.5$).

the span. As shown in figure 6.21 (*right*), in the wide wake state the phase angle is close to zero and remains approximately constant along the whole length of the body: the vortex shedding is in phase with the body's motion and the fluid forces follow the cross-flow displacement. However, this does not explain why in none of the flow conditions simulated in the convex configuration the in-phase shedding is associated with a lift coefficient that decreases with increasing arc-length s/D: the wide wake mode in the concave configuration is in fact the only flow regime where this phenomenon is observed. A possible explanation is given by the absence of interaction between cores and structure in the near wake of the concave body: even if the horizontal extension was excluded from the convex configuration, the lower part of the quarter ring would still interact with the cores and the dampening influence stemming from this part of the body would affect the shedding at the top. The only exception in the convex case is when a vortex dislocation takes place at the top of the body and the split vortex is convected downstream without being subject to the influence of the shear layers at lower spanwise positions: in this condition the vortex shedding forces are found to excite the body's vibration. A similar principle can be

used to explain why the body's motion is always damped for the wide wake mode, whereas the narrow wake mode is associated with flow excitation despite the higher forces in the lower part of the quarter ring.

In analogy with the convex configuration, a damping motion-generated force in-phase with the displacement ($\phi \approx 0°$) is dominant in the lower part of the body, whereas a vortex shedding-generated force out-of-phase with the displacement ($90° \leq \phi \leq 180°$) controls the upper part. At low frequencies, the latter is predominant in the upper part and the former in the lower part: this generates the spanwise variation in the phase angle and in the correlation coefficient of the lift force, R_{ff}, which is calculated using equation (5.4). As figure 6.23 shows, this is close to 1 at the top, where the vortex shedding is imposing its own positive phase angle, and goes to 0 in the lower part of the geometry, where it is not the shedding-generated force that is predominant but the motion-generated one. For the pair of input parameters illustrated in figure 6.23, $f_o = 0.9f_s$ and $A/D = 0.5$, the correlation coefficient has to be 0 in the lower part of the body as $\Delta\phi$ between the top and the bottom sections is equal to 90° (see also figure 6.21 (*right*)). At high frequencies the motion-generated force drives the shedding past the whole structure, leading to a constant phase angle along the span, whose value is equal to the one in the lower part of the body, $\phi \approx 0$: this gives rise to the constant correlation coefficient $R_{ff} \approx 1$ displayed in figure 6.23.

6.3.4 Effect of the radius of curvature on the vortex shedding mode

Since the wake dynamics depends significantly on the velocity variation along the axial direction, an interesting point would be to determine how the curvature influences such quantities and thus the vortex shedding mode. A set of simulations with a double radius of curvature $R = 25D$ has been performed with oscillation frequency $f_o = 1.1f_s$ and amplitude $A/D = 0.5$: these input parameters corresponds to the wide wake mode when $R = 12.5D$. Figure 6.24 (*left*) shows the lift coefficient iso-contours along the span of the body against time units: as in the wide wake mode

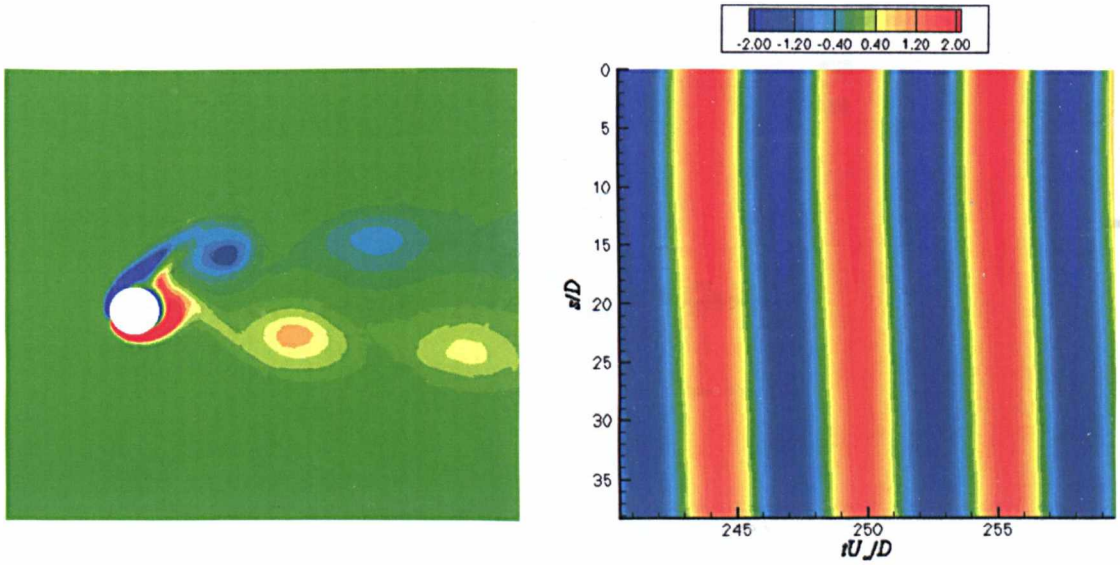


Figure 6.24: Concave body with $R = 25D$ in forced vibration at $f_o = 1.1f_s$ and $A/D = 0.5$. Time evolution of the sectional lift distribution along the span (*left*) and spanwise vorticity distribution in a slice located at $s/D = 0$ (*right*).

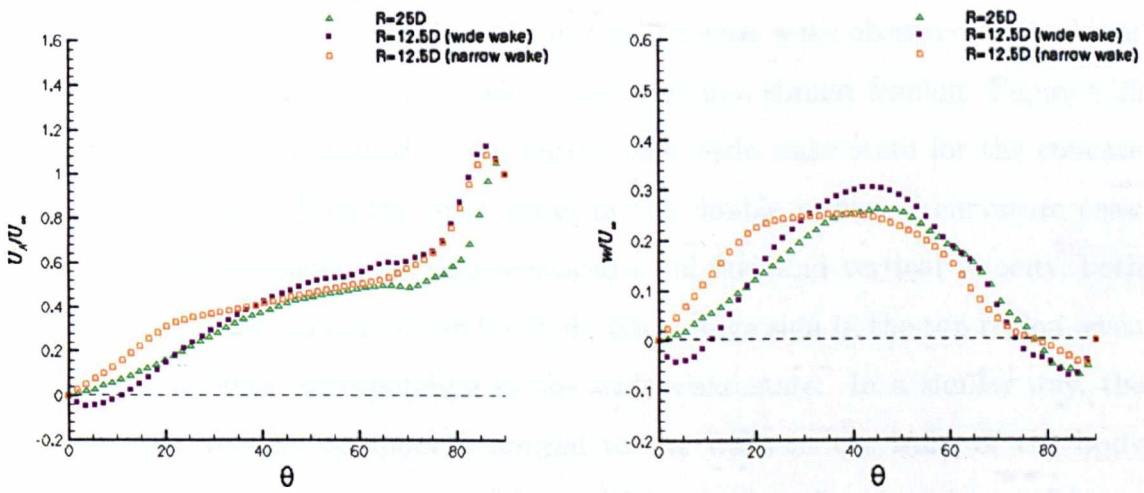


Figure 6.25: Time-averaged values of axial velocity (U_A/U_∞) and vertical velocity (w/U_∞) extracted along a line $0.3D$ downstream of the body in the radial direction. Concave body with $R = 25D$ in forced vibration at $f_o = 1.1f_s$ and $A/D = 0.5$, compared to the wide and narrow wake states observed for $R = 12.5D$.

observed past the original configuration with the same input parameters (see 6.4), the force magnitude mildly decreases from the top to the bottom of the quarter ring and the resulting shedding is in-phase with the body's oscillation.

However, the wake topology at $s/D = 0$ illustrated in figure 6.24 (*right*) shows

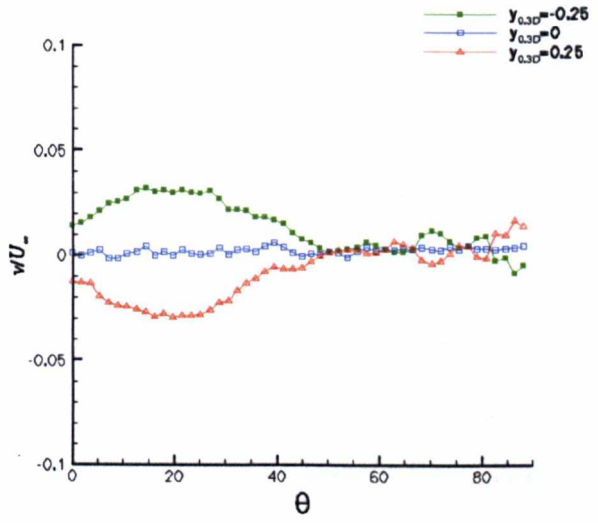


Figure 6.26: Time-averaged cross-flow velocity (v/U_∞) extracted along a line $0.3D$ downstream of the body in the radial direction. Concave body with $R = 25D$ in forced vibration at $f_o = 1.1f_s$ and $A/D = 0.5$.

that the wake width is smaller than the one in the wide wake observed at the lower radius of curvature, although the vortices are shed in a similar fashion. Figure 6.25 compares the results obtained in the narrow and wide wake state for the concave body with $R = 12.5D$ to the ones found in the double radius of curvature case: in this modified geometry, the time-averaged axial flow and vertical velocity, both extracted $0.3D$ downstream of the body, do not change sign in the top region, even at input parameters corresponding to the wide wake state. In a similar way, the time-averaged velocity component normal to the walls in the wake of the body with double radius of curvature does not exhibit any sign change and is positive at every spanwise location. Furthermore, the maximum value of the vertical velocity component w is equal to $0.26U_\infty$, hence only 4% higher than the one found for the narrow wake state in the case with $R = 12.5D$ and $f_o = 0.9f_s$. This suggests that the increment in the radius of curvature has weakened the wide wake mode, shifting its typical value towards the ones measured in the narrow wake mode for the original geometry. However, the gradient of the axial flow velocity, which directly influences the wake width, is very similar to the one found for the wide wake case at a lower radius of curvature, as figure 6.25 (*left*) shows.

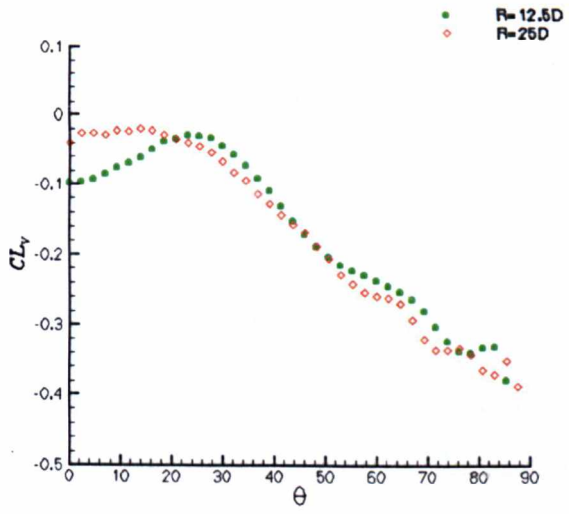


Figure 6.27: Time-averaged cross-flow velocity (v/U_∞) extracted along a line $0.3D$ downstream of the body in the radial direction. Concave body with $R = 25D$ in forced vibration at $f_o = 1.1f_s$ and $A/D = 0.5$.

The time-averaged value of the cross-flow velocity v extracted at the same downstream location of the previous data is presented in figure 6.26. A comparison with figure 6.18 confirms the similarities between the narrow wake mode and the shedding past the configuration with double radius of curvature at oscillation frequencies above f_s: the v velocity component is positive in the top region along a radial line at $0.3D$ downstream and $y = -0.25$, and negative on the other side of the wake, where $y = 0.25$: therefore, unlike the wide wake dynamics, the vortex cores tend to be convected towards the centreline. However, the magnitude of w is much lower than the one found for the narrow wake and shown in figure 6.18 (*left*): this can explain why the wake appears to be consistently wider in figure 6.24 than the typical narrow wake 2S shedding.

This decrease in the wake width has a direct effect on the energy transfer mechanism: as previously discussed, in all the wide wake states the energy is transferred from the structure to the flow and subsequently this mode will not develop in free vibration. Since the increase in the radius of curvature has weakened the physical mechanism underlying the formation of the wide wake mode, the configuration with the double radius of curvature is expected to have a higher density of energy than

the original one. Figure 6.27 confirms this hypothesis: although the integral of the energy along the span is still largely negative (principally due to the hydrodynamic damping arising from the lower part of the quarter ring), CL_V at $s/D = 0$ has increased by 60% in the modified geometry.

6.4 Free vibration simulations

The results obtained with forced vibration simulations have demonstrated that the concave geometry is more likely to be excited by the vortex shedding forces than the convex body. This may appear in contrast with the vortex suppression observed when the body is kept fixed and exposed to a uniform inflow: this case exhibits indeed stationary forces on the surfaces and steady non-interacting shear layers. Therefore one would expect that no vortex-induced vibration occurs if the body is left free to respond to the hydrodynamic forces. However, the free vibration simulations show that not only the body starts to shed vortices but also its motion is self-sustained and reaches asymptotically a certain oscillation amplitude, which depends on the structural damping ζ and on the reduced velocity V_r. Nevertheless, this is consistent with the large excitation region obtained with forced vibration simulations and illustrated in figure 6.3: section 6.4.2 shows that in fact the free response results are in excellent qualitative and quantitative agreement with the flow dynamics predicted in forced vibration. As highlighted in the map 6.3, the excitation region lies on the right-hand side of the critical curve and therefore concerns frequencies of oscillation below the Strouhal frequency. The results obtained with forced vibration demonstrate the physical relationship between the suppression mechanism observed in the fixed body case and the wide wake vortex shedding found in the left-hand side of the mode map 6.3 for $f_o > f_s$. The narrow wake mode observed when $f_o < f_s$ follows a different dynamics: it is thus not surprising that the wide wake mode never appears in free vibration and that the simulation with a reduced velocity corresponding to natural frequencies in this regime results in a dampened response with oscillation amplitude that tends to zero. All the cases presented in the next sections have a mass ratio $m^* = 3$.

6.4.1 Results with zero structural damping

In this section, the response of the body in the absence of structural damping is analysed at two different reduced velocities V_r: in Case 1 the reduced velocity V_r is equal to 7.62, which corresponds to a natural frequency of $0.8f_s$, whereas in Case 2 V_r is set to 6.77 to match a natural frequency of $0.9f_s$.

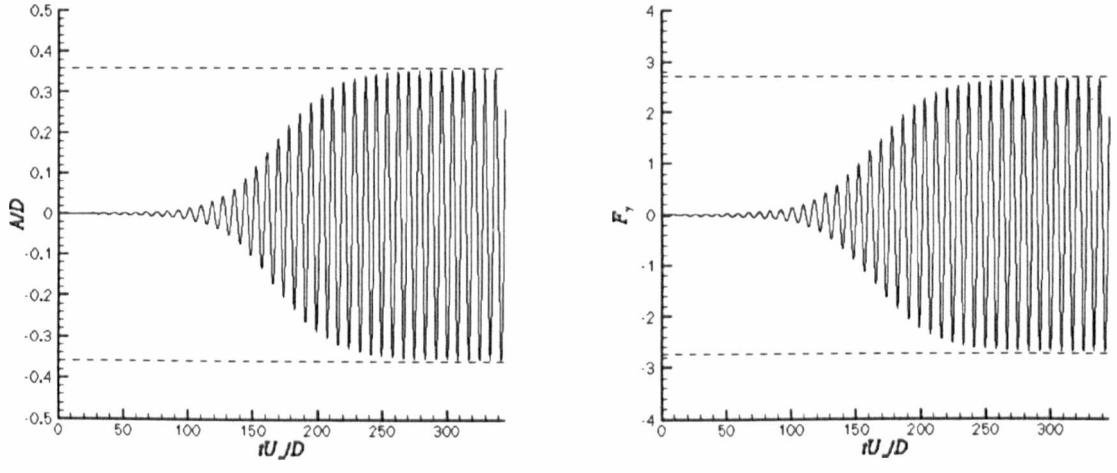


Figure 6.28: Concave body in free vibration, Case 1 with $\zeta = 0.0$. *Left*: oscillation amplitude A/D against non-dimensional time. *Right*: lift force F_y against non-dimensional time.

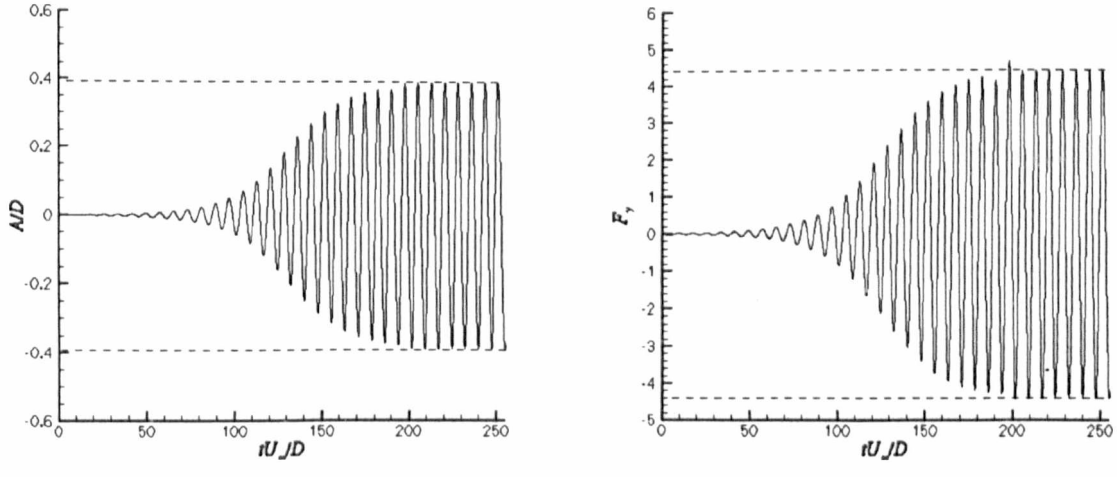


Figure 6.29: Concave body in free vibration, Case 2 with $\zeta = 0.0$. *Left*: oscillation amplitude A/D against non-dimensional time. *Right*: lift force F_y against non-dimensional time.

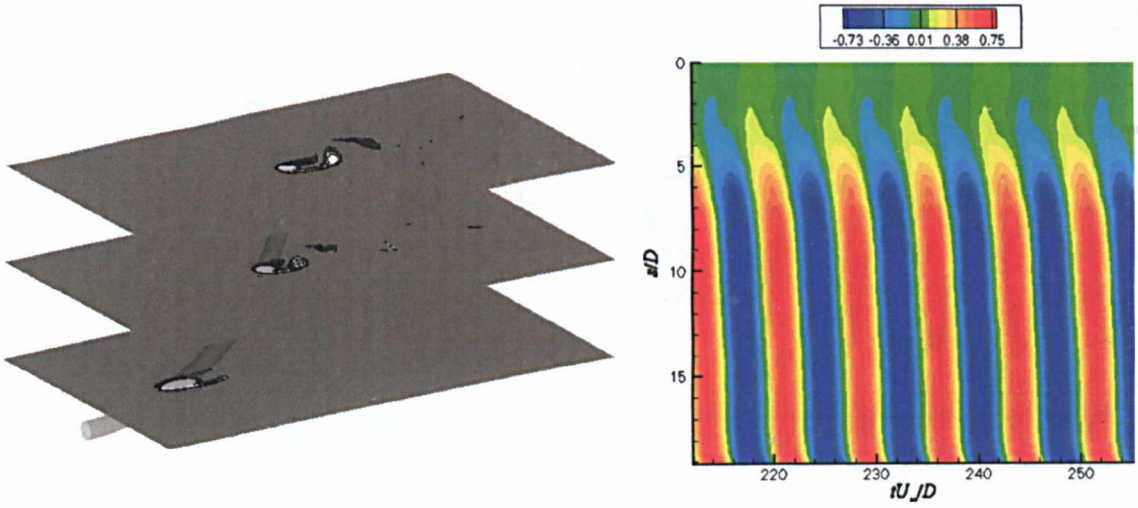


Figure 6.30: Concave body in free vibration, Case 2 with $\zeta = 0.0$. *Left*: Spanwise vorticity ω_z isocontours. *Right*: Time evolution of the sectional lift coefficient along the spanwise direction.

When the structural damping is equal to zero, Case 1 exhibits a maximum amplitude of $0.36D$ and Case 2 reaches a value of $A/D = 0.39$. Figures 6.28 and 6.29 show that in both cases these values are reached asymptotically without any modulation, neither in the amplitude nor in the lift force F_y (the peak in the force at $tU_\infty/D = 198$ being due to the restarting of the computation). In their two-dimensional numerical simulation at $Re = 100$, Shiels *et al.* (2001) observed a maximum amplitude of $0.46D$; their mass ratio corresponds to $m^* = 2.5$ in the present non-dimensionalisation and the reduced velocity is approximately the same.

The wake topology for Case 2 is illustrated in figure 6.30 through spanwise vorticity isocontours. The wake mode and the lift coefficient distribution are qualitatively similar to the 2S narrow wake observed in forced vibration simulations (see figure 6.9). Similar to the behaviour observed in forced vibration, the top sections exhibit a third harmonic response also in this case, although the PSD of the higher harmonic is lower compared to the one of the first harmonic: the latter occurs at a frequency equal to $0.8f_s$, hence slightly lower than the natural frequency calculated from the reduced velocity.

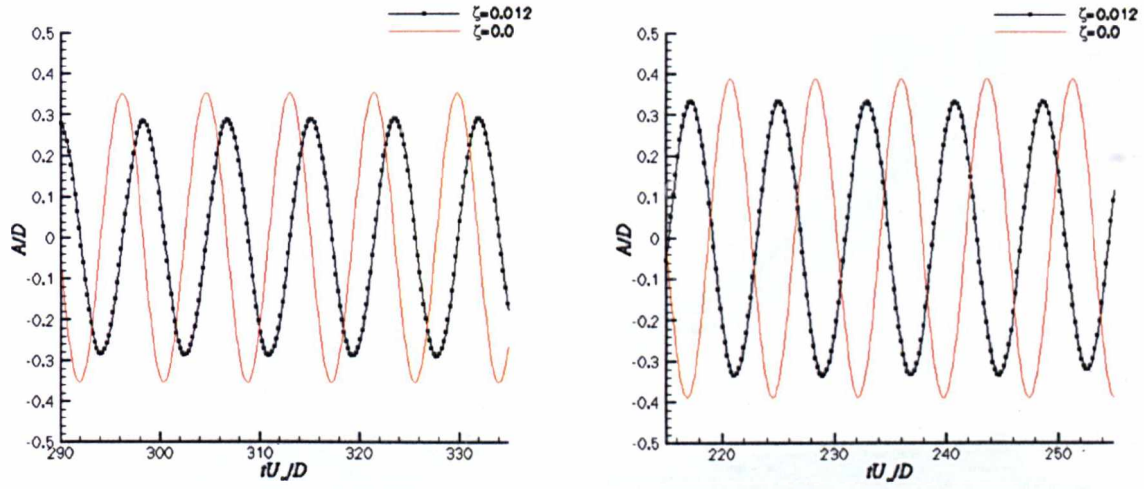


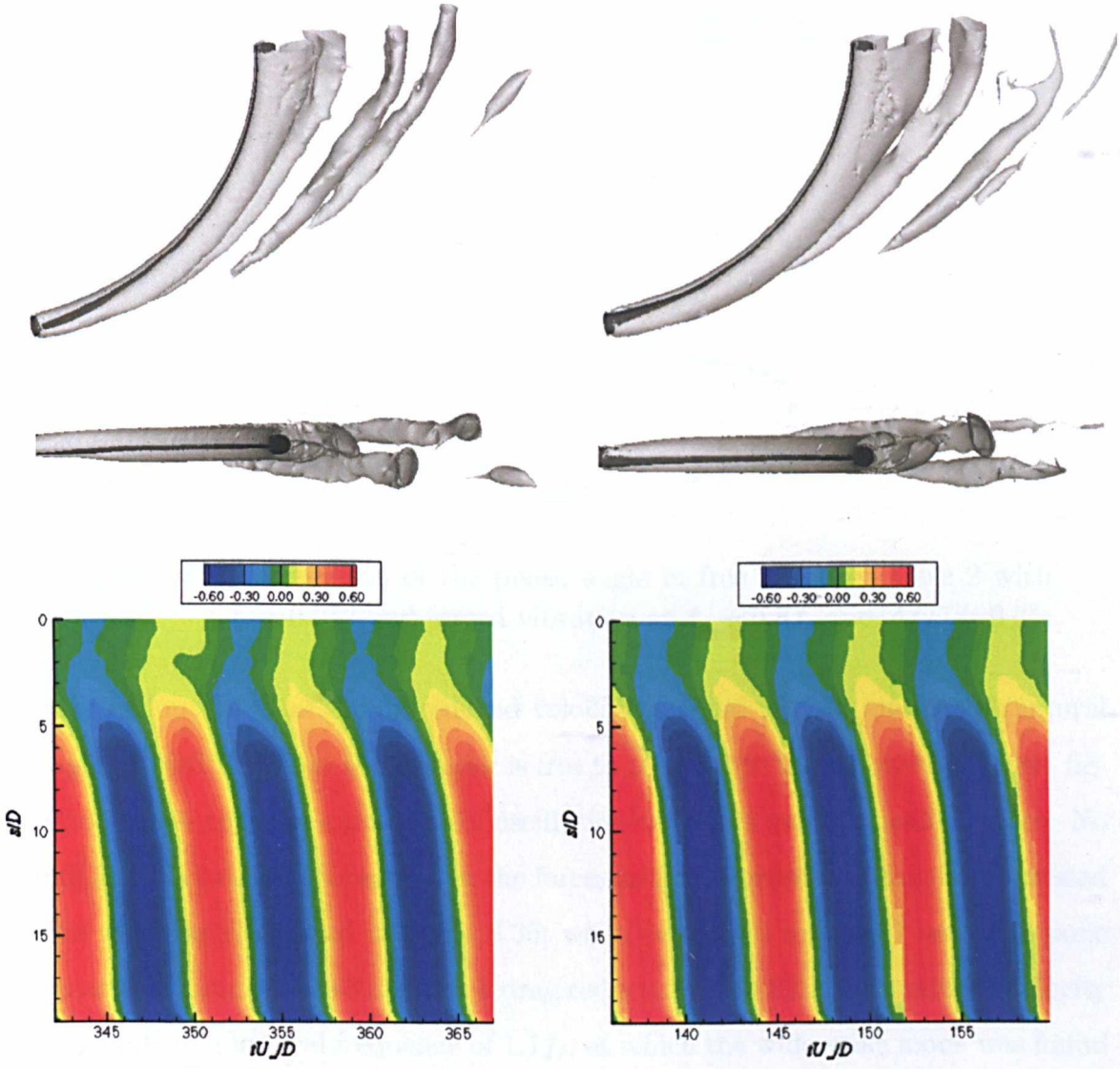
Figure 6.31: Oscillation amplitude A/D against non-dimensional time with and without structural damping ζ. *Left*: Case 1. *Right*: Case 2.

6.4.2 Effect of the structural damping on the vortex shedding

The effect of structural damping on the oscillation amplitude is illustrated in figures 6.31 for Case 1 and Case 2. When $\zeta = 0.012$, the maximum amplitude decreases from $0.36D$ to $0.29D$ in Case 1 ($V_r = 7.62$) and from $0.39D$ to $0.34D$ in Case 2 ($V_r = 6.77$).

These values of oscillation amplitude and frequency correspond to the centre of the shadowed area in the parameter plane of figure 6.3. The shedding frequency for Case 2 is 0.131, which corresponds to approximately $0.8f_s$ in the forced vibration simulation. This case can be compared to the forced vibration simulation performed at $f_o = 0.8f_s$ and $A/D = 0.35$. Figure 6.32 shows that the free and forced vibration results exhibit also marked similarities in both the wake topology and the distribution of sectional forces along the span. The phase angle evolution along the spanwise direction s/D for the two simulations is also compared in figure 6.33, which shows a maximum discrepancy of 9.8°.

These results have been obtained for two reduced velocities, $V_r = 6.77$ and $V_r = 7.62$, which generally correspond to the upper/lower branch response for a straight cylinder (see Shiels *et al.* (2001)). However, when free vibration simulations



FREE VIBRATION FORCED VIBRATION

Figure 6.32: Wake topology isosurfaces at $\lambda_2 = -0.1$ and sectional lift coefficient distribution. *Left*: free uniform translation for Case 2 with $\zeta = 0.012$. *Right*: forced uniform translation at $f_o = 0.8 f_s$ and $A/D = 0.35$.

of the concave body are performed at a lower reduced velocity, the configuration does not exhibit vortex-induced vibration and the oscillation is limited to very low values before decreasing naturally to zero. This may suggest that the initial branch is suppressed in the concave configuration, although more numerical simulations would be needed to confirm this hypothesis: unfortunately, in this study it has not been possible to simulate the whole range of reduced velocities corresponding to the

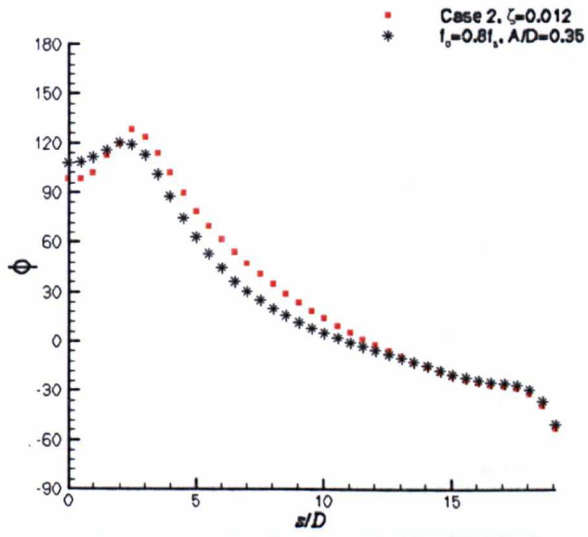


Figure 6.33: Comparison of the phase angle in free vibration Case 2 with $\zeta = 0.012$ and forced vibration at $f_o = 0.8f_s$ and $A/D = 0.35$.

lock-in region. In Case 3, the reduced velocity is equal to 5.52 and the structural damping to 0.012. When the cylinder is free to respond to the inflow conditions, figure 6.34 shows that the amplitude of oscillation decreases monotonically to zero. No significant fluctuation is observed in the forces and the vortex shedding is suppressed in the wake, as illustrated in figure 6.35; when compared to Case 1 with the same structural damping, Case 3 exhibits a drag reduction of 14.8%. This reduced velocity corresponds to a natural frequency of $1.1f_s$, at which the wide wake mode was found to occur in forced vibration simulations: as this wake state was associated with hydrodynamic damping at all the oscillation amplitudes tested ($0.1 < A/D < 0.5$), the absence of vortex-induced vibration in the free response simulation may be anticipated from the forced vibration results. Nevertheless more numerical simulations in this range of reduced velocities are required to confirm this hypothesis.

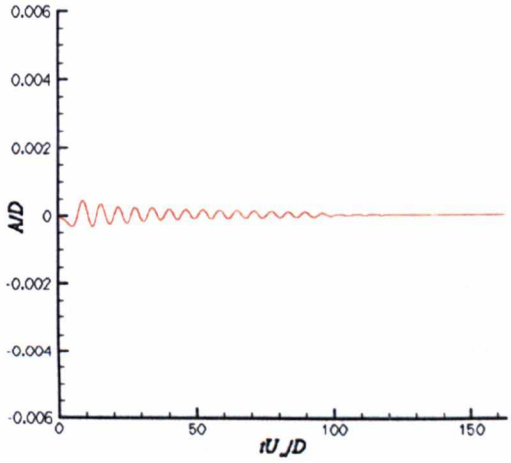


Figure 6.34: Concave body in free vibration, Case 3 with $\zeta = 0.012$: oscillation amplitude A/D against non-dimensional time.

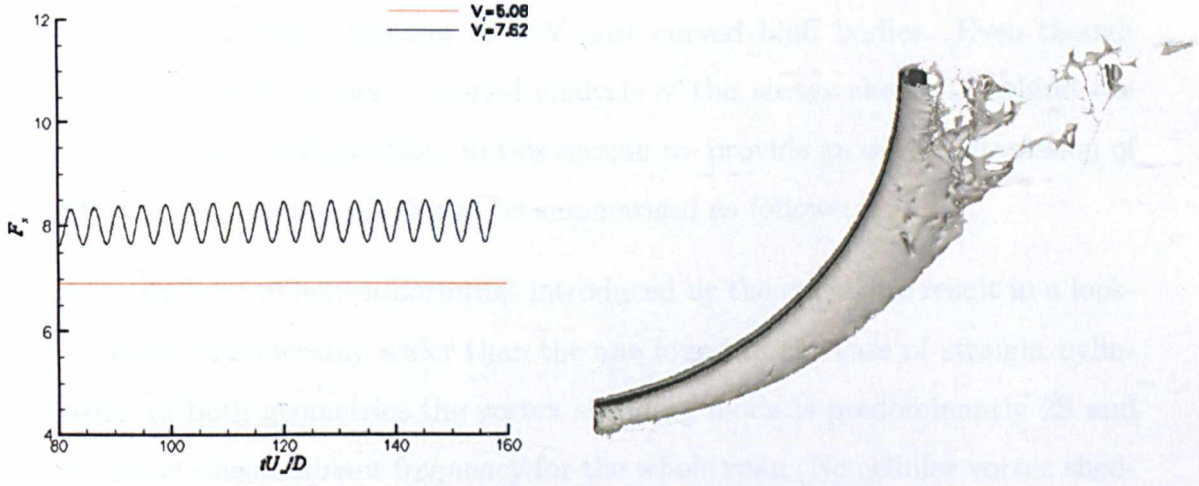


Figure 6.35: Concave body in free vibration, Case 3 and Case 2 with $\zeta = 0.012$. *Left*: drag force F_x against non-dimensional time. *Right*: isosurfaces for Case 3 at $\lambda_2 = -0.05$.

Chapter 7

Conclusions

The results presented aim to provide a general understanding of the influence of cylinder axial curvature on the mechanics of vortex shedding, yielding key information on the investigative approach needed to faithfully represent this phenomenon. In particular, forced and free vibration simulations have demonstrated how the wake dynamics triggered by non-straight geometries is affected by the motion of the body, adding an extra variable to an already complex problem. Although time limitations have restricted the number of physical parameters which can be varied in the simulations, the results presented in this work allow us to make conclusive remarks on some of the fundamental features of VIV past curved bluff bodies. Even though chapters 5 and 6 offer a more detailed analysis of the vortex shedding behind the convex and concave configuration, in this section we provide an overall discussion of the most relevant results, which can be summarised as follows:

- The geometrical non-uniformities introduced by the curvature result in a lock-in region considerably wider than the one found in the case of straight cylinders. In both geometries the vortex shedding mode is predominantly 2S and occurs at one dominant frequency for the whole span. No cellular vortex shedding is observed.

- The sectional flow approximation could not reproduce the vortex shedding past curved geometries. A fully three-dimensional approach is needed to correctly model the wake dynamics.

- In both configurations the part of the body aligned to the inflow acts as a hydro-dynamic damper for the whole structure: in the convex case, the force distribution in the horizontal extension is well predicted by equation (5.2) (Morison *et al.* (1950)).

- The length of the horizontal extension in the convex body does not influence the energy transfer mechanism and this configuration can be excited by the flow only when the horizontal addition is kept fixed in a roll-type motion about its axis.

- Vortex dislocations are observed in the wake of the convex configuration as a result of a frequency competition between the top and the bottom region of the body: two criteria are proposed to relate their spanwise position to the local cross-section diameter, to the curvature and to the imposed frequency.

- The narrow and wide wake topology observed past the concave body are related to the axial flow convection and to the gradient of the velocity component directed towards the top of the geometry. Only the narrow wake mode exhibits positive energy transfer: this mode was also successfully reproduced in free vibration simulations.

- The wide wake mode is associated with the steady wake observed past the fixed concave body, where a similar distribution of streamwise vorticity and axial flow takes place. It is suggested that the symmetry boundary condition imposed on the top plane has a strong influence on the wake mode.

- Forced vibration simulation could successfully approximate the wake dynamics and force distribution observed in free vibration.

Forced vibration simulations have shown how the lock-in phenomenon is strongly influenced by the deformation of the stagnation face: in the convex configuration, the lower boundary of the lock-in region in figure 5.5 appears shifted towards higher values of oscillation frequency, while in the concave case the lock-in region encompasses its two-dimensional counterpart on both sides, as shown in figure 6.3. In both

configurations, the flow region with high oscillation frequencies is characterised by in-phase shedding with cores bent according to the body's curvature, detaching from the shear layers in a 2S pattern: for the convex configuration this flow regime has been named "type A", whereas in the concave case it is referred to as a sub-regime of 2S shedding with a wide wake.

Close to the other boundary of the lock-in region (i.e. at low input frequencies of oscillation) two distinct shedding frequencies are observed, with a competition between the high frequency measured at the top of the body and the low one at the bottom: this phenomenon is particularly evident in the convex configuration, where it leads to a hybrid 2S-2P shedding generated by the alternation between the straight core shedding at the Strouhal frequency (which was also observed past the non-oscillating case) and the curved core shedding. In this latter mode, the vortex shedding is similar to type A, with the traditional interaction between the shear layers at a lower frequency always coinciding with the imposed frequency of oscillation. This type of shedding is found to be dominant, eventually taking control of the overall wake dynamics as the input frequency becomes closer to the Strouhal frequency. Consequently, the vortex dynamics in the lower half of the quarter ring, where the geometry is nearly parallel to the inflow direction, plays a crucial role in the convex geometry: in this region the cylinder behaves more like a slender body and the force distribution is correctly modelled by Morison's equation. This causes hydrodynamic damping, preventing the structure to be excited by the flow at all different combinations of amplitude and frequency of oscillation, and should thus be considered as an intrinsic feature of the convex body; however, at very low amplitudes the damping effect is attenuated and the structure can be excited by the flow, even though the positive energy transfer region for the convex configuration is considerably reduced when compared to the two-dimensional cylinder at the same Reynolds number.

Another interesting feature of this flow configuration is the presence of vortex dislocations that form periodically in the near-wake of the convex body at a frequency f_D equal to $f_{top} - f_{bottom}$. At this low Reynolds numbers the spontaneous vortex splitting is unusual; experiments in the previous research have shown that a

dislocation can be triggered by the introduction of spanwise non-uniformities, such as a ring of different diameter (Williamson (1992)). Based on these findings, two arguments are put forward to explain this phenomenon in the present case. The local cross-section of the curved body is an ellipse whose greater diameter D_e is larger than the circular cross-section diameter D: similar to the ring used by Williamson to force a dislocation at low Reynolds numbers, this introduces a different length scale in the problem. A relationship between diameter of the elliptic section and the dislocation position was found to hold in all the cases where the vortex splitting was observed. From a different perspective, the occurrence of the dislocation can be related to the angle of oblique shedding, in analogy with the relationship between the Strouhal number in the oblique and parallel shedding (Williamson (1989)). Substituting the value of the frequencies at the top and at the bottom of the body in this relationship yields a value for the angle of oblique shedding that identifies the same spanwise position for the dislocation given by the argument of the elliptical cross-section. This demonstrates that the spanwise position of the dislocation is primarily a function of the imposed frequency, whereas its occurrence is linked to the alternation between straight and curved core shedding: at low amplitudes and frequencies there is more time for the straight cores to form, while at high velocities the curved core shedding prevails.

To reduce the hydrodynamic damping from the lower region of the body, two modified convex geometries have been investigated: in the first case, the length of the horizontal extension has been halved, whereas the second change involved a double radius of curvature. The simulations have proved that the length of the horizontal extension does not alter the energy transfer mechanism: this result could be anticipated considering that the region which most affects the energy transfer is the lower half of the quarter ring, as shown by the spanwise distribution of the part of the lift coefficient in phase with the velocity. Similarly, the configuration with the double radius of curvature does not exhibit significant differences when compared to the original one: the time-averaged distribution of vertical normal and axial velocity extracted $0.3D$ upstream of the body shows a similar behaviour in both cases. This result confirms the importance of the axial flow convection along

the body's length in determining the distribution of the forces and their phasing: the shape of the leading edge is the predominant parameter and therefore a geometrical change involving a scaling of the radius of curvature does not have a significant effect on the flow dynamic, at least for the values analysed in this work. This is an important conclusion as it justifies the use of smaller models, hence reducing the size of the mesh and consequently the computational time.

As the two geometrical modifications did not yield substantial changes in the force distribution and vortex shedding phasing, a second type of motion has been imposed to the convex body to limit the damping contribution from the lower part of the body: the horizontal extension was kept fixed and an oscillatory roll motion about its axis was imposed to the body. Therefore, the amplitude of oscillation changes along the span according to the distance from the axis of each section, while the imposed frequency of oscillation remains constant. The imposed rotation led to positive excitation over large regions of the body's span, especially in the middle of the quarter ring, where the separation point was found to shift down the span: this gave rise to a constant phase change and to lift coefficient isocontours with a fixed inclination angle $\theta = 45°$ over the region of the body where the detaching point was moving. The resulting shedding appeared totally different from the modes observed in uniform cross-flow translation and was observed only in the case of a rotating geometry.

In the concave configuration, the shedding mode was again different from the 2S mode observed past the two-dimensional cylinder: a 2S mode of shedding with a wide wake and contracted shear layers was observed for oscillation frequencies above the Strouhal value, while a 2S mode with a narrow wake characterised the vortex shedding at lower oscillation frequencies. The wide wake mode was related to the steady wake with non-interacting shear layers observed past the non-oscillating body, which was found to suppress vortex shedding. The wide wake shedding was observed to be rather insensitive to changes in the oscillation amplitude: it seemed to be the result of the abrupt change of direction in the sinusoidal trajectory due to the high frequency of oscillation rather than being governed by the usual shear layer interaction described by Gerrard (1966).

Furthermore, the wide wake mode was associated in some cases to a very weak form of P+S shedding and always involved hydrodynamic damping. It is therefore not expected to occur in VIV problems: the free vibration simulations performed with input parameters set to match the ones in the wide wake mode confirmed this point, showing that the body could never be excited by the flow and exhibited an amplitude of response tending to zero. When compared to other simulations at different reduced velocities, this case also showed a drag reduction close to 15%, a value similar to the one obtained in the stationary body case. Both the dynamic controlling the onset of the wide wake mode in forced vibration and the vortex suppression in the absence of motion were strictly related to the convection of axial flow towards the top section of the body and to the subsequent vorticity redistribution in the wake of the body. A steep gradient of the axial and vertical velocity close to the surface of the body, as well as a change in sign in proximity of the top computational plane, were found to be common features of the two wake states. In the convex configuration, the axial flow convection pointed towards the bottom of the quarter ring and therefore its stabilising influence on the shear layers was directed away from the top of the body, which represents the critical region for the occurrence of vortex shedding. Similarly, it should be noted that the symmetry boundary condition imposed on the upper plane of the computational domain may play a key role in the vortex shedding past the concave configuration, as opposed to the convex geometry where the axial flow is convected in the opposite direction due to the different orientation of the curvature: the requirements prescribed by this boundary condition (i.e. $w = 0$ and $\frac{\partial u}{\partial z} = \frac{\partial v}{\partial z} = 0$) may be in conflict with the direction of the velocity vector in the sections just below the top plane. When the radius of curvature was doubled, the width of the wake in the wide wake mode appeared reduced: the time-averaged axial flow extracted $0.3D$ downstream of the body did not change in sign in the top region, suggesting a weakening of the wide wake mode due to the increment in the radius of curvature. This suggests that for less drastic curvatures the flow convected towards the top has more time to gradually adjust to the change of direction and satisfy the symmetry boundary condition on the upper plane; as previously discussed, this is not an issue in the convex configuration, where the axial

flow convection is directed towards the bottom of the body.

At frequencies of oscillation below the Strouhal value the mode of shedding changed to a narrow wake 2S which strictly resembled the vortex shedding past the two-dimensional cylinder. This mode was also characterised by the presence of higher harmonics in the lift signal at the top of the body and by a longer formation length. Further, the narrow wake 2S shedding was associated with positive energy transfer: free vibration results were in excellent agreement with the flow dynamics predicted by forced vibration simulations. Once the structural parameters in the free vibration were correctly set to match the forced vibration's amplitude and frequency, only minor differences in the wake topology and the spanwise distribution of sectional forces and of phase angle were observed in the two approaches.

Finally, it should be pointed out that in both configurations the vortex shedding within the lock-in region was dominated by one frequency along the whole length of the structure (the only exception being the convex body at very low amplitudes of oscillation): this contradicts the hypothesis that the shedding past curved geometries would result in cells with different shedding frequencies down the span of the body, as it is generally observed in the case of yawed or tapered cylinders. Such a behaviour would be predicted by a sectional approach based on the strip theory: by considering the component of the incoming flow normal to the body to be the solely responsible for hydrodynamic force generation, the sectional method neglects the axial convection of the flow and thus the physical dynamics related to it. Three-dimensional simulations have shown instead that this mechanism plays a crucial role in determining the vortex shedding mode and is significantly influenced by the orientation of the curvature. The absence of a hydrodynamic relationship among the two-dimensional planes represents a critical shortcoming in the application of the strip theory to non-straight geometries: the sectional code has no means to detect the orientation of the curvature and therefore cannot reproduce the radically different shedding features observed in the convex and concave configurations. The sectional approximation of the flow is thus not applicable in these conditions: the need of fully three-dimensional simulations poses severe limitations on the investigation of real-world offshore applications, especially conditioning the Reynolds number and

the aspect ratio of the pipes. However, the remarkably good agreement between the results in free and forced vibration encourages the use of the latter approach for VIV prediction, with a considerable saving in terms of computational time. Nonetheless, it should be remembered that forced vibration simulations can be used only as a preliminary to a fuller investigation, as they do not include the effect of important parameters such as mass ratio, stiffness and damping coefficients.

This work investigated the influence of curvature on the fluid dynamic loading on a structure of circular cross-section representing a simplified model for marine riser pipes. However, the simulations have been performed in conditions far from a real application environment: this work aims at offering a contribution on the fundamental vortex shedding mechanism of curved bodies and therefore only low Reynolds numbers have been considered. A natural extension of this research would be to study the effect of the Reynolds number variation, in the attempt to establish a relationship between the Reynolds and the Strouhal number in the case of curved geometries. Along the lines followed by previous research on straight cylinders, this direction of study may shed light on the occurrence of mode A and mode B in curved geometries and provide information on the types of instabilities that may develop. Simulations with different types of curvature could also be performed to gain more insight on the complex relationship between curvature and motion. In addition, it is suggested that a modified geometry with a vertical extension on the top of the quarter ring is tested to assess the influence of the top plane symmetry boundary condition on the vortex shedding, similar to the previous study on the fixed body. Finally, given the encouraging results obtained using the implementation of the moving frame of reference algorithm in the three-dimensional code, a more comprehensive study of these geometries in free vibration could lead to a complete picture of the phenomenon, potentially representing the final stage of this research.

Bibliography

Arkell, R. (1995). *Wake dynamics of cylinders encountering free surface gravity waves.* Ph. D. thesis, University of London.

Balasubramanian, S., Haan Jr., F., Szewczyk, A., & Skop, R. (2001). The occurrence of lock-in under highly sheared conditions. *Journal of Wind Engineering and Industrial Aerodynamics 89*, 757–784.

Barkley, D. & Henderson, R. (1996). Three-dimensional Floquet stability analysis of the wake of a circular cylinder. *Journal of Fluid Mechanics 322*, 215–241.

Bearman, P. (1965). Investigation on the flow behind a two-dimensional model with a blunt trailing edge and fitted with splitter plates. *Journal of Fluid Mechanics 21*, 241.

Bearman, P. (1967a). The effect of base bleed on the flow behind a two-dimensional body with a blunt trailing edge. *The aeronautical Quarterly 18*, 207–224.

Bearman, P. (1967b). On vortex streets wakes. *Journal of Fluid Mechanics 28*, 625–641.

Bearman, P. (1969). On vortex shedding from a circular cylinder in the critical Reynolds number regime. *Journal of Fluid Mechanics 37*, 577–587.

Bearman, P. (1984). Vortex shedding from oscillating bluff bodies. *Annual Review of Fluid Mechanics 16*, 195–222.

Bearman, P. (1998). Developments in the understanding of bluff body flows. *JMSE International Journal 41, Series B*, No.1.

Bearman, P. & Brankovic, M. (2004). Experimental studies of passive control of vortex-induced vibration. *European Journal of Mechanics, B 23*, 9–15.

Bearman, P., Downie, M., Graham, J., & Obasaju, E. (1985). Forces on cylinders in viscous oscillatory flow at low Keulegan-Carpenter numbers. *Journal of Fluid Mechanics 154*, 337–356.

Bearman, P. & Obasaju, E. (1982). An experimental study of pressure fluctuations on fixed and oscillating square-section cylinders. *Journal of Fluid Mechanics 119*, 297–321.

Bearman, P. & Owen, J. (1998). Reduction of bluff-body drag and suppression of vortex shedding by the introduction of wavy separation lines. *Journal of Fluids and Structures 12*, 123–130.

Bearman, P. & Tombazis, N. (1997). A study of the three-dimesional aspects of vortex shedding from a bluff body with a mild geometric disturbance. *Journal of Fluid Mechanics 330*, 85–112.

Berger, E. & Wille, R. (1972). Periodic flow phenomena. *Annual Review of Fluid Mechanics 4*, 313–340.

Bishop, R. & Hassan, A. (1964). The lift and drag forces on a circular cylinder oscillating in a flowing fluid. *Proceedings of the Royal Society of London. Series A. Mathematical and Physical Sciences 277*, 51–75.

Blackburn, H. (13-18 December 1998). A comparison of two- and three-dimensional wakes of an oscillating circular cylinder. In 13^{th} *Australian Fluid Mechanics Conference*, Monash University, Melbourne, Australia.

Blackburn, H. & Henderson, R. (1999). A study of two-dimensional flow past an oscillating cylinder. *Journal of Fluid Mechanics 385*, 255–286.

Blackburn, H. & Karniadakis, G. (1993). Two- and three-dimensional simulations of Vortex-Induced Vibration of a circular cylinder. In 3^{rd} *International Offshore & Polar Engineering Conference*, Volume 3, Singapore, pp. 715–720.

Blackburn, H., Marques, F., & Lopez, J. (2005). Symmetry breaking of two-dimensional time-periodic wakes. *Journal of Fluid Mechanics 522*, 395–411.

Blackburn, H., R.N., G., & Williamson, C. (2000). A complementary numerical and physical investigation of vortex-induced vibration. *Journal of Fluids and Structures 15*, 481–488.

Bloor, M. (1964). The transition to turbulence in the wake of a circular cylinder. *Journal of Fluid Mechanics 19*, 290.

Braza, M., Faghiani, D., & Persillon, H. (2001). Successive stages and the role of natural vortex dislocations in three-dimensional wake transition. *Journal of Fluid Mechanics 439*, 1–41.

Brede, M., Eckelmann, H., & Rockwell, D. (1996). On secondary vortices in the cylinder wake. *Physics of Fluids 8*, 2117–2124.

Carberry, J., Govardhan, R., Sheridan, J., Rockwell, D., & Williamson, C. (2004). Wake states and response branches of forced and freely oscillating cylinders. *European Journal of Mechanics, B 23*, 89–97.

Carberry, J., Sheridan, J., & Rockwell, D. (2001). Forces and wake modes of an oscillating cylinder. *Journal of Fluids and Structures 15*, 523–532.

Darekar, R. & Sherwin, S. (2001a). Flow past a bluff body with a wavy stagnation face. *Journal of Fluids and Structures 15*, 587–596.

Darekar, R. & Sherwin, S. (2001b). Flow past a square section-cylinder with a wavy stagnation face. *Journal of Fluid Mechanics 426*, 263–295.

Darekar, R. M. & Sherwin, S. J. (2001c). Flow past a square-section cylinder with a wavy stagnation face. *Journal of Fluid Mechanics 426*, 263–295.

Dutsch, H., Durst, F., Becker, S., & Lienhart, H. (1998). Low-Reynolds-number flow around an oscillating circular cylinder at low Keuleugan-Carpenter numbers. *Journal of Fluid Mechanics 360*, 249–271.

Eisenlohr, H. & Ecklemann, H. (1989). Vortex splitting and its consequences in the vortex street wake of cylinders at low Reynolds number. *Physics of Fluids A1*, 189–192.

Elston, J., Blackburn, H., & Sheridan, J. (2006). The primary and secondary instabilities of flow generated by an oscillating circular cylinder. *Journal of Fluid Mechanics 550*, 359–389.

Feng, C. (1968). The measurements of vortex-induced effects in flow past stationary and oscillating circular and D section cylinders. Master's thesis, University of British Columbia, Canada.

Flemming, F. & Williamson, C. (2005). Vortex-induced vibrations of a pivoted cylinder. *Journal of Fluid Mechanics 522*, 215–252.

Gaster, M. (1969). Vortex shedding from a slender cones at low Reynolds number. *Journal of Fluid Mechanics 38*, 565–576.

Gaster, M. (1971). Vortex shedding from a circular cylinder at low Reynolds number. *Journal of Fluid Mechanics 46*, 749–756.

Gerich, D. & Ecklemann, H. (1982). Influence of end plates and free ends on the shedding frequency of circular cylinders. *Journal of Fluid Mechanics 122*, 109–121.

Gerrard, J. (1966). Formation region of vortices behind bluff bodies. *Journal of Fluid Mechanics 25*, 401–413.

Gerrard, J. (1978). The wakes of cylindrical bluff bodies at low Reynolds numbers. *Philosophical Transaction of the Royal Society of London, Series A, Mathematical and Physical Sciences 288*, 351–382.

Govardhan, R. & Williamson, C. (2000). Modes of vortex formation and frequency response for a freely-vibrating cylinder. *Journal of Fluid Mechanics 420*, 85–130.

Graham, J. (1988). *Computation of viscous separated flow using a particle method. In: K.W. Morton, M.J. Baines (Eds.), Numerical Methods for Fluid Dynamics III (Inst. Math. Appl. Conf. Ser.)*, Volume 17. Oxford University Press.

Griffin, O. (1985). Vortex shedding from bluff bodies in a shear flow: a review. *ASME Journal of Fluids Engineering 107*, 298–306.

Gu, W., Chyu, C., & Rockwell, D. (1994). Timing of vortex formation from an oscillating cylinder. *Physics of Fluids 6*, 3677–3682.

Guermond, J. & Shen, J. (2003). A new class of truly consistent splitting schemes for incompressible flows. *Journal of Computational Physics 192*, 262–276.

Hammache, M. & Gharib, M. (1989). A novel method to promote parallel vortex shedding in the wake of circular cylinders. *Physics of Fluids A1*, 1611–1614.

Hammache, M. & Gharib, M. (1991). An experimental study of the parallel and oblique vortex shedding from circular cylinders. *Journal of Fluid Mechanics 232*, 567–599.

Henderson, R. (1995). A study of two-dimensional flow past an oscillating cylinder. *Physics of Fluids 7*, 2102–2104.

Hover, F., Techet, A., & Triantafyllou (1998). Forces on oscillating uniform and tapered cylinders in crossflow. *Journal of Fluid Mechanics 363*, 97–114.

Jauvtis, N. & Williamson, C. (2004a). The effect of two degrees of freedom on vortex-induced vibration at low mass and damping. *Journal of Fluid Mechanics 509*, 23–62.

Jauvtis, N. & Williamson, C. (2004b). A high-amplitude 2T mode of vortex-induced vibration for a light body in XY motion. *European Journal of Mechanics, B 23*, 107–114.

Jeong, J. & Hussain, F. (1995). On the identification of a vortex. *Journal of Fluid Mechanics 285*, 69–94.

Karniadakis, G. & Sherwin, S. (2005). *Spectral/hp element methods for computational fluid mechanics.* Oxford University Press.

Karniadakis, G. & Triantafillou, G. (1989). Frequency selection and asymptotic states in laminar wakes. *Journal of Fluid Mechanics 199*, 441.

Karniadakis, G. E., Israeli, M., & Orszag, S. A. (1991). High-order splitting methods for the incompressible Navier-Stokes equations. *Journal of Computational Physics 97*, 414–443.

Khalak, A. & Williamson, C. (1999). Motion, forces and mode transitions in vortex-induced vibrations at low mass-damping. *Journal of Fluids and Structures 13*, 813–851.

Krishnamoorthy, S., Price, S., & Paidoussis, M. (2001). Cross-flow past an oscillating circular cylinder: synchronization phenomena in the near wake. *Journal of Fluids and Structures 15*, 955–980.

Lam, K., Wang, F., Li, J., & So, R. (2004). Experimental investigation of the mean and fluctuating forces of wavy (varicose) cylinders in a cross-flow. *Journal of Fluids and Structures 19*, 321–334.

Lam, K., Wang, F., & So, R. (2004). Three-dimensional nature of vortices in the near wake of a wavy cylinder. *Journal of Fluids and Structures 19*, 815–833.

Leweke, T. & Provansal, M. (1995). The flow behind rings: bluff body wakes without end effects. *Journal of Fluid Mechanics 288*, 265–310.

Li, L., Sherwin, S., & Bearman, P. (2002). A moving frame of reference algorithm for fluid/structure interaction of rotating and translating bodies. *International Journal For Numerical Methods in Fluids 38*, 121–141.

Lu, X. & Dalton, C. (1996). Calculation of the timing of vortex formation from an oscillating cylinder. *Journal of Fluids and Structures 10*, 527–541.

Lucor, D., Imas, L., & Karniadakis, G. (2001). Vortex dislocations and force distribution of long flexible cylinders subjected to sheared flows. *Journal of Fluids and Structures 15*, 641–650.

Lucor, D. & Karniadakis, G. (2003). Effects of oblique inflow in Vortex-Induced Vibrations. *Flow, turbulence and combustion 71*, 375–389.

Lucor, D. & Karniadakis, G. (2004). Predictability and uncertainty in flow-structure interaction. *European Journal of Mechanics B/Fluids 23*, 41–49.

Marshall, J. (2003). Wake dynamics of a yawed cylinder. *Journal of Fluids Engineering 125*, 97–103.

Maull, D. & Young, R. (1973). Vortex shedding from bluff bodies in shear flow. *Journal of Fluid Mechanics 60*, 401–409.

Meneghini, J. & Bearman, P. (1995). Numerical simulations of high amplitude oscillatory flow about a circular cylinder. *Journal of Fluids and Structures 9*, 435–455.

Miliou, A. (2004). *Three-dimensional wake dynamics of curved cylinders.* Ph. D. thesis, Imperial College London.

Miliou, A., de Vecchi, A., Sherwin, S. J., & Graham, J. M. R. (2007). Wake dynamics of external flow past a curved cylinder with the free-stream aligned to the plane of curvature. *Journal of Fluid Mechanics 592*, 89–115.

Mittal, R. & Balachandar, S. (1995). Generation of stream-wise vortical structures in bluff body wakes. *Physical Review Letters 75*, 1300–1303.

Morison, J., O'Brien, M., Johnson, J., & Shaf, S. (1950). The force exerted by surface waves on piles. *Transactions of The American Institute of Mining and Metallurgical Engineers 189*, 149–157.

Mukhopadhyay, A., Venugopal, P., & Vanka, S. (1999a). Numerical study of vortex shedding from a circular cylinder in linear shear flow. *ASME, Journal of Fluids Engineering 121*, 460–468.

Mukhopadhyay, A., Venugopal, P., & Vanka, S. (1999b). Oblique vortex shedding from a circular cylinder in linear shear flow. *Computers and Fluids 31*, 1–24.

Nakagawa, K., Kishida, K., & Igarashi, K. (1998). Vortex-induced oscillation and lift of yawed circular cylinders in cross-flow. *Journal of Fluids and Structures 12*, 759–777.

Newman, D. & Karniadakis, G. (1996). Simulations if flow over a flexible cable: a comparison of forces and flow-induced vibration. *Journal of Fluids and Structures 10*, 439–453.

Newman, D. & Karniadakis, G. (1997). A direct numerical simulation study of flow past a freely vibrating cable. *Journal of Fluid Mechanics 344*, 95–136.

Nomura, T. & Hughes, T. (1992). An arbitrary Lagrangian-Eulerian finite element method for the interaction of fluid and a rigid body. *Computer Methods in Applied Mechanics and Engineering 95*, 115–138.

Nuzzi, F., Magness, C., & Rockwell, D. (1992). Three-dimensional vortex formation from an oscillating, non-uniform cylinder. *Journal of Fluid Mechanics 238*, 31–54.

Ongoren, A. & Rockwell, D. (1988). Flow structure from an oscillating cylinder Part 1. Mechanisms of phase shift and recovery in the near wake. *Journal of Fluid Mechanics 191*, 197–223.

Peiro', J., Peraire, J., & Morgan, K. (2004). *Felisa Manual.* Department of Aeronautics, Imperial College London.

Peiro', J. & Sayma, A. (1995). *A 3-D unstructured multigrid Navier-Stokes solver. In K.W. Morton, M.J. Baines (Eds.): Numerical Methods for Fluid dynamics, V.* Oxford University Press.

Peraire, J., Peiro', J., & Morgan, K. (1993). Multigrid solution of the 3-D compressible Euler equations on unstructured tetrahedral grids. *International Journal for Numerical Methods in Engineering 36*, 1029–1044.

Piccirillo, P. & Van Atta, C. (1993). An experimental study of vortex shedding behind linearly tapered cylinders at low Reynolds number. *Journal of Fluid Mechanics 246*, 163–195.

Ramberg, S. (1983). The effects of yaw and finite length upon the vortex wakes of stationary and vibrating circular cylinders. *Journal of Fluid Mechanics 128*, 81–107.

Roshko, A. (1954). On the development of turbulent wakes from vortex streets. *NACA report 1191*.

Roshko, A. (1955). On the wake and drag of bluff bodies. *Journal of the Aeronautical Sciences 124*, 124–132.

Roshko, A. (1993). Perspectives on bluff body aerodynamics. *Journal of Wind Engineering and Industrial Aerodynamics 49*, 79–100.

Ryan, K., Thompson, M., & Hourigan, K. (2007). Flow around a tethered body. *Journal of Fluid Mechanics 591*, 117–144.

Sarpkaya, T. (2004). A critical review of the intrinsic nature of vortex-induced vibrations. *Journal of Fluids and Structures 19*, 389–447.

Sherwin, S. & Karniadakis, G. (1996). Tetrahedral hp finite elements: algorithms and flow simulations. *Journal of Computational Physics 124*, 14–45.

Shiels, D., A., L., & Roshko, A. (2001). Flow-induced vibration of a circular cylinder at limiting structural parameters. *Journal of Fluids and Structures 15*, 3–21.

Sirisup, S., Karniadakis, G., Saelim, N., & Rockwell, D. (2004). DNS and experiments of flow past a wired cylinder at low Reynolds number. *European Journal of Mechanics, B 23*, 181–188.

Tatsuno, M. & Bearman, P. (1990). A visual study of the flow around an oscillating circular cylinder at low Keuleugan-Carpenter numbers and low Stokes numbers. *Journal of Fluid Mechanics 211*, 157–182.

Taubin, G. (1995). A signal processing approach to fair surface design. *Computer Graphics 29*, 351–358.

Taubin, G. (2001). Linear anisotropic mesh filtering. *IBM Research Report RC 22213*, T.J. Watson Research Center.

Techet, A., Hover, F., & Triantafyllou (1998). Vortical patterns behind a tapered cylinder oscillating transversely to a uniform flow. *Journal of Fluid Mechanics 363*, 79–96.

Thompson, M., Hourigan, K., & Sheridan, J. (1996). Three-dimensional instabilities in the wake of a circular cylinder. *'Experimental Thermal and Fluid Science 12*, 190–196.

Trim, A., Braaten, H., Lie, H., & Tognarelli, M. (2005). Experimental investigation of vortex-induced vibration of long marine risers. *Journal of Fluids and Structures 21*, 335–361.

Tritton, D. (1959). Experiments of the flow past a circular cylinder at low Reynolds number. *Journal of Fluid Mechanics 6*, 547–567.

Van Atta, C. & Gharib, M. (1987). Ordered and chaotic vortex streets behind circular cylinders at low Reynolds numbers. *Journal of Fluid Mechanics 174*, 113.

Vandiver, J., Allen, D., & Li, L. (1997). The occurrence of lock-in under highly sheared conditions. *Journal of Fluids and Structures 10*, 555.

Vikestad, K., Vandiver, J., & Larsen, C. (2000). Added mass and oscillation frequency for a circular cylinder subjected to vortex-induced vibrations and external disturbance. *Journal of Fluids and Structures 14*, 1071–1088.

von Kármán, T. (1912). *Nachrichten Gesellshaft Wissenshaften.* Gottingen.

Warburton, T. (1998). *Spectral/hp methods on polymorphic multi-domains: algorithms and applications.* Ph. D. thesis, Brown University.

Willden, R. (2003). *Numerical prediction of the Vortex-Induced Vibrations of marine riser pipes.* Ph. D. thesis, Imperial College London.

Willden, R. & Graham, J. (2001). Numerical prediction of VIV on long flexible circular cylinders. *Journal of Fluids and Structures 15*, 659–669.

Willden, R. & Graham, J. (2004). Multi-modal Vortex-Induced Vibrations of vertical riser pipe subject to a uniform current profile. *European Journal of Mechanics, B 23*, 209–218.

Willden, R., McSherry, R., & Graham, J. (2008). Prescribed cross-stream oscillations of a circular cylinder at laminar and early turbulent Reynolds numbers. *Proceedings of the Fifth Bluff Bodies and Vortex-Induced Vibration Conference, Brazil.*

Williamson, C. (1988). Defining a universal and continuous Strouhal-Reynolds number relationship for the laminar vortex shedding of a circular cylinder. *Physics of Fluids 31*, 3165.

Williamson, C. (1989). Vortex shedding in the wake of a circular cylinder at low Reynolds numbers. *Journal of Fluid Mechanics 206*, 579–627.

Williamson, C. (1992). The natural and forced formation of 'spot-like' vortex dislocations in transition of a wake. *Journal of Fluid Mechanics 243*, 393–442.

Williamson, C. (1996a). Three-dimensional wake transition. *Journal of Fluid Mechanics 328*, 345–407.

Williamson, C. (1996b). Vortex dynamics in the cylinder wake. *Journal of Fluid Mechanics 243*, 393–442.

Williamson, C. & Roshko, A. (1988). Vortex formation in the near wake of an oscillating cylinder. *Journal of Fluids and Structures 2*, 355–381.

Zdravkovich, M. (1982). Modification of vortex shedding in the synchronization range. *ASME, Transactions, Journal of Fluids Engineering 104*, 513–517.

Zdravkovich, M. (1990). On origins of hysteretic responses of a circular cylinder induced by vortex shedding. *Zeitschrift fur Flugwissenshaft und Weltraumforschung 14*, 47–58.

Zdravkovich, M. (1997). *Flow around circular cylinders*, Volume 1. Oxford University Press.